GNSS Reflectometry for Land Remote Sensing Applications

PhD Thesis Dissertation

by

Alejandro Egido Egido
Starlab Barcelona
alejandro.egido@starlab.es

Barcelona, May 2013

Supervised by:
Dr. Giulio Ruffini Forés
Starlab Barcelona

Tutored by:
Prof. Adriano José Camps Carmona
Signal Theory and Communications Dpt.
Universitat Politècnica de Catalunya

ABSTRACT

Soil moisture and vegetation biomass are two essential parameters from a scientific and economical point of view. On one hand, they are key for the understanding of the hydrological and carbon cycle. On the other hand, soil moisture is essential for agricultural applications and water management, and vegetation biomass is crucial for regional development programs. Several remote sensing techniques have been used to measure these two parameters. However, retrieving soil moisture and vegetation biomass with the required accuracy, and the appropriate spatial and temporal resolutions still remains a major challenge.

The use of Global Navigation Satellite Systems (GNSS) reflected signals as sources of opportunity for measuring soil moisture and vegetation biomass is assessed in this PhD Thesis. This technique, commonly known as GNSS-Reflectometry (GNSS-R), has gained increasing interest among the scientific community during the last two decades due to its unique characteristics. Previous experimental works have already shown the capabilities of GNSS-R to sense small reflectivity changes on the surface. The use of the co- and cross-polarized reflected signals was also proposed to mitigate nuisance parameters, such as soil surface roughness, in the determination of soil moisture. However, experimental evidence of the suitability of that technique could not be demonstrated. This work analyses from a theoretical and an experimental point of view the capabilities of polarimetric observations of GNSS reflected signals for monitoring soil moisture and vegetation biomass.

The Thesis is structured in four main parts. The first part examines the fundamental aspects of the technique and provides a detailed review of the GNSS-R state of the art for soil moisture and vegetation monitoring. The second part deals with the scattering models from land surfaces. A comprehensive description of the formation of scattered signals from rough surfaces is provided. Simulations with current state of the art models for bare and vegetated soils were performed in order to analyze the scattering components of GNSS reflected signals. A simplified scattering model was also developed in order to relate in a straightforward way experimental measurements to soil bio-geophysical parameters. The third part reviews the experimental work performed within this research. The development of a GNSS-R instrument for land applications is described, together with the three experimental campaigns carried out in the frame of this PhD Thesis. The analysis of the GNSS-R and ground truth data is also discussed within this part. As predicted by models, it was observed that GNSS scattered signals from natural surfaces are a combination of a coherent and an incoherent scattering components. A data analysis technique was proposed to separate both scattering contributions. The use of polarimetric observations for the determination of soil moisture was demonstrated to be useful under most soil conditions. It was also observed that forests with high levels of biomass could be observed with GNSS reflected signals. The fourth and last part of the Thesis provides an analysis of the technology perspectives. A GNSS-R End-to-End simulator was used to determine the capabilities of the technique to observe different soil reflectivity conditions from a low Earth orbiting satellite. It was determined that high accuracy in the estimation of reflectivity could be achieved within reasonable on-ground resolution, as the coherent scattering component is expected to be the predominant one in a spaceborne scenario.

The results obtained in this PhD Thesis show the promising potential of GNSS-R measurements for land remote sensing applications, which could represent an excellent complementary observation for a wide range of Earth Observation missions such as SMOS, SMAP, and the recently approved ESA Earth Explorer Mission Biomass.

RESUMEN

La humedad del suelo y la biomasa de la vegetación son dos parametros clave desde un punto de vista tanto científico como económico. Por una parte son esenciales para el estudio del ciclo del agua y del carbono. Por otra parte, la humedad del suelo es esencial para la gestión de las cosechas y los recursos hídricos, mientras que la biomasa es un parámetro fundamental para ciertos programas de desarrollo. Varias formas de teledetección se han utilizado para la observación remota de estos parámetros, sin embargo, su monitorización con la precisión y resolución necesarias es todavía un importante reto tecnológico.

Esta Tesis evalua la capacidad de medir humedad del suelo y biomasa de la vegetación con señales de Sistemas Satelitales de Posicionamiento Global (GNSS, en sus siglas en inglés) reflejadas sobre la Tierra. La técnica se conoce como Reflectometría GNSS (GNSS-R), la cual ha ganado un creciente interés dentro de la comunidad científica durante las dos últimas décadas. Experimentos previos a este trabajo ya demostraron la capacidad de observar cambios en la reflectividad del terreno con GNSS-R. El uso de la componente copolar y contrapolar de la señal reflejada fue propuesto para independizar la medida de humedad del suelo de otros parámetros como la rugosidad del terreno. Sin embargo, no se pudo demostrar una evidencia experimental de la viabilidad de la técnica. En este trabajo se analiza desde un punto de vista teórico y experimental el uso de la información polarimétrica de la señales GNSS reflejadas sobre el suelo para la determinación de humedad y biomasa de la vegetación.

La Tesis se estructura en cuatro partes principales. En la primera parte se evalúan los aspectos fundamentales de la técnica y se da una revisión detallada del estado del arte para la observación de humedad y vegetación. En la segunda parte se discuten los modelos de dispersión electromagnética sobre el suelo. Simulaciones con estos modelos fueron realizadas para analizar las componentes coherente e incoherente de la dispersión de la señal reflejada sobre distintos tipos de terreno. Durante este trabajo se desarrolló un modelo de reflexión simplificado para poder relacionar de forma directa las observaciones con los parámetros geofísicos del suelo. La tercera parte describe las campañas experimentales realizadas durante este trabajo y discute el análisis y la comparación de los datos GNSS-R con las mediciones in-situ. Como se predice por los modelos, se comprobó experimentalmente que la señal reflejada está formada por una componente coherente y otra incoherente. Una técnica de análisis de datos se propuso para la separación de estas dos contribuciones. Con los datos de las campañas experimentales se demonstró el beneficio del uso de la información polarimétrica en las señales GNSS reflejadas para la medición de humedad del suelo, para la mayoría de las condiciones de rugosidad observadas. También se demostró la capacidad de este tipo de observaciones para medir zonas boscosas densamente pobladas. La cuarta parte de la tesis analiza la capacidad de la técnica para observar cambios en la reflectividad del suelo desde un satélite en orbita baja. Los resultados obtenidos muestran que la reflectividad del terreno podría medirse con gran precisión ya que la componente coherente del scattering sería la predominante en ese tipo de escenarios.

En este trabajo de doctorado se muestran la potencialidades de la técnica GNSS-R para observar remotamente parámetros del suelo tan importantes como la humedad del suelo y la biomasa de la vegetación. Este tipo de medidas pueden complementar un amplio rango de misiones de observación de la Tierra como SMOS, SMAP, y Biomass, ésta última recientemente aprobada para la siguiente misión Earth Explorer de la ESA.

Acknowledgements

The current Thesis is the completion of a long process in which a lot of people have contributed in many significant ways. The first two people to whom I would like to express my most sincere gratitude are my Thesis advisor, Giulio Ruffini, for giving me the opportunity to developed this research at Starlab, and Adriano Camps, for his support and extremely useful advices during these years of intense work.

Very special thanks to all the crew at Starlab for making these years a once in a lifetime experience. I cannot name all the incredible people I met at Starlab and special moments we went though without turning this acknowledge section in a ten page chapter, but I would maybe like to point out Marco's extremely useful and helpful guidance during these years; the early days enlightenment of the French troupe at Starlab, Olivier and François, who together with Giulio and Marco, discovered me GNSS-R; the kind collaboration and cheerfulness of Xavi and Damià during the SAM project; Cristina's both iron fist and kind project management; the extremely enriching discussions I had with Miquel, Jose, and Esteve; and most especially to Erwan, aka Dr. *Morten Weat*, who helped me with the preparation, development, and made possible the success of most of the experimental campaigns presented in this work, and with whom I share so many special moments and *trip-tale*s. Thank you so much to all of you for helping me growing up so much not only technically, but also professionally and personally.

I would also like to thank people from other institutions, such as the technical officers at the European Space Agency, Nicolas Floury, Christopher Buck, Salvatore D'Addio, and Manuel Martin-Neira, who through their comments and support contributed to increase the quality of the projects. I should also have a special word for our colleagues at the Institute of Applied Physics (IFAC-CNR), Simonetta Paloscia, Emanuele Santi, Marco Brogioni, Simone Pettinato, and Giacomo Fontanelli who made possible the experimental campaigns of the LEiMON and GRASS projects; for Nazzareno Pierdicca from La Sapienza University in Rome for the valuable discussions and comments on the technical aspects of the observation technique, and particularly for Leila Guerriero, from the Tor Vergata University in Rome, with whom I had innumerable brain-watering conversations trying to link the theory of models with the reality of the data. I would also like to thank Jose Luis Álvarez-Pérez for his useful and clarifying insights on the scattering from rough surfaces. Last but not least, to Fran Fabra from IEEC with whom I shared some of the arduous moments of this long process.

I want to have some very special words for Ramon Torres, who opened me the door of the European Space Agency and allowed me to enter the world of Remote Sensing. My most sincere gratitude to him, as most probably without his initial push this Thesis would not have come true.

Thank you very much to all my friends and family who supported me and kept me going even in the toughest moments. Particularly, to my parents Felipe and Laura, and my sister Julia, who with your example of life-long effort and perseverance gave me the best encouragement I could have. And finally, and most importantly, to Ana. I can not possibly express with words all my gratitude for you. Your infinite kindness, patience, and understanding made this Thesis possible.

Contents

List of Figures

List of Tables

List of Acronyms

ADC	Analog to Digital Converter
AGB	Above Ground Biomass
AIEM	Advanced Integral Equation Model
ALOS	Advanced Land Observing Satellite
AMSR-E	Advanced Microwave Scanning Radiometer
AR	Axial Ratio
ASAR	Advanced Synthetic Aperture Radar
BOC	Binary Offset Carrier
BPSK	Binary Phase Shift Keying
C/A-code	Coarse Acquisition Code
CBOC	Composite BOC
CDMA	Code Division Multiple Access
CETEM	Centre for Microwave remote sensing
CS	Commercial Service
CYGNSS	Cyclone Global Navigation Satellite System
DDM	Delay-Doppler Map
DMR	Delay Mapping Receiver
DMSS	Directional Mean Square Slope
DoY	Day of the Year
DS-SS	Direct Sequence Spread Spectrum
ECV	Essential Climate Variables
EGNOS	European Geostationary Navigation Overlay Service
Envisat	Environmental Satellite
EOS	Earth Observing System
ERS	European Remote Sensing
ESA	European Space Agency
EU	European Union
EVI	Enhanced Vegetation Index
FDMA	Frequency Division Multiple Access
FDR	Frequency Domain Reflectometry
GLAS	Geoscience Laser Altimeter System
GNSS	Global Navigation Satellite System
GNSS-R	GNSS-Reflectometry
GSV	Growing Stock Volume
GO	Geometric Optics
GPS	Global Positioning System
ICESat	Ice, Cloud and land Elevation Satellite
ICF	Interferometric Complex Field
IEM	Integral Equation Model
IFAC-CNR	Institute of Applied Physics - Natural Research Council
IF	Intermediate Frequency
JAXA	Japan Aerospace Exploration Agency
KA	Kirchoff Approximation

LAI	Leaf Area Index
LEO	Low Earth Orbit
LIDAR	Light Detection and Ranging
LHCP	Left Hand Circular Polarization
LNA	Low Noise Amplifiers
M-code	Military Code
MCS	Master Control Station
MERIS	Medium Resolution Imaging Spectrometer
MIRAS	Microwave Interferometric Radiometer by Aperture Synthesis
MODIS	Moderate Resolution Imaging Spectroradiometer
NF	Noise Figure
OS	Open Service
PLF	Polarization Loss Factor
PLL	Phase Locked-Loop
PolInSAR	Polarimetric SAR Interferometry
NASA	National Aeronautics and Space Administration
NDVI	Normalized Difference Vegetation Index
P(Y)-code	Precise (Encrypted) Code
PALSAR	Phased Array type L-band Synthetic Aperture Radar
PARIS	PAssive Reflectometry and Interferometry System
PARIS-IOD	PARIS In Orbit Demonstrator
PO	Physical Optics
PRN	Pseudo-Random Noise
PRS	Public Regulated Service
PWC	Plant Water Content
REDD+	Reducing Emissions from Deforestation and Forest Degradation
RF	Radio Frequency
RHCP	Right Hand Circular Polarization
RMSE	Root Mean Square Error
SaR	Searh and Rescue Service
SAR	Synthetic Aperture Radar
SMAP	Soil Moisture Active Passive
SMC	Soil Moisture Content
SMOS	Soil Moisture and Ocean Salinity
SNR	Signal to Noise Ratio
SoL	Safety-of-Life Service
SPM	Small Perturbation Method
SPOT	Systeme Pour l'Observation de la Terre
TDR	Time Domain Reflectometry
TOW	Time Of the Week
TT-C	Tracking Transmission and Control
UK-DMC	UK Disaster Monitoring Constellation
UNFCCC	United Nations Framework Convention on Climate Change
VI	Vegetation Indices
VWC	Vegetation Water Content
WAAS	Wide Area Augmentation System
WAF	Woodward Ambiguity Function

Preface

The use of Global Navigation Satellite System (GNSS) reflected signals as sources of opportunity for remote sensing applications, commonly known as GNSS-Reflectometry (GNSS-R), has gained increasing interest among the scientific community over the last two decades. During this period, several applications based on a GNSS bistatic radar configuration have been developed taking advantage of the high availability and stability of GNSS signals.

In GNSS-R, a passive receiver simultaneously gathers the direct and reflected signals from various GNSS satellites to retrieve geophysical parameters from the scattering surface. This technique has already been proven to be an excellent asset to monitor the Earth, as demonstrated in numerous ground-based, airborne, and space-borne experiments.

With the modernization of Global Positioning System (GPS) (United States) and GLONASS (Russia), and the forthcoming arrival of Galileo (European Union), an increasing number of GNSS satellites broadcasting improved quality signals will be available, which will contribute to enhance the retrieval and coverage capabilities of GNSS-R. In this context, the European Space Agency (ESA) and the National Aeronautics and Space Administration (NASA) are promoting two dedicated GNSS-R spaceborne missions: the former, i.e., PARIS In Orbit Demonstrator (PARIS-IOD), is devoted to demonstrate the capabilities of the technique for a mesoscale altimetry mission; the latter, the Cyclone Global Navigation Satellite System (CYGNSS), is an 8 GNSS-R satellite constellation for the monitoring of cyclones and high wind events in the sub-tropical region.

The current PhD Thesis Dissertation is aimed at analyzing the capabilities of GNSS-R as a remote sensing tool for soil moisture and vegetation biomass monitoring. This research work was carried out at Starlab Barcelona, a company which has been an important and active part in the development of GNSS-R, with multiple activities in this field. The work presented here was performed fundamentally in the frame of three successive contracts with the European Space Agency. Chronologically, those are:

- The SAM project (An Innovative Microwave System for Soil Moisture Monitoring, 2007–2008, ESA/ESTEC Contract No. 20898/07/NL/ST/na), devoted to the design, development, and testing, of a polarimetric GNSS-R instrument for land applications.
- The LEiMON project (Land Monitoring with Navigation Signals, 2009–2011, ESA/ESTEC Contract No. 22117/08/NL/AF), focused on the investigation of the scattering properties of GNSS signals over bare and vegetated soils, through theoretical modeling and long term on-ground experimental campaign.

– The GRASS project (GNSS Reflectometry Analysis for Biomass Monitoring, 2011–2012, ESA/ ESTEC Contract No. 4000103329/11/NL/CVG), concentrated on the assessment of GNSS-R observables sensitivity to plant and forest biomass. Several airborne experimental campaigns and further theoretical modeling were performed for this purpose.

The work carried out in the LEiMON and GRASS projects is the result of a combined effort of: Starlab Barcelona, Spain; the Institute of Applied Physics - Natural Research Council (IFAC-CNR), Italy; and the Centre for Microwave remote sensing (CETEM), Italy. During these two projects Starlab was in charge of the GNSS-R instrument, the experimental campaigns, and the GNSS-R data analysis and interpretation, whereas IFAC-CNR and CETEM concentrated in the development of the scattering models to describe the interactions of GNSS signals with land surfaces. Apart from the previously listed projects, other GNSS-R related activities were developed during the course of this PhD which contributed to nurture this research work. A complete enumeration of these activities is provided in Appendix A. The publications that arose from those activities are gathered in Appendix B.

This Thesis is organized in four main parts. The first part deals with introductory concepts of the technique; in Chapter 1 the importance of soil moisture and vegetation is analysed, and the main remote sensing techniques that have been used so far for the monitoring of soil moisture and vegetation are considered. Chapter 2 provides an introduction to Global Navigation Satellite Systems and reviews the most important characteristics of the available signals in space. In Chapter 3 the state of the art in GNSS-R is examined, and the fundamental aspects of the technique are presented. The second part deals with the modeling of the measured GNSS signals; in Chapter 4 the main terrain scattering models over bare and vegetated soils are reviewed, and in Chapter 5 a model of the measured scattering coefficients as observed by a GNSS-R instrument is described. Part 3 reviews the experimental work undertaken within this research: in Chapter 6 the design and development of a polarimetric GNSS-R instrument for land observations is detailed; Chapter 7 describes the experimental campaigns performed during the three aforementioned projects; in Chapter 8, the analysis and main results obtained from the GNSS-R data acquired during the experimental campaigns are presented. The fourth and last part discusses the outlook of the technology. In Chapter 9, the prospects of a spaceborne GNSS-R receiver for monitoring soil moisture and vegetation are assessed, and finally, Chapter 10 gathers the general conclusions of the research and provides recommendations for future work.

Part I

Background

Chapter 1

Introduction

Land processes are of main relevance for the understanding of the Earth's system from both a scientific and economical point of view. Due to this fact, several remote sensing techniques have been used during the last decades to monitor key land bio-geophysical parameters, such as soil moisture and vegetation biomass, in local and global scales. This first introductory chapter reviews the general context for the development of this PhD Thesis. The next section discusses the importance of both soil moisture and vegetation above ground biomass. The second section reviews the remote sensing techniques that have been used until now to monitor these parameters. Finally, in the third section, the motivation of this research work is presented.

1.1 The Importance of Soil Moisture and Vegetation

Understanding the natural processes and the effects of human intervention in our planet is of paramount importance to guarantee a prosperous and sustainable living for future generations. Soil moisture and vegetation biomass are key parameters for this purpose. From a scientific point of view, both of them have been identified by the United Nations Framework Convention on Climate Change (UNFCCC) as Essential Climate Variables (ECV), needed to reduce uncertainties in our knowledge of the climate system [GCOS, 2012]. From an economical point of view, both soil moisture and vegetation are of major relevance in the agricultural sector, one of the biggest markets worldwide. Proof of this importance are the increasing efforts of national governments and space agencies, specially European Space Agency (ESA) and the US National Aeronautics and Space Administration (NASA), to measure these two parameters with the appropriate accuracy and resolution requirements. The next subsections review in more detail the relevance of these two parameters.

1.1.1 Soil Moisture as an Essential Climate Variable

To appreciate the relevance of soil moisture in climatological studies it is necessary to take into consideration its role within the hydrological cycle, i.e., the continuous circulation of water between the oceans, atmosphere and land in a never-ending process.

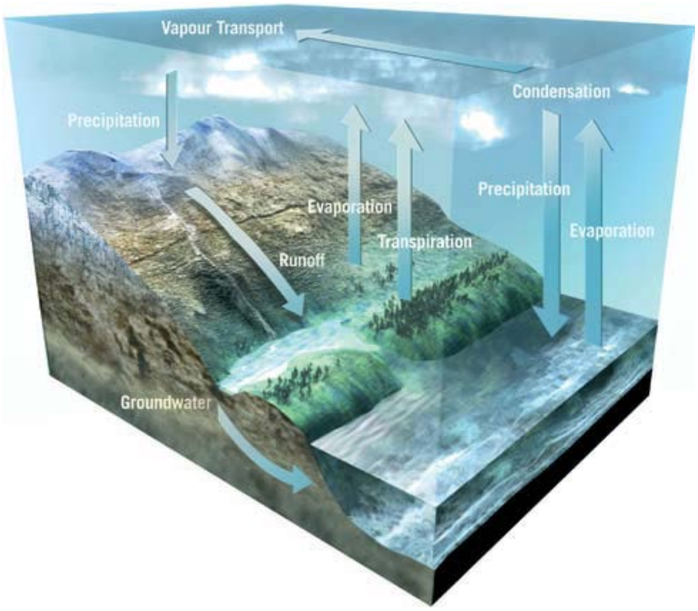

Figure 1.1: The Earth's water cycle [ESA, 2010].

The hydrological cycle determines the Earth's climate and is responsible for much of the natural weather variability. The cycle starts with the warming of the ocean surface by the effect of sunlight, mostly in the tropical areas, leading to the evaporation of the top layer of water. In this process, the oceans lose heat (latent heat of vaporization), which prevents the global temperature from rising, and the generated water vapor is driven away by winds from the tropics. When it condenses as rain, the latent heat stored in the vapor is released, warming the air, and inducing atmospheric circulation [NASA, 2008]. Figure 1.1 shows a pictorial representation of this process.

Despite the fact that 90% of the total atmospheric water vapor is generated over the oceans, the remaining 10% is provided by plant transpiration and evaporation from soil [ESA, 2010]. It is in this part where soil moisture plays an important role in the hydrological cycle as there is a direct link between soil moisture and atmospheric humidity; wet soils contribute to a large extent to air moisture, whereas dry soils have very little or negligible contributions. In addition, water storage in the soil affects its thermal conductivity and contributes to regulate the surface temperature through an evapo-transpiration process (in a similar way as for the oceans), thus having a remarkable impact on the water and energy fluxes in the land and lower atmosphere interface. Simulations with numerical weather prediction models have also shown that improved surface soil moisture measurements can lead to remarkable improvements in forecasts.

The measurement of soil moisture on global and regional scales could also be of great benefit for a vast number of applications and human activities. Perhaps, the most representative one is agriculture, as it is one of the most important aspects for life support of humans and livestock and constitutes the major available source of food. In addition, a wide variety of other products such as fibers, fuels and raw materials are obtained from the land. Economically, the agricultural sector represents a huge market that moves billions of Euros and involves millions of people around the globe. Due to the population increase, chemical industry diversification, and the rise in biofuel demand, there is a steadily increase in agricultural products demand. However, the cultivable land surface area is most of the times limited. In addition, the outcome

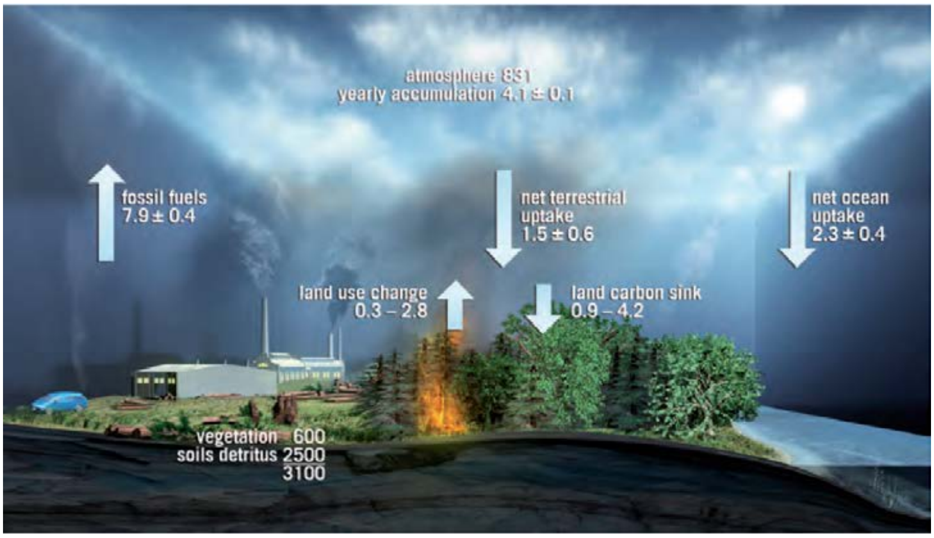

Figure 1.2: Pictorial Representation of the Earth's Carbon Cycle [ESA, 2012a]. The overimposed numbers and arrows on the figure show the estimated size of carbon pools and fluxes in gigatonnes (GtC) of carbon and GtC per year, respectively.

of agricultural processes depends on trends in the natural environment. Particularly important are the more than likely water shortages that many areas are going to face as a consequence of climate change. This urges the development of improved agricultural and water management techniques in order to keep the required harvest-yield and preserve accessible water reservoirs, for which soil moisture will undoubtedly be one of the primary variables to be closely monitored. Flood prediction, surface runoffs after rainfall events, drought monitoring, weather forecasting, are examples of other applications in which soil moisture observations could have a positive socio-economical impact.

1.1.2 Vegetation as an Essential Climate Variable

Vegetation is critical for life support of humans and animals, and in spite of severe human constructions, it covers much of the Earth's land surface constituting a parameter of prime importance in global climate through the carbon cycle.

In this continuous process carbon is exchanged between the atmosphere, land and oceans. This is crucial for life sustainability as it allows carbon to be reused throughout the biosphere and its organisms. It has also a major relevance in climate and climate change, as carbon exists in the atmosphere primarily in the form of CO_2 (among other compounds); one of the most important causes for the greenhouse effect and the most important human-generated greenhouse gas. Although levels of CO_2 in the atmosphere have fluctuated along different geological timescales, fossil fuel combustion and land-use change have generated in the last decades a drastic increase of CO_2 concentrations. This disturbance in the carbon cycle is believed to be the major contributor to global change [IPCC, 2007]. Quantifying carbon stocks and fluxes between the different pools is therefore essential for the understanding of the dramatic changes occurring in the Earth's system.

A fundamental parameter characterizing the spatial distribution of carbon in the biosphere is biomass, i.e., the amount of organic matter in a given space, which is 50%

constituted by carbon. The terrestrial biospheric carbon pool, biomass and soil organic matter, is roughly four times that of the atmosphere. Forests comprise around 80% of the total above-ground biomass, which represents a total carbon content equivalent to that of the atmosphere. Moreover, terrestrial carbon fluxes play a central role in the carbon cycle through carbon uptake associated with vegetation growth, and emissions from wild fires and land-use change due to human activity. There is a strong evidence that the terrestrial biosphere has acted as a net carbon sink over the last 50 years, absorbing one third of the CO_2 emitted by fossil fuel combustion [ESA, 2012a].

Given its clear relevance for the estimation of carbon inventories, the UNFCCC has set up an initiative for Reducing Emissions from Deforestation and Forest Degradation (REDD+) in order to promote the sustainable management of forests, reduce CO_2 emissions, and thereby mitigate climate change. The program comprises a set of market and financial incentives, which will also have some additional benefits for the countries where it is introduced due to the positive effect that REDD+ can have to alleviate poverty. The reliable monitoring of forests and the carbon accounting on which REDD+ is based is therefore essential to this program.

In addition to the great benefits that precise forest and vegetation biomass measurements can provide for climatological studies, the knowledge of vegetation cover provides also the basis for an optimized land resource management as well as regional development assessments. As in the case of soil moisture, monitoring of pastures and crops is of main importance for local and national governments in order to perform improved yield estimates, together with irrigation and harvest control. This will become even more important in the next decades due to the afore mentioned world's population increase and climate change, as global warming is likely to have a dramatic effect on harvest yields.

1.2 Remote Sensing Techniques for Measuring Soil Moisture and Vegetation Parameters

Nowadays the most common way to measure soil moisture is with in-situ sensors. Those can either be portable sensing probes that can be pushed directly into the ground and access tubes, or buried sensors hard-wired to a fixed meter or attached by long cables to a central data logger to monitor a certain area [Starlab, 2008]. In the case of vegetation, extensive in-situ campaigns are usually conducted to measure relevant vegetation parameters such as above ground biomass, vegetation water content, plant height, etc. These techniques, despite their high measurement reliability, remain inappropriate to cover regional and global scales given the vast amount of resources that would be necessary to perform such campaigns.

In order to bridge this gap, several remote sensing methods have been proposed for the estimation of soil moisture and vegetation. Depending on the source of the observed electromagnetic radiation, those can be separated among active and passive sensors. The former provide their own source of illumination and measure the power reflected back to the instrument or to a separate receiver. The latter gather the Sun radiation scattered off the Earth surface, or the natural radiation from bodies. The fundamental characteristics of these techniques are reviewed in the subsequent sections.

1.2.1 Soil Moisture Remote Sensing

Soil moisture remote sensing is based on the large contrast of the dielectric properties of wet and dry soils throughout most of the electromagnetic spectrum. Active and passive sensors have been used from airborne and spaceborne platforms for the estimation of the scattering properties of soil, which can then be used to estimate soil moisture. Among the active sensors used for this purpose, one could essentially identify microwave radars, while on the passive side, optical spectrometers and microwave radiometers are the most important ones.

1.2.1.1 Active Sensors for Soil Moisture Estimation

Microwave radars are probably the most commonly used instruments in remote sensing and have been extensively used for a wide number of different applications. Initially developed for military purposes, these systems soon became a very important tool for Earth observation purposes. Radars transmit electromagnetic pulses which are then received with the same (monostatic) or a different antenna (bistatic) from the transmitting one. The transmitted pulses are usually frequency modulated in order to be able to transmit high bandwidth signals in relatively long pulses, which allows to maintain high Signal to Noise Ratio (SNR) [Curlander and McDonough, 1991]. This is the so called Chirp signal. When the radar echoes are received they are cross-correlated with the transmitted pulse (matched-filtering). This process is known as pulse compression and results in a final range resolution that equals $X_r = c/2\Delta f$, where c is the speed of light, and Δf the Chirp signal bandwidth.

There are two types of radars, imaging and non-imaging radars. Non-imaging radars are altimeters and scatterometers. The former are primarily used to measure height over the oceans and the cryosphere. The latter are normally used to obtain wind speed and direction over the seas. Despite of their primary applications, all these types of radars have also been used to measure soil moisture over extended areas. See for example in Fig. 1.3 soil moisture maps obtained with the European Remote Sensing (ERS) scatterometer data, as shown in [Pathe et al., 2009].

Imaging radars can also be divided into real and synthetic aperture radars. These systems are set in a side-looking configuration in order to avoid ambiguities from targets on each side of the sub-satellite track. For both of them the range resolution is attributable to the high bandwidth of the transmitted signals. However, in the case of real aperture radars, the azimuth or along-track resolution is determined by the antenna beam-width and is dependent on the distance of the radar to the target. On the other hand, Synthetic Aperture Radars (SARs) are capable of taking advantage of the platform's movement to coherently combine a successive set of radar pulses, see Fig. 1.4(a). This creates a synthetic aperture that allows to improve the final along-track resolution.

In essence, what happens is that each single point on the surface is observed with a different Doppler frequency shift originated due to the relative movement of the platform and the single targets; at time $t = -\tau$ the radar starts seeing a target on the surface with the main beam of the antenna and Doppler frequency of $+f_{\mathrm{Dmax}}$; when the target is at the antenna's boresight, $t = 0$ for convention, the platform's radial velocity with respect to the ground equals 0, and therefore the Doppler frequency of the returned echoes is null; at $t = +\tau$ the point target on the aft edge of the antenna beam with a

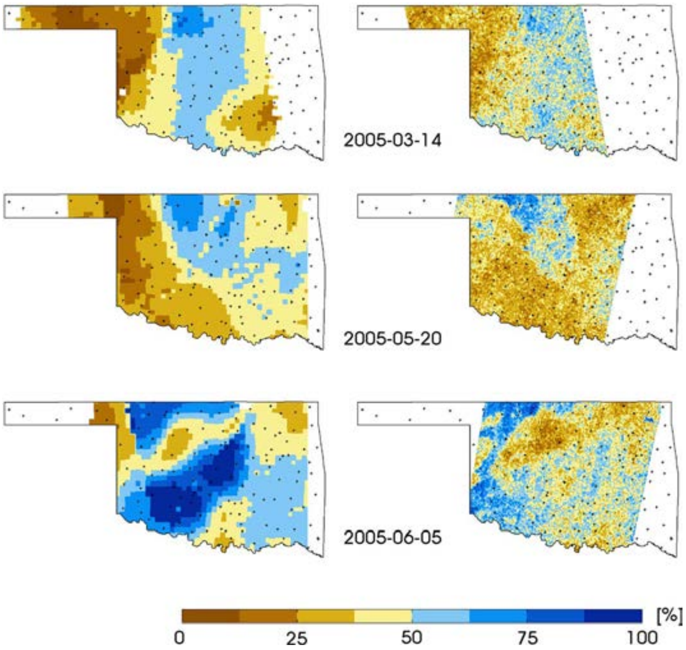

Figure 1.3: Surface soil moisture maps of Oklahoma retrieved from ERS scatterometer (left) and ASAR (right) measurements for three different dates in 2005, from [Pathe et al., 2009]. The ERS images have a resolution of 40 km, whereas the ASAR images have a resolution of 1 km.

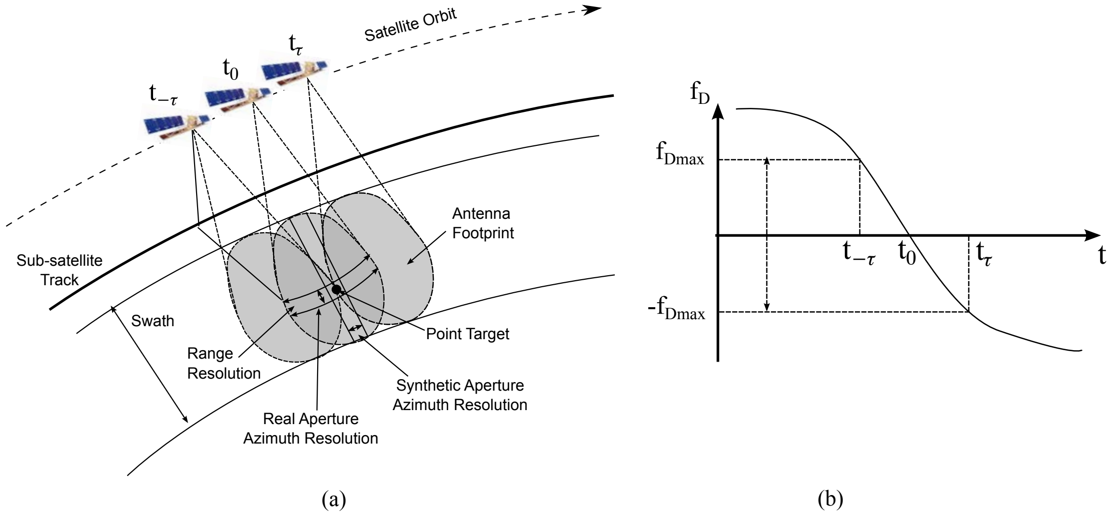

Figure 1.4: (a) SAR Geometry and (b) observed Doppler frequency shift for a single point on the surface throughout the whole illumination period, 2τ.

Doppler frequency shift of $-f_{\mathrm{Dmax}}$. See Fig. 1.4(b). The full Doppler bandwidth, Δf_D for each target is therefore $2f_{\mathrm{Dmax}}$. After some approximations it can be shown that $\Delta f_D = 2v_p/L$, where v_p is the platform's speed, and L is the antenna length on the along track dimension. Applying a matched-filter on the azimuth dimension it is possible to compress the Doppler bandwidth. The inverse of this value gives the capability that the radar has for differentiating targets along track in the temporal domain. Since the platform's velocity is v_p, it can be straightforwardly calculated that the maximum achievable resolution along track $L/2$.

It is worth noting here that unlike real aperture radars, the SAR along-track resolution does not depend on the geometry of the observation, nor on the range of the radar to the surface, but only on system parameters. The coherent processing of the received radar echoes together with the resolution provided by the high bandwidth chirp signals allows to generate very high resolution images that contain information on the intensity of the returned echoes from the scatters on the surface, which forms the final SAR image. These intensity values can be translated into soil moisture values by means of semi-empirical algorithms [Pathe et al., 2009; Barrett et al., 2009].

Figure 1.3 shows soil moisture maps over Oklahoma, USA, retrieved with the Advanced Synthetic Aperture Radar (ASAR) aboard ESA's Environmental Satellite (Envisat), with a resolution of 1 km. The results show an overall good agreement with the ERS-1 scatterometer data, however, the much finer resolution of the SAR data makes the map appear to have a much noisier behavior.

1.2.1.2 Passive Sensors for Soil Moisture Estimation

Passive sensors can be classified according to their operational frequency. At wavelengths close to the infrared and visible spectrum, optical instruments are used to gather the Sun's electromagnetic radiation scattered off the Earth's surface, whereas in the microwave spectrum, radiometers are used to collect the natural radiation from bodies at temperature different from absolute zero.

Multi-spectral and hyper-spectral sensors sample the electromagnetic spectrum from infrared to visible wavelengths. The main difference among them is that while multi-spectral instruments take a set of images at narrow bands through the observed spectrum, the hyper-spectral instruments perform a continuum sampling of the different electromagnetic bands with a much higher number of images at contiguous frequencies. The measured spectral reflectance, if augmented with existing soil and other geospatial information, can provide representative estimates of soil moisture relying on the variability of the spectral response of dry and wet soils in the visible and near-infrared regions. Wang et al. [2007] used data from the Moderate Resolution Imaging Spectroradiometer (MODIS) aboard NASA's Terra satellite to estimate soil moisture content for three different test sites over the United States during the period February 2000 through April 2004. It was shown that the Normalized Difference Vegetation Index (NDVI) could provide moderate correlation with the measured soil moisture under certain conditions. However, due to the short wavelength, optical signals provide information from only the top layer of the soil, and have limited ability to penetrate clouds and vegetation canopy. Because of these limitations, longer wavelengths are preferred for the estimation of soil moisture.

Microwave radiometers are the most widespread instruments for soil moisture remote sensing. These instruments are capable of measuring the naturally emitted radiation of bodies at physical temperatures above absolute zero. Thermal radiation mostly occurs in the far-infrared region, however it extends over the whole electromagnetic spectrum. Planck introduced in 1901 the concept of a blackbody radiator; this is an idealized material that absorbs all electromagnetic energy and in thermal equilibrium radiates back this energy isotropically. In the microwave region between 0.3 and 30 GHz the surface's spectral radiance or brightness, B, can be approximated by the Rayleigh–Jeans formula as a function of the physical temperature, T_{phys}, and the wavelength, λ, by the following expression [Elachi and van Zyl, 2006]:

$$B(\lambda) \simeq \frac{2\,k_B\,T_{\mathrm{phys}}}{\lambda^2}\,, \tag{1.1}$$

where k_B is the Boltzmann constant. For a narrow enough bandwidth Δf, in which the spectral radiance can be considered constant, the power emitted by a blackbody in that band yields:

$$P_{\mathrm{bb}}(\lambda) \simeq \frac{2\,k_B\,T_{\mathrm{phys}}}{\lambda^2}\Delta f\,. \tag{1.2}$$

For real materials, the incident energy is not completely absorbed as part of it is scattered off the body's surface, in the same way that only a part of the absorbed energy is re-radiated. These are the so called grey bodies. In general, the re-radiated energy is direction and polarization dependent. The final brightness temperature emitted by a body may be rewritten as a function of its physical temperature and a proportionally constant, called emissivity, ϵ, which is a function of the observation angles θ and ϕ, and the polarization:

$$T_{B,p} = \epsilon_p(\theta,\phi)\cdot T_{\mathrm{phys}}\,. \tag{1.3}$$

Emissivity and reflectivity, are related by $\epsilon_p = 1 - \Gamma_p$, where Γ_p is the Fresnel power reflection coefficient at p polarization. Both parameters are therefore governed by the dielectric properties of the ground and are polarization dependent. Thanks to the large variations of the soil's dielectric constant between dry and wet moisture conditions, it is possible to detect important variations in the brightness temperature, and ultimately relate these changes with land geophysical parameters.

Conventional real aperture radiometers, rely on the size of the receiving antenna to generate a narrow beam and therefore achieve the required resolution. The antenna is then mechanically steered in order to increase the instrument's field of view. As an example, the Advanced Microwave Scanning Radiometer (AMSR-E) onboard the Earth Observing System (EOS) Aqua satellite (NASA) is a polarimetric multifrequency instrument that incorporates a rotating parabolic reflector that creates a conical scanning, thus obtaining a total swath width of over 1400 km. In [Njoku et al., 2003], the polarization ratio in the C- and X- band channels (6.9 and 10.6 GHz) were used to estimate soil moisture on a global scale. However, at these frequency bands the emitted signal is highly affected by surface roughness and vegetation canopy; thus lower spectral bands are preferred for soil moisture remote sensing. Nonetheless, this technique has also some

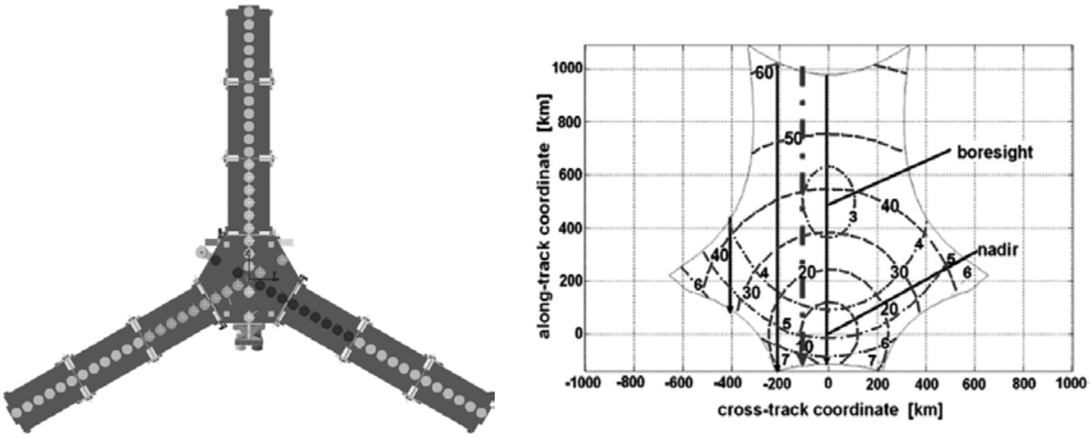

(a) (b)

Figure 1.5: (a) SMOS-MIRAS antenna configuration [Camps et al., 2005]; The Y-shaped distribution of the antenna array allows to generate a synthetic aperture by the cross-correlating of the signals received in each pair of antenna elements. (b) SMOS-MIRAS field of view; The incidence angles and the radiometric sensitivity are depicted in dashed and dashed dotted lines, respectively [Camps et al., 2005].

limitations; for a real aperture radiometer on-board a Low Earth Orbit (LEO) satellite working at L-band, a rotating antenna around 20 meters would be necessary in order to achieve the resolution and revisit time required for most soil moisture applications. This poses strong engineering constraints for its implementation on a spacecraft. Based on techniques which were formerly used by Thompson et al. [2001] in radio astronomy, a possible solution for this problem is to synthesize the antenna aperture by means of multiple correlations of the signals received by pairs of small distributed antennas.

In 2009 the European Space Agency launched the Soil Moisture and Ocean Salinity (SMOS) mission. SMOS was selected as the second Earth Explorer Opportunity mission, aiming at demonstrating 2-D interferometric radiometry from space to measure surface soil moisture and sea surface salinity [Barre et al., 2008]. The single payload aboard the SMOS satellite is the Microwave Interferometric Radiometer by Aperture Synthesis (MIRAS). The instrument consists of 69 separate receivers equally distributed over a Y-shaped antenna array, formed by three equally separated arms of 3.5 meters long and a central body, see Fig. 1.5(a). The antenna aperture is synthesized by the cross-correlation of the measurements from all possible receiver pairs on the antenna array, which at the selected orbital height of 758 km allows to achieve a resolution ranging from 30 km at nadir to over 70 km in the outer edges of the swath, Fig. 1.5(b). The instrument field of view, or swath, on the ground is about 1000 km wide, thus achieving a global soil moisture coverage every 3 days. In addition, as the satellite advances, multiple observations of the pixels in the field of view are obtained with different incidence angles. This allows to improve the final resolution and accuracy of the brightness temperature measurements, i.e., radiometric sensitivity, as was shown by Piles et al. [2009].

NASA is also developing a mission for the global monitoring of soil moisture which will provide global measurements of soil moisture and its freeze/thaw state [Entekhabi et al., 2010]. Its launch is scheduled for November 2014. The Soil Moisture Active Passive (SMAP) instrument comprises a radiometer and a synthetic aperture radar operating at L-band to combine collocated emissivity and backscattering measurements. The combination of both active and passive instruments would allow to benefit from the high sensitivity of radiometers to soil moisture and the finer achievable resolution of synthetic aperture radars [Das et al., 2011]. For this purpose SMAP incorporates a light weight mesh dish antenna of 6 meter diameter, shared by both the radar and the radiometer. In order to increase the instrument's coverage, the antenna rotates at a rate of 14.6 rpm, generating a conically scanning antenna beam with a constant surface incidence angle of approximately 40°. At an altitude of 680 km the scanning configuration yields a swath of about 1000 km, with a resolution of about 40 km for the radiometer and 1-3 km in the case of the synthetic aperture radar. Combining these two observations estimates of soil moisture in the top 5 cm of ground can be provided with a resolution of 10 km and a global coverage of 3 days.

1.2.2 Vegetation Remote Sensing

As in the case of soil moisture, vegetation remote sensing is based on the interaction mechanisms (scattering and attenuation) of electromagnetic waves with the various elements of vegetation. The different remote sensing methods can also the divided attending to the source of illumination in active and passive techniques.

1.2.2.1 Active Sensors for Vegetation Parameters Estimation

Among the active sensors used to measure vegetation parameters, one could differentiate between optical and microwave sensors. The former rely on a laser typically operating around the near infrared wavelengths ($\sim 1.05\,\mu$m) to illuminate the target. A scanning mirror sweeps the laser beam over the scene, and a photo-detector is then used to measure the laser pulse trip time with an accuracy of few nanoseconds. This technique is commonly known as LIDAR, which stands for Light Detection and Ranging. The operational principle is very similar to that of radars, however, the much higher frequencies give these systems very different characteristics from microwave systems. The observed pulses are directed to the photo-detectors by means of optical telescopes that collimate the received light in order to produce small footprints on the ground with relatively small apertures. In addition, thanks to the high achievable power by present lasers, it is possible to transmit very short pulses that allow to obtain very high vertical resolutions without hampering the signal to noise ratio of the backscattered echoes.

There are two types of lidar instruments currently in use for remote sensing applications: discrete-return and full-waveform lidars [Lim et al., 2003]. The former records one to several light returns arriving at the photo-detector from a small footprint, typically below one meter diameter. These systems provide an extremely high point sampling allowing a fine representation of ground and canopy surfaces in the horizontal plane, and they have been successfully used to map forest and terrain characteristics [Lefsky et al., 2002; Lim and Treitz, 2004; Evans and Hudak, 2007]. On the other side, full-waveform lidars record the reflectance of light as a function of time (waveform) for each footprint and operate with coarser resolution than their discrete counter part. This type of lidars have been used from airborne platforms for the estimation of the horizontal and vertical distribution of forest structure as well as vegetation parameters, such as mean canopy height and above ground biomass; [Means et al., 1999; Sun and Ranson, 2000; Lefsky et al., 2002; Koetz et al., 2006; Duong et al., 2012]. Data from the full waveform lidar Geoscience Laser Altimeter System (GLAS) aboard the NASA's Ice, Cloud and land Elevation Satellite, or ICESat [Abshire et al., 2005], were used in conjunction with MODIS

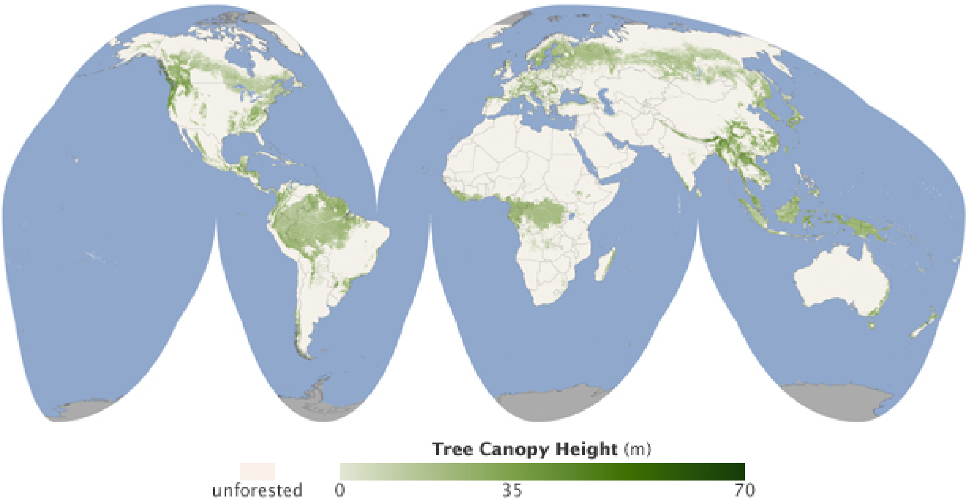

Figure 1.6: Global map showing forest canopy height, retrieved from [NASA News & Features Webpage, 2010].

data and other ancillary information to generate global forest canopy height maps [Lefsky, 2010; Simard et al., 2011], Fig. 1.6. Both full-waveform and discrete-return lidars are closely related and some studies have shown the capability of generating a full waveform with discrete lidar observations provided there is high enough horizontal sampling [Lefsky et al., 2002].

Synthetic aperture radars (SAR) have also been applied in vegetation remote sensing applications. In [Santoro et al., 2011] hyper-temporal series of C-band backscattering data from ASAR were used to estimate forests Growing Stock Volume (GSV).Vegetated and non-vegetated areas were classified with MODIS data. Over certain areas the GSV Root Mean Square Error (RMSE) with respect to the in-situ measurements was claimed to be around 30% with a saturation level of 300 t ha^{-1}. At L-band, Above Ground Biomass (AGB) was estimated by analyzing backscattering data from the Phased Array type L-band Synthetic Aperture Radar (PALSAR) aboard the Advanced Land Observing Satellite (ALOS), from the Japan Aerospace Exploration Agency (JAXA). In [Mitchard et al., 2009] four different areas in Africa covering savannas and woodlands were studied. AGB values were retrieved with a RMSE around 20% below 150 t ha^{-1}. This upper limit in the estimation is related to a saturation of the radar backscattering response towards high biomass values. To overcome this problem, in [Mitchard et al., 2011] ALOS PALSAR data were merged with Light Detection and Ranging (LIDAR) data (Ice, Cloud and land Elevation Satellite (ICESat) GLAS) to calculate the carbon stock of Gabon's Lopé National Park with a predicted uncertainty of ±25%. In this case, the radar backscattering data were used to segment the area under observation in different classes, for which a mean biomass value was obtained by estimating the mean canopy height from the lidar observations. Earlier campaigns have also investigated the capabilities of P-band SAR polarimetric observations to estimate forest AGB [Ferrazzoli et al., 1997; Saatchi et al., 2007; Le-Toan et al., 2011]. At this frequency, the penetration of the electromagnetic waves on the vegetation canopy is much higher than at C- and L- bands, thus, the backscattering response has a smaller saturation with increasing biomass. The combination of multi-frequency backscattering observations at different polarizations was also used for this purpose [Kurvonen et al., 1999; Hoekman and Quiriones, 2000; Englhart et al., 2012].

More sophisticated techniques, such as Polarimetric SAR Interferometry (PolInSAR) and SAR tomography, have also been proposed to overcome the loss of sensitivity of backscattering coefficients towards high biomass values. SAR interferometry relies on the combination of two complex radar images acquired at different epochs (images acquired in subsequent orbits) or slightly different positions (images acquired with two different apertures on the same platform). For the combination of the SAR images, one of the two is multiplied by the complex conjugate of the other. Considering that the noise statistics are the same for both radar images, the remaining phase contains information about the topography, and/or changes that could have occurred on the surface. Calculating the interferograms at different polarizations provide the full complex scattering matrix, which allows to better describe the interaction of radar signals with natural surfaces, [Cloude and Papathanassiou, 1998]. This technique was proven to be successful for the determination of forest biomass by the estimation of tree heights and other structural parameters, [Papathanassiou and Cloude, 2001; Garestier et al., 2008b,a; Garestier and Le Toan, 2010; Neumann et al., 2012]. The combination of polarimetric SAR intensity and interferometry measurements have been proposed as the primary measurement mode for the ESA's Biomass mission, recently selected as the next mission within ESA's Earth Explorers program [Le-Toan et al., 2011].

SAR tomography is a technique based on SAR interferometry that exploits multiple baseline observations to reconstruct the 3-Dimensional backscattering scattering properties of a vegetation layer [Reigber and Moreira, 2000; Fornaro et al., 2005]. The multiple baselines form a synthetic aperture in the vertical dimension. Provided that the radar pulses penetrate the vegetation layer and the phase coherency of the scene is maintained, it is possible to focus the radar echoes acquired during multiple repeat passes to resolve the vertical profile of the backscattered power [Fornaro et al., 2005; Cloude, 2007; Tebaldini and Rocca, 2012]. This technique is foreseen to be used as a secondary measurement mode on the Biomass Earth Explorer mission [Le-Toan et al., 2011].

1.2.2.2 Passive Sensors for Vegetation Parameters Estimation

Passive systems have also been widely applied in vegetation remote sensing. Among them, multi-spectral and hyper-spectral optical sensors have played a pivotal role. During the last decades, several instruments such as VEGETATION on the French Systeme Pour l'Observation de la Terre (SPOT) satellite, NASA's MODIS (onboard Terra and Aqua), and the Medium Resolution Imaging Spectrometer (MERIS) on-board the recently decommissioned Envisat, have been used to derive consistent data products of Vegetation Indices (VI). Those are obtained by combining the measured reflectance at two or more spectral bands, and are fundamentally dependent on vegetation parameters such as leaf chlorophyll, leaf area, canopy cover, and canopy architecture [Jiang et al., 2008].

Observables like the Normalized Difference Vegetation Index (NDVI), calculated as the combination of the spectral reflectance measured at the near infrared and red visible bands, and the Enhanced Vegetation Index (EVI), that incorporates a third observation in the visible blue band, have been used in a wide variety of applications for the monitorization and characterization of vegetation biophysical parameters, including Leaf Area Index (LAI), green vegetation fraction, gross primary product (GPP), and fraction of photosynthetically active radiation (faPAR) [Myneni et al., 1997; Huete et al., 2002;

Sims et al., 2006]. The availability of data from several sensors has allowed the intercalibration of vegetation indices among them, which provides the opportunity to shorten the observations repeat cycle, and improve the final estimation of vegetation parameters [Steven et al., 2003; Fensholt et al., 2006; Brown et al., 2006]. The study of continuous multiyear vegetation index datasets have allowed to determine the seasonality on rainforest canopy photosynthesis, which is on main relevance for the understanding of the dynamics of climate and carbon fluxes [Huete et al., 2006].

Passive microwave remote sensing systems have also been used for the estimation of vegetation parameters. In the case of SMOS, vegetation acts as a disturbing parameter which has to be accounted for and corrected from the soil moisture signal. However, given the multiangular and polarimetric observations of brightness temperatures performed by SMOS, it is possible to estimate the vegetation optical depth to correct the measured soil brightness temperature. This is done by means of the so called τ–ω vegetation model, which is integrated in the SMOS Level-2 soil moisture retrieval algorithm [Wigneron et al., 2007; Kerr et al., 2012]. In previous studies it was demonstrated that this parameter can be related to the Vegetation Water Content (VWC) [Jackson and Schmugge, 1991], and ultimately to vegetation biomass.

1.3 Motivation

Despite the recognized scientific and socio-economical relevance of soil moisture and vegetation above ground biomass, monitoring of these parameters at a global scale with the appropriate temporal and spatial resolutions still remains a major challenge. Direct measurements of soil moisture and vegetation parameters for the production of cover maps over large areas are intrinsically very expensive and require a huge man effort. In order to bridge this gap, several remote sensing techniques have been proposed, as has been show in the previous section. However, the experience gained from previous experimental campaigns and theoretical results suggest major limitations for the utilization of current remote sensing techniques on the monitorization of land bio-physical parameters.

In the case of monostatic radars, the simultaneous effects of soil roughness and vegetation cover decorrelate backscattering measurements from soil moisture. For vegetation monitoring, the early saturation of the radar response with increasing biomass poses a limitation in the application of this technique for forest monitorization, as the final estimation of above ground biomass can suffer from high uncertainties. In the case of microwave radiometers, despite the fact that their sensitivity allows to achieve high radiometric accuracies, the achievable spatial resolution is most of the times limited by the system configuration. Optical sensors, specially lidars, could represent a suitable solution for forest height measurements, which can then be converted to above ground biomass through allometric equations. However, their large dependency on weather conditions and narrow swaths from spaceborne platforms jeopardize their application to continuous monitoring of vegetation.

Previous experiments have already demonstrated the capability of GNSS bistatic scatterometers to sense small changes in land surface reflectivity. Furthermore, these systems present some advantages with respect to others currently used to retrieve soil moisture and vegetation biomass. First, GNSS signals lie in the L band, which is preferable due to its canopy penetration ability and the most sensitive band to both soil moisture variations and vegetation parameters. Secondly, in contrast to microwave radiometry, even though variations on thermal background influence land bio-geophysical observables, they do not dramatically contaminate the GNSS reflected signals. Thirdly, GNSS scatterometry from space has potentially higher spatial resolution than microwave radiometry, due to the highly stable carrier and code modulations of GNSS signals which enables the use of Delay Doppler mapping. However, the actual sensitivity of these measurements to bio-geophysical variables of interest, such as soil moisture content, and vegetation biomass, has still not been assessed in a conclusive way. The research work presented in this dissertation focuses on the assessment of these capabilities from a theoretical and experimental point of view.

Chapter 2

Global Navigation Satellite Systems

Global Navigation Satellite System (GNSS) are satellite constellations orbiting the Earth with the purpose of providing continuous position and timing information to any receiver anywhere on the globe. Such systems are used in an increasing number of applications, ranging from safety of life applications, such as air traffic control, to wildlife tracking, or the most common ones, such as navigation for conventional users. The vast potential of GNSS has led international governments to thoroughly promote this technology. At the time of writing, the American Global Positioning System (GPS) is the only fully operational GNSS. However, the Russian GLONASS system is now almost completely deployed, and the European Galileo is scheduled to be operational by 2014/2015, with full deployment scheduled by 2020. Other countries such as China and India are also planning their local or global navigation satellite systems. A total amount of more than 75 GNSS satellites will be available when these constellations are fully deployed. The potential compatibility and interoperability of the different systems could provide unprecedented coverage and positioning accuracy even for conventional users. The next sections review the fundamental aspects of GNSS systems and their transmitted signals characteristics.

2.1 A Brief History of Navigation

Since the 13th century, with the invention of the compass and the quadrant, new techniques have continuously been developed to allow humans explore the Earth. In early navigation days, the declination of the Sun was measured in order to determine the latitude of the observer. However, accurate navigation remained an unsolved problem until the second half of the 18th century. The reason for this was the difficulty of precisely estimating longitude. Measuring longitude is, to a large extent, equivalent to measuring time. Since the Earth rotates at an angular speed of 15° per hour, accounting for the time difference between a well known astronomical event at a fixed location, say the Sun's culmination at the Greenwich meridian, and the time at which the navigator sees those events (apparent local time) provides a direct estimation of the longitude with respect to the reference point. The problem was to keep the time of a distant reference point, as the epoch's pendulum clocks were not suitable to be used on an unstable platform such as a ship. It was not until the invention of the sextant and the marine chronometer that this problem could be solved. With the invention of radio, a new kind of assisted navigation was born. The wireless telegraph allowed by the beginning of the 20th century to transmit time signals to ships so that navigators could routinely check their chronometers.

With the development of yet another technology, i.e. artificial satellites, a new door was opened to the more precise line-of-sight radio navigation. The first satellite navigation system was the so called Transit. Further works and investigations led in the early 1970s to the NAVSTAR Global Positioning System (GPS). Operated by the U.S. Air Force for the U.S. Government, the GPS was originally developed as a military system, however, it soon demonstrated a significant potential for a large variety of civil applications. The full NAVSTAR satellite constellation was completely deployed by 1994, providing uninterrupted positioning in nearly every place in the world. Other countries have also developed their own local or global satellite navigation systems. In parallel to GPS, the Soviet Union started the development of GLONASS, which was fully operational by 1995. However, after the dissolution of the Soviet Union the constellation was left unassisted leading to important gaps in coverage and availability. Important efforts are currently being made by the Russian Federation to restore the full constellation. In the same way, both China and the European Union are developing their own satellite navigation systems. The Chinese COMPASS is expected to become a global navigation system by 2020, whereas Galileo, initially scheduled for 2010, is expected to become operational by 2014. However, the European system will not become in full service at least until 2020. The most relevant aspects of these GNSS systems are reviewed next.

2.2 The Navstar Global Positioning System

2.2.1 System Overview

The Navstar GPS consists of three main system segments; space, control, and user segment, Fig. 2.1. The space segment is composed of a constellation of a minimum of 24 operational satellites[1] distributed in 6 quasi-circular orbital planes, equally spaced around the equator with an inclination of 55 degrees. The GPS satellites are positioned within the orbits in such a way that four or more satellites are simultaneously in view at any location on the Earth. This is needed in order for the receiver to calculate its 3-D position and the time difference between the user's and the GPS time, as will be explained in section 2.2.4. The satellites have an average orbital height of 20200 km above the Earth's surface, and a revolution period of 11 hours and 58 minutes, thus the satellites' ground tracks are revisited every sidereal day.

The GPS control segment consists of a Master Control Station (MCS), plus five monitor stations, and three ground antennas distributed around the world. Its main tasks are to maintain the satellites' orbits through maneuvering commands, adjust satellite clocks and payload if necessary, update navigation data, and other health monitoring and maintenance activities of the constellation. The monitor stations collect ranging

---

[1] During the last years, the U.S. Air Force has maintained a standing constellation of 31 operational satellites, resulting in improved coverage and accuracy

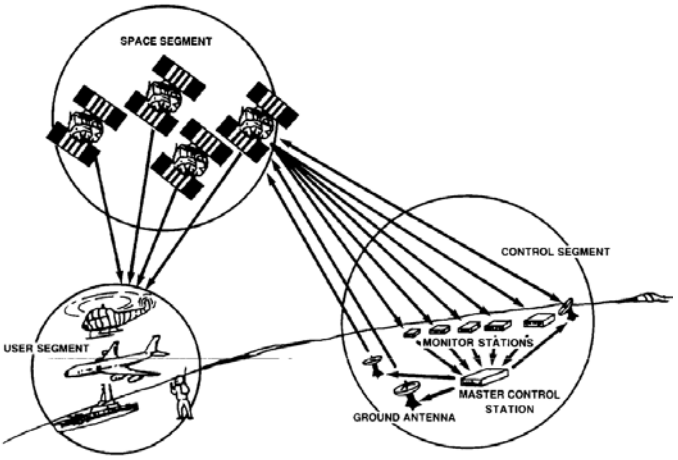

Figure 2.1: GPS segments, image courtesy of NASA.

information of all the GPS satellites, which is then sent to the MCS information to calculate the orbit's ephemerides and clock data.

This information is formatted into the navigation message and uploaded back to the GPS satellites through the ground antennas for retransmission to the user segment, which consists of the receivers that allow to record, decode, and process the GPS satellite signals in order to compute position, velocity, and time information.

2.2.2 GPS Multiple Access Technique

In order for the GPS satellite to broadcast navigation signals without significantly interfering with each other, a spread spectrum technique is used to modulate the GPS transmitted signals. The GPS navigation message is mixed with Pseudo-Random Noise (PRN) sequences generated at a much higher rate than the data transmission rate. This has the effect of spreading the energy of the transmitted navigation data over a much larger bandwidth than that of the original signal. By mixing again the spread-spectrum signal with the PRN codes, the signals are compressed back, and the original data can be recovered. This technique is known as Direct Sequence Spread Spectrum (DS-SS). Apart from lowering the power spectral density of the transmitted signals, and therefore reducing the probability of interference with other systems in the line of sight, spread spectrum signals do also have good properties against intentional jamming and spoofing attacks, certain tolerance to multipath, and the capability to obtain precise ranging information. The latter is particularly important in the case of GPS, since the precision in measuring the ranges between the transmitting satellites and the receiver will determine the final accuracy in the determination of position and time.

To illustrate this last point, let us consider a PRN code as a random sequence of pulses generated at a clock rate f_c, that can take an amplitude, a_n, equal to $+1$ or -1 with equal probability, Fig. 2.2(a). The duration of each pulse, T_c, is the inverse of f_c, thus we can express this sequence as [Garrison, 2007]:

$$s(t) = \sum_{n=-\infty}^{\infty} a_n \prod \left(\frac{t - nT_c}{T_c} \right) . \tag{2.1}$$

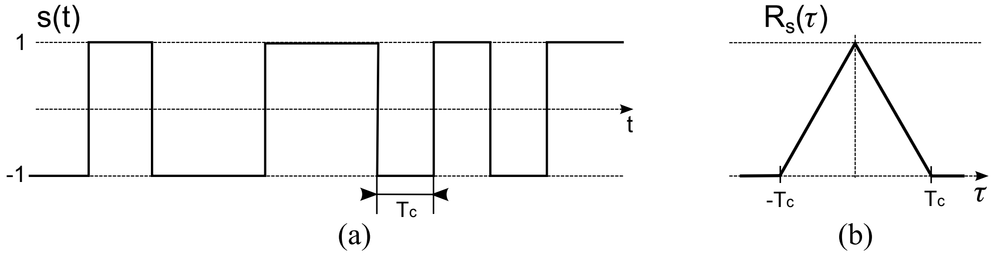

Figure 2.2: (a) PRN code segment. (b) Ideal PRN code autocorrelation

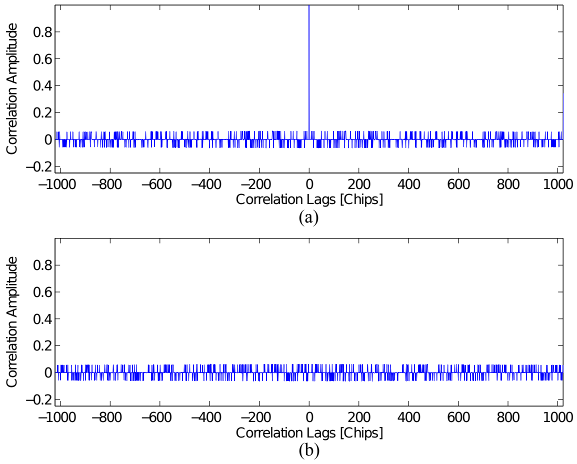

Figure 2.3: (a) GPS C/A-code PRN01 autocorrelation; (b) GPS C/A-code PRN01 and PRN02 cross-correlation.

The individual pulses of the random sequence are known as chips. The autocorrelation function of such infinite sequences would be a triangle of width $2T_c$, as shown in Fig. 2.2(b), and equal to zero outside the $(-T_c, T_c)$ range:

$$R_s(\tau) = \begin{cases} \left(1 - \frac{|\tau|}{T_c}\right), & |\tau| \leq T_c \\ 0, & |\tau| > T_c \end{cases} , \tag{2.2}$$

where τ is the correlation time lag. As can be seen from the previous equation, the higher the chipping rate the narrower the final correlation would be, thus, improving the ranging capabilities of the code.

Two types of PRN codes are used to spread the GPS signals, i.e. the Coarse Acquisition Code (C/A-code) and the Precise (Encrypted) Code (P(Y)-code). The C/A-code is the ranging code used for civil open-access applications. The total length of the code is 1023 chips generated at a clock rate of 1.023 MHz, resulting in a null-to-null bandwidth of 2.046MHz. C/A PRN codes belong to the so called Gold codes family, which are formed by the product of two PRN sequences, $G1$ and $G2$. These codes are generated by means of two 10-stage linear feedback shift registers [Parkinson and Spilker, 1996]. The relative delay between $G1$ and $G2$ generates the different C/A-code that are uniquely assigned to each GPS satellite. The resulting PRN codes have correlation properties similar to those of Gaussian noise, i.e. sharp autocorrelation, and low cross-correlation, as shown in Fig. 2.3. Due to the limited length of C/A-codes, the cross-correlation is not zero, however, the cross-correlation is as low as $-1/1023$ during 75% of the time, with a maximum of $63/1023$ that occurs in average 12.5% of the time. These values are acceptable for most applications and allow a single receiver to acquire signals from multiple GPS satellites at the same time without significant interference. This technique is known as Code Division Multiple Access (CDMA).

The P-code is a much longer code, with a total period of 1-week. It is also generated by means of linear feedback shift registers, but with a chipping rate of 10.23 MHz, which implies a signal bandwidth of 20.46 MHz. This code is normally encrypted by the Y-code, generated at the same rate, but its access is restricted to certain users, mainly for military applications. The final code has a total period of 238 weeks, but each satellite only transmits one portion of it that restarts every week. This makes the spoofing of this signal a completely arduous task.

2.2.3 GPS Signals

Each GPS satellite broadcasts ranging signals at two frequencies in L-band: L1 at 1575.42 MHz, and L2 at 1227.6 MHz. With the GPS modernization a third band is also being introduced, L5 at 1176.45 MHz, which will provide increased accuracy for safety-of-life transportation applications. All these three frequencies are multiples of a common reference clock of 10.23 MHz:

$$\begin{aligned} L1 &= 1575.42 \text{ MHz} = 154 \cdot 10.23 \text{ MHz} \\ L2 &= 1226.60 \text{ MHz} = 120 \cdot 10.23 \text{ MHz} \\ L5 &= 1176.45 \text{ MHz} = 115 \cdot 10.23 \text{ MHz}\,. \end{aligned}$$

The GPS signals are synchronously generated between each other in order to have a common time reference when solving the positioning equations. The signals are transmitted with Right Hand Circular Polarization (RHCP) so that the polarization rotation caused by the ionosphere does not affect the signal reception.

The broadcast navigation message contains the necessary information to compute the range between the transmitting satellite and the receiver. The data in the navigation message comprises, among others, the transmitting satellite vehicle identification number, time of transmission, the satellites' ephemerides, clock and atmospheric delay corrections, satellites health parameters, and other useful information for the final calculation of the receiver's position. A total of 25 frames of 1500 bits each are transmitted at a rate of 50 bps, which results in a total duration of the navigation message of 12.5 minutes.

The L1 signal is modulated by the C/A- and P(Y)-codes in the in-phase and quadrature components, respectively. The navigation message is superimposed on both codes. The analytical representation of the L1 transmitted signal on the carrier frequency f_{L1} can be written as:

$$s(t) = \sqrt{2P_{CA,L1}}D(t)CA(t)\cos(2\pi f_{L1}t + \phi_{L1}) + \sqrt{2P_{P,L1}}D(t)P(t)\sin(2\pi f_{L1}t + \phi_{L1})\,, \tag{2.3}$$

where $P_{CA,L1}$ and $P_{P,L1}$ are the transmitted powers in L1 for both C/A- and P-codes, $D(t)$ is the navigation message, $CA(t)$ and $P(t)$ are the C/A- and P(Y)-codes sequences, respectively; ϕ_{L1} represents an arbitrary carrier phase. Both PRN codes and navigation message are synchronously generated as they are based on the same reference clock.

The L2 signal is only modulated by the P(Y)-code. The mathematical representation of the signal is

$$s(t) = \sqrt{2P_{P,L2}}P(t)\cos(2\pi f_{L2}t + \phi_{L2})\,, \tag{2.4}$$

where $P_{P,L2}$ is the transmitted power in L2. No navigation data is usually transmitted in L2. The reason for transmitting at different frequencies is that by comparing the time of arrival of signals in both bands the additional delay introduced by the ionosphere can be estimated, as will be shown later.

GNSS signals arrive at the receiver with a certain delay and Doppler frequency, due to the relative position and velocity of transmitter and receiver. In order to recover the navigation message and to obtain precise ranging measurements, the received signals are correlated with a clean replica of the PRN codes with the appropriate delay and Doppler. The result is the so called cross-correlation waveform, from which positioning observables are obtained.

2.2.4 GPS Positioning Fundamentals

The basic observables for GPS positioning are the pseudoranges, i.e. the relative distance between the receiver and the transmitting satellite. For satellite k the measured pseudorange ρ^k can be expressed as [Parkinson and Spilker, 1996; Misra and Enge, 2006]:

$$\rho^k = \rho^k_T + c(\delta t_u - \delta t^k) + I^k + T^k + \epsilon^k\,, \tag{2.5}$$

where ρ_{kT} is the true pseudorange; δt_u and $t\delta^k$ are the receiver and satellite clock offsets, respectively; I^k is the ionospheric delay error; T^k is the additional delay introduced by the troposphere, and ϵ^k accounts for additional receiver hardware errors and measurement noise.

Combining the pseudoranges observed for the same satellite at different frequencies, the ionospheric delay I^k can be estimated. Neglecting noise and instrumental biases terms for simplicity in the next equations, the difference between the measured pseudoranges at L1 and L2, $\Delta\rho^k$ yields:

$$\Delta\rho^k = \rho^k_{L1} - \rho^k_{L2} = c(I^k_{L1} - I^k_{L2})\,.$$

The ionospheric delay varies inversely with the frequency squared, $\Delta I^k \cong I\alpha/f^2$, where I is the integrated electron density or total electron content along the propagation path of the signal, and $\alpha = 40.3\,\mathrm{m}^3/\mathrm{s}^2$. After straightforward manipulation of the previous equation, the ionospheric delay can be estimated as:

$$\Delta I^k_{L1} = \Delta\rho^k \frac{f^2_{L2}}{f^2_{L2} - f^2_{L1}}\,. \tag{2.6}$$

The tropospheric delay can also be estimated by means of a model [Misra and Enge, 2006], taking into account parameters such as temperature, pressure, humidity, and altitude of the receiver. In addition other errors such as satellite's position corrections, satellite's clock drifts, and relativistic errors can be mitigated through certain information contained in the navigations message. After accounting for all these errors, a corrected version of the initial pseudorange measurement, ρ_c^k, is obtained:

$$\rho_c^k = \rho_T^k + c\delta t_u + \tilde{\epsilon}^k \,, \tag{2.7}$$

where $\tilde{\epsilon}^k$ accounts for the residual pseudorange errors. Let the vectors $\mathbf{x}^k = (x^k, y^k, z^k)$ and $\mathbf{x}_r = (x_r, y_r, z_r)$ be the GPS satellite and receiver positions, respectively. The true pseudorange is

$$\rho_T^k = \sqrt{(x^k - x_r)^2 + (y^k - y_r)^2 + (z^k - z_r)^2} \,. \tag{2.8}$$

It is apparent from equations (2.7) and (2.8) that pseudorange measurements for at least four satellites are needed in order to solve the four unknowns: $\mathbf{x}_r$ and δt_u. This results in a nonlinear system of K equations. A simple approach to solve these equations is to linearize them about an approximate user position $\mathbf{x}_0$. The first order Taylor expansion of equation(2.8) about this initial guess point yields

$$\rho_T^k = \rho_0^k + \frac{x^k - x_0}{\rho_0^k}\delta x_r + \frac{y^k - y_0}{\rho_0^k}\delta y_r + \frac{z^k - z_0}{\rho_0^k}\delta z_r \,. \tag{2.9}$$

Introducing (2.9) in (2.7) we can readily write a linear system of equations where the new unknowns to be determined are the correction to be applied to our initial estimation $\delta\mathbf{x}_r = (\delta x_r, \delta y_r, \delta z_r)$ and δt_u. If $K \geqslant 4$ then the solutions are unique and the calculated corrections can be used to obtain the estimated user's position $\hat{\mathbf{x}}_r$:

$$\hat{\mathbf{x}}_r = \mathbf{x}_0 + \delta\mathbf{x}_r \,. \tag{2.10}$$

A Least Mean Square algorithm or a Kalman Filter can be used to solve this linear system of equations. The calculated user position $\hat{\mathbf{x}}_r$ is taken as $\mathbf{x}_0$ in the following iteration. The process can be repeated until the values of the position corrections $\delta\mathbf{x}_r$ are below a certain threshold.

2.2.5 GPS Modernization

As mentioned above, with the modernization of GPS, new bands and signals with different modulations are being transmitted. New GPS satellites of Blocks IIR(M) and IIF do already transmit the new civil codes in L2. The so called L2C code has the same 1.023 MHz chipping rate as the C/A-codes and so the same 2.046 MHz bandwidth, thus the same ranging precision and multipath performance as the C/A-code, however it will allow to have a more precise estimation of the needed ionospheric correction. The codes are also longer than the C/A; the medium-length code (CM), has 10230 chips that repeat every 20 ms, with navigation data modulated at 50 symbols per second (sps); the long code (CL) has 767250 chips and repeats every 1.5 seconds, and has no data modulation.

New military signals are also being introduced. Blocks IIR(M) and IIF incorporate the new Military Code (M-code) in both L1 and L2. This new signal is a Binary Offset Carrier (BOC) modulation, BOC(10,5). BOC signals are generated by modulating a sine wave carrier by the PRN code sequence and an additional square wave subcarrier. BOC modulations are usually denoted as BOC(m,n), where m is the ratio between the subcarrier frequency and the fundamental frequency, $f_0 = 1.023$ MHz, and n is the ratio

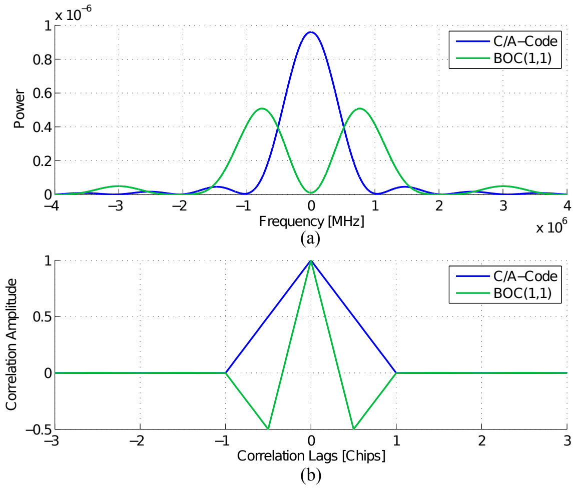

Figure 2.4: (a) Power spectrum of C/A-code and BOC(1,1) signals; (b) Autocorrelation functions for C/A-code and BOC(1,1) codes.

between the code chipping rate and f_0. Modulating with an additional subcarrier has a twofold effect: on one hand the signal's energy is spread over a larger bandwidth, and on the other hand the code autocorrelation is narrowed. This has the effect of reducing the delay error variance as this is inversely proportional to the RMS signal's bandwidth [Parkinson and Spilker, 1996, chapter 3]. In Fig. 2.4, where the power spectrum and cross-correlation waveforms are shown for a C/A-code and a BOC(1,1) modulation.

GPS satellites of Block IIF and the upcoming Block III also transmit the new civil signal in L5. It is composed of an in-phase data channel, I5, and a quadrature data-free channel, Q5, for robust carrier phase tracking. Like the C/A-code, the signal is a Binary Phase Shift Keying (BPSK) modulation, but with larger bandwidth (chipping rate equal to 10.23 MHz) and code length, thus reducing pseudorange error variance and multichannel interference. In addition, the transmitted power in L5 will be increased by 6 dB with respect to the current L1 power, which will also contribute to the improvement of the final SNR and tracking performance. A summary of the most relevant characteristics of GPS signals is provided in Table 2.1. A qualitative representation of the signal's spectrum is provided in Fig. 2.5.

2.3 Galileo

Galileo is the joint initiative of the European Union (EU) and ESA for a Global Navigation Satellite System under civilian control. The system was designed to be independent, but fully interoperable with both GPS and GLONASS. By offering dual frequency navigation as a standard, higher bandwidth signals, and more robust modulations schemes, sub-meter positioning accuracy is expected to be achieved. This new signals will also allow to guarantee the availability of the service under the most severe circumstances.

Galileo plans to provide four types of navigation services and a search-and-rescue service. There will be an open service, and three fee-based services controlled via encryption that will offer higher performance, availability and integrity. The *Open Service* (OS) results from the combination of open signals and will provide positioning and timing capabilities comparable to other GNSS systems. The *Safety-of-Life Service* (SoL)

Signal	Carrier	Modulation	Chip Rate [Mbps]	Bandwidth [MHz]	Code Length (chips)	Duration	Data Rate (bps)	Min Rx Power (dBW)
C/A-code	L1	BPSK	1.023	2.046	1023	1 ms	50	-158.5
P(Y)-code	L1	BPSK	10.23	20.46	-	1 week	50	-161.5
L1C	L1	BOC(1,1)	1.023	4.092	10230	10 ms	100	-157
M	L1	BOC(10,5)	5.115	30.69	?	?	?	-153
P(Y)-code	L2	BPSK	10.23	20.46	-	1 week	-	-161.5
M	L2	BOC(10,5)	5.115	30.69	?	?	?	-153
L2C (CM)	L2	BPSK	1.023	2.046	10230	10 ms	50	-160
L2C (CL)	L2	BPSK	1.023	2.046	767250	1.5 s	-	-160
I5	L5	BPSK	10.23	20.46	10230	1 ms	100	-155
Q5	L5	BPSK	10.23	20.46	10230	1 ms	-	-155

Table 2.1: Summary of GPS signal characteristics, from [Parkinson and Spilker, 1996], and [GPSW, 2010].

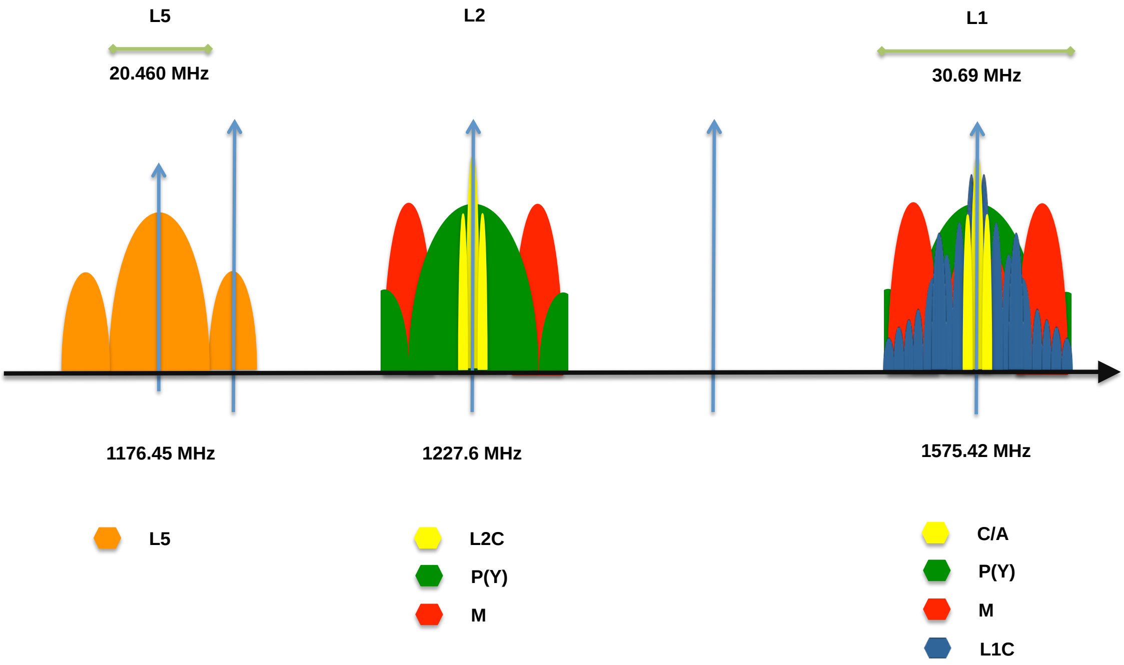

Figure 2.5: GPS signal spectrum

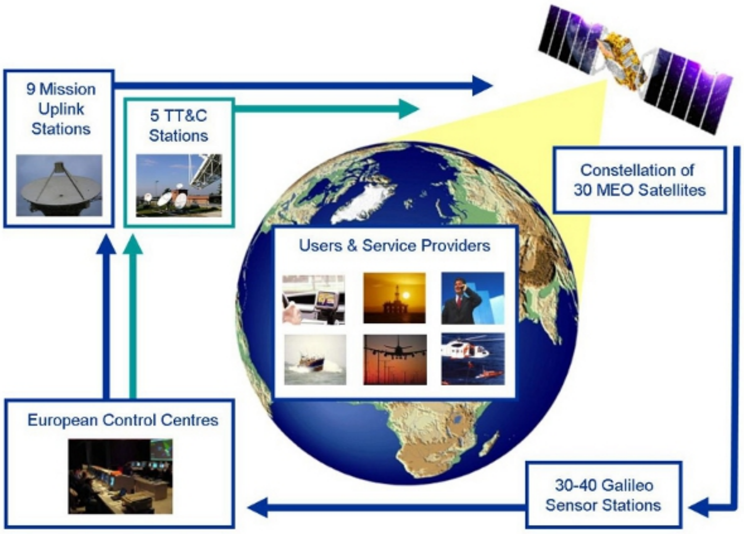

Figure 2.6: Galileo Architecture [EU, 2012].

improves the OS performance through the provision of timely warnings to the user when it fails to meet certain margins of accuracy (integrity). It is envisaged for transportation applications in which safety is crucial, such as running trains, guiding cars, and landing aircraft. The *Commercial Service* (CS) provides access to two additional encrypted signal, to allow for a higher data throughput rate and to enable users to improve accuracy. It is envisaged that a service guarantee will be provided for this service. The *Public Regulated Service* (PRS) is intended for government agencies and for military applications. Two PRS navigation signals with encrypted ranging codes and data will be available to provide position and timing with high continuity of service. Finally, the *Search and Rescue Service* (SaR) will allow specific users to send a distress alert signal that will be received by the Galileo satellites. A dedicated UHF channel will be used to download these data to ground segment and ultimately send the alert message to national rescue centers. Given that at least one Galileo satellite will be in view of any point on the Earth, a near real-time SaR service will be possible; it is expected that a distress signal will be able to be detected within 10 minutes with 98% probability and 100 meters accuracy.

2.3.1 Galileo System Architecture

As in the case of GPS, Galileo consists of a Space, Ground, and User Segment, see Fig. 2.6. The Space Segment comprises a constellation of 30 satellites (27 operational + 3 spares), positioned in three circular Medium Earth Orbit (MEO) planes at a nominal average orbit semi-major axis of 29601.297 km, with an inclination of 56° with respect to the equatorial plane. The orbital period is 14 hrs 4 min, and ground tracks repeat every ten days. The Ground segment consists of two control centers, five Tracking Transmission and Control (TT-C) sites, nine uplinks stations, and a whole network of Galileo sensor stations to monitor the health of the Galileo constellation. The User segment is again composed by all users receiving not only Galileo signals, but also GPS, and potentially other GNSS system's signals. Users will benefit for the interoperability of these systems, as both service availability and positioning precision will be improved.

At the time of writing, April 2013, the first two operational satellites of the Galileo constellation were already launched. Two additional ones will follow in the second half of 2012. That will be used to validate the Galileo concept both in space and on Earth. This is the so called In-Orbit Validation (IOV) phase. Once this is completed, another 14 satellites will be launched to reach the Initial Operational Capability by March 2014 (expected). The full operational capability (FOC) is expected to be achieved by the end of this decade [ESA, 2012b].

2.3.2 Signals in space

Galileo signals will be transmitted with RHCP in four frequency bands: E5a at 1176.45 MHz, E5b at 1207.14 MHz, E6 at 1278.75 MHz, and E1 at 1575.42 MHz. As in the case of GPS, all satellites will share the same frequency bands and use CDMA technique for multiple access. 10 different navigation signals will be transmitted four of which will be data-free channels (pilot channels) that will offer robust tracking of the satellite signal to aid in the recovery of navigation data and pseudorange measurements. The combination of these signals will allow the provision of the different services presented above.

New modulation schemes and higher bandwidth signals have been introduced for optimized tracking performances. Such is the case of the Galileo E1 signal which is composed of open signals and an encrypted signal. The public signal, defined in [EU, 2010], comprises a pilot and a data channel, E1B and E1C, respectively, which are meant to be used also for CS and SoL. The encrypted signal, known as E1A is reserved for PRS. E1B and E1C are Composite BOC (CBOC) modulated signals. Each CBOC is formed as linear combination of a BOC(1,1) and a BOC(6,1), the latter having 1/11 of the total power transmitted in E1B and E1C, in-phase and quadrature components of the signal. This has the effect of widening the signal spectrum, which results in narrower autocorrelation functions and improved tracking performances.

The E5 signal of Galileo is an open signal, to be used for OS, CS, and SoL. It is made up by two contiguous bands, E5a and E5b, each one carrying a QPSK modulated signal (two BPSK in-phase and quadrature channels for pilot and data) with a chip rate of 10.23 Mbps (20.46 MHz). These two signals can be combined to obtain an AltBOC(15,10) modulation with a nominal bandwidth of 51 MHz. A detailed explanation of AltBOC(15,10) generation is provided in [EU, 2010], section 2.3.1. Note that the nominal bandwidth of 51 MHz for the Galileo E5 signal comprises approximately the 78% of the total power, and that 90 MHz are needed to account for the 85% of the power [Lohan, 2010].

Regarding the E6 signal, it is expected to be used for Public Regulated Service (PRS) and Commercial Service (CS). The former will have a data channel modulated by a BOCcos(10,5), whereas the latter will incorporate in-phase and quadrature channels for data and pilot signal transmission with a BPSK modulation at 5.115 Mbps. The following Table and Figure wrap-up the most relevant characteristics of the Galileo signals.

Signal	**Modulation**	**Chip Rate [Mbps]**	**Bandwidth [MHz]**	**Code Length (prim.)**	**Code Length (sec.)**	**Duration Tiered Code (ms)**	**Data Rate (bps)**	**Min Rx Power (dBW)**
E1A	BOCcos(15,2.5)	2.5575	35.8	?	?	?	?	?
E1B	CBOC(6,1,1)	1.023	14.322	4092	-	4	250	-157(*)
E1C	CBOC(6,1,1)	1.023	14.322	4092	25	100	-	-157(*)
E5a-I	BPSK	10.23	20.46	10230	20	20	50	-155(*)
E5a-Q	BPSK	10.23	20.46	10230	100	10	-	-155(*)
E5b-I	BPSK	10.23	20.46	10230	4	4	250	-155(*)
E5b-Q	BPSK	10.23	20.46	10230	100	100	-	-155(*)
E5	AltBOC(15,10)	10.23	51.15	10230	-	-	-	-152
E6A	BOCcos(10,5)	5.115	30.69	?	?	?	?	?
E6B	BPSK	5.115	10.23	?	?	?	1000	-155(*)
E6C	BPSK	5.115	10.23	?	?	?	-	-155(*)

Table 2.2: Summary of Galileo signal characteristics, from [EU, 2010]. Minimum received power values marked with (*) represent the total power of the in-phase and quadrature components (50/50% I/Q power sharing).

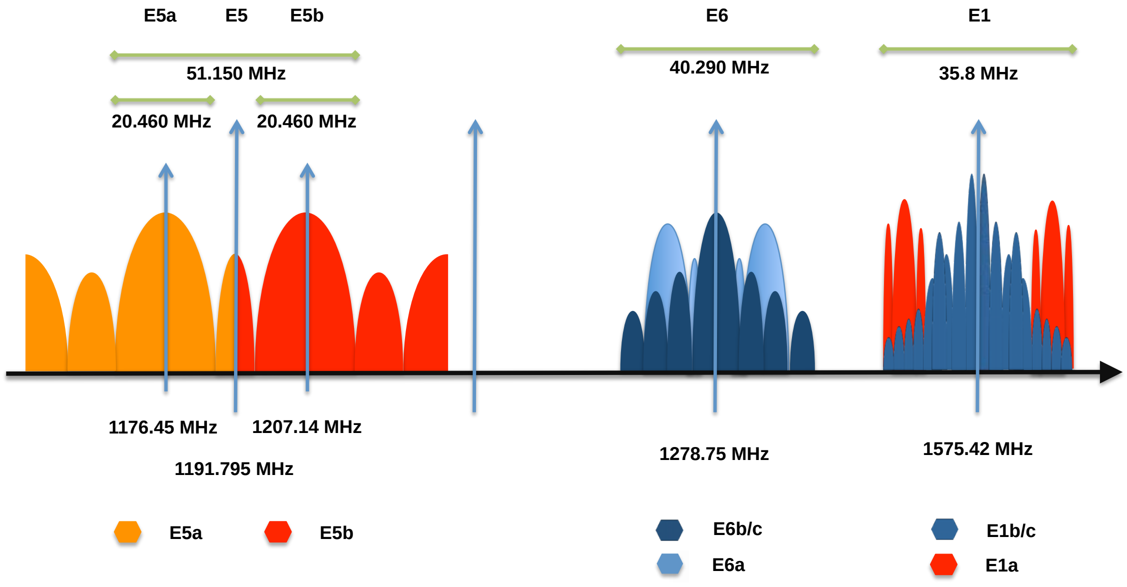

Figure 2.7: Qualitative Representation of the Galileo signal spectrum

2.4 Other Satellite Systems; Compatibility and Interoperability

Along with the global navigation systems, local augmentation satellites, such as the European Geostationary Navigation Overlay Service (EGNOS) and the American Wide Area Augmentation System (WAAS), provide improved accuracy by transmitting navigation corrections in a local scale from geo-stationary satellites. In addition, apart from GPS and Galileo, as stated above, other countries are also pursuing the development of their own global navigation system.

GLONASS is the Russian GNSS, which is very similar to GPS. The satellite constellation is composed of 24 space vehicles. In October 2011, the GLONASS constellation was fully restored for the first time since 1996. The satellites are distributed in three circular orbits at 19,100 km altitude with a 64.8 degree inclination and a period of 11 hours and 15 minutes. The satellites broadcast a standard precision (SP) signal and a restricted high precision (HP) signal at both L1 and L2 bands. SP signals are modulated by a 511 chips long PRN sequence, with a period of 1 ms, i.e. 0.511 Mcps. High precision codes are 1 second long and a chipping rate of 5.11 Mbps [Misra and Enge, 2006].

The main difference with respect to GPS is that all the satellites transmit the same spreading code for their SP signal, however each satellite transmits on a different frequency using a 14-channel Frequency Division Multiple Access (FDMA) technique. The 24 satellite constellation only uses 14-channels as antipodal satellite pairs share the same channel since they are not simultaneously visible by an Earth-based receiver. This multiple access design has some advantages with respect to CDMA, for instance, a single tone jammer can only take out at most one satellite signal in an FDMA system, but all signals in a CDMA system. On the other hand, a single receiver needs to synthesize many frequencies, which increases its complexity. In the recent years, GLONASS has indicated that, as part of the system modernization, the next satellite generation will introduce a new CDMA signal.

On its side, the People's Republic of China is developing COMPASS, a global navigation system which will comprise a constellation of 35 satellites, 5 of them in a geostationary orbit. The first navigation satellites were launched during the first half of 2012, and began offering navigation services for the Asia-Pacific region in December 2012. The full constellation is expected to be deployed by 2020 [Beidou, 2013]. The signals in space of this system will be located in E1, E2, E5b, and E6, thus overlaping with Galileo and GLONASS.

The sharing of spectral bands makes GNSS prone to interference. However, due to the orthogonality of the spreading codes, this has been proven to be insignificant. The compatibility of the systems allows to design receivers capable of simultaneously acquiring signals from more than one navigation system. With more available signals from independent systems it will be possible to improve the final navigation and positioning performances in terms of accuracy and reliability.

Chapter 3

Fundamental Aspects of GNSS Reflectometry

As discussed in the previous chapter, signals transmitted by GNSS satellites are highly stable, self-calibrated, and fully available providing a continuous global coverage. This makes them outstanding candidates to be used as sources of opportunity for remote sensing applications. With the increasing number of GNSS satellites in orbit, more navigation signals traverse the atmosphere and impinge on the Earth's surface, thus improving the spatial and temporal sampling of natural phenomena. GNSS-Reflectometry (GNSS-R) is based on the exploitation of GNSS scattered signals off the Earth surface for the estimation of bio– geo– physical parameters. The following sections review the most relevant aspects of this technology.

3.1 The GNSS-R Concept

GNSS Reflectometry is a form of bistatic radar [Skolnik, 1990]. While most radar systems, such as those used for monitoring air space, harbor approaches, and weather forecasting, combine the radar transmitter and receiver at the same site –the so called monostatic radar– bistatic systems use transmitters and receivers separated by a considerable distance. Such systems have been used for studying certain atmospheric phenomena and for military applications where simple line-of-sight reflections from the target of interest are inadequate or insufficient. The power observed by the receiver can be expressed by means of the bistatic radar equation:

$$P_{pq}^{r} = \frac{P_t \lambda^2}{(4\pi)^3} \int \frac{G_t G_r}{R^2 R_0^2} \sigma_{pq}^{0} dA \,, \tag{3.1}$$

where P_t is the transmitted power; G_t and G_r are the transmitter and receiver antenna gains, respectively; R and R_0 the ranges from transmitter to the target under observation, and from the target to the receiver; and finally σ_{pq}^{0} is the polarization dependent bistatic radar coefficient, with p and q the incident and scattered polarizations, respectively.

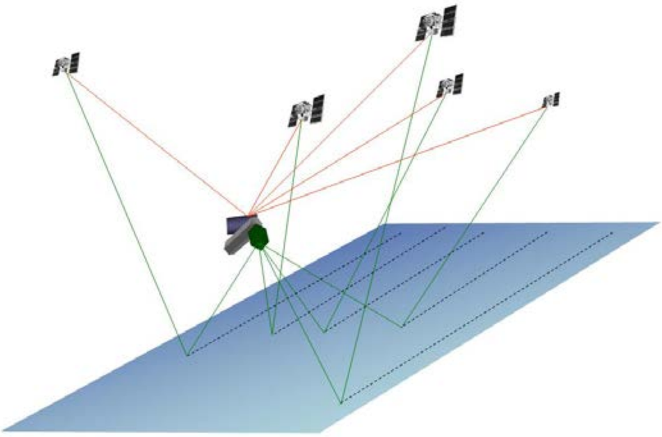

Figure 3.1: The GNSS-R concept: a single GNSS-R receiver collecting direct and reflected signals of multiple GNSS satellites.

The scattering coefficient (or normalized radar cross section) describes the object's ability to reradiate the incident energy into a certain direction. By definition this is the ratio between the scattered power density per unit area and the power density reradiated by an isotropic scatterer [Ulaby et al., 1986a]:

$$\sigma_{pq}^{0} = 4\pi R^{2} \frac{|E_{pq}^{s}|^{2}}{A\,|E_{p}|^{2}}\,, \tag{3.2}$$

where E_p and E_{pq}^s are the incident and scattered fields, A the total area of the illuminated surface, and R the distance of the point of observation to the centre of A.

The concept of bistatic radar can be extended to satellite signals. Since signals transmitted by a satellite get scattered off the Earth's surface, detecting these reflections by a separated passive receiver could provide some information about the surface. While, in principle, any satellite signal could be used, GPS (and other GNSS) turn out to be particularly useful. In GNSS-R a single receiver picks-up the direct and reflected signals coming from multiple GNSS satellites to retrieve geo-physical parameters of the scattering surface (multistatic configuration), Fig. 3.1. With the increasing number of GNSS satellites, a single receiver could potentially get signals from more than 20 emitters at the same time, thus obtaining a high number of independent observations of the same scene, which could either be used to increase the instrument's swath, or to reduce the noise in the estimation of geo-physical parameters.

Since it was first proposed about two decades ago, this technique has gained increasing interest among the scientific community. Several reasons can be identified as the foundations for this growing interest, however, two main ones can be pointed out. On one hand, the global availability and stability of GNSS signals enables their use as sources of opportunity. The passive nature of this concept allows for the production of cost and resource effective instruments. On the other hand, GNSS makes use of L-band radiation and is thus highly interactive with the natural scattering medium, but impervious to atmospheric conditions. Potential applications exploiting these signals are numerous. Among the geophysical parameters navigation signals are sensitive to, one can mention topography, surface roughness, moisture, ionospheric electron content, tropospheric water vapor, water salinity, and vegetation.

3.2 Technological Background

Until the early 90s, GNSS reflections constituted just parasitic multipath signals in positioning determination and therefore were considered an effect to be mitigated. The use of GPS signal reflections as sources of opportunity for remote sensing applications was initially proposed by Martin-Neira [1993] (ESA-ESTEC). In this fundamental work, it was proposed to account for the existent delay between the direct and the reflected signals over the ocean to retrieve altimetry information, i.e., the PAssive Reflectometry and Interferometry System (PARIS). Since then, several investigations followed this idea motivated by the vast amount of opportunities that this technology offered.

Katzberg and Garrison [1996] proposed to use the reflections of GPS signals over the ocean, to provide a better ionospheric correction to conventional altimeters. One year later, the same authors modified a conventional GPS receiver, referred to as Delay Mapping Receiver (DMR), to record power measurements of GPS reflected signals off the ocean [Katzberg and Garrison, 1997], opening the door to the scientific community to use GPS signals as a source of opportunity for remote sensing applications.

In 1999, Katzberg and Garrison presented some examples of GPS reflected signals to estimate altimetry measurements from airborne platforms above the ocean [Katzberg et al., 1999]. Several campaigns followed this experiment, demonstrating good precision in the determination of the aircraft altitude over the surface [Lowe et al., 2002b; Ruffini et al., 2003], and also from ground based platforms [Caparrini et al., 2007]. Precise in-land waters level estimation was also achieved in other works attending to the phase evolution of direct and reflected signals [Egido et al., 2009; Egido and Caparrini, 2010].

The concept was also proposed as a bistatic scatterometer to measure ocean surface wind speeds, and sea state, observing the sensitivity of delay maps to geo-physical parameters: [Komjathy et al., 2004; Elfouhaily et al., 2002; Garrison et al., 2002]. Significant effort was put on the theoretical modeling of the scattered signals, and on the understanding of the physical mechanisms behind the observed signal. Based on the Kirchoff Approximation (KA) and Geometric Optics (GO) limit, a commonly used model was put forward by Zavorotny and Voronovich [Zavorotny and Voronovich, 2000b]. This model is often used in conjunction with the ocean wave spectrum model developed by Elfouhaily et al. [Elfouhaily et al., 1997], as a mean to understand the physical mechanisms behind the observed signal scattering. Additional models have also been proposed, digging more deeply on the spectrum and polarization characteristics of the reflected signals [Zuffada et al., 2004; Thompson et al., 2005]. In this sense, in [Ruffini and Soulat, 2000], and [Elfouhaily et al., 2002], the use of Delay-Doppler Map (DDM) was proposed, in order to retrieve directional sea-surface roughness, or Directional Mean Square Slope (DMSS). This was also investigated in [Germain et al., 2004], and [Soulat, 2003]. The use of DMSS for sea surface salinity measurements calibration was discussed in [Sabia et al., 2007] and [Marchan, 2009].

Given the highly reflective nature of water, GNSS-R research was initially focused on the application of this technique for the monitorization of water surfaces. However, the interest has now moved towards cryosphere and land. In [Belmonte-Rivas, 2007] an airborne experimental campaign was conducted in the Arctic sea ice to test the performance of GNSS-R for mapping sea ice conditions. Other studies are currently investigating the characterization of sea-ice and dry snow signatures with GNSS scattered signals [Fabra et al., 2010, 2012]. This PhD Thesis deals with the application of GNSS bistatically scattered signals for land remote sensing applications; the first works related to this topic date from 2000, and 2002, when the SNR of GPS reflected signals was used to relate changes in the observed signals with terrain features. The use of multi-polarization observations for soil moisture monitoring was first proposed in [Zavorotny and Voronovich, 2000a]. Other works have recently used the interference pattern of direct and reflected signals to estimate both soil moisture and crop height [Rodriguez-Alvarez et al., 2011]. This technique was also used by Larson and Zavorotny [Larson et al., 2010; Zavorotny et al., 2010] to estimate soil moisture from GPS geodetic stations. These works and other relevant experiments are reviewed more in depth in a later section.

An important breakthrough of this technology was the first observations of GNSS reflected signals from a space-borne platform, reported by Lowe et al. in [Lowe et al., 2002a]. Both GPS and GLONASS signals were recorded using the high gain antenna mounted in the Shuttle bay for the SIR-C campaign during the receive-only calibration phase of the imaging radar. Later, a GPS receiver added to an UK Disaster Monitoring Constellation (UK-DMC) satellite as a secondary payload gave the possibility to Gleason et al. [Gleason et al., 2005] to prove that, notwithstanding its weak power, scattered signals could be detected above the background noise from low earth orbits. These works paved the way for the European Space Agency initiative of an in-orbit demonstrator [Martin-Neira et al., 2011], the so called PARIS-IOD. The prime objective of this initiative is to demonstrate the capabilities of the technology as an ocean altimeter. In addition, the PARIS-IOD is aimed at investigating the use of GNSS-R for sea surface roughness, soil moisture, biomass, and ice monitoring applications from space, which will lay the foundations for an operational GNSS-R mission.

Given its configuration, GNSS-R has many similarities with conventional bistatic radars. However, the final received signal has some specific characteristics due to the properties of GNSS signals. Those are reviewed in the following sections.

3.3 The Scattering Geometry

In specular reflection it is usually considered that a plane wave impinges an indefinitely extended flat surface. All surface points are illuminated by the incident wave with a linearly varying phase and reflect in phase in the illumination direction in the form of another plane wave. Since the surface is an infinite plane, there is no distinction among re-radiating points, and therefore it can be assumed that the reflection occurs at the specular point. This point provides the shortest path for the transmitter-surface-receiver geometry and ensures that the incident angle is the same as the scattering angle.

The plane wave hypothesis is however a simplification of the reflection process. Actually, the electromagnetic field originated at the transmitter is a spherical wave. As a consequence, the phase of the impinging wave varies quadratically from point to point of the illuminated area and remains close to the one of the specular point within the first Fresnel zone. The latter is defined as the locus of points on the surface whose path differ less than $\lambda/2$ with respect to the delay of the specular point. Points outside this region contribute destructively and constructively to the final scattered field in an alternating way, thus canceling out, to a large extent, their final contribution to the scattered field. In conclusion, even for a perfectly flat surface the reflection is occurs within an extended area in the vicinity of the specular point [Beckmann and Spizzichino, 1963].

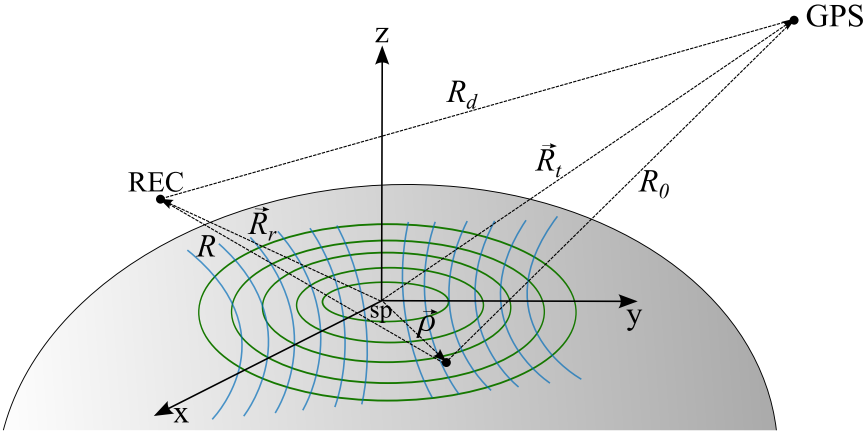

Figure 3.2: GNSS-R Scattering Geometry; the specular point (SP) is located at the center of the cartesian coordinate system. Iso-delay and iso-Doppler lines are represented in green and blue respectively.

As the surface becomes rougher, other points on the surface at distant regions from the nominal specular point are prone to have the proper orientation to redirect the incident wave towards the receiver's antenna, thus contributing to the final received power. The active scattering area finally contributing to the reflected signal is known as glistening zone. The scattering geometry is depicted in Fig. 3.2. Without loss of generality it can be assumed that the specular point is located at the origin of our reference system, with the propagation plane contained in the YZ plane. The transmitter and receiver positions are defined by vectors $\vec{R}_t$ and $\vec{R}_r$, respectively. The distance of any point on the surface, $\vec{\rho}$, to the specular point can be calculated as:

$$\delta(\vec{\rho}) = R_0(\vec{\rho}) + R(\vec{\rho}) - (|\vec{R}_t| + |\vec{R}_r|)\,, \tag{3.3}$$

where R_0 and R are the distances from transmitter and receiver to the scattering point on the surface. Assuming a flat Earth approximation and indefinitely distant transmitter and receiver for a point at $\vec{\rho} = (x, y, 0)$, the previous equation can be approximated as:

$$\delta \approx \sqrt{x^2 + (y + h\tan\theta)^2 + h^2} - y\sin\theta - \frac{h}{\sin\theta}\,, \tag{3.4}$$

where h_0 and h are the heights of both transmitter and receiver to the tangent plane, and θ is the incidence angle. The locus of points with constant delay with respect to the specular point, i.e. iso-range lines, describe ellipses on the surface whose semi-major and semi-minor axes are obtained, respectively, by:

$$a = \frac{\sqrt{\delta(\delta + 2\,h\,\cos\theta)}}{\cos^2\theta} \approx \frac{\sqrt{2\,\delta\,h\cos\theta}}{\cos^2\theta}\,, \tag{3.5}$$

and

$$b = \frac{\sqrt{\delta(\delta + 2\,h\,\cos\theta)}}{\cos\theta} \approx \frac{\sqrt{2\,\delta\,h\cos\theta}}{\cos\theta}\,, \tag{3.6}$$

where the quadratic term of δ can be disregarded if it is much smaller than the receiver's height over the surface. This will be the case for most airborne and spaceborne scenarios.

Apart from different delays, points on the glistening zone have different Doppler shifts due to differences in the transmitter-surface-receiver geometry. For transmitter and receiver velocities $\vec{v_t}$ and $\vec{v}_r$, the Doppler shift for each point on the surface can be calculated as:

$$f_D(\vec{\rho}) = (\vec{v_t} \cdot \hat{m}(\vec{\rho}) + \vec{v_r} \cdot \hat{n}(\vec{\rho}))/\lambda \,, \tag{3.7}$$

where $\hat{m}$ and $\hat{n}$ represent the unit vectors of the incident and scattered waves, respectively, calculated as $\hat{m} = \vec{R}_0/|R_0|$ and $\hat{n} = \vec{R}/|R|$. The locus of points with equal Doppler shift describe hyperbolas on the surface; these are known as iso-Doppler lines. A pictorial representation of the scattering geometry and the iso-Delay and iso-Doppler lines is depicted in Fig. 3.2.

The size and shape of the iso-Delay and iso-Doppler lines depend on the transmitter and receiver geometry. For instance, the size of the first chip zone increases with the receiver's height, extending to several km for a spaceborne platform, and to some hundreds of meters for a low altitude receiver. On its side, the magnitude of the Doppler shift depends on the receiver and transmitter velocity (normalized to their height). It can be shown [Hajj and Zuffada, 2003] that for a spacecraft receiver the GNSS velocity contributes to Doppler shift by less than 5%. In low velocity aircraft flying horizontally or stationary geometries of ground-based receivers, the Doppler shift of the direct and reflected signals is virtually the same and determined essentially by the transmitter velocity. However, as will be shown later, even for low altitude stationary receivers there is a residual Doppler shift between the direct and the reflected signal that needs to be compensated to perform some types of observations.

3.4 Direct and Reflected GNSS Signal Modeling

For a given time t, the GNSS signal at a receiver's location $\vec{R}_r$ can be expressed as:

$$u_d(\vec{R}_r, t) = \sqrt{\frac{P_t G_t}{4\pi}}\, a\left(t - \frac{R_d}{c}\right) \frac{e^{-jkR_d}}{R_d} e^{-j2\pi(f_c+f_D)t} \,, \tag{3.8}$$

where P_t and G_t stand for the transmitted power and GNSS satellite antenna gain, respectively; $a(t)$ represents the modulating PRN code; f_c is the GNSS carrier frequency; k is the associated wavenumber $(2\pi/\lambda)$; f_D is the Doppler frequency shift originated due to the relative velocity of transmitter and receiver; and R_d is the distance between transmitter and receiver, $R_d = |\vec{R}_r - \vec{R}_t|$, Fig. 3.2. The previous equation can also be used to express the field reflected from a perfectly flat surface; in such a case it can be considered that the actual source can be replaced by a mirrored one below the surface, assuming it as a punctual source at a distance $R_{0,\text{sp}} + R_{\text{sp}}$,

$$u_{r,\text{sp}}(\vec{R}_r, t) = \sqrt{\frac{P_t G_t}{4\pi}} \mathcal{R}_{\text{sp}}\, a\left(t - \frac{R_{0,\text{sp}} + R_{\text{sp}}}{c}\right) \frac{e^{-jk(R_{0,\text{sp}}+R_{\text{sp}})}}{R_{0,\text{sp}} + R_{\text{sp}}} e^{-j2\pi(f_c+f_{D,\text{sp}})t} \,, \tag{3.9}$$

where $R_{0,\mathrm{sp}}$ and R_{sp} are the distances from transmitter and receiver to the specular point, as depicted in Fig. 3.2. $\mathcal{R}_{\mathrm{sp}}$ is the Fresnel reflection coefficient at the specular point.

For a rough surface, the reflected field can be expressed, under KA, as the superposition of all scattered fields from each single point on the surface. The Kirchhoff approximation assumes that the radius of curvature at any point on the surface is much larger than the wavelength, thus the fields are considered to be reflected from an infinite tangent field at that point. In a similar way as Zavorotny and Voronovich [2000b], the final scattered field as observed by the receiver yields:

$$\begin{aligned} u_r(\vec{R}_r, t) = \frac{i\sqrt{P_t G_t}}{4\pi} \int\limits_s \sqrt{G_r(\vec{\rho})}\mathcal{R}(\vec{\rho})\, a\left(t - \frac{R_0(\vec{\rho}) + R(\vec{\rho})}{c}\right) \cdot \\ \cdot \frac{e^{-jk(R_0(\vec{\rho})+R(\vec{\rho}))}}{R_0(\vec{\rho})R(\vec{\rho})} e^{-i2\pi(f_c+f_D(\vec{\rho}))t} \, (\vec{q}\cdot\hat{N})\, d\vec{\rho}, \end{aligned} \tag{3.10}$$

where G_r is the receiver antenna gain. P_t and G_t can be considered constant for all the scattering surface. $\vec{q}$ is the scattering vector defined as $\vec{q} = k(\hat{m} - \hat{n})$, with k the wavenumber, and $\hat{N}$ is the vector normal to the local tangent plane. $\vec{q}$ corresponds to the bisecting vector of the incident and scattered fields and defines the plane that would specularly reflect the incident wave in the direction of the receiver. It can be decomposed in its transversal and vertical components as $\vec{q} = \vec{q}_\perp + q_z\hat{z}$. In the case of a smooth surface both $q_z\hat{z}$ and $\hat{N}$ are almost aligned, thus $\vec{q}\cdot\hat{N} \approx q_z$. For a rough surface the dot product can be approximated by $\vec{q}\cdot\hat{N} \approx q^2/q_z$.

In order to be able to detect GNSS signals, the direct and reflected fields are cross-correlated with the PRN code replica for a given delay offset, τ, and a frequency shift with respect to the carrier, f. The correlation can be expressed as:

$$Y(\tau, f) = \frac{1}{T_i}\int_{T_i} u_{d,r}\, a(t-\tau)\mathrm{e}^{i(f_c+f)t}dt\,, \tag{3.11}$$

with T_i the coherent integration time. For the direct signal, when the correlation is maximum the PRN codes of both incoming signal and replica are aligned, i.e. τ corresponds to the signal propagation delay from transmitter to receiver, which provides ranging information for positioning (pseudoranges), and f matches the Doppler shift due to the relative velocity between the GNSS satellite and receiver. In the case of the reflected signal, this interpretation is more complicated. Substituting Eqn. (3.10) in (3.11), and assuming that the scene is frozen for the integration time Ti, the integration order can be exchanged [Zavorotny and Voronovich, 2000b], thus it can be written that

$$Y(\tau, f) = \frac{i\sqrt{P_t G_t}}{4\pi} \int\limits_s \sqrt{\frac{G_r(\vec{\rho})\lambda^2}{4\pi}}\mathcal{R}(\vec{\rho})\chi(\delta\tau, \delta f)\frac{e^{-jk(R_0(\vec{\rho})+R(\vec{\rho}))}}{R_0(\vec{\rho})R(\vec{\rho})} e^{-i2\pi(f_D(\vec{\rho})-f)t}\,(\vec{q}\cdot\hat{N})\, d\vec{\rho}, \tag{3.12}$$

obtaining the so called complex waveform. $\chi(\vec{\rho};\delta\tau,\delta f)$ is known in radar terminology as the Woodward Ambiguity Function (WAF), which can be approximated by

$$\chi(\vec{\rho};\delta\tau,\delta f) \approx \Lambda(\delta\tau)\,\mathrm{S}(\delta f)\,. \tag{3.13}$$

$\Lambda(\delta\tau)$ is the PRN code autocorrelation function representing the impulse response of the system in the time domain, Eqn. (2.2). In this case, $\delta\tau$ is the difference of the selected delay τ and the delay of any point on the surface at $\vec{\rho}$: $\delta\tau = \tau - (R(\vec{\rho}) + R_0(\vec{\rho}))/c$. $\mathrm{S}(\delta f)$ accounts for the system response in the Doppler dimension, with $\delta f = f_D(\vec{\rho}) - f$, and $f_D(\vec{\rho})$ the Doppler shift evaluated at any point on the surface. This has the form of a complex sinc function:

$$\mathrm{S}(\delta f) = \frac{\sin(\pi\delta f T_i)}{\pi\delta f T_i} e^{-i\pi\delta f T_i}\,. \tag{3.14}$$

Taking the absolute squared value of the waveforms obtained by Eqn. (3.12) and averaging over a sufficiently long time interval we obtain that

$$< |Y(\tau,f)|^2 >= \frac{T_i^2 P_t G_t \lambda^2}{(4\pi)^3} \iint_A \frac{G_r(\vec{\rho})}{R^2(\vec{\rho})R_0^2(\vec{\rho})}\,\sigma_{pq}^0\,\chi^2(\vec{\rho};\delta\tau,\delta f)d\vec{\rho}, \tag{3.15}$$

where σ_{pq}^0 is the polarization dependent bistatic radar coefficient [Zavorotny and Voronovich, 2000b]. The previous result is the so called delay-Doppler map, and accounts for the averaged GNSS scattered power on the surface as a function of delay and frequency. From this equation it can be readily seen that the GNSS scattered power after correlation comes from the intersection of four spatial zones:

- The receiver antenna footprint projected on the surface $G_r(\vec{\rho})$ (the transmitting antenna gain, G_t, projected on the surface can be considered to be constant).
- The annulus zone defined by the delay filtering Λ^2 function: due to the PRN code autocorrelation properties, for a given delay τ, the integral in Eqn. (3.15) contains only the part of the scattering surface such that $|\tau - (R(\vec{\rho}) + R_0(\vec{\rho}))| < \tau_c$, where τ_c is the PRN code chip period. In the case that τ corresponds to the specular delay, this region is an ellipse around the specular point, i.e. the first-chip zone, whose size can be obtained by equations (3.5) and (3.6).
- The Doppler zone, defined by the Doppler filtering S^2 function: as shown in Eqn. (3.14), the Doppler impulse response resembles a sinc function whose width is the inverse of the coherent integration time T_i. Alike the previous case, only points on the surface whose Doppler shift satisfies $|f_D(\vec{\rho}) - f| < 1/T_i$ contribute to the scattered power. This is analogous to apply a spatial band pass filter on the the reflected signal.
- The scattering coefficient σ_{pq}^0, which is determined by the dielectric and physical properties of the surface. For rough surface, σ_{pq}^0 is extended to areas away from the specular point forming what is known as the glistening zone. As a result, when performing the correlation of a GNSS reflected signal with the PRN code replica, the cross-correlation waveforms are smeared out towards higher delay lags that can reach up to several chips in the case of very rough surfaces (specially for receivers at very high amplitudes or LEO orbits).

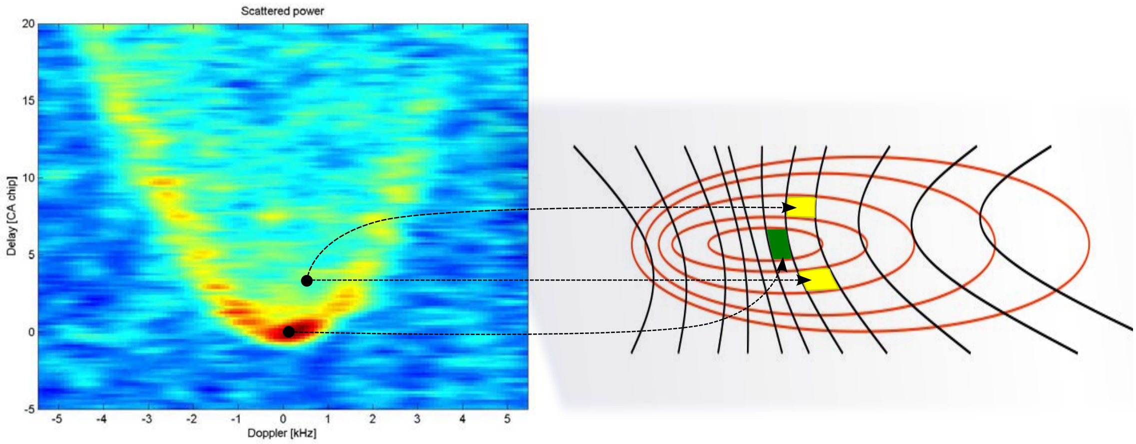

Figure 3.3: Delay-Doppler Map and iso-Range and iso-Doppler lines on the surface. The DDM was obtained from the UK-DMC experiment data [Gleason, 2006b].

The relative weight of each of these zones in the final scattered power depends on the bistatic geometry. For instance, for a spaceborne receiver, the χ^2 function is the limiting factor for the received scattering power at each (τ, f) pair. However, for low altitude receivers, it is most of the times the receiving antenna pattern the one determining the area of the surface contributing to the received power. It is also worth noting here that by choosing different (τ, f) pairs different regions on the surface can be selected. This is explained further in the following section.

3.5 GNSS Reflectometry Observables

3.5.1 The Delay-Doppler Map

Equation (3.15) describes the distribution of the GNSS scattered power as a function of delay and frequency. This is commonly known as DDM, which constitutes the GNSS-R fundamental observable. As mentioned above, by selecting different (τ, f) pairs the contributions coming from different cells on the surface can be observed due to the spatial filtering of the WAF. These cells are the intersections of iso-delay and iso-Doppler stripes at any point on the surface with a width determined by the GNSS PRN code chip for the delay and by the coherent integration time for the Doppler. In order to illustrate this, Fig. 3.3 shows a DDM obtained with data from the experiment on-board the UK-DMC satellite [Germain et al., 2005], and a pictorial representation of the iso-delay and iso-Doppler lines on the Earth's surface. The DDM coordinates are referenced with respect to the specular point, so that the delay and Doppler pair $(0, 0)$ corresponds to the specular point itself.

The DDM "horseshoe" shape is primarily due to the frequency filtering, indicated by the sinc function in Eqn. (3.13). At iso-Doppler lines far from the specular point, the limited frequency bandwidth determined by the coherent integration time filters out the contributions from the specular point in favor of those at distant iso-range ellipses, thus displacing the reflected GNSS correlation towards higher delays. The horseshoe ridge occurs for (τ, f) pairs corresponding to regions on the surface where the iso-Doppler lines

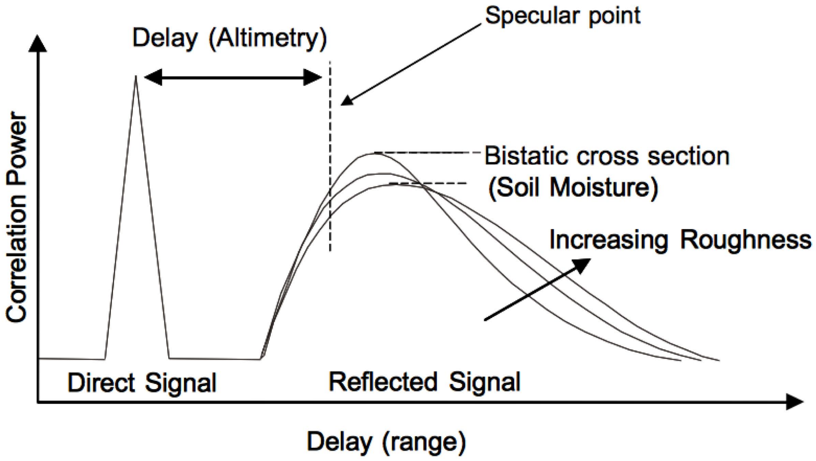

Figure 3.4: Direct and reflected waveforms representation, from [Masters, 2004].

are tangent to the iso-delay lines. These points can be linked to unique cells, as shown in Fig. 3.3 for the specular point. For other DDM points outside this ridge, the iso-delay annulus intersect the iso-Doppler stripes at two points, thus leading to an ambiguity when relating some DDM (τ, f) pairs to cells on the surface.

The DDM can be used to estimate sea state and DMSS [Germain et al., 2004; Sabia et al., 2007]. As mentioned above, the rougher the scattering surface, the more probable is for regions far away from the specular point to contribute to the final scattered power, contributing to smear the DDM towards higher Doppler frequencies. On the contrary, for a flat surface, the scattering is produced around the specular point, and therefore the DDM will be more concentrated around the $(0, 0)$ point. This behavior can be modeled by Eqn. (3.15). Using the bistatic radar coefficient σ^0 provided in [Zavorotny and Voronovich, 2000b] and [Elfouhaily et al., 1997] the two-dimensional probability distribution function of surface slopes can be estimated, and from there geophysical parameters such as DMSS or significant wave height [Soulat, 2003; Sabia et al., 2007]. Other studies have also used the DDM normalized volume to determine the sea state [Marchan, 2009].

3.5.2 The Direct and Reflected Complex Waveforms

By selecting the Doppler frequency of the specular point, the reflected cross-correlation waveforms are obtained. Fig. 3.4 provides a qualitative representation of direct and reflected waveforms for different surface conditions, showing the possible measurements that can be extracted from GNSS-R waveforms. For instance, the displacement of the reflected with respect to the direct waveforms is due to the excess path traveled by the reflected signal before reaching the receiver. By measuring this additional delay, the height of the receiver over the surface can be estimated and from there derive sea altimetry information [Ruffini et al., 2003], [Martin-Neira, 1993]. For ground-based receivers where the flat Earth approximation applies, the basic GNSS-R altimetry equation can be written as:

$$c\,\tau_i = 2h\sin(\epsilon_i) + \mathrm{SB}\,, \tag{3.16}$$

where τ_i is the measured delay between the direct and reflected waveforms for the ith satellite, ϵ_i is the satellite's elevation angle, and h is the height of the receiver over the surface. SB represents the system bias, which accounts for the electrical path difference of the direct and reflected channels, which also needs to be estimated. For airborne and spaceborne receivers the previous altimetry equation can no longer be applied, since the flat Earth approximation does not longer hold and other effects such as tropospheric and ionospheric delay need to be taken into account [Ruffini et al., 2003], [Martin-Neira et al., 2011].

The additional length of the reflected signal path incurs in a phase difference of the direct and reflected electromagnetic fields, which can be measured from the complex cross-correlation waveforms. Relative phase measurements provide very precise ranging observables; ground-based altimetry precisions of few centimeters have been achieved with this technique [Egido and Caparrini, 2010]. However, phase measurements of the reflected signal can only be obtained over relatively flat surfaces, where the coherency of the signal is kept, limiting the applicability of this technique to calm waters such as water reservoirs, lakes and closed-up harbors. This technique has also been used to monitor seasonal ice level variations [Fabra et al., 2012].

The shape of the waveform and the inclination of the waveform's trailing edge can be used to obtain sea state and wind estimates; as explained above, when observing a rough surface, the energy of the impinging signal is no longer reflected from a small region around the specular point, but it is distributed over an extensive region on the surface known as the glistening zone. This produces a skewness on the reflected waveform that can be modeled in order to estimate sea state and wind information [Garrison et al., 2002].

Finally, accounting for the waveform's peak amplitude, the bistatic radar coefficient can be estimated. This is the primary observable for soil moisture estimation and vegetation biomass. As mentioned above, the scattered signal is mostly Left Hand Circular Polarization (LHCP), however, due to rough surface scattering mechanisms and the usually low dielectric constant of soils, there is a non-negligible RHCP scattered signal that can be detected and used to estimate bio-geophysical parameters. This was initially proposed in [Zavorotny and Voronovich, 2000a], however, the validity of the technique remained an open question. The research and experimental work presented in this Thesis are based on this principle.

Other observables can be obtained attending to the evolution along time of GNSS-R signals. The interferometric pattern technique [Rodriguez-Alvarez et al., 2011], uses a single vertically polarized antenna to measure the interference pattern of the direct and reflected signals, which contains soil moisture, vegetation, and altimetry information. Another observable, known as the Interferometric Complex Field (ICF), is defined as the time series of the direct and reflected waveform's peak ratio [Ruffini and Soulat, 2004]. By performing this ratio, most propagation effects common to the direct and reflected channels can be cancelled out, i.e. ionospheric effects, tropospheric effects, receiver clock errors, and antenna radiation pattern, if assumed that the direct and reflected antennas are identically built. The ICF contains information about the surface reflectivity and the surface roughness, which has a direct application in coastal areas; by calculating the correlation of this complex signal, the surface's coherence time can be estimated and from there the sea state [Caparrini et al., 2007], [Valencia et al., 2010].

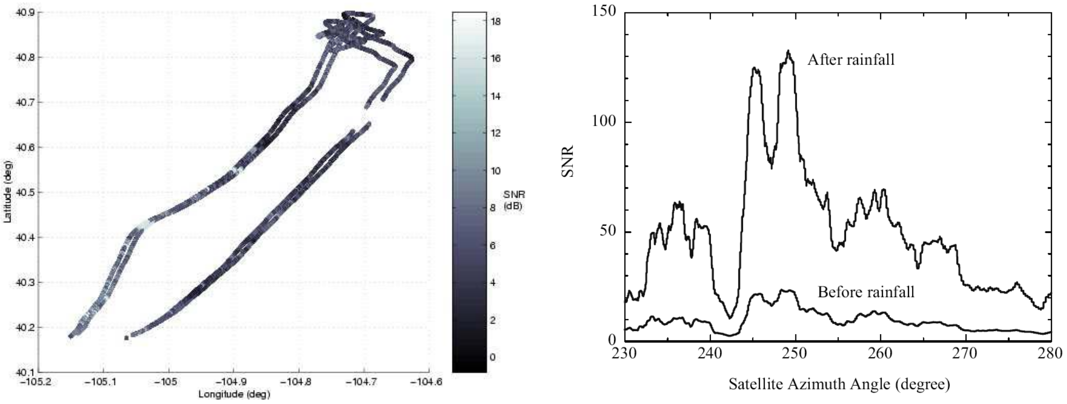

(a) (b)

Figure 3.5: (a) SNR airborne measurements over land surfaces, [Masters et al., 2000]; (b) Comparison between two reflected signals for the same GPS satellite obtained before and after a rain event, [Zavorotny et al., 2003]

3.6 Previous GNSS-R Activities for Land Applications

In many of the studies mentioned above, serendipitous land reflections were captured from an airborne platform while recording ocean reflection of GPS signals, thus opening the way to a series of experimental campaigns aimed at demonstrating the correlation of the GNSS-R signal to land features.

The first reference found in the literature regarding the estimation of surface reflectivity by means of GPS reflected signals was provided by Kavak et al. [1998]. In this work, the authors used a single GPS receiver to measure the power of the combination of direct and reflected GPS signals (multipath) arriving at a single GPS antenna in vertical position. Multipath signals reflect off the ground before arriving at the GPS antenna; they create constructive and destructive interference patterns that cause oscillations in the GPS observations. The technique is known as interferometric pattern technique. The frequency of the oscillations is dependent on the GPS frequency and the distance of the reflecting surface from the antenna. The power variation between the maxima and minima of the interference pattern is dependent on the surface's reflectivity. An experiment was carried out over three different surfaces, grass, asphalt, and a water body to verify this hypothesis, however it was found that in the case of water the measured peak–to–peak power was the lowest of the three. This was linked to the fact that the surface was wavy, and therefore less power was coherently reflected than in the previous cases.

In a later work Masters et al. [2000], used the DMR receiver [Katzberg and Garrison, 1997] to provide a proof-of-concept for determining soil moisture from GPS reflected signature. During Spring 2000 an airborne campaign based in Colorado was carried out together with in situ soil moisture measurements. The fluctuations of the measured SNR appeared to correlate with ground features, however this first experiment did not allow the authors to draw reasonable conclusions about the potential of the technique in soil moisture retrieval.

Since then, several experiments have demonstrated the capability of GPS bistatic scatterometers to obtain high enough SNR in order to sense small changes in surface reflectivity, from both ground and airborne platforms. Zavorotny et al. [2003] mounted the DMR, on top of a 300 meters tall stationary tower. Measurements were carried out during summer and fall 2002. The main purpose of this experiment was to demonstrate sensitivity of GNSS-R signals to soil moisture and to validate the theoretical work proposed in [Zavorotny and Voronovich, 2000a], in which the use of the ratio of two orthogonal polarizations of the reflected signal was proposed to obtain soil moisture observables independent of the surface roughness. For that, five different antennas were used in the experiment: a low gain LHCP antenna and 4 high gain (12 dB) antennas at the two linear polarizations (H and V), and at the two circular polarizations (RHCP and LHCP). Soil moisture measurements were recorded at 6 cm depth with a Time Domain Reflectometry (TDR) probe. Cross-correlation waveforms were obtained when the specular point fell within the footprint of the high gain antenna. The averaged SNR vs. GPS satellite azimuth showed an increase in reflected power after rainfall, when the soil was very wet or standing water was present. The bistatic SNR vs. the soil moisture measurements performed by the TDR showed good correlation only for high values of soil moisture, whereas for dry conditions the correlation was poor. The authors suggested that the penetration of L-band signals in dry soil conditions could be higher than the measurement range of the TDR probes. Authors report also that the polarization ratios of the measured data did not show to be independent of the soil roughness, and they attribute this unexpected result to soil moisture inhomogeneity.

The Soil Moisture Experiment (SMEX02) Campaign conducted in Iowa (USA) during June and July 2002 used the DMR receiver to record GNSS-R data. The equipment was set to track signals from the highest elevation satellite in view, resulting in incidence angles from 15° to 35° [Masters et al., 2004]. The observed area consisted mainly of flat agricultural land where corn and soybean crops were growing. The SNR of the scattered power was used as the unique observable to record the changes in surface reflectivity. A qualitative interpretation of the data was reported, based on the assumption that the GPS transmitted power did not change noticeably over the experiment periods. A spatial correlation between the data and the field boundaries, as well as with cover types, was observed. Change detection images were also produced, Fig. 3.6(a), which enhanced widespread precipitations after a given date. The GPS reflected SNR was plotted versus in situ volumetric soil measurements of the first centimeter depth for 31 field sites, and a correlation coefficient of 0.7 was found [Masters, 2004]. The corn field samples correlate slightly more ($r^2 = 0.73$) with the GPS reflected SNR measurements than the soybean crop ($r^2 = 0.70$). The large dispersion of data, apparent in Fig. 3.6(b) suggests that, besides Soil Moisture Content, GPS measurements depend on other geophysical parameters (such as soil roughness or vegetation biomass) or observational parameters (such as incidence angle), which were not supervised[1].

The DMR receiver was also flown on an aircraft, at about 2 km height, near Las Cruces (New Mexico) on October 2002 [Torres, 2004]. This area is naturally deserted with low soil moisture contents throughout the year, with some agricultural fields which are kept at relatively high soil moisture content for crop production. In addition, the crossing of the Rio Grande river offers places where GPS signals can reflect from bodies of water. The GPS reflected data were first analyzed superimposing the reflected signals over digital orthoquad imagery in order to relate the reflections with the natural

---

[1] In [Masters et al., 2004] most of the measured reflection waveforms resembled the direct signal correlation waveform without spreading to longer delays. This indicates that the scattering was mainly specular from the first Fresnel zone which, for a receiver height at 1.1 km, has a diameter of about 30 m. According to authors this assumption is supported by the abrupt change of reflected SNR over roads and streams.

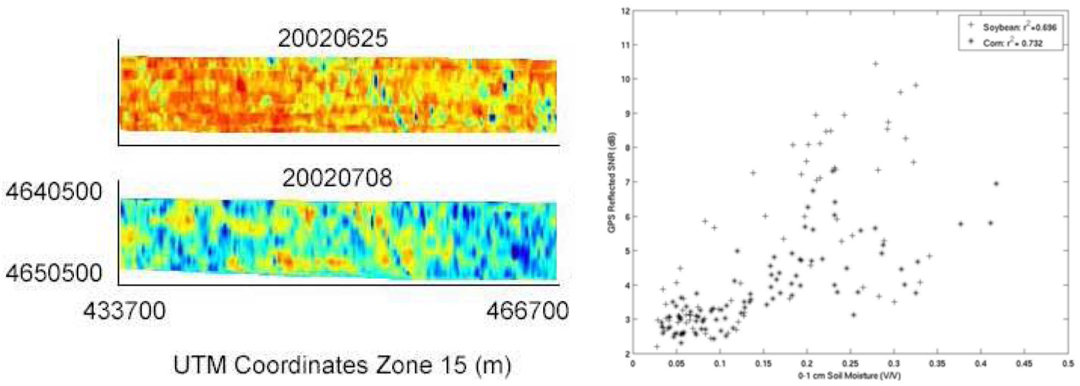

(a) (b)

Figure 3.6: (a) GPS bistatic radar reflected SNR over the SMEX02 study area; red colors show low SNR corresponding to dry soils; whereas blue colors correspond to high SNR, indicating wet soil conditions [Masters et al., 2004]. (b) GPS scattered SNR versus volumetric in situ measurements for field sites containing soy beans and corn crops [Masters, 2004].

characteristics of the surface: the amplitude of the reflected signals reached its maxima at the river crossings, as well as over wet agricultural land. In addition, it was observed that the GPS signals intermitted over fields with trees. The dielectric constant of the observed surface was obtained inverting the modulus of the Fresnel reflection coefficient at vertical polarization (assuming the latter to be equal to the RL polarized one for low incident angles and assuming also a negligible imaginary part of the dielectric constant), and the soil moisture was calculated by a semi-empirical model [Hallikainen et al., 1985]. Despite the fact that no ground-truth data was recorded during the campaign, the obtained results correspond on average to typical soil moistures of the New Mexico area.

As a follow-on of [Masters et al., 2004], Katzberg et al. [2006] performed the calibration of the data recorded during the SMEX02 campaign and attempted the first calibration of reflected GPS signals and estimation of surface dielectric constant compared to surface truth. Two approaches were followed to calculate the ratio between the top and the bottom channels: this ratio was then used to scale the power ratio to be inverted in the retrieval of reflectivity. In first approach the reflectivity measured over a water body present in the campaign area was set to 63 %. The second one assumed a third order polynomial to fit the direct signal vs. elevation angle, in order to represent a relatively constant source of illumination, attributing fluctuations to multipath interferences. The surface reflectivity was estimated considering a specular reflection, and by a model that considered the surface topography. The results with both approaches were very similar as the slopes of the area under observation were below 10° in almost all cases. The soil dielectric constant was extracted from the retrieved reflectivity by inverting the Fresnel reflectivity. In the same way, the dielectric constant was obtained from the recorded ground-truth data using the model proposed by Wang and Schmugge [1980]. The presence of vegetation was taken into account by means of a polarization independent loss factor, [Ulaby et al., 1986b], which is a function of the plant biomass and height. The trend of the GPS measured soil dielectric constant vs. soil moisture content reproduced the measured one, though showing a certain underestimation. It was observed that taking into account the surface roughness through the waveform matching does not yield significant variation in the results of the soil moisture retrieval, while average soil moisture estimation improves if vegetation effect is taken into account. A

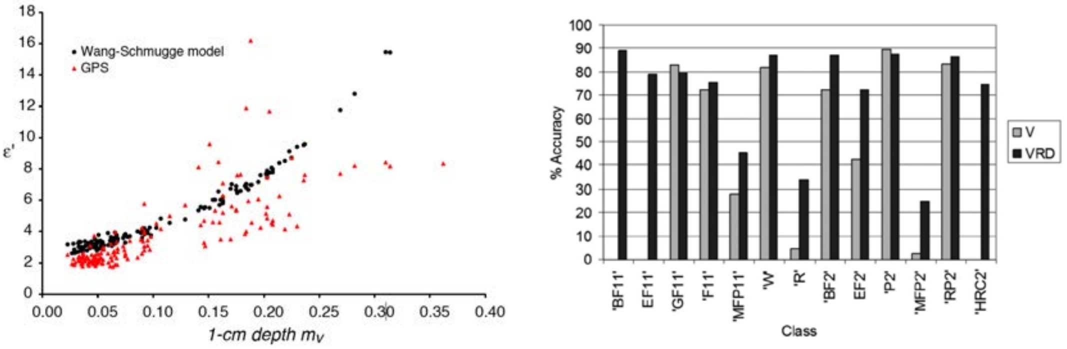

(a)

(b)

Figure 3.7: (a) Measured and theoretical dielectric constant over corn and soybeans fields compared to soil moisture values at the top-most layer of soil [Katzberg et al., 2006]. (b) Classification of sites for visible only and visible plus reflectivity and dispersion measurements [Grant et al., 2007].

better agreement was shown if soil moisture measured in the top 1 cm layer of soil was used instead of the TDR measurements of the top 5 cm. In Figure 3.7(a) the estimated dielectric constant is compared to the theoretical one for the top-most soil layer.

A terrain classification exercise was with GNSS-R carried out in [Grant et al., 2007] using GPS data collected during the SMEX03 campaign which took place in Georgia. An aircraft at 300 m flew over 4 different sites carrying on board both the NASA GPS receiver and a down-looking digital camera. The images were manually segmented and used as ground truth together with soil moisture measurements. A supervised maximum likelihood classification algorithm was applied in a feature space including the measurements at three visible wavelengths and two waveforms parameters: surface reflectivity, derived from the peak of the waveform, and the dispersion, proportional to the width of the waveform. These two features were related, respectively, to the relative sizes of the specular and diffuse components. In particular, the peak of the reflected waveform was found fitting the reflected signal to an ideal Λ function; similarly the peak of the direct waveform was found. Then, the average instrument noise was subtracted from the estimated reflected peak power, and this value was finally normalized to the direct estimated peak power. The dispersion parameter is a weighted sum of the normalized squared correlation values which exceed the noise value, with a weight that increases linearly from 0 to the number of measurements above the noise value. The GPS measurements improved the classification accuracy of about 13.41% with respect to that obtainable by means of visible images only, see Fig. 3.7(b). The improvement is larger for classes with larger soil moisture content, a parameter which does not affect the spectral signature at shorter wavelengths.

The interferometric pattern technique has been more recently used to determine soil moisture and vegetation development. Rodriguez-Alvarez et al. [2008, 2011] demonstrated experimentally and with theoretical simulations that the Interferometric Pattern oscillates as a function of the elevation angle, passing through a notch at vertical polarization. The elevation angle at which the notch appears and its amplitude varies with the Soil Moisture and the vegetation height. These two parameters were used to develop a retrieval algorithm to estimate both vegetation height and soil moisture. Two field experiments were carried out in this study in Lleida and Zamora, Spain. Two GPS receivers were connected to a passive antenna at Vertical and Horizontal polarizations,

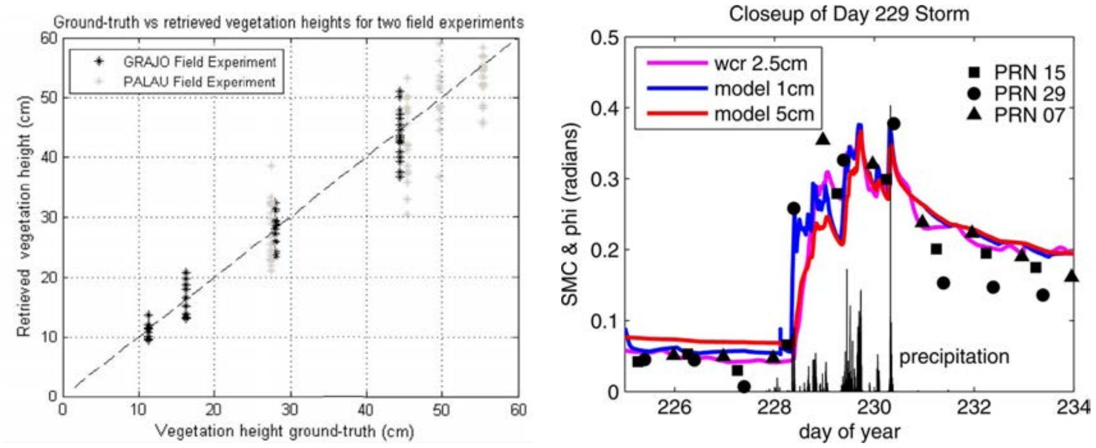

(a) (b)

Figure 3.8: (a) Vegetation height retrieved with GNSS-R data versus ground truth, [Rodriguez-Alvarez et al., 2011] (b) Comparison of phase variation measurements with ground-truth soil moisture and precipitation, [Larson et al., 2010]

mounted on a mast at 2 meters from the ground, with the boresight pointing towards the horizon. The observation angle to obtain the notch measurements was automatically swept thanks to the the change in elevation angle during the GPS satellite passage. The results showed satisfactory estimation of both plant height and soil moisture. For the two plants studied, barley and wheat, height errors were below 5 cm with a correlation coefficient with respect to ground-truth of 0.9, as can be observed in Figure 3.8(a); for soil moisture errors were estimated to be below 5% for both experiments.

The interferometric pattern technique was also used in [Larson et al., 2010; Zavorotny et al., 2010] for the determination of soil moisture with the SNR measurements of permanent geodetic GPS stations. In this case, the reflected signal goes through the back-lobe of the up-looking RHCP antenna, however the multipath signal is still strong enough to create the interference pattern. The antenna radiation pattern at both polarizations for elevation angles between +30° and −30° were considered in the so called multipath modulation pattern. In this study it was considered that scattered energy from the incoming GPS signal comes from an effective reflecting layer. The amplitude and phase of the interference patterns together with the effective height of the multipath reflector were calculated. It was demonstrated that the effective reflector depth varies from a depth of 1 to 6 cm, for wet and dry soils, respectively. Both phase and effective height were used to relate the measurements with the soil moisture measured by probes, yielding correlation coefficients from 0.76 to 0.9 and from 0.68 to 0.86 for both measurement parameters, respectively. The highest dispersion in the measurements was observed for dry soils. However, this was linked to the fact that for small rain events the wetting fronts do not propagate to the full sensing depth whereas the GPS measurements have a fast response to changes in the first cm of soil. This can be seen in the interference pattern phase and measured soil moisture response for a precipitation event, shown in Fig. 3.8.

GPS reflected signals over land were also observed from spaceborne platforms, as presented in [Gleason, 2005, 2006a]. In this works, spaceborne data collected over land by the modified GPS receiver on-board the UK-DMC satellite were examined for four different sites on three dates was examined. The data were incoherently averaged over

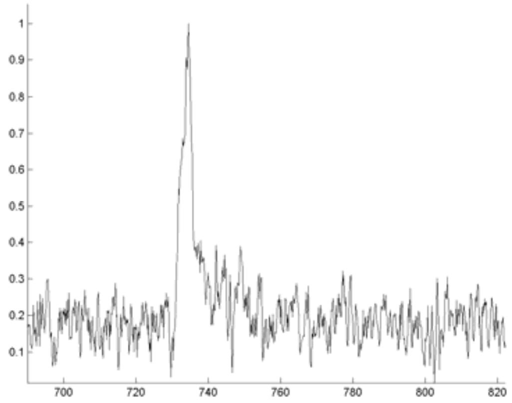

Figure 3.9: Waveform detected over land during the UK-DMC experiment [Gleason, 2005]. The horizontal axis is the C/A-code correlation chips and the vertical axis is the correlation magnitude.

100 looks of 1 ms each. Figure 3.9 shows a waveform detected during this experiment over a mixed area of bluff, hills, and farmland in North America. Clear signals were detected and significant variations were observed from different terrains, responding to visible surface features, such as the crossing of a river. This demonstrated the feasibility of GNSS-R for land applications from spaceborne platforms. Delay Doppler Maps were also examined. They are sensibly narrower both in delay and frequency with respect to those collected over ocean, the largest spreading being shown by a DDM collected over a mountainous region. The author suggested that this dispersion was due to the effect of topography, however it was concluded that more efforts in modeling land reflections must be devoted to understand the relative importance of coherent and incoherent scattering over land surfaces from orbital heights.

3.7 Summary and Conclusions

This chapter has presented the state of the art and fundamental aspects of GNSS-R. As has been explained, GNSS-R is a remote sensing technique based on the use of GNSS signals as sources of opportunity. The high availability and stability of these signals makes them excellent candidates for this purpose. In GNSS-R a single receiver picks up the signals from several satellites at the same time. Given its passive nature, a relatively low-cost receiver can have an wide field of view with low cost and low power consumption.

The technique was initially proposed in 1993, as a way to measure ocean topography by accounting for the delay of the direct and reflected signals. Given its interesting characteristics, a wide number of other scientific applications arose, including sea state, sea surface winds monitoring, and ionospheric monitoring. The interest in this technique soon moved from ocean to land applications, as several studies demonstrated the capabilities of GNSS-R to sense small changes in the reflectivity of soil, and therefore opening the door for soil moisture estimation.

Several methods have been proposed to estimate soil moisture with GNSS-R. Among them, one can mention the measurement of the reflected signal SNR, and the characterization of the interferometric patterns when the direct and reflected signals add up coherently at a single antenna. The latter has shown remarkable results for the estimation of soil moisture over bare and vegetated areas, for which a method was implemented in order to simultaneously estimate the vegetation development stage. Another technique based on the comparison of the polarizations of the reflected signals was initially proposed in [Zavorotny et al., 2003], as a way to decouple the measurements from soil roughness effects. Despite of the high initial expectations of the technique, the experimental data did not show a reasonable correlation with soil moisture.

The approach adopted in this research work follows the rationale initially presented in [Zavorotny et al., 2003]. Ample efforts were performed during this PhD Thesis to understand the scattering process and measurement technique from a physical and engineering point of view in order to maximize the information to be extracted out of the GNSS-R polarimetric observables.

Part II

Models

Chapter 4

Terrain Scattering Models

Models of electromagnetic wave interaction with surfaces and inhomogeneous media describe in a general way the scattering properties of natural terrains. However, the wide variability of soil and vegetation conditions makes it extremely complicated to provide a precise description of the scattering mechanisms involved in each case. Models are, in any case, highly valuable to improve our understanding of the physical processes governing the electromagnetic waves scattering mechanisms and in the development of reliable inversion algorithms for bio-geophysical parameters retrieval. For a bistatic radar system observing a soil surface the final scattered power is a function of the soil dielectric properties, the surface roughness and the vegetation canopy. This chapter discusses the combined effect of these elements in the final scattered signal.

4.1 Soil Surface Characterization

Natural terrains can be considered as a mixture of soil particles, air voids, and liquid water, which to a large extent determine the soil properties. Soil permittivity and surface roughness are the two dominant factors in the scattering from soil surfaces. The former is determined by the combination of the soil's constituents, and the latter is given by the small scale geometrical structure of the ground. These two parameters are discussed more in depth in the following sections.

4.1.1 Soil Dielectric Models

Electromagnetically, a wet soil is, in general, a dielectric mixture of air, bulk soil, bound water, and free water. The complex dielectric constants of bound and free water are functions of the electromagnetic frequency, the physical temperature, and the salinity. The dielectric constant of soil is a function of these three parameters, the soil physical structure (including bulk soil density and shape of soil particles), the soil texture, and the total volumetric water content. A semi-empirical model based on a dielectric mixing approach and validated by an extensive set of experimental data was proposed in [Hallikainen et al., 1985; Dobson et al., 1985]. This model computes the complex permittivity of the soil as a function of volumetric soil moisture, for a given values of the bulk density and soil texture, represented by the relative percentages of silt, sand

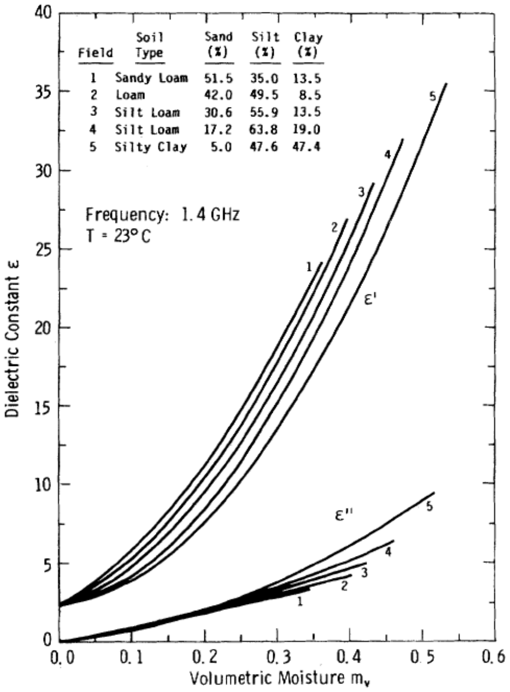

Field	Soil Type	Sand (%)	Silt (%)	Clay (%)
1	Sandy Loam	51.5	35.0	13.5
2	Loam	42.0	49.5	8.5
3	Silt Loam	30.6	55.9	13.5
4	Silt Loam	17.2	63.8	19.0
5	Silty Clay	5.0	47.6	47.4

Figure 4.1: Measured soil dielectric constant at 1.4 GHz for different soil types as a function of total volumetric soil moisture [Hallikainen et al., 1985].

and clay. This model has had a wide acceptance among the scientific community, and has been used in the SMOS Level 2 Soil Moisture Processor. In Fig. 4.1 the complex dielectric constant of soil at 1.4 GHz is shown for a wide range of soil types and soil moisture values.

Soil moisture remote sensing with GNSS-R relies on the variability of the ground dielectric properties associated to the soil humidity level. As can be observed from the figure, higher concentrations of water in the soil yield higher dielectric constants, which in turn results in higher reflectivity. This leads to the possibility of relating reflected signal's peak power to soil moisture. For a perfectly flat surface, the soil's reflectivity is driven by the Fresnel reflection coefficients, that depend on the polarization of the incident wave. In a local incidence plane, considering that the reflective surface is non-magnetic, i.e. $\mu_r = 1$, the co-polar Fresnel reflection coefficients for horizontal and vertical polarization can be expressed as:

$$\begin{aligned} \mathcal{R}_{hh} &= \frac{\cos\theta - \sqrt{\varepsilon_r - \sin^2\theta}}{\cos\theta + \sqrt{\varepsilon_r - \sin^2\theta}}, \\ \mathcal{R}_{vv} &= \frac{\varepsilon_r \cos\theta - \sqrt{\varepsilon_r - \sin^2\theta}}{\varepsilon_r \cos\theta + \sqrt{\varepsilon_r - \sin^2\theta}}, \end{aligned} \tag{4.1}$$

where θ represents the local incidence angle, ε_r is the complex dielectric constant, and the subindices pq represent the Fresnel reflection coefficient for a wave with an incident polarization p and scattered polarization q. For a perfectly flat reflecting surface, the

Soil Moisture Estate	Soil Moisture Content	Dielectric Permittivity
Dry	5%	$\varepsilon_r = 3.23 - 0.33i$
Moist	20%	$\varepsilon_r = 9.5 - 1.8i$
Wet	35%	$\varepsilon_r = 20.8 - 3.75i$

Table 4.1: Dielectric constant values for three different soil moisture contents. From [Ulaby et al., 1986b, chap. 19].

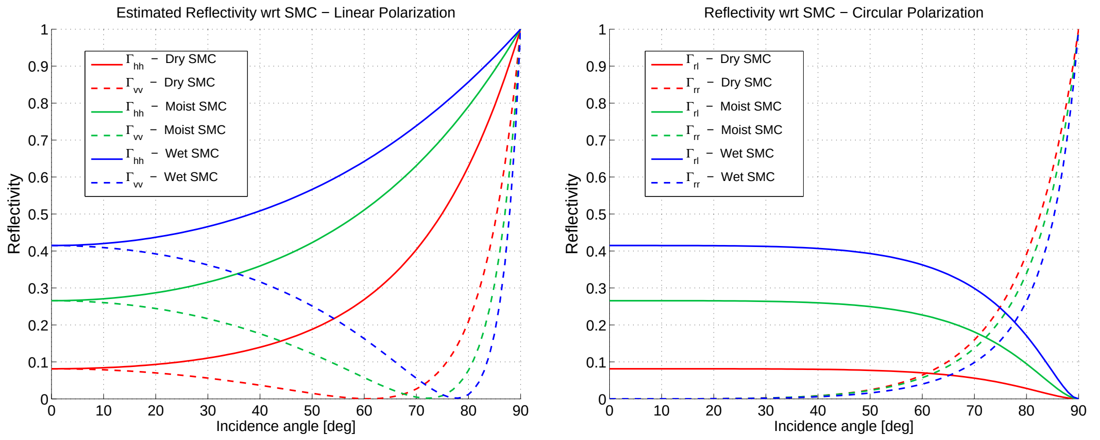

(a) (b)

Figure 4.2: Simulated soil reflectivity for three different soil moisture conditions; dry, moist, and wet, as specified in Table 4.1. (a) Linear polarization Γ_h (solid lines) and Γ_v (dashed lines) reflectivity. (b) Circular polarization Γ_{rl} (solid lines) and Γ_{rr} (dashed lines) reflectivity.

cross-polarization reflection terms, $\mathcal{R}_{hv}$ and $\mathcal{R}_{vh}$, can be neglected as those arise from out of plane scattering. The reflectivity, defined as the absolute squared value of the Fresnel reflection coefficients, is shown for the h and v polarizations in Fig. 4.2(a) for three different ε_r values corresponding to three different soil moisture conditions on a standard silty loam soil (soil type 3 in Fig. 4.1), from [Ulaby et al., 1986b, chap. 19]. These values are gathered in Table 4.1.

In the case of GNSS, the transmitted signals are RHCP, which can be interpreted as a linear combination of the horizontal and vertical polarization components. This can be expressed in matrix form by means of the transition matrices between the linear (hv) and the circular (rl) polarization bases:

$$\mathcal{T}_{hv\to rl} = \frac{1}{\sqrt{2}}\begin{bmatrix} 1 & -i \\ 1 & i \end{bmatrix} \quad , \quad \mathcal{T}_{rl\to hv} = \frac{1}{\sqrt{2}}\begin{bmatrix} 1 & 1 \\ i & -i \end{bmatrix}, \tag{4.2}$$

The reflection coefficients in circular polarization can then be obtained as:

$$\begin{bmatrix} \mathcal{R}_{ll} & \mathcal{R}_{lr} \\ \mathcal{R}_{rl} & \mathcal{R}_{rr} \end{bmatrix} = \mathcal{T}_{hv\to rl}\begin{bmatrix} \mathcal{R}_{hh} & \mathcal{R}_{hv} \\ \mathcal{R}_{vh} & \mathcal{R}_{vv} \end{bmatrix}\mathcal{T}_{rl\to hv} = \frac{1}{2}\begin{bmatrix} \mathcal{R}_h + \mathcal{R}_v & \mathcal{R}_h - \mathcal{R}_v \\ \mathcal{R}_h - \mathcal{R}_v & \mathcal{R}_h + \mathcal{R}_v \end{bmatrix}, \tag{4.3}$$

Figure 4.2(b) depicts the soil's reflectivity for right-right and right-left polarizations vs. incidence angle, for three soil moisture conditions. The values of ε_r were taken from

[Ulaby et al., 1986b, chap. 19]. It can be observed that Γ_{rl} presents a good sensitivity to soil moisture variations at almost all incidence angles. Conversely, Γ_{rr} is very small for incidence angles up to 60 deg, thus the reflected power in RHCP would be negligible, and the sensitivity to soil moisture is also very low. However, it was determined from simulations that near grazing incidence angles Γ_{rr} increases significantly, and surpasses Γ_{rl}, especially in situations of low soil moisture content, where the depolarization is higher due to lower dielectric constant. It is therefore concluded that there would be a non-negligible RHCP signal component in the reflected signal, increasing towards grazing incidence angles.

Despite the fact that the Fresnel reflection coefficients provide a description of the reflectivity characteristics of the ground based on ε_r, there are other geophysical parameters that could possibly influence the scattering process. Therefore, as stated above, knowing the dielectric properties of soil does not suffice to completely characterize the scattering mechanisms from natural terrains. For instance, the small scale structure of the reflecting surface has an important impact in the scattering process that can be described by means of its statistical properties.

4.1.2 Soil Surface Roughness Models

A rough surface can be described by a vertical displacement with respect to a mean flat plane located at $z = 0$, $\zeta(\vec{\rho})$. Thus, the position of a certain point on the surface can be expressed as $\vec{R}_s = \vec{\rho} + \zeta(\vec{\rho})\hat{z}$. The direct evaluation of the surface roughness can be performed by contact devices, such as needle profilometers, or laser profilers. However, the exact characterization of natural terrain is an arduous task. Usually, the study of scattering in remote sensing is performed by means of random rough surface models, where the elevation of the surface with respect to some mean plane is assumed to be a stationary stochastic process with a Gaussian height distribution. The surface standard deviation, σ_ζ^2, also referred to as surface roughness, is the root mean square of the actual surface deviation from this average surface. However, knowing the surface standard deviation does not provide a complete description of the surface geometrical properties. It is also important to know how the local surface deviation relates to the deviation from the mean at other points on the surface.

An isotropically rough surface can be described by a one-dimensional random function $\zeta(x)$ with zero mean, i.e. $\langle\, \zeta(x) \,\rangle = 0$. For a stationary random process the autocorrelation of the surface heights yields

$$\langle\, \zeta(x)\zeta(x - \Delta x) \,\rangle = \sigma_\zeta^2\, C(\Delta x)\,, \tag{4.4}$$

where C is the autocorrelation function of the surface heights as a function of the displacement Δx. The most common ACF used in remote sensing of land surfaces are the Gaussian ACF:

$$C(\Delta x) = \exp(\frac{\Delta x^2}{l^2})\,, \tag{4.5}$$

and the exponential ACF:

$$C(\Delta x) = \exp(-\frac{|\Delta x|}{l})\,, \tag{4.6}$$

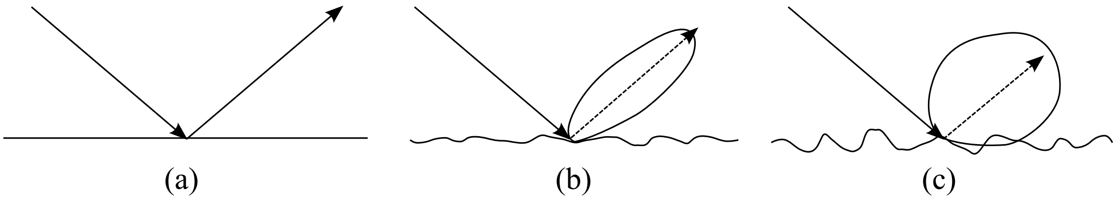

Figure 4.3: Specular and diffuse scattering components for three different soil roughness conditions; (a) completely smooth surface, (b) slightly rough surface, (c) rough surface. As the surface gets rougher, the energy is reradiated in other directions different from the specular.

where l stands for the surface correlation length, i.e. the separation Δx after which the deviation from the mean surface for two points are statistically independent. Mathematically, this corresponds to the length after which the autocorrelation function of the surface decays below $1/e$. More complex characterizations, based on fractal descriptions of the surface, have also been proposed. However, for L-band signals, the height standard deviation and correlation length suffice to describe the surface roughness as it is generally expected to be much smaller than the wavelength.

4.2 Rough Surface Scattering

The scattering of electromagnetic waves from a surface is strongly influenced by the surface geometrical properties. For a perfectly smooth surface illuminated by a plane wave, the energy is reradiated into the specular direction with scattering amplitude equal to the Fresnel reflection coefficients [Balanis, 1989]. In this case, no scattered energy will be received in any other direction, Fig. 4.3(a).

As the surface gets rougher, a diffuse scattering component appears. Different criteria exist to decide whether a surface can be considered "smooth" or "rough". The most commonly used one is the Rayleigh criterion that classifies a terrain as rough if the surface roughness satisfies $\sigma_z > \lambda/8\cos\theta$, where λ is the wavelength, and θ is the incidence angle [Ulaby et al., 1986b]. A more stringent one introduced by Fraunhoffer suggests that a surface can only be considered as smooth if the surface height standard deviation satisfies $\sigma_z > \lambda/32\cos\theta$.

For a slightly rough surface, i.e., still satisfying the Rayleigh criterion, the specular scattering component is still the predominant one, however, some of the incident power is reradiated now in other directions, Fig. 4.3(b). The amount of energy scattered in directions other than the specular one depends on the magnitude of the surface roughness with respect to the wavelength. In the extreme case in which the surface is very rough, the energy of the incident wave is isotropically scattered in all directions, Fig. 4.3(c). In the next subsections the formation process of the total scattered field from a rough surface is reviewed together with a deeper insight on the weight of the specular and diffuse scattering components depending on the surface roughness.

4.2.1 Distribution of scattered fields

The total field scattered by a rough surface can be considered as the combination of elementary waves coming from multiple individual scatterers on the surface. These elementary waves can be described as random phasors of the form $A_i e^{j\phi_i}$, where both the amplitudes of the individual waves, A_i, and their phases, ϕ_i, are random variables [Beckmann and Spizzichino, 1963]. The current section is devoted to provide an understandable insight of the process in which these random scattered waves combine together in order to generate the final scattered field. In order to discuss the distribution of the scattered fields over rough surfaces, let us consider the sum

$$U = re^{j\psi} = \sum_{i=1}^{n} A_i e^{j\phi_i} \,. \tag{4.7}$$

The above equation is in essence a random phasors combination in the complex plane. For rough surfaces, or off-specular scattering directions, A_i can be considered to have similar values, and ϕ_i to be uniformly distributed in the interval $[-\pi, \pi]$. In that case, it can be demonstrated that the probability density function of r follows a Rayleigh distribution [Beckmann and Spizzichino, 1963], and ψ is also uniformly distributed. An interesting result is that if the sum is decomposed in its real and imaginary parts, it can be shown by the Central Limit Theorem that $x = \Re(U)$, and $y = \Im(U)$ follow a Gaussian distribution, which is a quite general result provided that ϕ_i are equally distributed, and have finite mean and variance.

In the case of scattering over a slightly rough surface in the specular direction, certain phase bands are amplified, and therefore the uniform distribution of the phase does not longer apply. Indeed, the single scatterers' phase distribution can be directly linked to the surface height distribution; for a Gaussian surface with a height standard deviation σ_z, the associated phase is also normally distributed with a standard deviation that can be calculated as:

$$\sigma_{\phi_i} = 2\, k\, \sigma_z \cos\theta \,, \tag{4.8}$$

where k represents the wavenumber, and θ the incidence angle. The additional 2 factor accounts for the two way travel distance of the wave in the reflection process. In this situation the random complex vectors add up together privileging a certain direction in the complex plane, i.e. the mean of the phase, thus creating a distribution of the total scattered field which is no longer centered about zero. The final distribution of the scattered field U can be represented, in a general case, by a constant vector plus a Hoyt vector, which is defined by as a 2-Dimensional Gaussian distribution with mean value zero and unequal variances s_1 and s_2.

In [Beckmann and Spizzichino, 1963] the authors assert that outside a narrow cone about the direction of specular reflection, the amplitude of the field scattered by a rough surface is always Rayleigh distributed; if the surface is very rough, and grazing incidence is excluded, the amplitude of the scattered field is Rayleigh-distributed everywhere. In addition, if the amplitude of the field scattered by a rough surface is not Rayleigh-distributed, it is never distributed with the Rice distribution (constant vector plus Rayleigh vector), but with the distribution resulting from a constant vector plus a Hoyt vector.

Several simulations were performed in order to verify these statements and to obtain a good understanding of the combination process of random phasors that results in the formation of the final scattered field. The simulations were performed through a Monte-Carlo approach in order to reduce the uncertainty in the averaging process. The scene was considered to be composed of an arbitrary number of 100 independent scatterers and the field was considered to have 10000 samples. In order to provide coherency to the field, each sample was replicated 51 times, and filtered with a low pass filter of order 51. The reader should note here that these tests do not aim to simulate scattered fields over rough surfaces, but just the summation process of random phasors.

The first performed simulation considered the single scatterers with an uniformly distributed phase ϕ_i and normally distributed amplitudes A_i, with standard deviation equal to the mean value ($\mu_{A_i} = \sigma_{A_i} = 1$). This can be mathematically represented as $A_i = 1.0 + 1.0\mathcal{N}$, where $\mathcal{N}$ is a normal distribution with zero mean and unit standard deviation. The individual phasors were averaged to generate the final field U. The representation in the complex plane of the obtained field, and the amplitude histograms are shown in Fig. 4.4. The resultant field U is a Rayleigh vector, as predicted by Beckmann and Spizzichino [1963]. As can be seen in Fig. 4.4(a), the field is concentrated about the complex plane origin, and the histograms of the field's amplitude, Fig. 4.4(b), fits a Rayleigh distribution (red curve on the plot).

The statistical parameters defining a Rayleigh distribution have also been verified with the simulated data. For instance, the ratio between the standard deviation and the mean of the U field amplitude was calculated and yields 0.529, very close to the theoretical Rayleigh distribution value: 0.523 [Ulaby and Dobson, 1989]. In addition, the asymmetry ratio K, defined in [Beckmann and Spizzichino, 1963] as the variance ratio of the real and imaginary field components, s_1 and s_2, respectively, is very close to one, as expected for a Rayleigh vector.

For the second test the same amplitude distribution as in the previous one was selected, but with a Gaussian distribution of the single scatterers' phase, with mean $\mu_{\phi_i} = 0$ and standard deviation $\sigma_{\phi_i} = 45°$. This implies an enhancement of certain phase bands, which as commented before, forces the total field to take a certain direction on the complex plane. In this case, since the distribution was selected to be centered about zero, the privileged direction follows the real axis.

In Fig. 4.5 the results for this simulation are shown. As observed in the figure, the total field U is displaced from the centre, by a certain value α. When this value is subtracted from the distribution, the field is again concentrated in the complex plane origin. In both cases the fields have an ellipsoidal distribution on the complex plane, i.e the real and imaginary components standard deviation are not equal, in agreement with what was predicted in [Beckmann and Spizzichino, 1963]. Figure 4.5(b) shows that the amplitude distribution of the field does not match a Rayleigh distribution, however after subtracting the mean, the distribution is again centered about the origin of the complex plane, thus the histogram resembles the theoretical Rayleigh curve. The Rayleigh ratio is in this case equal to 0.53 in amplitude and 1.046 in power, close to the theoretical values; 0.523 and 1, respectively.

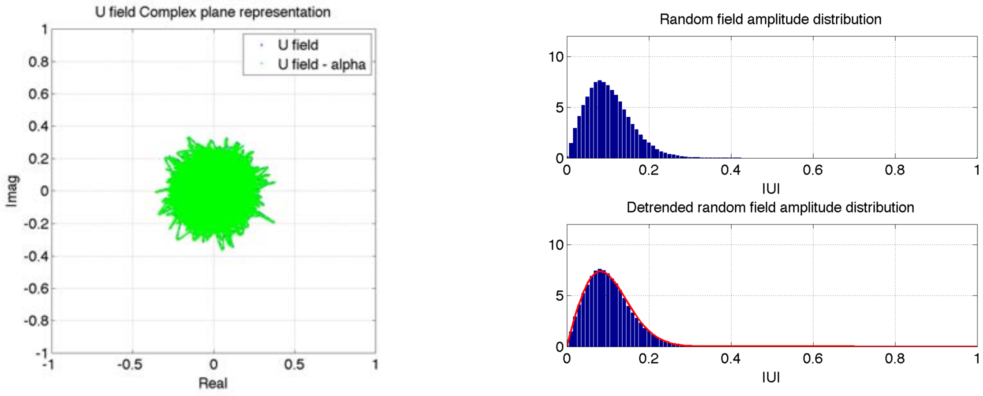

(a) (b)

Figure 4.4: Random field generation for a uniformly distributed phase ϕ_i and $A_i = 1.0 + 1.0\mathcal{N}$; (a) Representation of the U field in the complex plane; (b) amplitude distribution histograms; (b) up: U field amplitude distribution; (b) down: U field minus mean amplitude distribution. In red Rayleigh fit to the distribution.

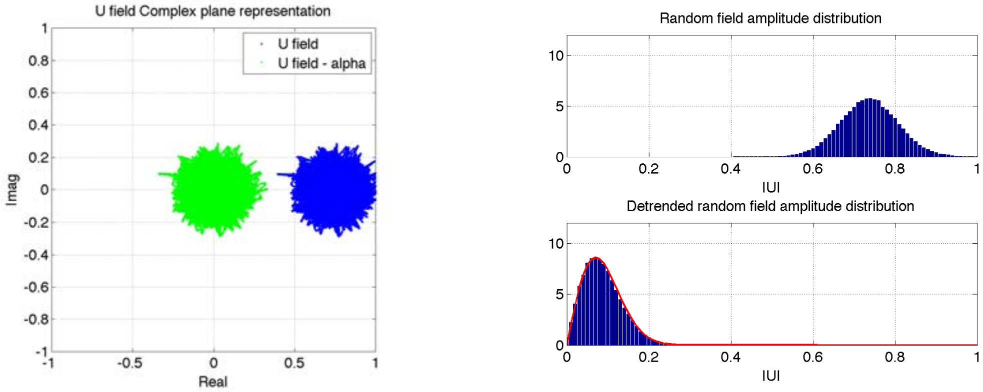

(a) (b)

Figure 4.5: Random field generation for a Gaussianly distributed phase with $\sigma_i = 45°$ and $A_i = 1.0 + 1.0\mathcal{N}$; (a) Representation of the U field in the complex plane; (b) amplitude distribution histograms; (b) up: U field amplitude distribution; (b) down: U field minus mean amplitude distribution. In red Rayleigh fit to the distribution.

Amplitude	$\sigma_\phi = 15$	$\sigma_\phi = 30$	$\sigma_\phi = 45$	$\sigma_\phi = 60$	$\sigma_\phi = 90$	$\sigma_\phi = 180$
1.0 + 0.1$\mathcal{N}$	$\alpha = 0.966$	$\alpha = 0.872$	$\alpha = 0.735$	$\alpha = 0.578$	$\alpha = 0.292$	$\alpha = 0.006$
	$R = 0.011$	$R = 0.021$	$R = 0.045$	$R = 0.081$	$R = 0.213$	$R = 0.520$
	$K = 0.423$	$K = 0.414$	$K = 0.561$	$K = 0.711$	$K = 0.919$	$K = 1.001$
	$s_1 = 0.011$	$s_1 = 0.019$	$s_1 = 0.033$	$s_1 = 0.047$	$s_1 = 0.065$	$s_1 = 0.071$
	$s_2 = 0.025$	$s_2 = 0.045$	$s_2 = 0.059$	$s_2 = 0.067$	$s_2 = 0.071$	$s_2 = 0.071$
1.0 + 0.5$\mathcal{N}$	$\alpha = 0.966$	$\alpha = 0.872$	$\alpha = 0.735$	$\alpha = 0.578$	$\alpha = 0.290$	$\alpha = 0.007$
	$R = 0.050$	$R = 0.054$	$R = 0.070$	$R = 0.102$	$R = 0.239$	$R = 0.522$
	$K = 1.719$	$K = 0.925$	$K = 0.777$	$K = 0.806$	$K = 0.936$	$K = 0.999$
	$s_1 = 0.049$	$s_1 = 0.047$	$s_1 = 0.052$	$s_1 = 0.060$	$s_1 = 0.073$	$s_1 = 0.079$
	$s_2 = 0.028$	$s_2 = 0.051$	$s_2 = 0.067$	$s_2 = 0.073$	$s_2 = 0.079$	$s_2 = 0.079$
1.0 + 1.0$\mathcal{N}$	$\alpha = 0.966$	$\alpha = 0.871$	$\alpha = 0.735$	$\alpha = 0.579$	$\alpha = 0.291$	$\alpha = 0.007$
	$R = 0.100$	$R = 0.103$	$R = 0.117$	$R = 0.150$	$R = 0.301$	$R = 0.523$
	$K = 2.705$	$K = 1.391$	$K = 1.028$	$K = 0.935$	$K = 0.965$	$K = 1.000$
	$s_1 = 0.096$	$s_1 = 0.091$	$s_1 = 0.086$	$s_1 = 0.088$	$s_1 = 0.096$	$s_1 = 0.100$
	$s_2 = 0.036$	$s_2 = 0.065$	$s_2 = 0.084$	$s_2 = 0.094$	$s_2 = 0.099$	$s_2 = 0.100$

Table 4.2: Random field generation simulation results for different amplitude and phase distributions.

4.2.2 Effect of Amplitude and Phase Distribution of Single Scatterers

In order to determine the effect of the individual scatterers' amplitude and phase distributions on the final scattered fields, several simulations were performed assuming Gaussian statistics for both amplitude and phase with different σ_{A_i} and σ_{ϕ_i} values, as specified in Table 4.2.

A general trend observed in these results is a decay on the mean value of the total scattered field, α, with respect to σ_{ϕ_i}. This result is in line with the theoretical expectations of the surface roughness effects on the scattering process. Indeed, as shown by Beckmann and Spizzichino [1963], for slightly rough Gaussian surfaces the reflectivity is expected to be reduced by an exponential factor, L_{σ_z}, of the form:

$$L_{\sigma_z} = e^{-4k^2\sigma_z^2\cos^2\theta}\,. \tag{4.9}$$

The simulation results for the different σ_{ϕ_i} were compared with the theoretical model presented above. The selected σ_{ϕ_i} values shown in Table 4.2 were converted to their corresponding surface roughness standard deviation, σ_z, by using Eqn. (4.8). In Fig. 4.6 the obtained α values were represented with L_{σ_z} as a function of the surface height standard deviation is shown. As can be observed from the figure, there is a complete correspondence of the theoretical values and the simulations results. On the contrary, α is independent of the amplitude distribution, showing that the phase noise of the single scatterers, and in extension the surface roughness, is the main non-instrumental parameter influencing an eventual bias in the determination of the surface reflectivity.

The effect of σ_{ϕ_i} is also noticeable in the standard deviation of the real and imaginary components, s_1 and s_2. Since the phase distributions were selected to be centered about 0, variations in the imaginary part are more important since they change with a $\sin(x)$ function, whereas in the real part the change is with a $\cos(x)$, for x values close to zero. For low values of σ_{ϕ_i}, the distribution asymmetry factor, K, defined as the ratio of s_1 over s_2 is bigger than 1 since most of the noise of the distribution is due to the amplitude noise of the scatterers. As the phase gets noisier K tends to 1, being in some

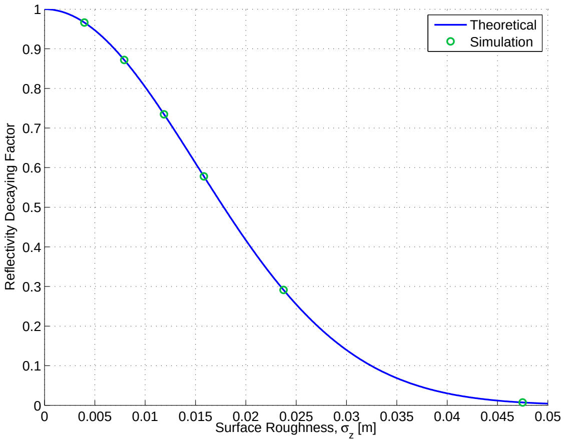

Figure 4.6: Reflectivity decaying factor as a function of surface roughness. The theoretical values of the reflectivity decaying factor (solid blue curve) are represented together with the mean field amplitude obtained from the simulations (green circles).

cases smaller than 1, which means that the effect of the phase noise is more important than the effect of the amplitude noise. As stated in [Beckmann and Spizzichino, 1963], if α is not equal to 0, K is only equal to 1 in some exceptional cases, showing that the total scattered field follows a Hoyt distribution.

In light of the previous results, it can be stated that the effect of an increasing phase dispersion of the individual scatterers is twofold; first, the distribution approaches the origin of coordinates, at the same time that the arch in which the field is distributed in the complex plane is widened. In the same way, the effect of an increasing amplitude noise is a growth in the dispersion of the real and imaginary distribution components. This impacts in how quickly the amplitude of the final scattered fields tends to a Rayleigh distribution. The parameter R, defined as the ratio of the scattered field amplitude mean and standard deviation, $R = \langle |r| \rangle / \sigma_{|r|}$, tends to the theoretical value of a Rayleigh distribution, i.e. 0.523, towards higher values of σ_{ϕ_i}; however, as can be seen in Table 4.2, for an amplitude distribution of $A_i = 1.0 + 1.0\mathcal{N}$ this value is attained faster than in the two other cases. The distribution of the scattered field in the complex domain determines also the coherent and incoherent scattering components of the signal, which is discussed in the next section.

4.2.3 Coherent and incoherent components in the scattered fields

Terms such as coherent and incoherent scattering have been avoided in the previous section since they could be misleading and need a more extensive definition. As stated by Beckmann, the difference among both types of scattering lies in the way the power of the waves coming from individual scatterers combine to generate the final scattered field. Taking as reference Eqn. (4.7), the power of the total scattered field can be calculated as:

$$W = |u|^2 = \left| \sum_{i=1}^{n} A_i e^{j\phi_i} \right|^2 . \tag{4.10}$$

Considering that A_i are constant and equal to 1, it is straightforward to see, that if all scatterer's phases, ϕ_i, have the same value, the power of the resultant scattered field yields n^2, being n the number of scatterers contributing to the total field. However, it can be shown that if ϕ_i is an uniformly distributed random variable over a 2π interval, the total power of the field equals n. It is demonstrated that the phase of the total field is also uniformly distributed over the same interval, and as mentioned in the previous section, by the Central Limit Theorem the distribution of the real and imaginary parts of the field follow a Gaussian distribution.

In that sense, coherence and incoherence can be defined as follows: if the phase of a wave is uniformly distributed over an interval of length 2π it will be called incoherent; whereas if the phase of the wave is constant, it will be called coherent. Between these two limit cases there is a gradual and continuos transition between a coherent and an incoherent scattered wave.

It is also shown in [Beckmann and Spizzichino, 1963] that in directions different from the specular one, the scattering is always incoherent. The scattering will also be incoherent in the specular direction if the surface is very rough. However, if the surface is smooth, the phases of the individual scatterers would be the same, and therefore the scattering would be coherent. Between these two situations there is a continuous transition from coherence to incoherence. The relative weight of the coherent and incoherent components in the total scattered field. Considering a Gaussian surface, i.e. the individual scatterers have normally distributed phases, the field's mean power can be written as:

$$\left\langle r^2 \right\rangle = \alpha^2 + s_1 + s_2 \,, \tag{4.11}$$

where r denotes the amplitude of the field, s_1 and s_2 are, as in the previous section, the variance of the distribution's real and imaginary components, and $\alpha = \langle u \rangle$ is the expectation of the scattered field, representing the displacement of the distribution with respect to the origin. This relationship can be verified with the simulation results shown above.

In the previous equation two different contributions to the total mean power can be identified; a constant component α, and a random part specified by the variances s_1 and s_2, which represent the coherent and incoherent scattering components, respectively. The relative weight of coherent and incoherent scattering components is given, as in [Beckmann and Spizzichino, 1963], by the parameter B, defined as

$$B^2 = \frac{\alpha^2}{s_1 + s_2} \,. \tag{4.12}$$

This parameter goes from ∞, for coherent scattering, down to 0, in a completely incoherent scattering situation. The effect of roughness in the relative weight of both scattering components can be seen from the simulations presented in the previous section. The results are gathered in Table 4.3. It should be noted that, as the phase standard deviation increases the B parameter tends rapidly towards smaller values due to an increase in the relative weight of the incoherent scattering component with respect to the coherent one. This demonstrates that as the surface becomes rougher, the scattering becomes more incoherent, being in the limit completely Rayleigh distributed, i.e. $B = 0$.

Summarizing the above, it can be said that the total field scattered from a random rough surface in the specular direction is composed of a constant coherent component,

Amplitude	$\sigma_\phi = 15$	$\sigma_\phi = 30$	$\sigma_\phi = 45$	$\sigma_\phi = 60$	$\sigma_\phi = 90$	$\sigma_\phi = 180$
$\mathbf{1.0 + 0.1}\mathcal{N}$	$B^2 = 1227.4$	$B^2 = 305.06$	$B^2 = 114.85$	$B^2 = 49.32$	$B^2 = 9.16$	$B^2 = 0.01$
$\mathbf{1.0 + 0.5}\mathcal{N}$	$B^2 = 295.14$	$B^2 = 155.06$	$B^2 = 76.00$	$B^2 = 36.48$	$B^2 = 7.28$	$B^2 = 0.00$
$\mathbf{1.0 + 1.0}\mathcal{N}$	$B^2 = 87.51$	$B^2 = 61.32$	$B^2 = 36.93$	$B^2 = 20.03$	$B^2 = 4.43$	$B^2 = 0.00$

Table 4.3: Relative weight of the coherent and the incoherent scattering components of a field formed by individual waves with different Gaussian amplitude and phase distributions.

and a random, Hoyt-distributed incoherent component. The former comes from the reflection of the incident wave in the vicinity of the specular point, while the latter is the combination of waves coming from scatterers off the specular, that add up together in the receiver antenna phase centre. For rougher surfaces, the constant component is diminished while the dispersion of the Hoyt-distribution increases, becoming the incoherent component the predominant one, being in the limit, i.e. for very rough surfaces, completely incoherent. This is also the case for scattering in the non-specular direction, in which the field amplitude follows a Rayleigh distribution.

It is worth noting here that the B values obtained in this analysis do not accurately represent the actual situation of the relationship between the coherent and incoherent scattering components of GNSS scattered signals off soil surfaces. This is due to the fact that the incoherent scattering component is not precisely calculated, as some diffuse scattering effects are not accounted for with these simulations. For that appropriate scattering models need to be used. A brief description of these models and their mathematical formulation are provided in the following section.

4.3 Scattering from Soil Surfaces

The current section provides a description of the currently accepted scattering models that are capable of reproducing, within certain conditions, the scattering of electromagnetic waves from bare and vegetated soils. Some simulations are also provided in order to analyze the impact of soil bio-geophysical parameters in the coherent and incoherent components of the scattered signals.

4.3.1 Bare Soils Scattering Models

As discussed in the previous section an incident wave upon a rough surface boundary is partly reflected in the specular direction and partly scattered in all directions. The former is often referred to as the coherent component, whereas the latter is known as the diffuse or incoherent scattering component. The magnitude of the power carried by the coherent component is generally bigger than the incoherent scattering for smooth surfaces and decreases to negligible values as the surface becomes very rough with respect to the wavelength. In general, the total scattered power measured by a bistatic radar receiver P^r_{pq} can be expressed as in [de Roo and Ulaby, 1994]:

$$P^r_{pq} = P^c_{pq} + P^i_{pq}\,, \tag{4.13}$$

where subscripts p and q denote the incident and scattered polarization, and P^c_{pq} and P^i_{pq} are the power of the coherent and incoherent components, respectively.

4.3.1.1 The coherent scattering component

The magnitude of the power carried by the coherent component, P_{pq}^{c}, can be written as [de Roo and Ulaby, 1994]:

$$P_{pq}^{c} = \Gamma_{pq} \frac{P_t \lambda^2 G_t G_r}{(4\pi)^2 (R_{sp} + R_{0,sp})^2} \,, \tag{4.14}$$

where Γ_{pq} is the surface reflectivity, and R_{sp} and $R_{0,sp}$, the distances from the transmitter and receiver to the specular point, respectively. It is worth noting here that the coherent component depends on the transmitter and receiver antenna radiation patterns, as well as on the ranges to the specular point. Equation (4.14) assumes that those variables are constant in the vicinity of the specular point. However, in order to consider them for the calculation of the coherent component, the equation should be expressed by means of the bistatic radar equation, Eqn. (3.1), including a dependency on a bistatic scattering coefficient, which will be dependent on the characteristics of the transmitting and receiving antennas.

Two approaches are essentially reported in the literature for the computation of the coherent component produced by scattering from a rough surface. Both of them are valid for surfaces with small surface height standard deviations and small surface slopes. The first one considers the incident plane as a plane wave, whilst the other considers the sphericity of the incident wave front. The first one is valid for large (many correlation lengths) illuminated area, but for real cases the formulation of the coherent scattering coefficient proposed by Fung and Eom [1983] is preferred. The latter takes into consideration the spherical shape of the wave front impinging on the surface when produced by a real antenna. The consideration of a plane incident wave can be valid for computing the incoherent component, since the incidence wave can be considered plane within a roughness correlation length, but this is not true for the coherent component associated to an extended mean (plane) surface.

Using a scattering radar cross section to represent the coherent scattering component transfers the properties of the antenna to a parameter (the scattering coefficient) which should express a property of the surface only. However, it can be demonstrated that the coherent received power can be calculated substituting the coherent scattering coefficient, calculated according to the theory developed in [Fung and Eom, 1983], into the radar equation Eqn. (3.1).

4.3.1.2 The incoherent scattering component

The incoherent component of the total scattered power assuming a bistatic scattering coefficient σ_{pq}^{0} is given by the bistatic radar equation, rewritten here for convenience:

$$P_{pq}^{i} = \frac{P_t \lambda^2}{(4\pi)^3} \int \frac{G_t G_r}{R^2 R_0^2} \sigma_{pq}^{0} dA \,. \tag{4.15}$$

This equation can be directly linked to Eqn. (3.15). Computing the incoherent contribution requires analytical models of the bistatic radar coefficient, which are obtained

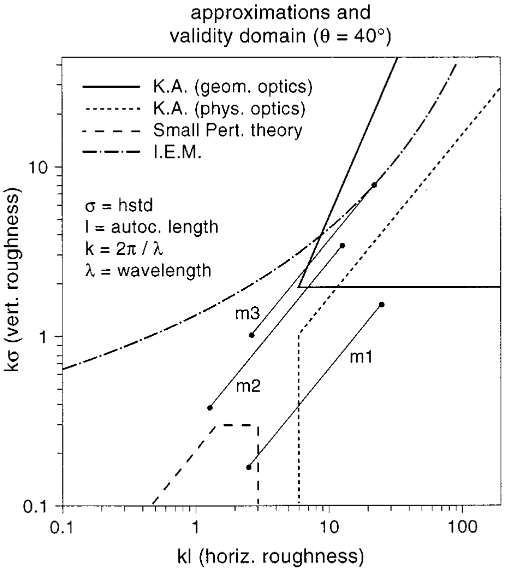

Figure 4.7: Validity domains of various scattering model approximations [Macelloni et al., 2000].

by adopting different approximations on the equations describing the interaction of the incident electromagnetic field with a random surface. The most common approaches in the literature in order to obtain the scattering coefficients of dielectric rough surfaces are the Kirchoff Approximation (KA), under the Physical Optics (PO) and Geometric Optics (GO) solutions, the Small Perturbation Method (SPM) and the Integral Equation Model (IEM). These models can be classified in three families, which follow approximatively the historical evolution: the low-frequency models (SPM and variants), the high-frequency approximation (Kirchhoff and variants) and the so-called unified methods, which aim at bridging the gap between the former two.

All these models have restricted validity limits due to the different approximations adopted in order to obtain analytical solutions of the scattering coefficients, usually determined by the soil surface characteristics with respect to wavelength, i.e. the roughness standard height σ_z and the correlation length l_z. The applicability limits of these scattering models has been frequently discussed in the literature, however an exact criterion has not yet been adopted. In [Macelloni et al., 2000] both model simulations and experimental measurements were performed in order to validate the scattering models mentioned above, assuming the limits represented in Fig. 4.7.

Kirchhoff Method - Stationary Phase Approximation (Geometrical Optics) The Kirchhoff Method is based on the assumption that the wavelength of the incident wave is much shorter than the horizontal variations of the surface, and the so called radius of curvature is sufficiently large so that the surface can be locally seen as a smooth reflecting infinite plane tangent to the surface. In its stationary phase approximation, it is assumed that all the scattering occurs along directions for which there are specular points on the surface. In this situation, the expression of the scattering coefficient is proportional to the surface slopes probability density function. The KA-GO scattering model is widely used to represent GNSS-R signal scattering from sea surfaces.

Kirchhoff Method - Scalar Approximation (Physical Optics) Using the stationary phase approximation only the non-coherent scattering is considered. However, for a surface with small slopes scattering occurs also in the specular direction in a coherent way, thus the scalar approximation needs to be used. The power in the incoherent reflected field may be given by a Taylor series in surface slope distributions. Selecting the zeroth order term slopes are ignored in the surface local coordinate system, leading to a decoupling of polarizations in the vector scattering equations. As a result, co-polarized scattering in the plane of incidence is fairly accurate, but cross-polarized scattering is zero. In [de Roo and Ulaby, 1994] the Taylor series is expanded to the second order term in order to include depolarization in the incidence plane. In this same paper, the scalar approximation was used successfully to model bistatic scattering from moderately rough surfaces.

Small Perturbation Method - SPM The SPM is valid when the surface variations are much smaller than the electromagnetic wavelength and the slopes of the rough surface are relatively small. In this model, the random surface is decomposed into its Fourier spectral components, thus the scattered waves consists of a spectrum of plane waves. The final scattered fields can then be calculated from the diffraction integral by making use of the calculated surface fields [Ulaby et al., 1986a]. Although smooth terrains do usually fall into the region of applicability of this model, the SPM fails to consider the coherent component of the scattered fields.

Two Scale Model The two scale model assumes that the surface roughness is composed by a large scale and a small scale fluctuation. The final scattering coefficient is calculated as the linear combination of the large scale and small scale roughness contributions. The former is calculated by means of the KA-GO model, whereas the latter is obtained averaging the small scale SPM scattering coefficient over the probability density function of the large scale roughness tilt angle. This model has a major limitation, that is the boundary selection between a slightly rough and a very rough surface.

Integral Equation Models The IEM extends the validity range of the method to surfaces with greater variations. Assuming a plane wave impinging on a rough surface, the far-zone scattered field in the medium above the surface is calculated with the field integral equations, i.e. the Stratton-Chu formula [Fung et al., 1992; Fung, 1994]. To obtain an accurate estimation of the total tangential field, the basic idea is to solve the integral equation to which the tangential field on the surface must obey. The IEM adds a complementary term to the classical Kirchhoff tangential field, and it reduces to the geometric optics limit for high frequencies and also to the SPM at low frequencies (small scale roughness). The method relies on iterative Monte Carlo simulations to compute the scattered fields. Given a surface roughness and correlation length, random surfaces are generated for which the far fields are calculated. After several iterations the averaged field converges to the final solution. This method is computationally expensive and has a major limitation, as only one roughness scale can be chosen to generate the surfaces.

Additional refinement works were carried out to remove some of the original approximations done by the initial IEM. These new models are called the IEM2M model [Álvarez-Pérez, 2001], and the Advanced Integral Equation Model (AIEM) [Wu and Chen, 2004; Pierdicca et al., 2007]. The latter combines the high accuracy in evaluating the scattering coefficients with a high versatility in modeling the various statistics of the soil (Gaussian, Exponential, Two scale, etc.).

4.3.1.3 Coherent and incoherent scattering components simulations

During the LEiMON project, the AIEM bistatic scattering model presented in [Pierdicca et al., 2007] was integrated by the Tor Vergata and La Sapienza Universities within a GNSS simulator to study the scattering components observed from a GNSS-R receiver in various scenarios [Brogioni et al., 2010; Egido et al., 2011]. Several simulations were performed with this software for a low altitude ground-based receiver to investigate the effects of varying surface roughness and soil moisture on the observed signals. In order to perform realistic estimations of the observed signals by a GNSS-R receiver, different aspects related to the antenna and receiver characteristics were also considered for these simulation, which will be reviewed in depth in the next chapter.

Figure 4.8 shows the simulated coherent and incoherent scattering components of the Γ_{rl} and Γ_{rr} reflection coefficients as observed by a GNSS-R receiver for three different Soil Moisture Content (SMC): SMC = 5%, SMC = 20%, and SMC = 35%; and a constant surface roughness, σ_z =2 cm. As can be observed from the plots, in the case of Γ_{rl} both the coherent and incoherent components increase with soil moisture in a very consistent way. The difference between both scattering components is coincident in the three considered soil moisture conditions with a maximum deviation of 0.3 dB towards high incidence angles. For Γ_{rr}, the coherent components experiences also an increase with higher SMC values, however this behavior cannot be seen in the incoherent scattering component.

A remarkable aspect is the increasing trend of Γ_{rl} with incidence angle, in opposition to the decreasing trend expected by the Fresnel reflection coefficients, see Fig. 4.8. As will be explained in section 5.4.1, this is a consequence of the polarization loss factor of the up-looking and down-looking receiving antennas with respect to the incoming wave.

The effect of varying surface roughness on the reflectivity can be observed in Fig. 4.9. The Γ_{rl} and Γ_{rr} reflection coefficients were obtained for a fixed soil moisture, SMC = 20%, and three different surface roughness conditions; $\sigma_z = 0.7$ cm, $\sigma_z = 1.5$ cm, and $\sigma_z = 3.0$ cm. The results show a remarkable decrease of the coherent components on both Γ_{rl} and Γ_{rr} for increasing roughness. On the other hand, the incoherent component increases from 0.7 cm to 2.0 cm, and decreases from 2.0 to 3.0 cm. However, the ratio with respect the coherent component steadily decreases, i.e. the signal becomes more incoherent. In the case of $\sigma_z = 3.0$ cm, the incoherent component surpasses the coherent one for low incidence angle. Towards higher incidence angle, the incoherent component decreases, as the observed effective surface roughness is also lower.

From these results it can be inferred that the surface roughness is the parameter that has the strongest impact on the coherency of incoherency of the reflected signal; whereas the soil moisture does not significantly change the ratio between the coherent and the incoherent components, the surface roughness strongly modifies this relationship, and makes the reflected signal to be dominated by the incoherent component in the case of high σ_z.

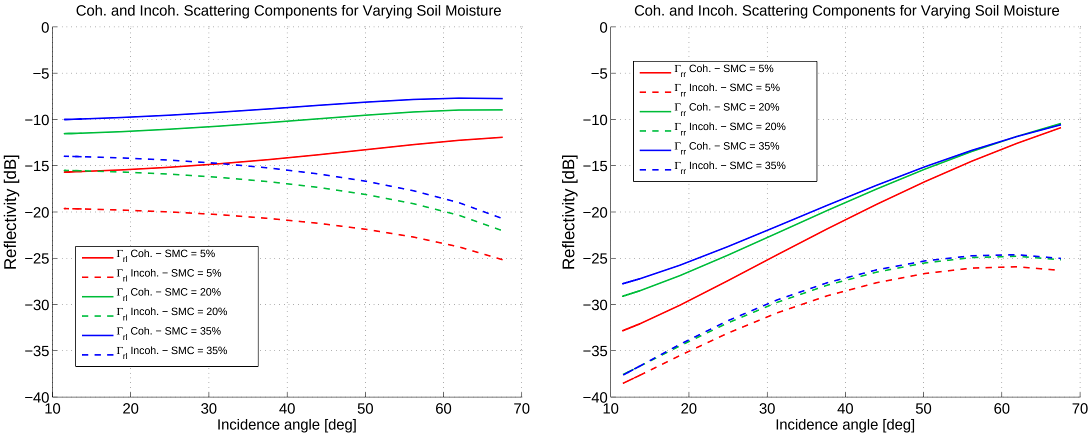

(a) (b)

Figure 4.8: Simulated (a) Γ_{rl} and (b) Γ_{rr} coherent and incoherent reflection coefficients for a fixed surface roughness, $\sigma_z = 1,5$cm, and varying soil moisture conditions.

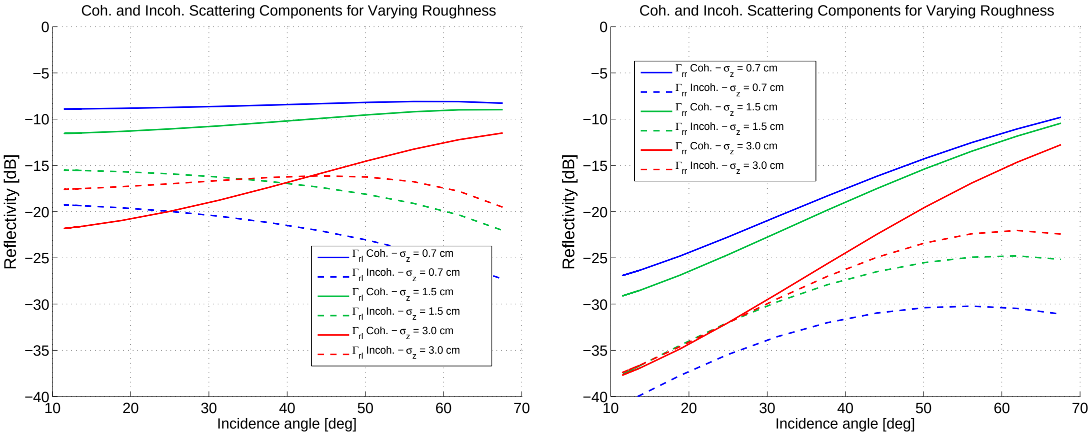

(a) (b)

Figure 4.9: Simulated (a) Γ_{rl} and (b) Γ_{rr} coherent and incoherent reflection coefficients for fixed soil moisture conditions, SMC = 20%, and varying surface roughness.

4.3.2 Vegetated Soils Scattering Models

The electromagnetic interaction of microwaves and vegetation is an extremely complicated process, mainly due to the fact that the signal wavelength is of the same order of magnitude as typical vegetation element dimensions. Extensive efforts aimed at deriving suitable models have been made for many years, leading to a wide amount of works looking for a physical explanation of the electromagnetic response of vegetated soils. Three main approaches can be found in the literature: semi-empirical models [Attema and Ulaby, 1978], continuous layer models [Fung and Ulaby, 1978], and discrete models. The latter are, indeed, widely recognized to be the most suitable scattering models for vegetation. The main advantages of discrete models are their ability to represent the fundamental electromagnetic properties of single elements, and the possibility to combine vegetation scattering theories with advanced soil scattering theories. Moreover, the required inputs are reasonably related to variables really measured on the fields.

4.3.2.1 Vegetation discrete models

Vegetation discrete models consists in three main parts: subdivision of the canopy in single elements, and selection of suitable geometrical shapes for simulation; modeling electromagnetic properties, i.e., permittivity, extinction and scattering cross section of the elements; combination of single contributions in order to obtain the total scattering coefficients.

Subdivision into single elements: The soil is, as for bare soil models, described as an homogeneous half-space with rough interface. Stems or trunks are described as near vertical dielectric cylinders. Leaves of crops or deciduous trees have a facet like geometrical structure, making disc shapes suitable for them. For some small leaves, such as alfalfa and soybean ones, simple circular discs can be appropriate. For long leaves, such as wheat and corn ones, leaf bending and local irregularities of the surface are not negligible. In this case a simple approximation, such as subdividing the leaf into several small discs, proved to be valid [Fung, 1994]. Needle-like leaves of coniferous trees are represented by thin prolate ellipsoids, with two axes much smaller than the third one. Realistic distributions of dimensions and orientations are usually chosen depending on the vegetation type and/or the stage of development. Growth model [Bracaglia et al., 1995], or allometric equations [Kasischke et al., 1994; Pierdicca et al., 2007] can be included at this step of the electromagnetic procedure.

Simulating permittivity and scattering of single elements: Assuming a low frequency approximation, i.e., wavelength much larger than thickness of vegetation elements, the absorption cross section, bistatic scattering cross section and extinction cross section of single vegetation elements can be modeled as presented in [Schiffer and Thielheim, 1979]. This scattering models require the vegetation permittivity as input, which can be obtained from models proposed in [Ulaby and El-Rayes, 1987] and [Matzler, 1994].

Combining elements: In order to combine the scattering coming from the multiple single elements several methods can be identified in the literature. A rather simple method is based on a first-order version of the Radiative Transfer theory [Durden et al., 1989; Macelloni et al., 2001]. According to this approach, the incoming wave is supposed to suffer three fundamental effects by vegetation elements, i.e., backscattering, specular scattering (i.e., downward scattering toward the ground floor in the specular direction with respect to the incident one) and attenuation. The scattering and attenuation functions of the vegetation layer are obtained by adding incoherently the scattering and attenuation functions of the scattering objects embedded in the canopy, and averaging over their dimensions and orientation. For soil, only backscattering and specular scattering are considered. A well known model based on this approach is MIMICS [Ulaby et al., 1990]. In general, the first order approach shows the advantage of a relative simplicity, since scattering processes are simulated only in two directions (i.e. the backward and the specular ones). On the other hand, multiple scattering effects are neglected. This can lead to underestimate vegetation backscattering, especially when the vegetation elements are large with respect to the wavelength. This is the case of crops at higher frequencies and forests also at L band.

To include multiple scattering effects, a valid solution is given by the Matrix Doubling algorithm, originally proposed in [Twomey et al., 1966] to solve scattering problems in atmospheric media. In [Eom and Fung, 1984] the method was extended to ensembles of dielectric discs, representing leaves, over the soil. Further studies applied the method to complex canopies including leaves, stems and petioles overlying soil [Bracaglia et al., 1995], and forests [Ferrazzoli and Guerriero, 1995]. To apply this technique, the bistatic scattering cross sections of the various vegetation elements need to be obtained first. The vegetation is described as a three layer medium: the top layer containing leaves and twigs, the middle layer containing vertical stems and trunks, and the bottom layer representing the underlying rough soil. The top and middle vegetation layers are subdivided further into N sublayers thin enough to neglect scattering interactions inside the same sublayer. For each sublayer, both the upper and the lower half-spaces are subdivided into discrete intervals of amplitude $\Delta\theta$ of the incidence and scattering off-normal angles, θ and θ_s, respectively. The incidence and scattering azimuth angles are denoted by ϕ and ϕ_s, respectively. The assumed scattering geometry is represented in Figure 4.10. Considering azimuthal symmetry, the dependency of the scattering is with the difference $\phi_s - \phi$. The sublayer behavior is characterized by the dimensionless scatter $\boldsymbol{S}$ and transmission $\boldsymbol{T}$ matrices, representing the ratio $I_{s,t}/I$ between the specific scattered or transmitted intensity $I_{s,t}$ and the specific incoming intensity I. Each element of the scattering matrix for the incoming and scattered polarizations p and q, and for specific incoming and scattered intervals θ_j and θ_{si}, respectively, is then defined by the relationship [Ferrazzoli and Guerriero, 1995],

$$S_{pq}(\theta_j;\theta_{si};\phi_s-\phi) = \frac{n\Delta z\,\Delta\theta\,\sin\theta_j}{4\pi\cos\theta_{si}}\sigma_{pq}(\theta_j;\theta_{si};\phi_s-\phi)\,, \tag{4.16}$$

where n represents the scatterer density (m^{-3}) in each sublayer, Δz is the sublayer thickness and σ_{ijpq} is the bistatic scattering cross-section averaged among the θ and θ_j angles belonging to the jth and ith intervals. In order to correctly account for both scattering and attenuation effects, the diagonal elements of the transmission matrices $\boldsymbol{T}$ are defined as the sum of the forward downward scattering term and a quantity equal to $(1-K_q^e(\theta_j))$, where $K_q^e(\theta_j)$ is the fraction of incident power traveling within the j-th angular interval at q polarization which undergoes extinction in the considered sublayer.

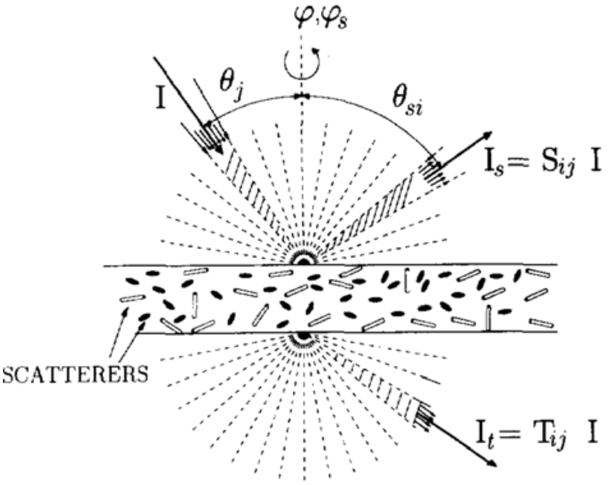

Figure 4.10: Vegetation scattering geometry; elementary scattering sublayer and scattering angles [Ferrazzoli and Guerriero, 1995].

In order to represent the azimuthal dependence of the scattering functions of the vegetation with acceptable fineness subdivision and without incurring in increasing the computational complexity, the scattering and transmission functions are Fourier transformed with respect to $\phi_s - \phi$. In this way, each sublayer is characterized by M pairs of matrices, $\boldsymbol{S_m}$ and $\boldsymbol{T_m}$, corresponding to the m-th Fourier component by which the azimuthal dependence is represented. The various contributions are then combined by means of the so called Matrix Doubling algorithm. For two adjacent sublayers characterized by scattering and transmission matrices $\boldsymbol{S_{1m}}$, $\boldsymbol{T_{1m}}$ and $\boldsymbol{S_{2m}}$, $\boldsymbol{T_{2m}}$, the overall scattering and transmission matrices are obtained by the relationships [Eom and Fung, 1984]:

$$\boldsymbol{S_m} = \boldsymbol{S_{1m}} + \boldsymbol{T_{1m}} \boldsymbol{S_{2m}} (\boldsymbol{1} - \boldsymbol{S_{1m}} \boldsymbol{S_{2m}})^{-\boldsymbol{1}} \boldsymbol{T_{1m}} \,, \tag{4.17}$$

and,

$$\boldsymbol{T_m} = \boldsymbol{T_{2m}} (\boldsymbol{1} - \boldsymbol{S_{1m}} \boldsymbol{S_{2m}})^{-\boldsymbol{1}} \boldsymbol{T_{1m}} \,. \tag{4.18}$$

By reiterating the process over the N sublayers, the Fourier components of the scattering and transmission matrices of the whole vegetation layer can be obtained. Analogously, a scattering matrix for the soil, proportional to the soil bistatic scattering coefficient, is calculated, and the same Matrix Doubling algorithm is then applied to combine soil and vegetation scattering, and therefore obtain the total Fourier transformed scattering and transmission matrices $\boldsymbol{S^t_m}$ and $\boldsymbol{T^t_m}$, respectively. The elements of the overall scattering matrix $S^t_{pq}(\theta_j; \theta_{si}; \phi_s - \phi)$ can be obtained as the sum of the Fourier series with the coefficients from $\boldsymbol{S^t_m}$. The polarization dependent overall bistatic scattering coefficient, $\sigma^0_{pq}(\theta_j, \phi; \theta_{si}, \phi_s)$, defined as:

$$\sigma^0_{pq}(\theta_j, \phi; \theta_{si}, \phi_s) = \frac{4\pi}{\Delta A} \cdot \frac{dp_{\Omega p}(\theta_{si}, \phi_s)}{dp_{Aq}(\theta_j, \phi)} \,, \tag{4.19}$$

with $dp_{\Omega p}(\theta_{si}, \phi_s)$ the p-polarized power density per unit angle in the ϕ_s direction scattered by the area ΔA, and $dp_{Aq}(\theta_j, \phi)$ the q-polarized incident power per unit area, can be readily calculated as:

$$\sigma^0_{pq}(\theta_j, \phi; \theta_{si}, \phi_s) = \frac{4\pi}{\Delta A} \cdot \frac{dI_{skp}(\phi_s)\, \Delta A\, \cos\theta_j}{dI_{kq}(\phi)\, \Delta\theta\, \sin\theta_{si} d\phi} = \frac{4\pi}{\Delta\theta} \cdot \frac{\cos\theta_j}{\sin\theta_{si}} \cdot S^t_{pq}(\theta_j; \theta_{si}; \phi_s - \phi)\,. \quad (4.20)$$

When considering scattering in the specular direction $\phi_s = \phi = \phi_{sp}$, and the incidence angle $\theta_j = \theta_{si} = \theta_{sp}$, the coherent scattering from the soil in the specular direction attenuated by vegetation, must be taken into account. Therefore, in this case the scattering coefficient is made up of two terms [Ferrazzoli et al., 2000]:

$$\sigma^0_{pq}(\theta_{sp}, \phi_{sp}; \theta_{sp}, \phi_{sp}) = \sigma^{0i}_{pq}(\theta_{sp}, \phi_{sp}; \theta_{sp}, \phi_{sp}) + \sigma^{0c}_{pq}(\theta_{sp}, \phi_{sp}; \theta_{sp}, \phi_{sp})\,, \quad (4.21)$$

where σ^{0i}_{pq} represents the incoherent scattering coefficient calculated with Eqn. (4.20), and σ^{0c}_{pq} is the coherent scattering coefficient of the soil, attenuated by the overlaying vegetation layer, and calculated with the formulation proposed in [Fung and Eom, 1983]. For the particular case of a GNSS-R system, based on this representation of the scattering in a coherent and incoherent components two regimes can be identified; when the vegetation biomass is low, the specular scattering coefficient is mainly due to the attenuated coherent scattering from the soil; when the vegetation biomass is large, this term can be of the same order of magnitude of vegetation volume scattering, while all other contributions (i.e. incoherent scattering from soil and interactions between soil and vegetation) can be considered negligible. The specular scattering coefficient $\sigma^{0,sp}$ can thus be simplified in the form [Pierdicca et al., 2007; Ferrazzoli et al., 2010],

$$\sigma^{0,sp} = \sigma^{0c}(\theta_j = \theta_{si}, \phi_s = \phi)\frac{1}{L^2} + \frac{\sigma^{0veg}(\theta_j = \theta_{si}, \phi_s = \phi)}{2\sigma^{veg}_e}(1 - \frac{1}{L^2})\,, \quad (4.22)$$

where $1/L^2$ is the two way loss factor, $\sigma^{0,soil}$ the soil coherent scattering coefficient, σ^{veg} is the average vegetation scattering cross section in the specular direction, σ^{veg}_e is the average extinction cross section of vegetation. The latter two quantities can be computed as a weighted average over all the vegetation elements, considering their shapes and the distributions of dimensions and orientations [Pierdicca et al., 2007], [Ferrazzoli et al., 2010].

4.3.2.2 Vegetation Scattering Simulations

The effect of vegetation on GNSS reflected signals was also analyzed by means of the LEiMON simulator. A surface with varying Plant Water Content (PWC) over a soil with fixed soil moisture (SMC = 20%) and surface roughness conditions ($\sigma_z = 1.5$ cm) was simulated. Apart from the bare soil case, sunflowers with a PWC of 2 and 7 kg/m^2 were considered, corresponding to plants at a primary and full development stage, respectively.

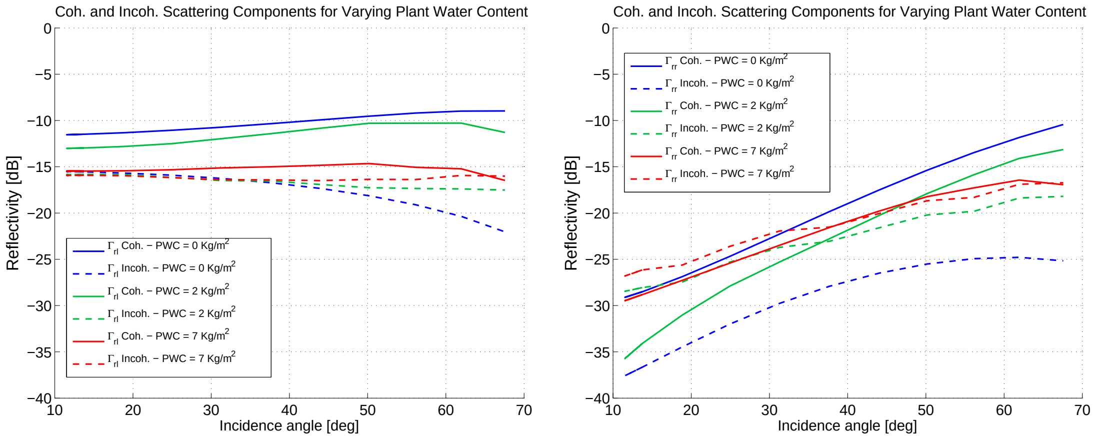

(a) (b)

Figure 4.11: Simulated (a) Γ_{rl} and (b) Γ_{rr} coherent and incoherent reflection coefficients for fixed soil moisture and surface roughness conditions, SMC $= 20\%$ and $\sigma_z = 1,5$cm, and varying Plant Water Content (PWC).

The results for this simulation are gathered in Fig. 4.11. In the first place, it can be seen from the simulated reflection coefficients that the coherent component of Γ_{rl} is reduced due to the effect of increasing PWC, Fig. 4.11(a). From a bare soil situation to the fully developed sunflower, the coherent scattering component decreases by almost 4 dB in the case of low incidence angles. This difference grows for high incidence angles due to the longer path that the impinging GNSS waves travel through the vegetation layer. On the other hand, the Γ_{rl} incoherent scattering component does not exhibit a noticeable variation between the three simulated development stages. This could be linked to the fact that the additional incoherent scattering component produced by the presence of vegetation is cancelled out by the additional attenuation.

The Γ_{rr} coherent scattering coefficient does not show a clear behavior with vegetation, as can be noticed from Fig. 4.11(b). As for the incoherent scattering component at rl polarization, this is likely to be due to the combined effect of an additional depolarization originated in the vertical structure of the vegetation and an increasing attenuation due to the larger absorption in the vegetation layer. It is also observed that the incoherent component experiences a very strong increase in the presence of vegetation, surpassing the coherent scattering component for low incidence angles in the case of fully developed sunflowers.

4.4 Summary and Conclusions

The dielectric properties of soil are intrinsically related with its moisture content. This has the effect of changing the terrain reflectivity, which can be measured by accounting for the relative amplitudes of the direct and reflected GNSS signals. Other nuisance parameters can influence the measurement. The most important one is the soil surface roughness. As has been discussed, the surface small scale roughness has the effect of reducing the surface reflectivity by an exponentially decaying factor. In addition, an increasing roughness originates a diffuse scattering component, thus generates the scattering to be composed of a coherent and an incoherent scattering components. Coherency and incoherency are related with the capabilities of the reflecting surface to keep a certain phase history; for a completely coherent signal its phase will be completely coherent, whereas the phase of an incoherent signal is random and uniformly distributed between $-\pi$ and π.

The current state of the art scattering models were presented. Simulations with a software implementing the AIEM, [Pierdicca et al., 2007], were performed to determine the effect of the soil bio-geophysical parameters on the coherent and incoherent scattering components. This simulator was developed by the Tor Vergata and Sapienza Universities during the LEiMON project [Egido et al., 2011]. It was observed that for normal roughness situations, the coherent component is significantly higher than the incoherent one; up to 10 dB and 6 dB higher for a low and a mid surface roughness condition, respectively. However, for high surface roughness conditions, the incoherent component surpasses the coherent one.

In the same way, the vegetation scattering models have been presented. A model based on the multiple combination of scattered waves on the discrete components of the vegetation was discussed in depth. This model was also implemented in the simulation software, which allowed to study the effects of increasing vegetation on the signal. Sunflower plants at three different development stages were considered for this analysis. As has been observed, an increasing vegetation biomass produces an increasing attenuation on the Γ_{rl} reflection coefficient, whereas it increases remarkably the incoherent scattering component on Γ_{rr}. The incoherent component of Γ_{rl} remains relatively stable, which contributes to reduce the coherent vs incoherent component ratio to 0 dB for fully developed sunflowers.

As has been observed from these simulations, the signal characteristics change with the soil conditions. The relative weight of the coherent and incoherent scattering components on the finally received signals should be taken into consideration when performing the soil reflectivity measurements.

Chapter 5

GNSS-R Polarimetric Observables for Land Applications

When GNSS signals impinge on the Earth, the scattering surface leaves its imprint on the reflected signal in several ways; one of them is through the bistatic scattering coefficient, which is determined by the dielectric and surface structure and depends on the polarization of the incident and scattered waves. Signals transmitted by GNSS satellites are to a large extent RHCP. When reflecting from the Earth's surface, the electromagnetic waves suffer a polarization rotation, and therefore most of the power is reflected in LHCP. However, there is also a non-negligible component of the signal scattering in RHCP mainly due to the finite conductivity of the reflecting media and the surface characteristics. Studying the relative weights of both polarizations of the reflected signal can provide valuable information for the determination of soil moisture. In addition, new studies using bistatic scattering models based on the polarimetric analysis of the reflected signal [Pierdicca et al., 2007] suggest the possibility of considering the effect of vegetation in the scattering process in a two fold way; first, improve the accuracy in the estimation of soil moisture, and second, obtain on-ground vegetation estimates such as the biomass.

The current chapter provides a description of the process to obtain polarimetric measurements from GNSS-R signals for land observations out of the basic GNSS-R observables, i.e., the direct and reflected complex waveforms, and the associated nuisance parameters that need to be taken into account in order to obtain reliable measurements.

5.1 Reflectivity Measurements with GNSS-R Signals

As discussed in the previous chapter, scattered GNSS signals off terrain surfaces are a combination of both a coherent and an incoherent component. The former is originated around the specular direction and is driven by the well known Fresnel reflection coefficients; the latter has a more omnidirectional nature and is related to the diffuse scattering mechanisms that occur due to the random soil surface structure and the multiple-scattering effect among the different vegetation elements. As seen in section

4.2.1, the total scattered field can be represented as the combination of n randomly distributed scatterers:

$$u(t) = r(t)e^{j\psi(t)} = \sum_{i=1}^{n} A_i(t)e^{j\phi_i(t)} \,. \tag{5.1}$$

The independent variable t is explicitly shown to denote the field variability with time. The coherent component is obtained as the expectation of the scattered field, whereas the incoherent one accounts for the fluctuating component around the expected value. Its power is calculated as the sum of the variances of the real and imaginary components of the u field:

$$P^{\mathrm{coh}} = \alpha^2 = |\langle u(t)\rangle_t|^2 \qquad ; \qquad P^{\mathrm{incoh}} = \sigma^2_{\Re(u)} + \sigma^2_{\Im(u)} = s_1 + s_2 \,. \tag{5.2}$$

Considering that the coherent component is originated in the vicinity of the specular point, it can be readily seen from Eqns. (3.8) and (3.9) that in the case of $R_{0,sp} \gg R_{sp}$, which is always true for ground-based and airborne receivers, soil reflectivity estimates can be obtained from the ratio of the reflected and direct fields, $u_{r,sp}$ and u_d, respectively. The objective then would be to separate the coherent and incoherent contributions of the scattered fields in both polarizations, in order to obtain estimations of the co- and cross-polarization Fresnel reflection coefficients.

As explained in section 3.4, in order to detect u_d and $u_{r,sp}$, the received signals need to be cross-correlated with the PRN code replica, resulting in the direct and reflected complex waveforms which will finally be the fundamental observables for the GNSS-R polarimetric measurements. The surface reflectivity, Γ_{pq}, could then be written as the ratio of the direct and reflected waveforms at different polarizations, $Y_{d,r;p,q}(\tau, f)$. Considering that f is aligned with the Doppler frequency shift of the direct signal, and applying the variable change $\tau' = \tau - R_d$, with R_d the range between the transmitting satellite and the receiver, the estimated surface reflectivity, Γ'_{pq}, is obtained as:

$$\Gamma'_{pq} = \left| \left\langle \frac{Y_{r,q}(\Delta\tau, f)}{Y_{d,p}(0, f)} \right\rangle \right|^2 \,, \tag{5.3}$$

where $\langle\cdot\rangle$ denotes the averaging operator along time, and $\Delta\tau$ is the delay difference between the direct and reflected paths. In the case of ground-based or low altitude receivers this could be calculated with the simple equation $c\,\Delta\tau = 2\,h\,\cos\theta$, with θ the incidence angle. By selecting $\tau' = 0$ and $\tau' = \Delta\tau$ for the direct and reflected waveforms, respectively, it is ensured that the waveforms' peaks are selected. For low altitude receivers, it can also be assumed that the Doppler frequency shifts of the direct and reflected channels are the same[1], $f_d \approx f_r = f$.

The ratio between the direct and reflected waveform's peak time series is known as the Interferometric Complex Field (ICF), which entails the suppression of common

---

[1] As will be shown later, there is a residual Doppler difference that leads to a phase drift on the reflected signal which needs to be accounted for and corrected before performing the waveform averaging in the complex domain. Indeed, the phase coherency needs to be maintained for the whole averaging time, otherwise the final result tends rapidly to zero.

errors in the direct and reflected channels such as propagation noise, clock drift errors, Doppler tracking errors, etc:

$$\mathrm{ICF}(t) = \frac{Y_{r,q}(t;\Delta\tau, f)}{Y_{d,p}((t;0,f)} = \frac{R(t)}{D(t)} = \frac{r(t)}{d(t)}\, e^{-i(\phi_r(t)-\phi_d(t))}\,. \tag{5.4}$$

$D(t)$ and $R(t)$ are, respectively, the direct and reflected waveform peaks time series, i.e. the direct and reflected complex fields, with their associated amplitudes, $d(t)$ and $r(t)$, and phases $\phi_d(t)$ and $\phi_r(t)$. $r(t)$ and $\phi_r(t)$ govern the final amplitude and phase of the ICF, and have different random behaviors depending on the characteristics of the observed surface.

The previous equations show how the surface reflectivity could be estimated out of the direct and reflected GNSS waveforms in an ideal case in which the direct and reflected signals are not affected by thermal noise. In order to account for the effects of noise in the estimation of the reflectivity, the cross-correlation waveform statistics are derived next.

5.2 Mean Waveform Amplitude Derivation

The amplitude of the averaged waveform, $|\langle Y(\tau, f)\rangle|$, is analyzed in this section. Subscripts for channel and polarization have been dropped for the sake of clarity. In this case, a GNSS signal with infinite sampling rate, and infinite quantization samples has been considered for simplicity:

$$s(t) = a(t)\cdot e^{i\left(2\pi f t+\phi_f(t)\right)} + n(t)\,, \tag{5.5}$$

where f is the carrier or Intermediate Frequency (IF) of the system plus a certain Doppler, $\phi_f(t)$ are the phase variations due to the physical phenomena involved, $a(t)$ stands for the modulating PRN code with amplitude equal to 1, and $n(t)$ is the thermal noise. This signal would then be affected by the reflection process, however for the purpose of the current section the geophysical noise phase and amplitude fluctuations have been ignored. The thermal noise is characterized by its autocorrelation function

$$\big\langle n(t), n(t')\big\rangle = \sigma^2 e^{(t-t')^2/\tau_n^2}\,, \tag{5.6}$$

where the symbol $\langle\cdot\,,\cdot\rangle$ stands for the dot product

$$\langle a(t), b(t)\rangle = \frac{1}{T}\int_0^T a^*(t)\, b(t)\,\mathrm{d}t\,, \tag{5.7}$$

and σ^2 and τ_n the noise variance, and noise coherence time, respectively. Having chosen the amplitude of the signal equal to 1, the voltage SNR can be written as:

$$\mathrm{SNR}_V = \frac{1}{\sigma}\,. \tag{5.8}$$

Assuming that the Doppler frequency of the incoming signal is known, the replica delayed by a certain time τ is given by:

$$r_\tau(t) = a_\tau(t) \cdot e^{i(2\pi f t)} \,. \tag{5.9}$$

The normalized cross-correlation of the signal with the replica, i.e. the complex voltage waveform, is defined as:

$$Y(\tau) = \frac{\langle s(t), r_\tau(t) \rangle}{\sqrt{\langle s(t), s(t) \rangle \langle r_\tau(t), r_\tau(t) \rangle}} \,. \tag{5.10}$$

Examining separately the constituents of the previous equation, we obtain:

$$\langle r_\tau(t), r_\tau(t) \rangle = \frac{1}{T} \int_0^T a_\tau(t) \cdot e^{-i2\pi f t} \cdot a_\tau(t) \cdot e^{i2\pi f t} \mathrm{d}t = 1 \,, \tag{5.11}$$

then,

$$\begin{aligned}
\langle s(t), s(t) \rangle &= \frac{1}{T} \int_0^T \left[a(t) \cdot e^{i\left(2\pi f t + \phi_f(t)\right)} + n(t) \right]^* \left[a(t) \cdot e^{i\left(2\pi f t + \phi_f(t)\right)} + n(t) \right] \mathrm{d}t \\
&= \frac{1}{T} \int_0^T \left(1 + |n(t)|^2 + a(t) \cdot n(t) \cdot e^{-i\left(2\pi f t + \phi_f(t)\right)} + a(t) \cdot n^*(t) \cdot e^{i\left(2\pi f t + \phi_f(t)\right)} \right) \mathrm{d}t \\
&= 1 + \sigma^2 + 2 \cdot \mathrm{Re} \left[\frac{1}{T} \int_0^T a(t) \cdot n^*(t) \cdot e^{i\left(2\pi f t + \phi_f(t)\right)} \mathrm{d}t \right] \,,
\end{aligned} \tag{5.12}$$

and finally:

$$\begin{aligned}
\langle s(t), r_\tau(t) \rangle &= \frac{1}{T} \int_0^T \left[a(t) \cdot e^{i\left(2\pi f t + \phi_f(t)\right)} + n(t) \right]^* \left[a_\tau(t) \cdot e^{i2\pi f t} \right] \mathrm{d}t \\
&= \frac{1}{T} \int_0^T \left(a(t) \cdot a_\tau(t) \cdot e^{-i\phi_f(t)} + a_\tau(t) \cdot n^*(t) \cdot e^{i2\pi f t} \right) \mathrm{d}t \,.
\end{aligned} \tag{5.13}$$

The cross-correlation waveform is written as:

$$Y(\tau) = \frac{\frac{1}{T} \int_0^T \left(a(t) \cdot a_\tau(t) \cdot e^{-i\phi_f(t)} + a_\tau(t) \cdot n^*(t) \cdot e^{i2\pi f t} \right) \mathrm{d}t}{\sqrt{1 + \sigma^2 + 2 \cdot \mathrm{Re} \left[\frac{1}{T} \int_0^T a(t) \cdot n^*(t) \cdot e^{i\left(2\pi f t + \phi_f(t)\right)} \mathrm{d}t \right]}} \,. \tag{5.14}$$

If $\sigma^2 \gg 1$, as it is the case for GNSS signals, the peak value can then be approximated by

$$Y(0) \approx \frac{\frac{1}{T} \int_0^T \left(e^{-i\phi_f(t)} + a_\tau(t) \cdot n^*(t) \cdot e^{i2\pi f t} \right) \mathrm{d}t}{\sigma} \,. \tag{5.15}$$

Analyzing the previous equation one can identify that the second term of the integrand in Eqn. includes a fast rotating phasor that tends to zero when the coherent integration is performed. On the other hand, the phase term $\phi_f(t)$ can be considered constant during the averaging time T. Finally, taking the average along time, it can be written that

$$\langle Y(0)\rangle = \frac{\frac{1}{T}\left\langle e^{-i\phi_f(t)}\right\rangle \int_0^T \mathrm{d}t}{\sigma} = \frac{\left\langle e^{-i\phi_f(t)}\right\rangle}{\sigma}\,. \tag{5.16}$$

Considering that $\phi_f(t)$ does not change significantly along time, as it is the case for GNSS receivers implementing the tracking of the signal by means of a Phase Locked-Loop (PLL), it can be readily seen that the amplitude of the averaged waveform peaks yields the SNR_V. This result can also be extrapolated to the reflected signal; as discussed in section 4.2.2, in the case of a slightly rough surface, the incoming signal $s(t)$ would be defined by a Hoyt-vector, i.e. a two-dimensional Gaussian distribution displaced from the origin, thus, the averaging of $\exp(-i\phi_f(t))$ yields a non-zero value, and therefore the same reasoning applies.

Attending to the previous results, Eqn. (5.3) can then be rewritten in terms of the voltage SNR of the direct and reflected signals, $\mathrm{SNR}_{V,d}$ and $\mathrm{SNR}_{V,r}$:

$$\Gamma'_{pq} = \left|\left\langle \frac{Y_{r,q}(\Delta\tau)}{Y_{d,p}(0)}\right\rangle\right|^2 = \left|\left\langle \frac{r(t)}{d(t)}\, e^{i(\phi_d(t)-i\phi_r(t))}\right\rangle\right|^2 = \left|\frac{\sigma_d}{\sigma_r}\left\langle e^{i(\phi_d(t)-i\phi_r(t))}\right\rangle\right|^2 = \left|\frac{\mathrm{SNR}_{V,r}}{\mathrm{SNR}_{V,d}}\right|^2, \tag{5.17}$$

and elaborating further the previous equation:

$$\Gamma'_{pq} = \left|\frac{\mathrm{SNR}_{V,r}}{\mathrm{SNR}_{V,d}}\right|^2 = \frac{N_d}{N_r}\,\frac{P_{r,q}}{P_{d,p}} = \rho\,\frac{P_{r,q}}{P_{d,p}}\,, \tag{5.18}$$

where Γ'_{pq} is expressed as the received reflected and direct signal power ratio in q and p polarizations, $P_{r,q}$ and $P_{d,p}$, weighted by a factor, ρ, i.e., the ratio between the direct and reflected noise powers, N_d and N_r. Γ'_{pq} is defined as the apparent power reflectivity. This parameter is of main importance as it represents the measurable reflectivity value performed by GNSS-R observations.

In the next section the effect of thermal noise on the determination of the reflectivity is analyzed. The factor ρ can have important implications, as differences in the direct and reflected channels SNR are likely to occur. The impact of the different noise sources on the apparent power reflectivity is discussed in depth in the next section.

5.3 Thermal Noise Effect in GNSS-R Reflectivity Measurements

GNSS-R reflectivity measurements are obtained through the ratio of the averaged direct and reflected waveform peaks. Variations in soil moisture, roughness, and vegetation, modify the GNSS reflected signal power seen by the receiver, thus varying accordingly the waveform peaks. However, these parameters are not the only ones intervening in the geophysical observables, since the waveform peaks are directly proportional to the signal to noise ratio of the received signal. In other words, variations on the system noise can also modify the observables, thus biasing the estimation of the geophysical parameters.

5.3.1 Thermal Noise in a Receiver

It can be demonstrated that the noise power at the terminals of a resistor, P_n can be calculated by the well known expression $P_n = k\,T\,B$, where k is the Boltzmann constant, T is the physical temperature of the resistor, and B is the noise bandwidth of the measurement system. The direct relationship between noise power and temperature allows to represent the noise in a system by an equivalent noise temperature that will account for the receiver's thermal noise.

Noise in a receiver can be described by two noise components: the noise entering from the antenna into the input terminals of the receiver and the noise generated by the receiver itself. Those are commonly known as source noise, and receiver noise.

The source noise corresponds to the noise at the antenna output. It is composed of an external noise, originated from the total brightness temperature observed by the antenna from relatively distant noise sources, T_{ant}, and the thermal noise arising in the lossy portions of the antenna structure due to the antenna physical temperature, T_{phys}. The noise temperature at the antenna terminals, T_A, can be calculated as follows [Curlander and McDonough, 1991]:

$$T_A = \eta_l T_{\text{ant}} + (1 - \eta_l)\, T_{\text{phys}}\,, \tag{5.19}$$

where η_l represents the antenna thermal efficiency, and T_{ant} the scene brightness temperature seen by the antenna. η_l is inversely proportional to the antenna loss factor, and can be written as $\eta_l = G_0/D_0$, being D_0, and G_0, the antenna directivity and gain at its boresight, respectively. On the other hand, T_{ant} is calculated weighting the direction dependent brightness temperature of the scene, $T_B(\theta, \phi)$, by the antenna radiation pattern, $D(\theta, \phi)$.

The previous expression can be further parametrized introducing the concept of main beam efficiency, η_M, defined as the contribution to the antenna directivity of the main beam with respect to the overall directivity. In this case, T_{ant} can be written as:

$$T_{\text{ant}} = \eta_M T_{\text{ML}} + (1 - \eta_M)\, T_{\text{SL}}\,, \tag{5.20}$$

where T_{ML} and T_{SL} stand for the main lobe and side lobe brightness temperatures, respectively. For a more detailed derivation of the antenna temperature and the possible external noise sources see [Curlander and McDonough, 1991, Chapter 2].

The receiver noise refers to the thermal noise introduced in the system due to internal sources. The intrinsic receiver noise density, N_{int} defines an equivalent noise temperature T_e; i.e. the temperature at the input of a noiseless receiver necessary to produce at its output the noise originated by its intrinsic sources. To characterize the receiver intrinsic noise, a noise factor F is commonly used. The standard noise factor is defined as the ratio of the total available output noise density, with the input source at a standard temperature $T_0 = 290\text{K}$, and the output noise density attributable to the input. Having a receiver with a certain electrical gain G, the noise factor yields:

$$F = \frac{N_{int} + GkT_0}{GkT_0} = 1 + \frac{T_e}{T_0} \,. \tag{5.21}$$

The receiver's noise factor can also be interpreted as the degradation of the signal to noise ratio at the output of the receiver with respect to the input. If expressed in dB, the noise factor is commonly referred to as Noise Figure (NF). For a cascade of receivers (e.g. amplifiers) characterized by their gains, and noise factors, the noise factor formula can be extended by the following expression known as the Friis noise formula, [Ulaby et al., 1986b, Chapter 6]:

$$F = F_1 + \frac{F_2 - 1}{G_1} + \frac{F_3 - 1}{G_1 G_2} ... + \frac{F_N - 1}{G_1 G_2 ... G_{N-1}} \,. \tag{5.22}$$

In an equivalent way, this can be expressed in terms of the receiver's noise temperatures:

$$T = T_1 + \frac{T_2}{G_1} + \frac{T_3}{G_2 G_3} ... + \frac{T_N}{G_1 G_2 ... G_{N-1}} \,. \tag{5.23}$$

The previous expressions can also be applied in the case of having lossy systems in the receiver cascade, considering that the loss L equals $1/G$. The numbering of the components' noise factors and gains is sequential, starting at the input of the receiving chain. From the previous equations it can be deduced that having an amplifier with a low noise factor and/or high gain at the input of the chain, is the most desirable situation in order to prevent degradation of the signal to noise ratio in the receiving chain.

5.3.2 Noise in a GNSS-R Receiving Chain

In terms of noise, a conventional GNSS receiver can be modeled by the chain shown in Fig. 5.1. From this model, the noise figure of the whole chain and the system temperature at the input of the receiver can be calculated. The former gives an insight of the performance of the system with respect to noise. The latter represents the final noise temperature at the input of the GPS receiver, considering external and intrinsic noise sources, and determines the final signal to noise ratio of the GNSS signal.

For a GNSS-R receiver, the noise should be evaluated for the direct and reflected channels; apart from eventual thermal gradients in the instrument, and mismatches in the gain and losses of both receiving chains, the most important difference in terms of the final noise of the system are due to the difference between the up-looking and down-looking antenna temperatures.

The current analysis is concentrated in the system temperature, T_{sys}, as it provides a clearer insight of how variations on the noise temperature in the different parts of the receiving chain affect the final signal to noise ratio. The system temperature is defined as the sum of the receiver and antenna noise temperatures, T_R and T_A, respectively:

$$T_{\text{sys}} = T_A + T_R \,. \tag{5.24}$$

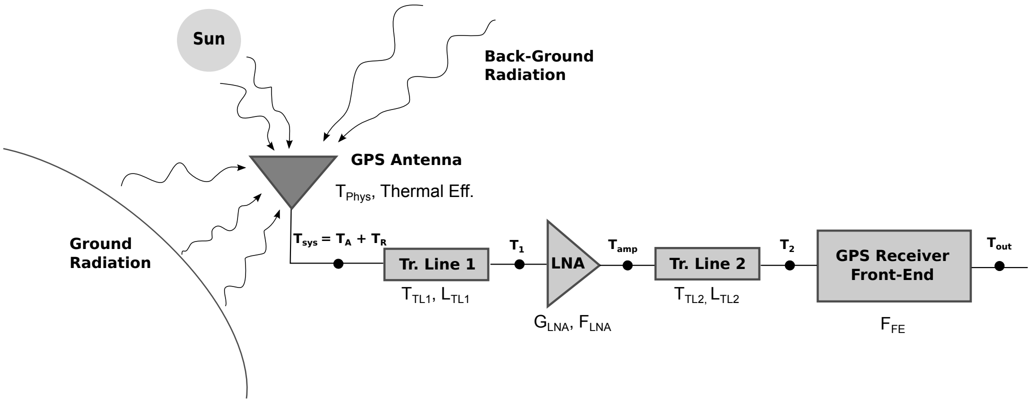

Figure 5.1: GNSS receiving chain noise model.

	$\mathbf{TL_1}$	**LNA**	$\mathbf{TL_2}$	**FE**
Gain / Loss (dB)	-1	14	-3	-10
Phyhsical Temperature	290K	290K	290K	290K
Noise Factor (dB)	1	0.5	3	10
Component Noise Equivalent Temperature	75.09K	35.39K	288.63K	2610K
Temperature Contribution to $\mathbf{T_R}$	75.09K	44.55K	14.47K	261K
Accumulated Noise Equivalent Temperature	75.09K	119.64K	134.1K	395.1K

Table 5.1: Receiver Noise Equivalent Temperatures – Typical Values

5.3.2.1 GNSS Receiver Noise Temperature

The calculation of the receiver equivalent noise temperature T_R can be done following the Friis formula presented in the previous section:

$$T_R = T_{e_{\mathrm{TL1}}} + T_{e_{\mathrm{LNA}}} L_{\mathrm{TL1}} + \frac{T_{e_{\mathrm{TL2}}} L_{\mathrm{TL1}}}{G_{\mathrm{LNA}}} + \frac{T_{e_{\mathrm{FE}}} L_{\mathrm{TL1}} L_{\mathrm{TL2}}}{G_{\mathrm{LNA}}} , \tag{5.25}$$

where $T_{e_{\mathrm{Elem}}}$, L_{Elem} and G_{Elem}, are respectively the the noise equivalent temperature, losses, and gain of the different components in the receiving chain. The calculation of the noise equivalent temperatures can be obtained by applying Eqn. (5.21).

Typical values of these parameters for conventional receivers can be found in Table 5.1. In the case of the transmission lines, the noise factor equals the losses, whereas for the amplifier and front-end the noise factors were obtained from the manufacturer's specifications. The losses of the second transmission line (TL$_2$) can vary significantly depending on the instrument configuration. A standard value of -3 dB was selected for this analysis.

For simplicity, it was considered that the physical temperature of all the elements in the receiving chain equals $T_0 = 290$ K. The results of the calculations of the receiver noise equivalent temperature are gathered in the table above. The total receiver equivalent noise temperature, T_R, was calculated to be 395.1 K. The overall noise factor of such a system was calculated to be 3.79 dB.

Antenna Parameter	**Value**
Thermal Efficiency (η_l)	0.7
Gain at Borersight (G_0)	7 dBi
Half Power Beamwidth (HPBW)	80 deg
Main Beam Efficiency (η_M)	0.75

Table 5.2: GNSS receiving antenna typical noise parameters.

	T_{phys}	$T_{\text{phys}}(1-\eta_l)$	T_{ML}	T_{SL}	T_B	T_A
Direct Antenna	290 K	87 K	5 K	100 K	20.13 K	107.1 K
Reflected Antenna	290 K	87 K	261 - 174 K	100 K	109.8 K	241 - 196 K

Table 5.3: Direct and Reflected antenna temperatures. The range obtained for the reflected antenna temperature is due to the variation of the surface emissivity.

The most important contribution to the noise of the whole receiving chain comes from the GNSS front-end, which amounts to almost 66% of the total receiver noise temperature. This implies that changes in the physical temperature of the transmission lines are going to be of little impact in the final noise. For instance, if considered a physical temperature of 320 K in both transmission lines, the final noise receiver temperature yields 404 K, which represents an increase of barely 2%.

It can also be inferred from this analysis that all lossy elements in the receiving chain before the pre-amplification stage have a direct impact in the overall noise figure of the system. Therefore, it is highly desirable to have the first transmission line and the noise figure of the amplifier as low as possible in order to preserve a high signal to noise ratio.

5.3.2.2 Direct and Reflected Antenna Noise Temperature

For the analysis of the antenna physical temperature, and the final calculation of the total system temperature, the problem is separated among the direct and the reflected channels, provided the difference in background temperature of the scenes.

The antenna noise temperature was calculated using Eqn. (5.19). The selected antenna parameters are given in Table 5.2. The antenna thermal efficiency was set to 0.7, which represents a standard value for a GPS patch antenna. The gain at boresight of the antenna, as well as its half power beam-width were taken from the datasheets of conventional GPS antennas. The main beam efficiency of the antenna, η_M, was calculated approximating the radiation pattern by a squared cosine as a function of the off-boresight angle, which yields a value of 0.75.

The physical and brightness temperatures of both the direct and reflected antennas to perform the calculation of T_A are gathered in table 5.3. The physical temperature of both antennas was selected to be equal to $T_0 = 290$ K. For the direct antenna, provided that the propagation losses of the atmosphere at L-band are very low, the brightness temperature for the main beam, T_{ML}, was set to 5 K, close the background radiation. For the side lobe temperature, the value selected equals 100 K, as it is a combination of both the ground temperature and the sky temperature. This gives a final T_A equal to 107.1 K, in agreement with the expected values provided in [Parkinson and Spilker, 1996] and [Misra and Enge, 2006]. For the down-looking antenna, T_{ML} was set to the soil brightness temperature. This is calculated weighting the soil physical temperature, by the soil emissivity, defined as:

$$\epsilon = 1 - \Gamma \,, \tag{5.26}$$

where Γ is the soil reflectivity. The hypothesis of specular reflection is valid for this situation, since it provides a worst case scenario in terms of emissivity variability. As shown in Fig. 5.8, the soil reflectivity can vary between 0.1 and 0.4 for a dry, and wet soil, respectively. For a soil physical temperature equal to T_0, the soil brightness temperature varies between thus has a variability close to 100 K, which in the end, turns into a T_A variation between 240 and 196 K.

These variations in the antenna temperature are the ones which will ultimately affect the most in the estimation of the surface reflectivity. Despite the fact that the total system noise is dominated by the receiver noise (note that T_R is 200 to 300 K higher than T_A), the latter can be accounted for and corrected by means of a calibration chain. The equivalent temperatures of the up-looking and down-looking antennas are the main instrumental parameters affecting the estimation of the reflectivity in terms of noise. The effect in the final estimation is discussed next.

5.3.3 Thermal Noise Impact on Surface Reflectivity Estimations

As discussed in the previous section, the fact that the direct and reflected channels have different equivalent noise temperatures leads to a bias in the estimation of the soil reflectivity. As mentioned above, despite the fact that for a GNSS system it is the receiver noise temperature the one usually governing the final system temperature, the impact of the difference in up-looking and down-looking antenna temperatures is strong enough to introduce changes in the estimation of surface reflectivity.

In Fig. 5.2(a) the actual and estimated Γ are depicted for the calculated direct and reflected noise temperatures. The bias in the estimation of this parameter can be readily observed. Apparently the error increases with the reflectivity, however, in Fig. 5.2(b) the relative error is shown. As can be seen from this second plot, the relative error actually decreases with reflectivity. This result can be more clearly understood if the reflectivity is translated into emissivity; lower reflectivity, implies higher emissivity, thus, the soil brightness temperature increases, leading to a larger difference between the direct and reflected antenna temperatures. It can be proven that other parameters affecting the final antenna temperature different from the soil reflectivity do not have such an important impact in the estimation. For instance varying the soil physical temperature for a dynamic range of 50 K, which is a rather extreme situation, leads to a variation in the reflectivity relative error of less than 2.5%.

Besides the estimation bias, the noise in the direct and reflected amplitude measurements should also be considered, as this impacts directly on the final noise of the reflectivity measurements. The observable variance can be calculated by means of the error propagation formula [Bevington and Robinson, 1969]. The final variance of $\hat{\Gamma}$, can be written as:

$$\sigma_{\Gamma'}^2 = \frac{1}{\mu_d^2}\sigma_r^2 + \frac{\mu_r^2}{\mu_d^4}\sigma_d^2 - 2\frac{\mu_r}{\mu_d^3}\sigma_{dr} \,, \tag{5.27}$$

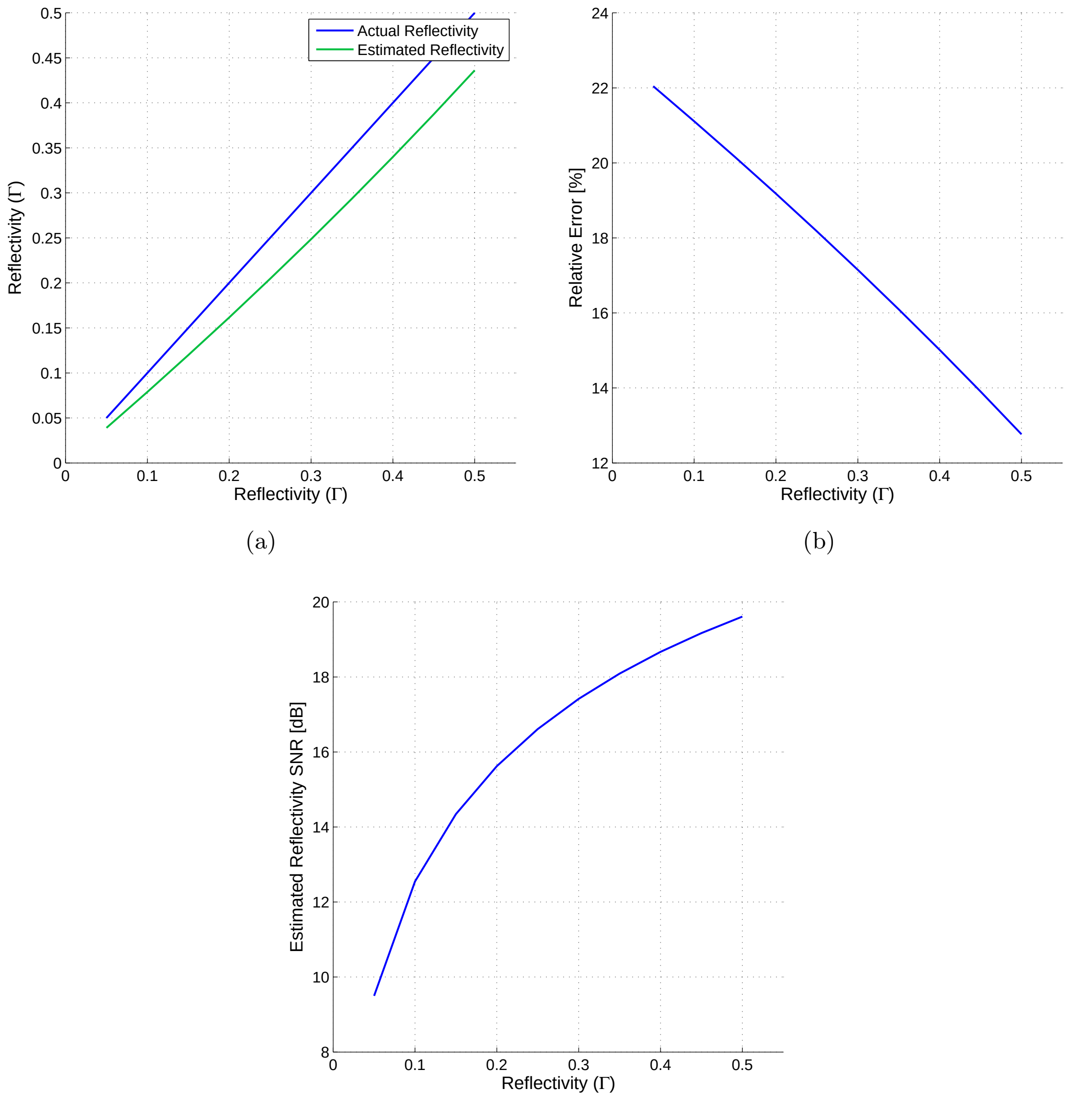

(a)

(b)

(c)

Figure 5.2: Noise effects in the estimation of reflectivity: (a) Actual (blue) and estimated (green) reflectivity values; (b) Relative error of the estimated reflectivity with respect to the actual one; (c) Estimated reflectivity mean value over standard deviation (SNR of the reflectivity measurement)

where μ_d^2 and μ_r^2 are the direct and reflected signal mean power, σ_d^2 and σ_r^2 are the direct and reflected signal variance, calculated as the direct and reflected noise power, and σ_{dr} is the covariance of both signals. Considering that the direct and reflected signals are only affected by thermal noise, the latter can be neglected given the uncorrelated nature of thermal noise. For typical mean power and variance values of the direct and reflected signals, the noise in the reflectivity measurements can be estimated. In Fig. 5.2(c) the measured mean over standard deviation of the reflectivity is depicted. This ratio can be considered as the SNR of the estimated apparent reflectivity Γ'. As can be readily seen, the SNR increases with reflectivity, which implies a more accurate measurement. For a receiver with higher noise temperature this ratio is expected to decrease significantly, which will turn into a poorer estimation of soil geo-physical parameters.

5.4 Antenna Issues

As in most remote sensing applications, having an accurate knowledge of the antenna radiation properties is of main importance. This is particularly true for polarimetric systems, as small variations in the antenna characteristics can have an important impact in the final measurements. Apart from variations in the radiation pattern of the antennas, aspects such as the antenna polarization mismatch, the cross-polarization isolation, and the orientation of the antenna should be considered. Those are discussed next.

5.4.1 Polarization Loss Factor on the Direct and Reflected Channels

In general, the polarization of an incident wave is not coincident with the receiving antenna polarization plane, mainly due to the fact that most of the times the antenna plane is not orthogonal to the electromagnetic wave propagation direction. In other words, the polarization vectors of the incident wave and the receiving antenna are not aligned. Due to the reciprocity theorem of antennas, the same applies for a transmitting antenna, thus, the problem should be considered both in transmission and reception. For linear polarization, the orientation of the antenna and the incident field needs also to be taken into account. For circular polarized antennas, this requirement can be relaxed, however, there is a polarization loss dependent on the incidence angle of the incoming wave. This is commonly known as polarization mismatch or polarization loss factor, which can be described in terms of the incident wave and antenna polarization vectors. Following [Balanis, 2005, chapter 2], the incident electric field can be written as:

$$\mathbf{E}_i = \hat{\boldsymbol{\rho}}_w E_i \, , \tag{5.28}$$

where $\hat{\boldsymbol{\rho}}_w$ is the polarization unit vector of the wave. Likewise, the polarization of the receiving antenna can be described as:

$$\mathbf{E}_a = \hat{\boldsymbol{\rho}}_a E_a \, , \tag{5.29}$$

with $\hat{\boldsymbol{\rho}}_a$ is the polarization vector of the antenna. The Polarization Loss Factor (PLF), is calculated as:

$$\mathrm{PLF} = |\hat{\boldsymbol{\rho}}_w \cdot \hat{\boldsymbol{\rho}}_a|^2 \, . \tag{5.30}$$

The power collected by a receiving antenna whose polarization is not aligned with the polarization of the incident wave can then be written as [Balanis, 2005]:

$$P_r = P_{\text{inc}} \frac{\lambda^2 G_r(\theta, \phi)}{4\pi} |\hat{\boldsymbol{\rho}}_w \cdot \hat{\boldsymbol{\rho}}_a|^2 \,, \tag{5.31}$$

where P_{inc} is the power of the incident wave, and $G_r(\theta, \phi)$ is the direction dependent gain of the antenna. The effect of the polarization loss factor for both direct and reflected channels is considered next.

According to IEEE standards, the polarization vectors of the RHCP and LHCP antennas, can be written as:

$$\begin{aligned} \hat{\boldsymbol{\rho}}_{a,r} &= \frac{\hat{\mathbf{a}}_{\theta_a} - j\hat{\mathbf{a}}_{\phi_a}}{\sqrt{2}} \\ \hat{\boldsymbol{\rho}}_{a,l} &= \frac{\hat{\mathbf{a}}_{\theta_a} + j\hat{\mathbf{a}}_{\phi_a}}{\sqrt{2}} \,. \end{aligned} \tag{5.32}$$

For simplicity, it will be assumed here that the transmitted GNSS signals are purely RHCP at the satellite's antenna boresight. Thus the polarization vector of the transmitted wave can be expressed as:

$$\hat{\boldsymbol{\rho}}_{w,d} = \frac{\hat{\mathbf{a}}_{\theta_w} + j\hat{\mathbf{a}}_{\phi_w}}{\sqrt{2}} \,, \tag{5.33}$$

Considering for simplicity that in the case of circular polarizations $\hat{\mathbf{a}}_{\phi_w}$ and $\hat{\mathbf{a}}_{\phi_a}$ are the same, the polarization mismatch yields

$$\text{PLF}_{t,R} = |\hat{\boldsymbol{\rho}}_{w,d} \cdot \hat{\boldsymbol{\rho}}_{a,r}|^2 = \frac{(1+\cos\psi)^2}{4} \,, \tag{5.34}$$

where ψ is the angle subtended between the antenna boresight direction (always considered to be pointing towards the center of the Earth) and the receiver's location on the surface, see diagram in Fig. 5.3. The value of ψ can be calculated by means of the following simple trigonometric equation, derived using the sine rule:

$$\psi = \arcsin\left(\frac{R_E \, \sin(\theta)}{R_E + h}\right) \,, \tag{5.35}$$

where R_E is the radius of the Earth, h is the height of the transmitting satellite with respect to the surface, and θ is the incidence angle. This is shown as a function of the incidence angle on Fig. 5.4. Due to the high altitude of the orbiting GNSS satellites, the maximum value of ψ, corresponding to a grazing incidence scenario, yields 14°, thus, the effect in the polarization loss factor on the transmitter's side is much less important than on the receiver's side.

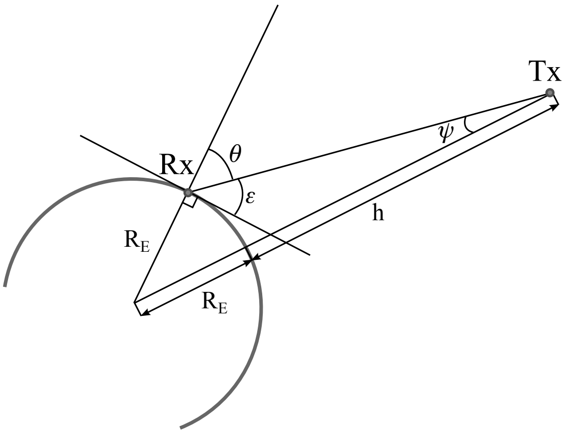

Figure 5.3: Tx and Rx geometry.

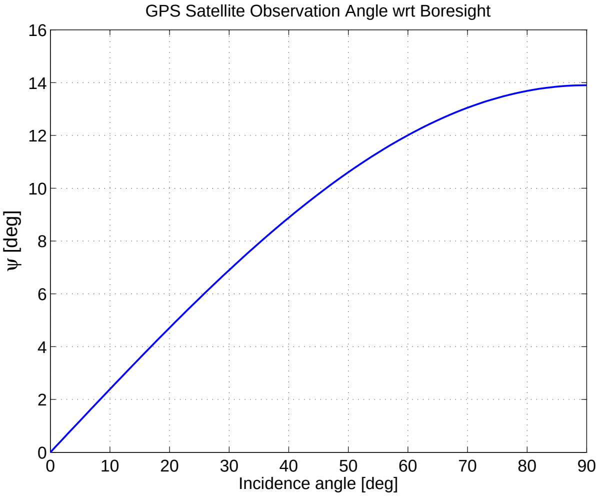

Figure 5.4: Observation angle from a GPS satellite with respect to the antenna boresight as a function of the incidence angle on the local reference plane on the Earth's surface.

In order to calculate the effect of the polarization loss factor on the received the geometry of the direct and reflected channels can be depicted as shown in Fig. 5.5. For the direct signal, Fig. 5.5(a), the incident wave can be assumed as purely RHCP in the direction of propagation, and if the antenna is parallel to the local mean surface, the polarization loss factor can be expressed in terms of the satellite's incidence angle, θ, as in [Balanis, 2005],

$$\mathrm{PLF}_{d,r} = |\hat{\boldsymbol{\rho}}_{w,d} \cdot \hat{\boldsymbol{\rho}}_{a,R}|^2 = \frac{(1+\cos\theta)^2}{4}\,. \tag{5.36}$$

In the case of the reflected signal, the geometry can be represented as in Fig. 5.5(b). It is considered here that the reflected wave is composed of a vertical and horizontal components driven by the Fresnel reflection coefficients in each of the linear polarizations, $\mathcal{R}_h$ and $\mathcal{R}_v$. The polarization vector of the reflected wave can then be written as:

$$\hat{\boldsymbol{\rho}}_{w,r} = \frac{\mathcal{R}_v \hat{\mathbf{a}}_{\theta_w} + j\mathcal{R}_h \hat{\mathbf{a}}_{\phi_w}}{\sqrt{2(\mathcal{R}_v^2 + \mathcal{R}_h^2)}}\,. \tag{5.37}$$

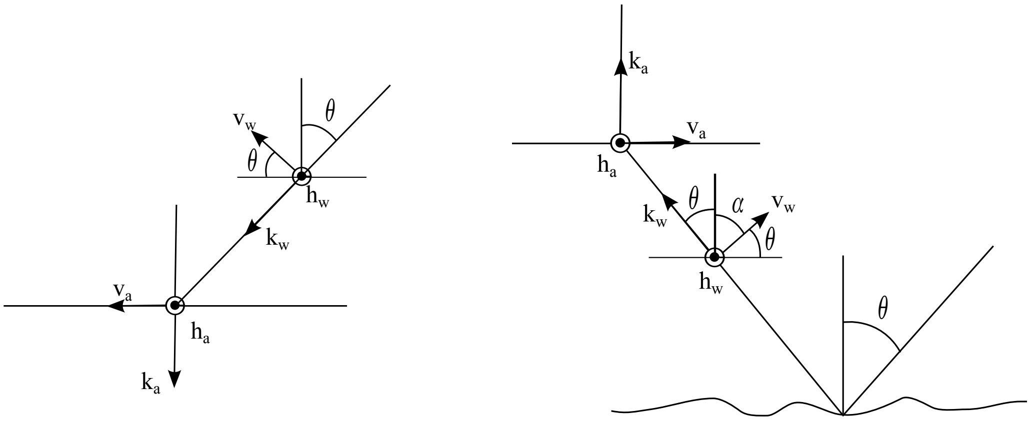

(a) (b)

Figure 5.5: Incident wave and antenna unitary vectors for the case of the direct (a) and reflected signals(b).

For the LHC polarization, and considering as in the previous case that $\hat{\mathbf{a}}_{\phi_w} = \hat{\mathbf{a}}_{\phi_a}$,

$$\mathrm{PLF}_{r,l} = \left|\hat{\boldsymbol{\rho}}_{w,r} \cdot \hat{\boldsymbol{\rho}}_{a,l}\right|^2 = \frac{\left|(\mathcal{R}_v \hat{\mathbf{a}}_{\theta_w} + j\mathcal{R}_h \hat{\mathbf{a}}_{\phi_w}) \cdot (\hat{\mathbf{a}}_{\theta_a} + j\hat{\mathbf{a}}_{\phi_a})\right|^2}{4\left(\mathcal{R}_h^2 + \mathcal{R}_v^2\right)} = \frac{\left(\mathcal{R}_h - \mathcal{R}_v \cos\theta\right)^2}{4\left(\mathcal{R}_h^2 + \mathcal{R}_v^2\right)}, \tag{5.38}$$

and for the RHCP case,

$$\mathrm{PLF}_{r,r} = \left|\hat{\boldsymbol{\rho}}_{w,r} \cdot \hat{\boldsymbol{\rho}}_{a,r}\right|^2 = \frac{\left|(\mathcal{R}_v \hat{\mathbf{a}}_{\theta_w} + j\mathcal{R}_h \hat{\mathbf{a}}_{\phi_w}) \cdot (\hat{\mathbf{a}}_{\theta_a} - j\hat{\mathbf{a}}_{\phi_a})\right|^2}{4\left(\mathcal{R}_h^2 + \mathcal{R}_v^2\right)} = \frac{\left(\mathcal{R}_h + \mathcal{R}_v \cos\theta\right)^2}{4\left(\mathcal{R}_h^2 + \mathcal{R}_v^2\right)}. \tag{5.39}$$

The polarization loss factor for both direct and reflected antennas have a major impact on the determination of Γ'_{pq}, the apparent power reflectivity measurements, and therefore need to be taken into account in order to relate the scattering models with the actual GNSS-R measurements.

5.4.2 Antenna Cross-Polarization

Another important parameter to account for when performing polarimetric measurements is the receiving antenna cross-polarization isolation. When referring to the polarization of antenna, it is said that an antenna is right hand or left hand circularly polarized depending on its nominal polarization, however a certain cross-talk exists between both channels.

The fraction of power received in the orthogonal polarization with respect to the antenna's nominal one is known as cross-polarization isolation. For circularly polarized antennas it is also common to provide this value in terms of the axial ratio, defined as the ratio of the orthogonal components of the antenna's electric. The following equation can be used to link both concepts:

$$\alpha = \left(\frac{r-1}{r+1}\right), \tag{5.40}$$

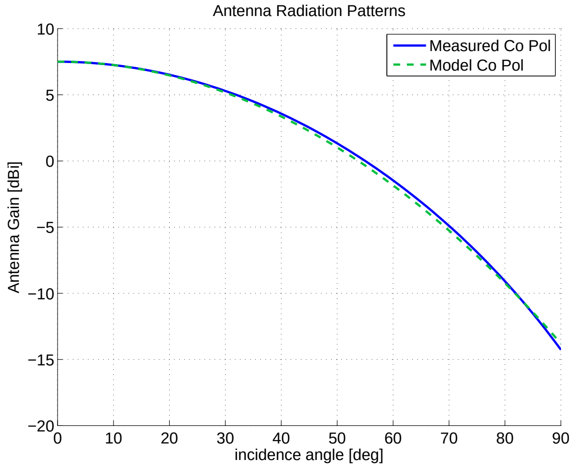

Figure 5.6: Antenna pattern for the co-polarized signal; in solid blue measured pattern, in dashed green the antenna model.

where α denotes the cross-polarization isolation and r the axial ratio. Assuming that α is less than one and possibly small, as shown in the figure, the collected power at both circular polarizations can be written as:

$$\begin{aligned} P_r &= P_{\mathrm{inc},r}\cdot(1-\alpha)+P_{\mathrm{inc},l}\cdot\alpha \\ &\qquad\qquad\qquad\qquad\quad , \\ P_l &= P_{\mathrm{inc},l}\cdot(1-\alpha)+P_{\mathrm{inc},r}\cdot\alpha\,, \end{aligned} \tag{5.41}$$

with $P_{\mathrm{inc},r}$ and $P_{\mathrm{inc},l}$ the incident power on the antenna at RHC or LHC polarizations, respectively.

5.4.3 Antenna Pattern Simulation

A Gaussian pattern was used to account for the antenna directivity in the main beam. The antenna directivity and beamwidth specified by the antenna manufacturer were used for the antenna model, which accounts also for the polarization loss factor specified in the previous section. The measured antenna radiation pattern provided by the antenna manufacturer is represented with the co-polarization antenna model in Fig. 5.6. As can be observed, both antenna model and measured radiation pattern have an excellent correspondence up to incidence angles of 90°. This antenna model was finally used to relate the GNSS-R observations with the geophysical parameters.

5.5 A Simplified Scattering Model for GNSS-R Soil Reflectivity Measurements

The current section presents a simplified model for GNSS-R reflectivity measurements, that allows to compare in a straightforward way the experimental results with what it is expected from theory. This toy model includes a simplified bistatic scattering model for moderately rough surfaces, and accounts for the most important instrumental effects that have an impact on the reflectivity measurements, mainly due to the antenna issues that have been presented in the previous section and mismatches in the signal to noise ratio of the direct and reflected receiving channels.

5.5.1 Scattering Properties of Moderately Rough Surfaces

As has been shown in Chapter 3, in general, a scattering surface can be considered as a set of multiple local scattering planes with different orientations. The final scattered wave would be the random combination of all the reflections coming from the individual scatterers. In a global sense, the scattering surface presents cross-polarization reflection coefficients which are non-equal to zero. This incurs in a depolarization of the incident wave [Ulaby et al., 1986b]. In addition, an extra depolarization of the signals is produced due to the finiteness of the dielectric constant of most scattering surfaces.

The conditions presented above could be alleviated in order to formulate a simplified scattering model. Previous investigations [de Roo and Ulaby, 1994] have shown that forward scattering from rough random surfaces, is a combination of a coherent and an in-coherent components, e.g., the Physical Optics model. In the case of moderately rough surfaces, such as most soil surfaces at L band, the coherent component predominates over the incoherent component. Because of that, it can be assumed to a first extent that the soil reflectivity is mainly driven by the Fresnel reflection coefficients for different soil moisture contents and incidence angles.

The second assumption relies in the fact that the coherent scattering of the incident wave is mainly produced in the vicinity of the specular point. It can therefore be considered that the out-of-plane scattering contributions could be neglected. In this situation, the local scattering geometry shown in Fig. 5.7 applies as a general case, and the depolarization only comes from the dielectric nature of the soil. If the soil was a perfect conducting surface, the coefficients with sub-indexes ll and rr would equal zero, hence assuming a pure right hand circularly polarized incident wave the reflected signal would be a pure LHCP wave. However, since the soil has a finite and complex dielectric constant the reflected signal contains components in both LHCP and RHCP.

The Fresnel reflection coefficients for the circular polarizations are expressed as linear combinations of the vertical and horizontal reflection coefficients, as shown in Eqn. (4.3). The power reflectivity, represented by Γ_{pq}, can be calculated as the squared absolute value of the Fresnel reflection coefficients for a smooth surface, R_{pq}. However, as the surface is not strictly smooth, the coherent nature of the reflected power is decreased, and some power is scattered in directions other than specular. For a slightly rough surface, and considering that the roughness can be modeled as a bidimensional Gaussian distribution, the effect on the final reflectivity can be described an exponentially decreasing factor with the surface height standard deviation as discussed in section 4.2,

$$\Gamma_{pq} = |\mathcal{R}_{pq}(\theta)|^2 \, e^{-4k^2\sigma_z^2\cos^2\theta}, \tag{5.42}$$

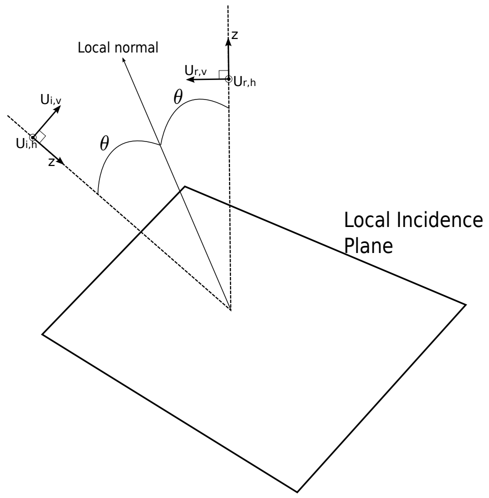

Figure 5.7: Local incidence plane geometry.

where k is the wavenumber, and σ_z represents the surface height standard deviation. Combining this simplified scattering model with the description of the antenna issues provided in the previous section, the power collected by the up-looking and down-looking receiving antennas can be readily calculated in order to produce the final measured reflectivity model.

5.5.2 Vegetation Effect on the Coherent Scattering Component

The effect of vegetation on GNSS reflected signals can be represented as an additional attenuation factor on the received signal power, [Ulaby et al., 1986b; Kerr et al., 2012]. This attenuation factor, γ, can be expressed in terms of the vegetation nadir optical depth, τ_0:

$$\gamma = \exp(-\,2 \cdot \tau_0/\cos\theta)\,, \tag{5.43}$$

where θ is the incidence angle. The 2 factor in the previous equation accounts for the two way attenuation of the GNSS signals along the incident and reflected paths through the vegetation layer.

For most crops and low vegetation τ_0 can be written as a function of the PWC, in [kg/m^2]. The following linear relationship is commonly provided in the literature, [Jackson and Schmugge, 1991]:

$$\tau_0 = b \,\cdot\, \mathrm{PWC}\,. \tag{5.44}$$

The parameter b is a function of the canopy type/structure, polarization, and wavelength. Previous studies showed that at 1.4 GHz, a value of b within the range 0.12 ± 0.03 was found to be representative for most agricultural crops and low vegetation [Jackson and Schmugge, 1991]. However, in the case of sunflowers, a lower value of b is needed to match the predicted attenuation by the scattering models presented in section 4.3.2. This could be due to the vegetation structure of this particular crop. For $b = 0.06$, PWC= 7 kg/m^2, and an incidence angle of 30°, the vegetation transmissivity yields 0.38, which corresponds to -4.21 dB, an attenuation very similar to the one shown in Fig. 4.11 with respect to a bare soil scenario.

5.5.3 Modeled GNSS-R Estimated Reflectivity

The different effects discussed in the previous sections have an important impact on the final measured direct and reflected signal power, thus in the measured reflectivity by a GNSS-R receiver. In order to be able to represent all these effects in a compact and clear way, they can be expressed in matrix form, using the transition matrices between linear and circular polarization bases, $\mathcal{T}_{hv\rightarrow rl}$ and $\mathcal{T}_{rl\rightarrow hv}$, as shown in Eqn. (4.2) and (4.3). Considering that the emitted GNSS signals are mostly RHCP, in the circular basis it can be written that:

$$P_t = \begin{bmatrix} 1-\beta \\ \beta \end{bmatrix} , \tag{5.45}$$

where β represents the cross-polarization isolation of the GNSS satellites transmitting antennas. The received direct signal power in right and left polarizations can be expressed in matrix form as:

$$\begin{bmatrix} P_{d,r} \\ P_{d,l} \end{bmatrix} = K_d \cdot \mathcal{X}_r \cdot \left(\mathcal{T}_{hv\rightarrow rl} \cdot \Pi_r \cdot \Pi_t \cdot \mathcal{T}_{rl\rightarrow hv}\right)^2 \cdot \mathcal{X}_t \cdot P_t \, , \tag{5.46}$$

where $\mathcal{X}_r$ is the receiver cross-polarization isolation matrix, and Π_r and Π_t represent the polarization loss factor on both receiver and transmitter sides, as expressed in Eqn. (5.38) and (5.39). In the case of the reflected signal, the same equation applies including the polarization dependent Fresnel reflection coefficients, $\mathcal{R}_{pq}$:

$$\begin{bmatrix} P_{d,r} \\ P_{d,l} \end{bmatrix} = K_r \cdot \mathcal{X}_r \cdot \left(\mathcal{T}_{hv\rightarrow rl} \cdot \Pi_r \cdot \mathcal{R}_{pq} \cdot \Pi_t \cdot \mathcal{T}_{rl\rightarrow hv}\right)^2 \cdot \mathcal{X}_t \cdot P_t \, . \tag{5.47}$$

The final expression for the received direct power can be written as:

$$\begin{aligned} \begin{bmatrix} P_{d,r} \\ P_{d,l} \end{bmatrix} = K_d \cdot \begin{bmatrix} 1-\alpha & 0 \\ 0 & \alpha \end{bmatrix} \cdot \Bigg(\frac{1}{\sqrt{2}} \begin{bmatrix} 1 & 1 \\ i & -i \end{bmatrix} \frac{1}{2} \begin{bmatrix} 1 & 0 \\ 0 & \cos\theta \end{bmatrix} \cdot \\ \cdot \frac{1}{2} \begin{bmatrix} 1 & 0 \\ 0 & \cos\psi \end{bmatrix} \cdot \frac{1}{\sqrt{2}} \begin{bmatrix} 1 & -i \\ 1 & i \end{bmatrix} \Bigg)^2 \cdot \begin{bmatrix} 1-\beta \\ \beta \end{bmatrix} , \end{aligned} \tag{5.48}$$

and for the reflected signal,

$$\begin{aligned} \begin{bmatrix} P_{r,l} \\ P_{r,r} \end{bmatrix} = K_r \cdot \begin{bmatrix} 1-\alpha & 0 \\ 0 & \alpha \end{bmatrix} \cdot \Bigg(\frac{1}{\sqrt{2}} \begin{bmatrix} 1 & 1 \\ i & -i \end{bmatrix} \cdot \frac{1}{2\sqrt{\mathcal{R}_h^2 + \mathcal{R}_v^2}} \begin{bmatrix} 1 & 0 \\ 0 & \cos\theta \end{bmatrix} \cdot \\ \cdot \begin{bmatrix} \mathcal{R}_h & 0 \\ 0 & \mathcal{R}_v \end{bmatrix} \cdot \frac{1}{2} \begin{bmatrix} 1 & 0 \\ 0 & \cos\psi \end{bmatrix} \cdot \frac{1}{\sqrt{2}} \begin{bmatrix} 1 & -i \\ 1 & i \end{bmatrix} \Bigg)^2 \cdot \begin{bmatrix} 1-\beta \\ \beta \end{bmatrix} , \end{aligned} \tag{5.49}$$

where $K_{d,r}$ represents a variable accounting for the antenna gain and the free-space propagation losses for the direct and reflected channels:

$$K_{d,r} = \frac{\lambda^2\, G(\theta,\phi)}{4\,\pi\, L_{d,r}}\,. \tag{5.50}$$

Taking into consideration the derivation of the mean waveform amplitude provided in section 5.2, the apparent reflectivity measurements at both polarizations, Γ'_{rl} and Γ'_{rr}, can be finally written as:

$$\Gamma'_{rl} = \rho\,\frac{P_{r,l}}{P_{d,r}} \qquad , \qquad \Gamma'_{rr} = \rho\,\frac{P_{r,r}}{P_{d,r}}\,. \tag{5.51}$$

Recall that ρ was defined as the ratio of the direct and reflected noise powers. Considering this value as a constant parameter, the influence of soil moisture and surface roughness in the final measured reflectivity can be estimated by means of the previous equations. For low altitude receivers, it can be assumed that the propagation losses of the coherent scattering component are the same for both direct and reflected signals; likewise, the receiving directions of the direct and reflected signals can be considered to be the same, thus, if both up-looking and down-looking antennas have a similar radiation pattern the ratio of K_r over K_d cancel out when calculating the rl and rr reflection coefficients.

5.5.4 Simulations of the Apparent Power Reflection Coefficients

Simulations were performed in order to determine the effect of both soil moisture and soil roughness conditions in the final apparent power reflection coefficients at both polarizations. The transmitter and receiver cross-polarization isolation parameters were set as constant parameters with standard values; i.e. for the GNSS transmitting satellite the cross-polarization was set to 24 dB, as this value corresponds to the standard 1.2 dB Axial Ratio (AR) [GPSW, 2010]. For the receiving antenna, the cross-polarization isolation was initially set to 25 dB.

For a given standard soil roughness, e.g. 1 cm, the reflectivity was calculated for 3 different soil moisture conditions, represented by different ϵ_r values, as specified also in Table 4.1. The simulation results of Γ'_{rl} and Γ'_{rr} are shown in Fig. 5.8. As can be observed, Γ'_{rl} shows a sensitivity over 6 dB between the dry and wet soil moisture cases for incidence angles up to 45 deg. Γ'_{rr} presents also a noticeable sensitivity with respect to soil moisture, but has very low values, specially for dry soil conditions. Γ'_{rl} is over 17.5 dB higher than its cross-polarized counterpart for low incidence angles. Nonetheless, it was determined that for near grazing incidences, Γ'_{rr} increases significantly, and surpasses Γ'_{rl}, especially in situations of low soil moisture content with higher depolarization due to lower dielectric constant. This can also be seen in 5.8(b), where the ratio of the co- and cross- polarization reflection coefficients is shown. This observable shows a sensitivity to soil moisture of 3.5 dB for an incidence angle of 40 deg, however, for low incidence angles or grazing incidences, the sensitivity to soil moisture is not appreciable.

This ratio is affected by the cross-polarization isolation of the receiving antennas. The higher this value is, the more sensitive the measurements would be to changes

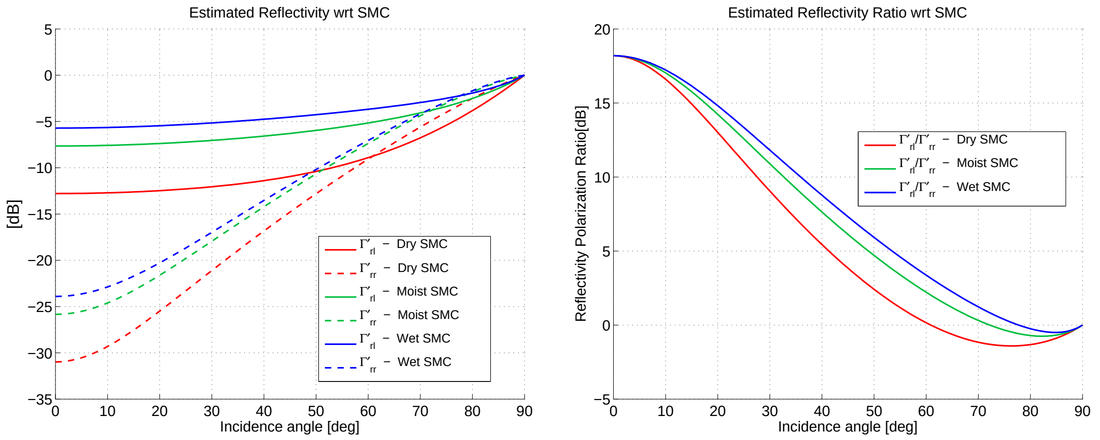

(a) (b)

Figure 5.8: Simulated soil reflection coefficients for three different soil moisture conditions, see Table 4.1, and constant surface roughness, $\sigma_z = 1$ cm. 25 dB Antenna Cross-Polarization Isolation. (a) Γ'_{rl} (solid lines) and Γ'_{rr} (dashed lines) apparent reflectivity. (b) Soil reflection coefficients ratio, Γ'_{rl} over Γ'_{rr}.

in the soil dielectric properties, as it will be possible to better discriminate variations occurring independently in both reflection coefficients. In other words, if antennas with moderate cross-polarization rejection capabilities are considered, the estimation of Γ'_{rl} and Γ'_{rr} get "contaminated" by the presence of LHCP reflected signal on the RHCP down-looking antenna and vice versa. A simulation was performed selecting antennas with a cross-polarization isolation of 15 dB; the difference between the measured Γ'_{rl} and Γ'_{rr} power reflection coefficients is reduced to 12.3 dB at zero degree incidence angle, and the observed variability of the reflection coefficients ratio between dry and wet soil conditions decreases to 2.5 dB. This can be observed in the panels of Fig. 5.9. Therefore, this parameter should be carefully analyzed when choosing the antennas to perform polarimetric observations.

The effect of soil roughness was also considered; the reflection coefficients were calculated for a constant soil moisture, represented by a fixed ϵ_r set to 9.5 - 1.8i, and three different roughness conditions in comparison with the typical wavelength of GNSS signals. The surface height standard deviation, σ_z, was set to 1 cm for a smooth soil, 2 cm for an intermediate rough soil, and to 3 cm for a rough soil. The results are shown in Fig. 5.10. As can be seen, there is a remarkable decrease in both Γ'_{rl} and Γ'_{rr} due to the effect of increasing roughness. For instance, a variation of -15.1 dB can be observed from the smoother to the rougher condition, see Fig. 5.10. However, if the ratio between reflection coefficients is considered, Fig. 5.10(b), there is not a noticeable difference between the rough and smooth surface conditions, suggesting that this parameter could be an optimum observable for soil moisture estimation, as it is scarcely sensitive to soil roughness variations.

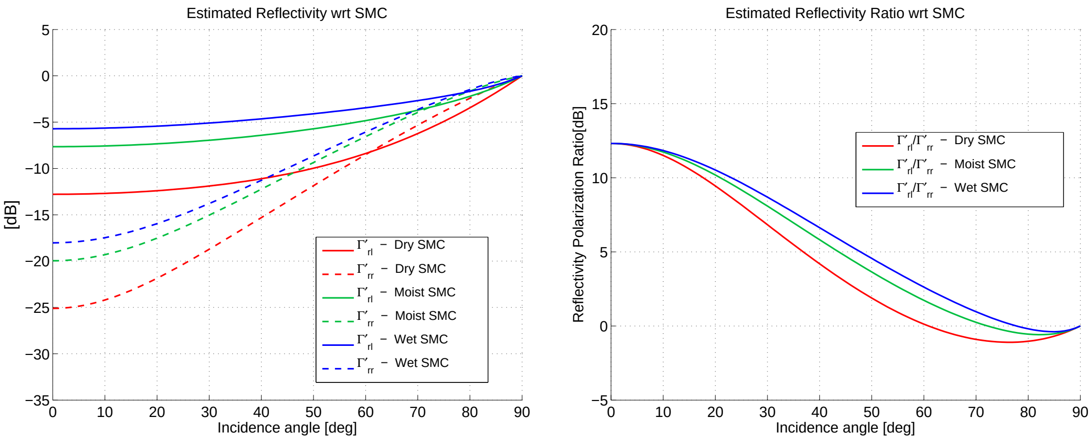

(a) (b)

Figure 5.9: Simulated soil reflection coefficients for three different soil moisture conditions, see Table 4.1, constant surface roughness, $\sigma_z = 1$ cm. 15 dB Antenna Cross-Polarization Isolation. (a) Γ'_{rl} (solid lines) and Γ'_{rr} (dashed lines) apparent reflectivity. (b) Soil reflection coefficients ratio, Γ'_{rl} over Γ'_{rr}.

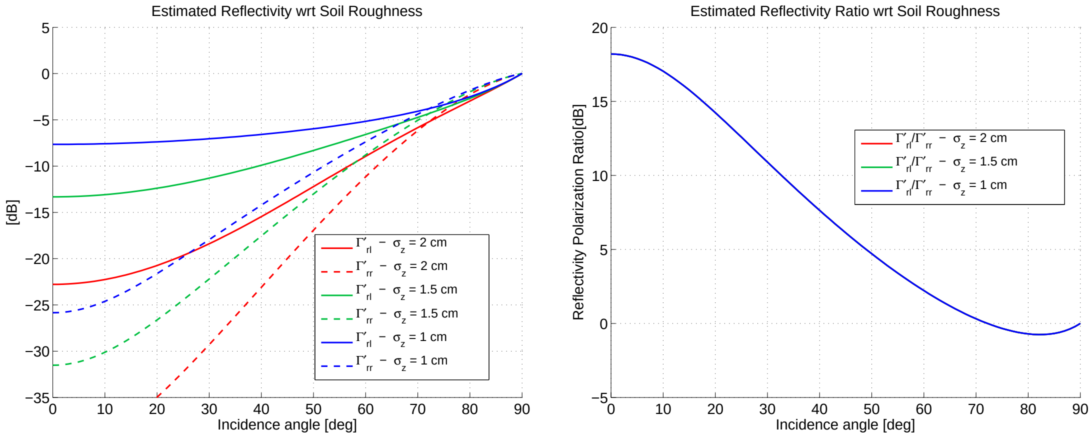

(a) (b)

Figure 5.10: Simulated soil reflection coefficients for three different soil roughness conditions and constant soil moisture; $\epsilon_r = 9.5 - 1.8i$. (a) Γ'_{rl} (solid lines) and Γ'_{rr} (dashed lines) apparent reflectivity. (b) Soil reflection coefficients ratio, Γ'_{rl} over Γ'_{rr}.

5.6 Summary

A method to retrieve the soil reflectivity from the direct and reflected complex waveforms has been discussed in this chapter. The analytical derivation of the complex waveforms amplitude has been presented. By performing the coherent averaging of the ICF, it was demonstrated that the ground reflectivity can be measured, weighted by a factor that equals the ratio of the direct over the reflected noise powers. The impact of the different noise sources on the reflectivity measurement was also considered. It was observed that the effect of noise is higher when the soil reflectivity is lower. The impact of the antenna characteristics was also analyzed and the effect of the antennas polarization loss factor was derived. The latter is particularly important when doing polarimetric measurements. Finally, a simplified scattering model that accounts for the previously mentioned effects was proposed in order to relate in a straightforward way GNSS-R observations with soil bio-geophysical parameters.

Part III

Experimental Work

Chapter 6

Design and Development of a GNSS Reflectometer

A GNSS reflectometer was designed and developed to study the properties of the scattered GNSS signals off land surfaces. This instrument was built within the framework of the SAM project. Several upgrades in the design were implemented as the research work progressed, within the LEiMON and GRASS projects. The next sections describe the main characteristics of this instrument.

6.1 The SAM Sensor

The SAM sensor was designed based on Oceanpal, an instrument designed and developed at Starlab Barcelona for coastal GNSS-R applications. As can be seen from the instrument block diagram shown on Fig. 6.1, two logical separated sections can be distinguished in the instrument; those are a Radio Frequency (RF) section, and a Digital Signal Processing section. The former comprises the GPS antennas, calibration chain, and GPS front-ends, that include also the Analog to Digital Converter (ADC). The digitized signals are then parallelized and processed in the SAM GNSS-R software receiver section.

Unlike conventional GNSS-R instruments, the SAM sensor comprises an up-looking RHCP antenna, and two down-looking RHCP and LHCP GPS antennas, that enables the reception of both polarization components in the reflected signal. An RF switch selects among the reflected RHCP and LHCP antennas, which are processed in a sequential way. Passive GPS antennas were selected in order to avoid gain mismatches between the direct and reflected channels.

The calibration chain is another main aspect of the SAM sensor; since the main observable for land applications is the SNR ratio of the direct and reflected GNSS signals, it is of main importance to have a precise relative calibration between the two receiving channels. In the initial SAM sensor design, two operation modes were defined: measurement and calibration mode. In measurement mode, the signals from the up-looking and down-looking antennas were directed through two transfer switches to the Low Noise Amplifiers (LNA), and then to the GPS front-end, as shown in Fig. 6.2(a). The transfer

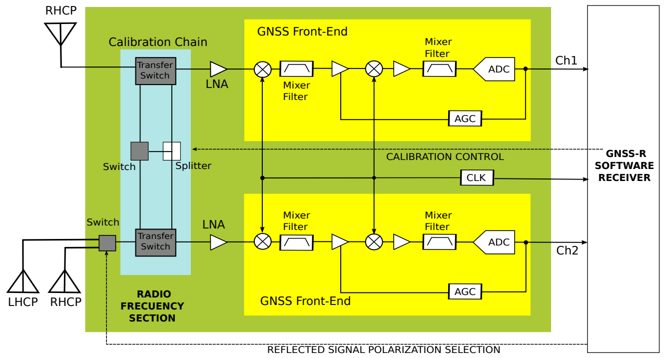

Figure 6.1: Block diagram of the SAM sensor receiving chain.

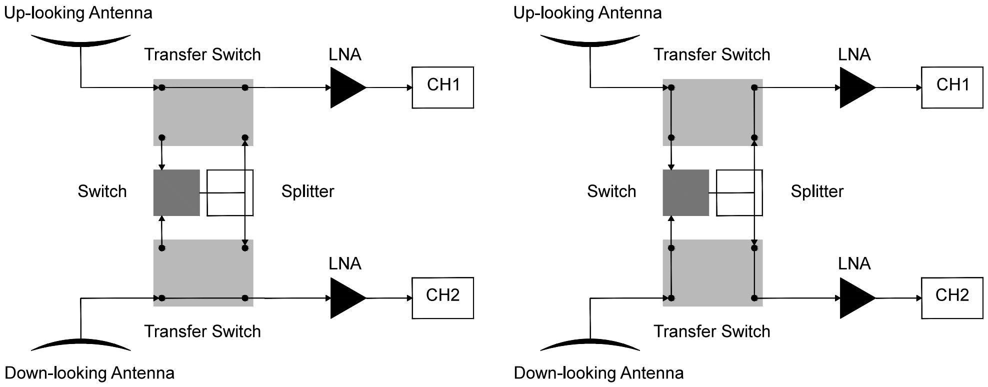

(a) (b)

Figure 6.2: Initial design of the SAM Calibration Chain: (a) Measurement Mode, (b) Calibration Mode.

switch is an RF mechanical component with very low insertion losses, thus a small fraction of SNR is lost in these components. In calibration mode, Fig. 6.2(b), the transfer switches directed the incoming signal to a power splitter, where the signal was equally distributed so that the same power was available at the input of both receiving channels. An additional switch allowed to select among the direct or reflected signals to perform the calibration. Any differences in the observed SNR will be caused by a mismatch in the receiving chain, which will be accounted for while performing the apparent reflectivity estimation. The noise figure of the receiving chain in measurement mode was estimated to be of 2.88 dB, accounting for cable losses, transfer switch losses, and LNA noise figure.

After the pre-amplification of the RF signal, the down-conversion to intermediate frequency and sampling of the signal is done in two commercial MAXIM GPS front-ends. A common high stability clock drives the operation of both front-ends. The RF signal at L1 is down-converted in the receiver to a first intermediate frequency of 20.46 MHz. After that, the signal is down-sampled at 16.366 MHz to a final IF of 4.092 MHz. The sampling of the signals is done with 1 bit quantization. Both direct and reflected channel bit streams are then passed to a CPLD, which parallelizes the bits and sends them to an acquisition board in order to store these raw data in a computer's hard drive.

The raw data is finally processed by the SAM software receiver, which performs the acquisition and tracking of the GPS signals. The receiving chain is based on a pair of twin GNSS receivers working in a master-slave configuration. The master GPS processor detects and tracks the GPS signals available in the direct channel while the slave GPS processor blindly despreads the signals in the reflected channel. The result of this processing is a set of direct and reflected complex waveforms, which are the basic observables of the GNSS-R sensors in order to produce higher order products.

6.2 Calibration Chain Upgrade

The original SAM calibration method was based on a simultaneous measurement of the signal from the up-looking antenna which was equally split to feed channel 1 and channel 2. With these measurements, it was possible to estimate the SNR difference between both receiving channels. After this calibration phase, two measurement phases would follow, one with Direct and LHCP reflected, and one with Direct and RHCP reflected, as illustrated in Fig. 6.3(a). This operation method implies that one third of the total acquisition time is used only for calibration purposes. As the signal of the up-looking antenna is directed to both channels no scientific information can be extracted from these data. In addition, the presence of a power splitter previous to the LNA implies an increase of 3dB in the overall noise factor of the receiving chain during the calibration stage.

During the LEiMON project a significant upgrade was implemented on the instrument's calibration chain. The idea behind the new calibration approach is that over short time periods (from 15 seconds up to 5 minutes) the received GPS signal power can be assumed to be constant; as the transit time of navigation satellites is very long, and changes on the active components of the receiver chain due to thermal variations are negligible in short time scales, this assumption is valid for our calibration purposes. The relative calibration of the direct and reflected receiving channels can thus be done by switching the direct signal received on the up-looking antenna between channels 1 and 2. This calibration method can be implemented with a single transfer switch, as depicted on the panels of Fig. 6.4. The new calibration method allowed to reduce the complexity of the reception circuit. At the same time, as the power splitter was removed from the system, the noise figure of the calibration chain was reduced to 1.58 dB, thus improving the overall system SNR.

The new calibration scheme is illustrated in Fig. 6.3(b). As can be observed, four measurement stages are necessary in order to receive the direct signal with both channels and the two polarizations of the reflected signal. Using the 4 measurement stages 5 potential calibration points could be obtained during the whole measurement cycle, however only 3 were finally consider as the calibration is only performed with the direct signal. One of the most interesting characteristics of this calibration method is that as there is not a dedicated calibration stage all the retrieved data can be used to obtain scientific measurements. An image of the antenna rig and the integrated calibration chain are provided in Fig. 6.5(a) and Fig. 6.5(b), respectively.

Extensive tests were carried out in order to determine the performance of the calibration chain and the overall stability of the instrument. Figure 6.6 shows the SNR for each of the data acquisition stages. The SNR values were calculated as the mean of the power waveform peak, over the standard deviation of the peaks. The continuous line accounts for the mean of all four stages, which, as it is observed, is placed most of the

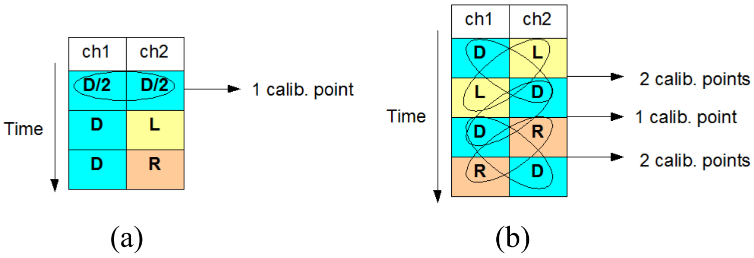

Figure 6.3: (a) Initial calibration scheme for the SAM instrument; the calibration was performed in the first stage of the acquisition with the direct signal in both receiving channels. (b) Calibration scheme for the upgraded calibration chain. The direct signal is alternated between the two receiving channels in successive stages.

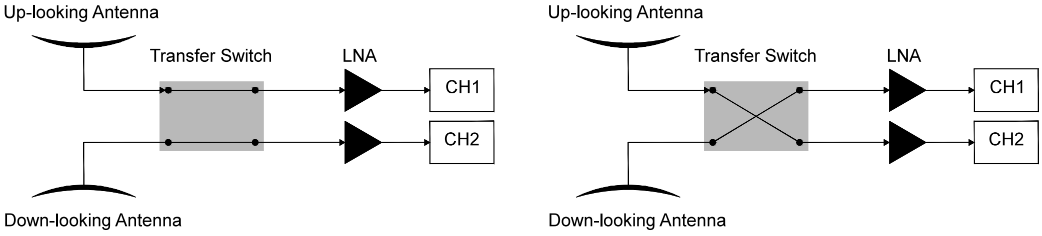

(a) (b)

Figure 6.4: Upgraded calibration chain diagram in the two stages of the acquisition.

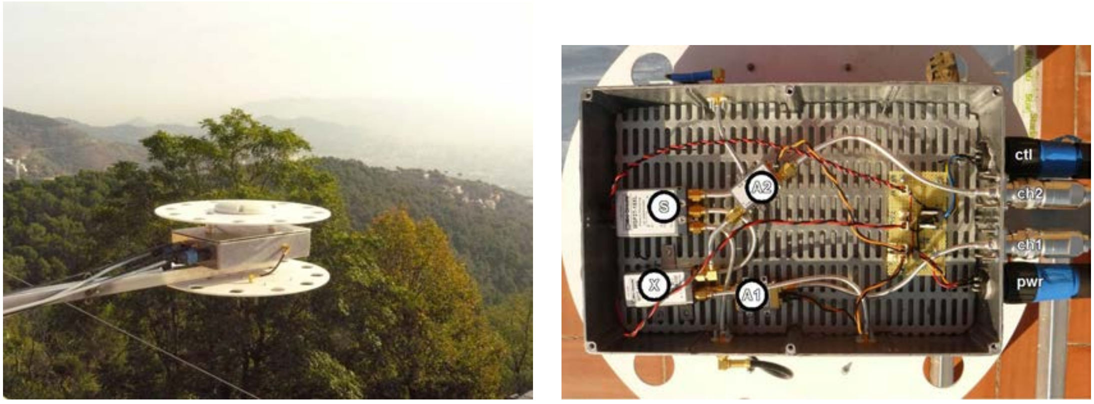

(a) (b)

Figure 6.5: (a) General view of the LEiMON antenna rig. The calibration chain was placed between the up-looking and down-looking antennas. (b) Calibration chain components.

time above 20 dB SNR, with a mean value around 25 dB. The fluctuations in the SNR of the direct signal are due to the different satellites in view for each data take.

The stability of the system is shown in Fig. 6.7, where the waveform peak power ratio between consecutive measurements stages are shown. This represents the estimated calibration constant used for the relative calibration of the two instrument's channels. For each data take, the calibration constant is computed for each PRN between two consecutive measurement stages. This gives for each measurement cycle 3 calibration points per visible PRN, which are then averaged together in order to obtain the final calibration constant. On the top panel of Fig. 6.7, the calibration points are represented in circles, while the line shows the average value of the three calibration points. As can be seen, the power ratio among channels is concentrated around 100% (the same measured power in both receiving channels) with a maximum discrepancy of 15%. The fluctuations along time, are caused by changes in the channel gain due to temperature variations.

The measurement-to-measurement variation of the calculated calibration constant is shown on the bottom panel of Fig. 6.7. The time between measurements was in this case around 10 minutes. It was observed that these values stayed below 3% in almost the whole observation period, with a mean difference of 1.15% for all the analyzed data. This corresponds to an average relative error in calibration below 0.1 dB within each data take.

6.3 Sensitivity and Cross-Polarization Isolation Improvement

During the LEiMON project, it was determined that the instrument's sensitivity and cross-polarization isolation of the receiving antennas had to be improved in order to be able to receive the extremely low signals reflected in RHCP. For the sensitivity upgrade some modifications were done on the RF receiving section of the SAM instrument. Namely, the attenuations introduced by passive elements between the receiving antenna and the LNAs were reduced by connecting the receiving antennas with ultra-low loss cables and reducing at maximum the number of elements between the transfer switch and the LNA.

In order to test the instrument, the signal from the direct antenna was divided with a 3 dB splitter. In the reflected channel an additional splitter was included to divide the signal to the LHCP and RHCP down-looking channels. In order to test the system's sensitivity, an additional attenuation of 10dB, and 20dB, was introduced to the LHCP, and RHCP channels, respectively. This produces an attenuation of 13, and 23 dB for the LHCP, and RHCP channels, which corresponds to typical reflectivity values in these polarizations. For high SNR GPS satellites, the mean measured reflectivity values are 12.8dB for the LHCP, and 22dB for the RHCP channel. This values are considered to be sufficient to perform reliable sensitivity measurements.

In addition, the polarization properties of the GPS receiving antennas were also improved. During the LEiMON project it was found that the cross-polarization isolation of conventional GPS antennas had to be improved in order to perform precise GNSS-R polarimetric measurements. The cross-polarization isolation of the GPS antennas used

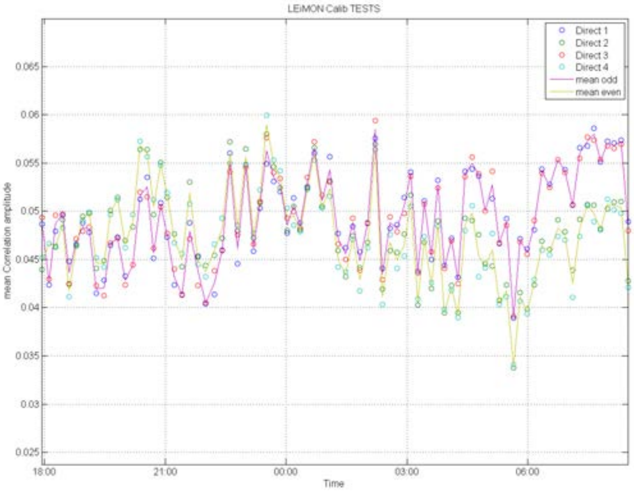

Figure 6.6: Direct waveform mean peak power for the 4 measurement steps. The solid lines represent the averaged values for each reception channel.

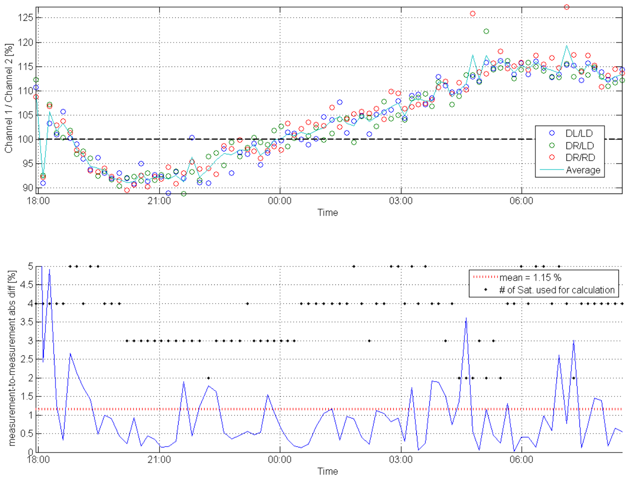

Figure 6.7: Top: calibration constant (ch1/ch2) vs. time. Bottom: Derivative of the calibration constant over time.

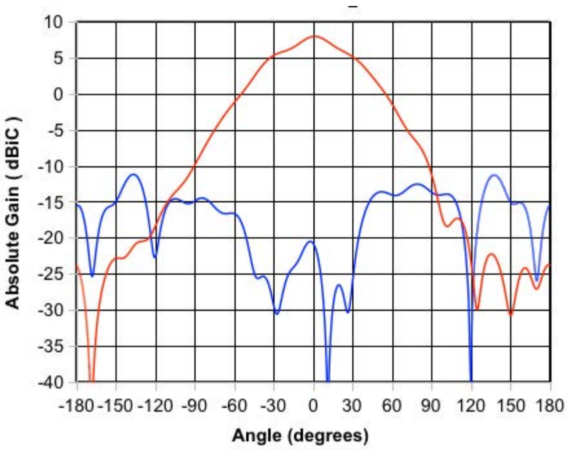

Figure 6.8: GPS L1 antenna co (in red) and cross (in blue) polarization radiation patterns for the LHCP component.

during the SAM and LEiMON experiments was of -17dBs. New GPS antennas were selected with a stringent cross-polarization isolation requirement for the main beam of -24 dB, which roughly corresponds to the axial ratio of GPS transmitted signals, i.e. 1.2 dB. The newly selected antennas were dually polarized with a cross-polarization rejection better than 25 dB both at boresight and within the main beam. These antennas were used during the GRASS experimental campaigns. The co- and cross-polarization radiation patterns for the LHCP signal component are shown in Fig. 6.8.

Chapter 7

Experimental Campaigns

The current chapter presents the experimental campaigns performed during this research work. Those were devoted to gather significant GNSS-R datasets for different purposes: firstly, to validate the SAM GNSS reflectometer; secondly, to study the scattering properties of GNSS signals from land surfaces; and finally, to assess the sensitivity of a GNSS-R system towards land bio-geophysical parameters, such as soil moisture and above ground biomass. The next sections describe these experimental campaigns. The data analysis and experimental results are presented in a following chapter.

7.1 Los Monegros Experiment

During the SAM sensor validation, an experimental flight campaign was carried out in June 2008 over Los Monegros, a semi-arid area close to Zaragoza, Aragon, Spain. The purpose of this experiment was to test the SAM sensor and to verify that small soil reflectivity changes could be observed with such an intrument. The SAM sensor was installed on-board a helicopter that covered the test-site overflew areas with very different reflectivity properties.

7.1.1 Test Site Description

In Fig. 7.1 an image of the area of interest can be seen. This area is particularly interesting for soil moisture experiments for several reasons. First, the area of analysis is remarkably flat, which allows neglecting terrain slope variations. Second, there is a group of seasonal salty lakes in the area that provides a wide range of soil moisture values. And finally, the presence of irrigated crop fields allowed the observation of different soil types.

The area was divided in three sub-zones as can be seen from the figure. The first one is mainly composed of bare semi-arid terrain, and comprises some of the seasonal lakes mentioned above. The second and third sub-zones comprise mainly irrigated crop-fields with different soil moisture conditions.

Figure 7.1: Los Monegros Experiment test-site area. The three different observation sub-zones are shown on the image. The dark blue curves over-imposed are the calculated helicopter tracks obtained with the processing of the direct GPS signals recorded by the GNSS-R sensor.

7.1.2 Instrument Installation

The SAM sensor was installed with the help of the helicopter provider company. A full view of the aircraft is provided in Fig. 7.2(a). The direct GPS antenna was placed on top of the tail fin, Fig. 7.2(b), whereas the reflected GPS antennas, RHCP and LHCP, were placed at the bottom of the fuselage Fig. 7.2(c). This location was not the preferred one, as multipath of the reflected signal could occur in the helicopter's landing skids, however it was mandatory due to flight regulation reasons. High elevation satellites, above 45°, were used in order to mitigate this effect.

The calibration chain was placed inside the helicopter where the main engine is located, since it was the closest accessible place to the direct and reflected antennas. The Radio Frequency Unit and Data processing unit were placed inside the cabin from where the instrument was controlled.

7.1.3 Campaign Execution

The total flight time was around three hours, in which several passes over each of the sub-zones were executed. A navigation GPS was used in order to set several way-points for the definition of the aircraft track. During the experiment, a continuum set of raw data for the direct and the reflected signal was acquired. For the reflected signal, RHCP and LHCP were recorded alternatively in order to produce a polarimetric dataset. The analysis of the data was concentrated in the non-polarimetric measurements, i.e., soil reflectivity analysis on the Γ_{rl} reflectivity component.

Due to an unexpected event, the flight track was not recorded in the navigation GPS. The SAM sensor position throughout the campaign was therefore determined out of the GPS direct signals recorded in the GNSS-R instrument. For this, the GPS satellite's

(a)

(b)

(c)

Figure 7.2: Installation of the SAM sensor on the helicopter: (a) General view of the helicopter used for the SAM experimental campaign. (b) and (c) provide a detailed view of the installation of the direct and reflected antennas, respectively.

position were calculated based on a Lagrange polynomial interpolation International GNSS Service (IGS) SP3 files at the time of emission of the signals. The emission time for each data take were determined from the Time Of the Week (TOW) that is transmitted in subframe of the GPS navigation message. Once the satellites positions were known, the relative pseudoranges between the PRN satellites in view were obtained and the sensor position was finally calculated. The pseudorange measurements were obtained after an averaging of 1 second of data. Ionospheric corrections were not included in the calculation of the helicopter track, which could lead to errors, especially in the vertical dimension. This could affect afterwards, in the determination of the specular point positions. The GPS positioning algorithm was tested with some of the data recorded at Starlab premises, obtaining an estimated precision of around 20 meters; an acceptable value for the purposes of our application.

The determined helicopter tracks over the three different sub-zones are provided in Fig. 7.1. No ground-truth information is available to validate this calculated track. However, it can be seen that, as expected, the calculated tracks fit into the sub-zones, and the turning points of the subsequent passes are aligned with the sub-zone edges.

An in-situ campaign was conducted during the same day of the flight in order to gather ground-truth ancillary data to validate the SAM measurements. The in-situ campaign was performed by Tragsatec, a subsidiary company of the Spanish Ministry of Agriculture, Fisheries and Food. Soil samples were gathered around the seasonal lakes and on adjacent crop fields in order to measure their soil moisture content. The in situ measurements were collected in a concentric way with a separation of 20 m in the Noth-South and East-West directions. The volumetric water content of the samples was finally obtained in the laboratory by standard wet/dry weighting process.

7.2 LEiMON Experimental Campaign

The LEiMON Experimental Campaign was carried out on an agricultural area near along the Pesa River. The test site was located south from Florence, Italy, in a crop field between the villages of Cerbaia and Montespertoli (43.673N, 11.128E). The campaign took place from March to September 2009. In this time period, an entire crop growing season was covered, and due to the seasonal rains, a high variability of soil moisture content was observed. In order to obtain different soil roughness conditions, the field was worked in different ways over the campaign. Throughout the experimental campaign, both GNSS-R data and ancillary data were continuously acquired. The next subsections describe the GNSS-R instrument used and the experimental campaign execution.

7.2.1 Instrument Deployment

The GNSS-R instrument was installed at the center of the experimental test site. The SAM instrument antennas were attached to a hydraulic boom and raised at a height of 25 meters above the ground, see Fig. 7.3(a). The instrument's radio frequency and data processing sections were installed on a shelter close to the hydraulic boom. This shelter was also used to install other instrumentation for the ancillary data recording. An aerial view of the experimental test site is presented in Fig. 7.3(b). The boom and antenna positions are depicted in the image.

In order to procure the highest possible variability of soil conditions, the agricultural field was divided along a north-south line, splitting the experimental field in two halves, as seen in Fig. 7.3(b). The over imposed polygons, and polar axis show the distribution of the East and West fields. The radial dimension is expressed in meters in order to provide the reader an insight of the field's size. The two sides of the field were worked in different ways, and had different soil conditions depending on the period of the campaign. For simplicity, from now on the East, and West sides of the field will be referred to as East and West field.

The GPS satellites' azimuth angle was used to assign the reflectivity measurements obtained for each individual satellite to its corresponding side of the field. Thus, satellites with an azimuth angle between 100° and 270° were assigned to the East field, and

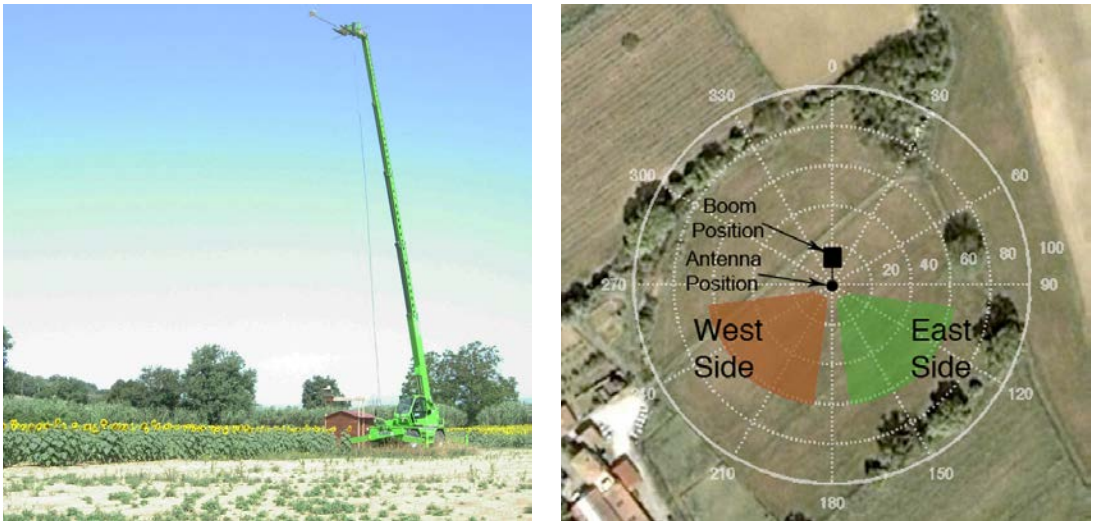

(a) (b)

Figure 7.3: (a) Experimental set-up of the GNSS-R instrument on the hydraulic boom. In the picture, the two sides of the field can be observed, with the bare East field and a fully vegetated West field with sunflowers. (b) Aerial image of the experimental field; The location on the field of the boom and antennas are shown, as well as the areas on the East and West fields from which GNSS reflected signals are acquired.

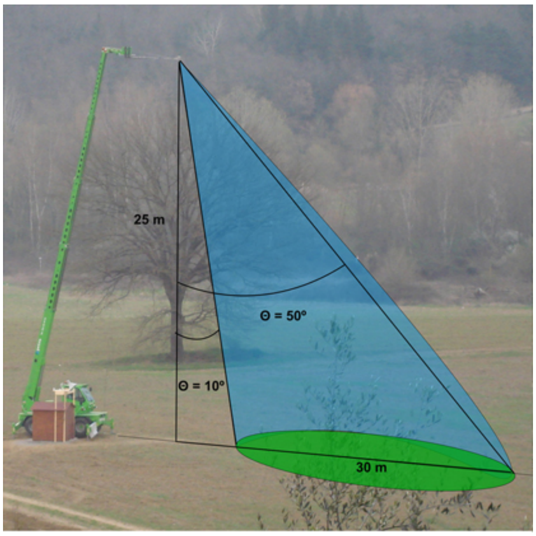

Figure 7.4: Side view of the GNSS-R instrument on the hydraulic boom. In order to avoid undesired reflections, only satellites with an incidence angle between 10 and 50 degree were considered. The scattering area considered for the analysis is shaded in green.

Date	Works on East Field	Works on West Field
24^{th}–27^{th} March	Plowed	Plowed
28^{th} March	Harrowed	Rolled
3^{rd} May	Plowed	Plowed
5^{th} May	Sorghum seeding	Plowed
10^{th} May	-	Sunflower seeding
19^{th} June	Sorghum re-seeding	-
4^{th} August	Sorghum cut	-
23^{rd} August	Sorghum cut	Sunflower harvesting

Table 7.1: Summary of the most important field works performed during the experimental campaign

satellites with azimuth between 190° and 260° to the West field, as depicted in Fig. 7.3(b). A 20° azimuth gap was allowed between both field sides to avoid mixed-pixel effects on the reflected signals. In addition, only reflectivity measurements obtained from satellites with an incidence angle between 10° and 50° were considered in order to avoid undesired reflections. The lower limit is set so that multipath signals from the boom structure could be avoided, whereas the upper limit corresponds to the beam-width of the receiving antenna. In Fig. 7.4 a sketch is provided in order to illustrate this situation.

7.2.2 Field Works

A summary of the works performed on each field is provided in Table 7.1. The field works started towards the end of March. First, both fields were prepared with a general ploughing. After that, the East field was harrowed, while the West field was rolled, obtaining a much rougher soil surface on the East field. On early May, both fields were ploughed again, in order to prepare them for seeding. Two different types of crop were selected in order to determine the effect of different types of vegetation on GNSS-R signals. On the East field, sorghum was planted, whereas sunflower was the selected crop for the West field. Unfortunately, due to adverse weather conditions, the sorghum could not sprout in a first term, and therefore a second seeding was carried out on mid June. Despite this additional effort, the seeding was done on a very late period of the year for this type of crop, and therefore the sorghum did not succeed to sprout. On the contrary, the sunflowers acquired a significant height and PWC on their maximum development stage. On August 23^{rd}, the sunflowers were harvested, and the biomass removed from the experimental site. The campaign lasted until mid September, time in which both fields remained bare.

7.2.3 Ground Truth Data

The ground truth and ancillary data comprised continuous soil moisture measurements, surface roughness, and plant development parameters. In addition, a meteorological station was installed on the site. Further details about the recorded ground-truth data are provided next.

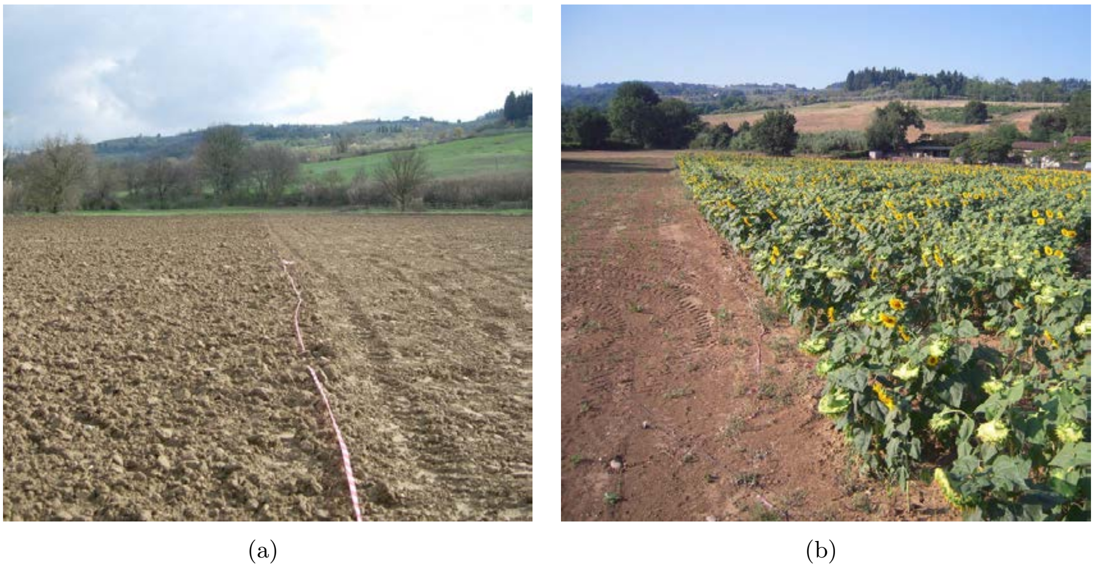

(a) (b)

Figure 7.5: View of the LEiMON experimental test site from the hydraulic boom (South direction) at two different moments during the campaign. (a) April 2009: East field, harrowed; West field, rolled. (b) July 2009: East field, bare; West field, fully vegetated.

Meteorological Data

A meteorological station was installed on the test site to record parameters such as external air temperature, humidity, air pressure, wind speed, last minute rain, and daily rain. See Fig. 7.6(a). The measurements were averaged every half hour. The weather during the duration of the campaign was characterized by an alternation of dry and rainy periods, mostly concentrated during the second half of April, and in late June. This allowed to cover two full soil moisture cycles during the campaign.

Soil Moisture

Soil moisture measurements of the first 10 cm of soil were continuously registered by six Frequency Domain Reflectometry (FDR) probes DELTA-T SM 200 installed on the field and uniformly distributed over the field. These probes measure the volumetric soil moisture by responding to changes in the apparent dielectric constant of moist soil. A hand-held TDR probe IMKO TRIME DataPilot and soil gravimetric measurements were used to calibrate the FDR probes. As no significant differences were observed between the probes in the East and West sides, the calibrated FDR probe signals were averaged together in order to obtain a general SMC value for the whole experimental site. An image of an installed FDR probe is provided in Fig. 7.6(b).

Soil Roughness

Surface roughness was measured using a 1.2 m long needle profilometer with a sampling interval of 0.4 cm, see Fig. 7.6(c). Three contiguous profiles were acquired for each measurement in order to diminish the effect of possible irregularities in the terrain in the reconstruction of the surface roughness profile. The achieved profiles were then digitized and re-sampled at a constant interval in order to calculate the height standard deviation σ_z, and the correlation length l_c.

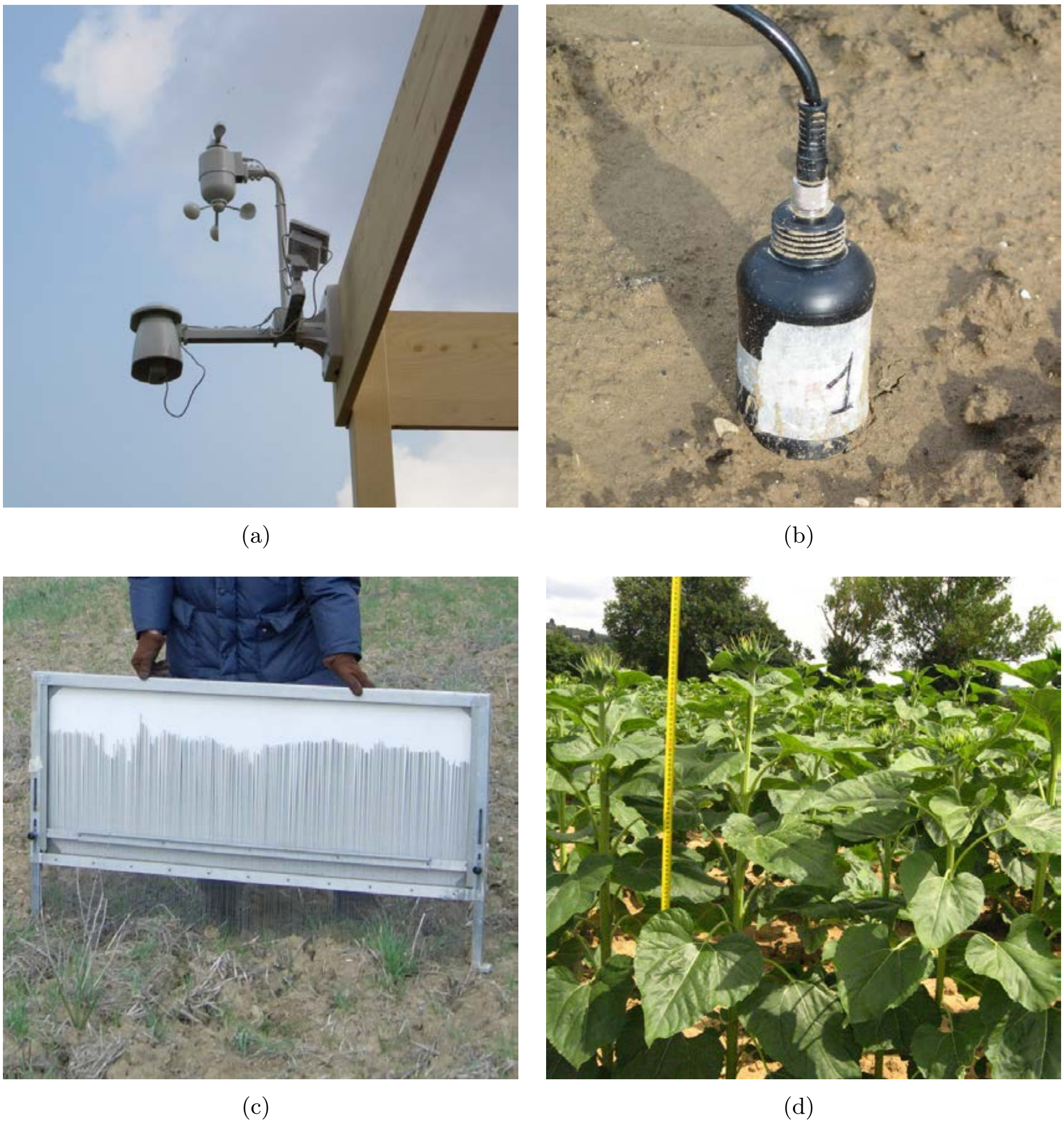
(a) (b) (c) (d)

Figure 7.6: LEiMON ground truth measurement techniques: (a) Meteorological station. (b) Soil moisture probe. (c) Needle profilometer. (d) Sun flower characterization.

Vegetation

Vegetation parameters such as plant density, leaf and stalk dimensions, number of leaves per plant, plant water content and moisture were measured periodically on a weekly basis following standard measuring procedures as described in Cihlar et al. [1987]. The plant height, the leaf dimensions (length, width and thickness) and the stalk dimensions (length and diameter) were directly measured on the field on a sample of 3-4 plants in 2-3 spots of the field by using a centimeter and a caliper, Fig. 7.6(d). The plant water content (PWC, in kg of water per square meter) were measured as the difference between the fresh and the dry weight of the plant and normalized to the surface unit (m^2). The plant moisture (M_v, in percentage) is obtained by normalizing the PWC by the fresh weight.

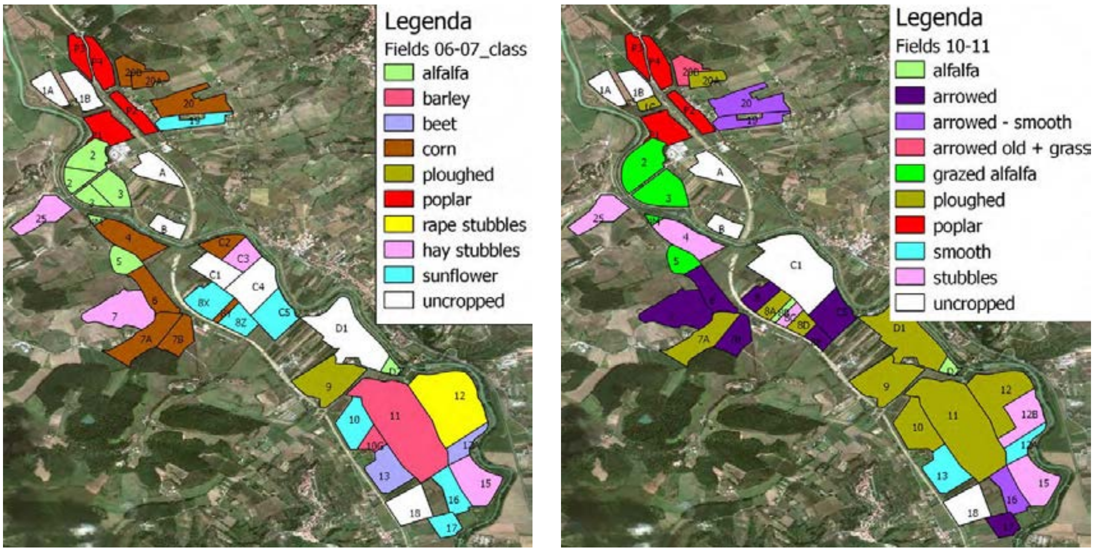

(a) (b)

Figure 7.7: Classification maps of the Ponte A Elsa Test Site; crop types and field working condition are differentiatied according to the colour scale shown in the legend, for the July (a) and November (b) campaigns, from Paloscia et al. [2013].

7.3 GRASS Experimental Campaign

The aim of the GRASS project experimental campaigns was to study the sensitivity of GNSS-R signals to vegetation biomass from both herbaceous crops and forest and its combined effect with soil moisture and surface roughness. In order to retrieve GNSS reflections over a high diversity of land bio-geophysical parameters, two airborne campaigns were conducted in July and November 2011 over two different test sites in the Italian Tuscany. The following subsections describe the two areas under analysis and the execution of the experimental campaign.

7.3.1 Experimental Test Sites Description

7.3.1.1 Ponte a Elsa Test Site

The first test site considered for the GRASS experimental campaigns was an agricultural area between the villages of Ponte a Elsa and Castelfiorentino, Florence, Italy. The area is characterised by large and flat agricultural fields of about 3-6 ha, and covers a total extension of about 10 km^2 along the Elsa River. At the time of the campaign, the fields were cropped with different vegetation types such as wheat, sunflower, rape oil seed, and alfalfa. The crops distribution and field conditions varied between the July and November flight campaigns as a result of the works performed on the fields during that period. The field conditions for both the July and November experiments are shown in Fig. 7.7(a) and 7.7(b), respectively.

As a consequence of the big diversity of crops planted on the area, a high variety of land bio-geophysical parameters could be observed. In addition, due to the seasonal rains in Autumn over Tuscany, it was also possible to observe very different soil moisture conditions between the July and the November campaigns.

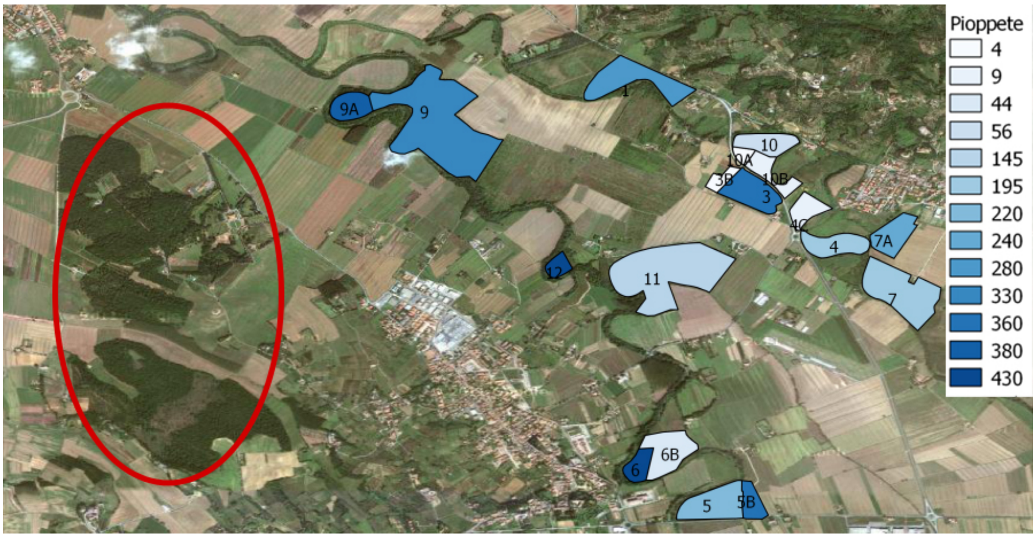

Figure 7.8: Forcoli test-site classification; The poplar plots with different biomass are classified according to the colour scale shown in the legend in m^3/ha, from Paloscia et al. [2013].

7.3.1.2 Forcoli Test Site

In spite of the different types of crops and field working conditions on the Ponte a Elsa test site, a small range of above ground biomass could be observed due to the fact that the poplar plots in that area were rather small and in an homogeneous development stage. In order to observe a wider biomass range, a second test site was selected around the village of Forcoli, 18 km South-East from Ponte a Elsa. This area is scattered with poplar plots of different ages, and have therefore different biomass conditions.

In Fig. 7.8 a classification map of the Forcoli test site is shown. The above ground biomass in m^3/ha is depicted according to the legend's colour scale for different poplar plots in the area. In addition to the plots in bluish colours, the area surrounded by the red ellipse in the figure was also considered in this study. This is known as the Camugliano reserve, a densely populated private forest that could not be characterised by standard measurement methods as access for this was not granted. The forest was finally characterised by visual inspection.

Due to adverse wind conditions during the July campaign, the Forcoli test site could only be overflown during the November flight campaign. However, this did not jeopardize the analysis given the high temporal stability of forest biomass.

7.3.2 Campaign Execution

The SAM sensor was installed on an ultralight aircraft in order to overfly the two test sites described in the previous section. A general view of the aircraft used for the experiments is provided in Fig. 7.9(a). The instrument was placed on the rear seat of the plane, as can be seen on Fig. 7.9(b). In order to power the instrument, a truck battery connected to an inverter was used. The up-looking and down-looking antennas were installed in such a way that the antenna plane were parallel to the ground when the aircraft was in flight, Fig. 7.9(c). A detailed picture of the down-looking antenna is provided in Fig. 7.9(d). An additional antenna ground-plane was installed in order

(a) (b)

(c) (d)

Figure 7.9: GRASS experimental campaign GNSS-R Instrument Installation: (a) General view of the ultralight aircraft. (b) Interior view of the aircraft's cabin with the instrument on-board. (c) Detailed view of the direct and reflected antenna installation. (d) Detailed view of the reflected antenna installation and ground-plane.

Figure 7.10: GRASS Flight 1: Aircraft track over water reservoir.

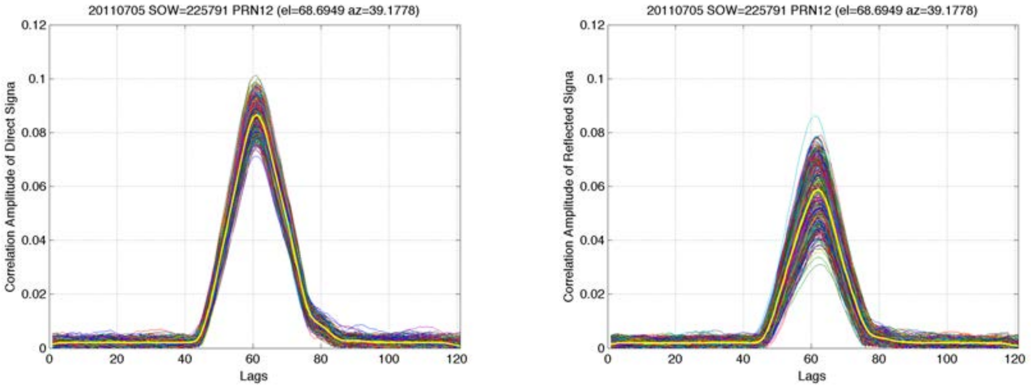

(a) (b)

Figure 7.11: (a) Direct and (b) reflected waveforms correlation amplitude over the lake during Flight1.

to prevent the direct signal from leaking through the down-looking antennas backlobes. A Septentrio AsterX GPS navigation receiver with an Inertial Navigation System (INS) was installed on the plane in order to geo-locate the GNSS-R measurements and to monitor the aircraft's attitude.

During the flight campaigns, the GNSS-R instrument was configured to acquire data in a continuous mode. The reflected LHCP and RHCP signal polarizations were acquired sequentially in periods of 18 seconds. The processing of the data was performed on-ground.

As mentioned above, two flight campaigns were carried out, each one of them consisting on two flights. The first experimental campaign took place between the 5th and 7th July 2011. A test flight and a scientific flight were successfully completed. The former, was done to verify the correct functioning of the whole equipment. For that, a flight over an artificial water reservoir was performed. Figure 7.10 shows the aircraft tracks over the lake. GNSS reflections were acquired over the water surface, showing high SNR for both direct and reflected signals. Figures 7.11(a) and 7.11(b) show the direct and reflected waveforms at RHCP and LHCP polarizations, respectively, for PRN-12 (elevation angle

	Parameter	**Units**
Soil	Volumetric Soil Moisture (SMV_V)	cm^3/cm^3 (%)
	Soil Roughness (σ_z)	cm
	Correlation Length ($L_c z$)	cm
Crops	Crop type	–
	Plant Height	cm
	Plant Density	plants/m
	Stem Diameter	cm
	Plant Biomass	kg/m^2
	Plant Water Content (PWC)	kg/m^2
	Plant Moisture (M_V)	%
Forest	Tree species	–
	Tree density	trees/m
	Tree height	m
	Trunk diameter	cm
	Crown insertion	m
	Understory	–

Table 7.2: Summary of the most important field works performed during the experimental campaign

68°). The strong reflection over the water allows to observe the characteristic triangular waveform shape even in the reflected waveforms. The correlation amplitude ratio between the direct and reflected waveforms yields a value around 0.7 which corresponds to the reflectivity of water for an incidence angle around 20 degree.

The scientific flight of the first campaign covered the Ponte a Elsa area. Several parallel passes over the test-site were done in order to obtain an appropriate sampling of the area under analysis. The height of the aircraft over the surface was around 150 meters, and the separation between successive passes was set to 150 meters, roughly corresponding to the antenna beam-width projected on the surface. A total area of 7.5 by 1,25 km was covered. Figure 7.12(a) shows the complete flight track, and Fig. 7.12(b) shows a zoom view of the tracks over the agricultural test-site.

The second campaign was carried out between November 9th and 10th 2011. Two flights were also performed to cover the Ponte a Elsa and Forcoli test-sites. The tracks of these flights are shown in Fig. 7.12(c) and 7.12(d), respectively. During Flight 3, the artificial lake was also overflown in order to acquire reflected signals for calibration purposes.

7.3.3 Ground Truth Data

A collocated ground truth measurement acquisition campaign was carried out at the same time as the flight experimental campaigns. The measured parameters for both the Ponte a Elsa and Forcoli test sites are gathered in Table 7.2.

Vegetation parameters were measured by conventional method, PWC and Mv were obtained by drying plants in an oven for 24 h at 80 °C. Soil surface roughness on bare fields was obtained by means of a needle profilometer. Average volumetric soil moisture values for the most representative fields were obtained by a portable TDR probe. Soil samples were also collected to obtain the gravimetric soil moisture in order to calibrate of the TDR probes.

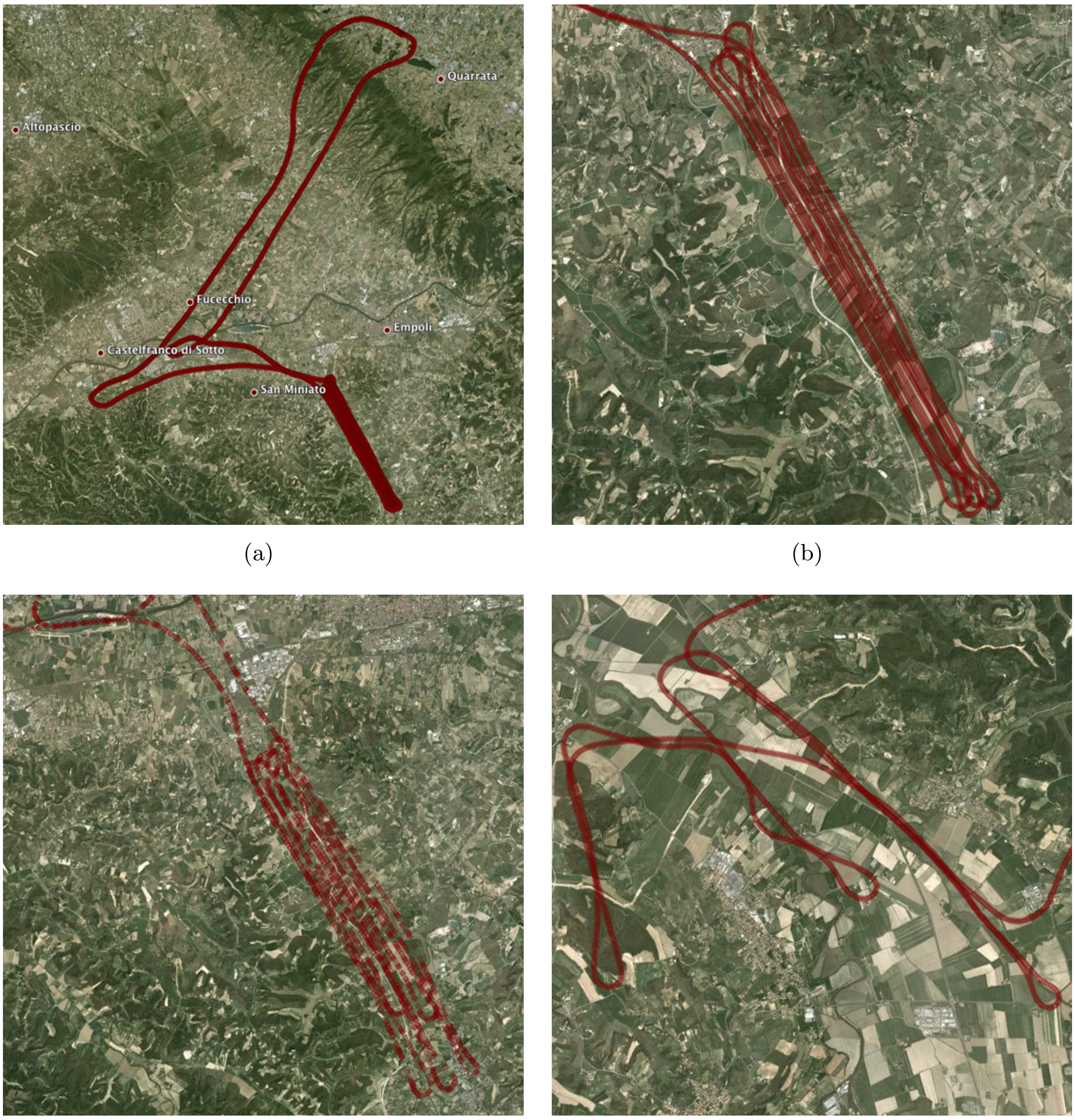

(a) (b)

(c) (d)

Figure 7.12: Flight tracks for the GRASS experimental campaigns: (a) Flight 2 full track; (b) Flight 2 detailed track view over the Ponte a Elsa test-site; (c) Flight 3 detailed track view over the Ponte a Elsa test-site; (d) Flight 4 detailed track view over the Forcoli test-site

7.4 Summary

Three experimental campaigns were executed in the frame of this PhD Thesis, each one of them associated to one of the ESA projects in which this research work was developed. The first of those was the SAM experimental campaign, dedicated to validate the SAM GNSS-R receiver. The instrument was installed on-board a helicopter in order to overfly a semi-arid area known as Los Monegros, Zaragoza, Spain. That specific test site was particularly interesting for the experiment as the seasonal lakes in the area provided a wide range of reflectivities that could be observed with the SAM sensor. The flight was complemented with an in-situ campaign during which soil samples were gathered in order to determine their moisture content by a wet-dry weighting process.

The second experimental campaign is referred to as the LEiMON campaign, devoted to analyze the effects of soil bio- geo-physical parameters on the GNSS reflected signals. For that, the GNSS-R instrument was installed for a six months campaign on a crop field near Montespertoli, Florence, Italy. During this period a complete sunflower development cycle was covered, and thanks to the seasonal rains in the area, a wide range of soil moisture conditions could also be observed. GNSS-R and ground truth data were continuously acquired throughout the whole duration of the experiment.

The third experimental campaign was the GRASS campaign. Its purpose was to determine the effect of vegetation on the GNSS-R signals, and to determined their sensitivity to forest above ground biomass. Two experimental test-sites were defined, close to Ponte a Elsa, and Forcoli, Tuscany, Italy. The former is a crop field area along the Elsa river. The latter is an agricultural area scattered with poplar plots at different development stages. Two flight campaigns, each one consisting of 2 flights, took place between July and November 2011, in order to cover the two test-site areas. In-situ measurements were also performed to characterize the most relevant soil bio- geo-physical parameters for the fields under observation.

Chapter 8

Data Analysis - Experimental Results

The analysis of the data gathered during the experimental campaigns is discussed in this chapter. The the first section deals with the data gathered during the SAM airborne experiment, used for the validation of the SAM sensor. The second section details the data analysis performed during the LEiMON project, focused on analyzing the scattering characteristics of GNSS signals reflected off land surfaces. The third section covers the results obtained for the GRASS experimental campaign, aimed primarily at determining the sensitivity of GNSS-R signals to soil bio-geophysical parameters, especially forest above ground biomass. A final section gathers the most important results and conclusions extracted from this analysis.

8.1 Los Monegros Experiment

The current section introduces the data analysis performed for the SAM experimental campaign. The processing stages for the airborne campaign data are explained next. The same data analysis approach was also used for the GRASS experiment. As will be shown later, the measured reflectivity values were used to produce a soil moisture map of the observed area.

8.1.1 Data Processing Chain

The GNSS-R data processing was performed in several steps, from the direct and reflected channels GNSS raw-data down to the geo-located and calibrated reflectivity values. The different stages of the processing are shown in the diagram on Fig. 8.1. The processing starts with the GNSS-R polarimetric raw data, i.e. the direct and reflected signal bitstreams, that are passed to the CStarlight processor for the generation of the complex cross-correlation waveforms. The Navigation GPS data is used in order to concentrate the PRN search and tracking to just the GPS satellites in view at the time of the data acquisition. The coherent integration time was set to its maximum for a conventional GPS C/A-code, i.e. 20 ms, as a way to reduce as much as possible the effect of thermal noise in the data, and to limit the incoherent scattering component.

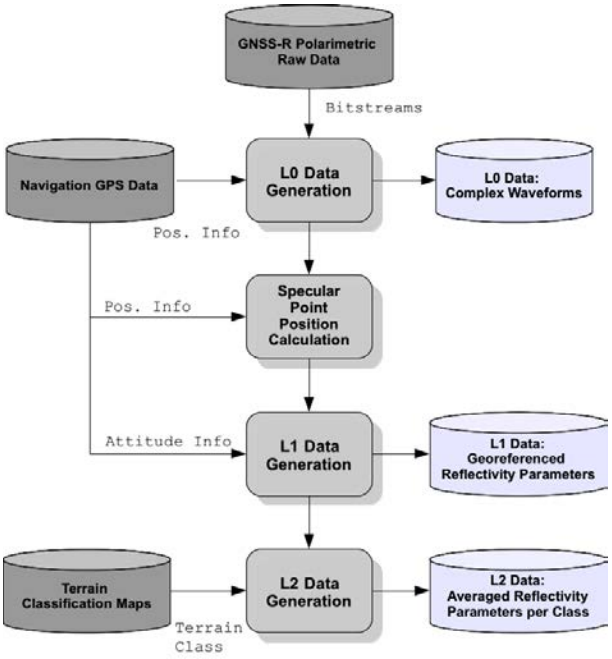

Figure 8.1: SAM GNSS-R data processing chain.

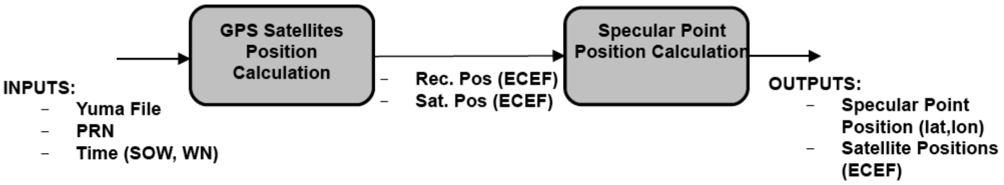

Figure 8.2: Satellite position and specular point position calculation modules architecture.

The GPS navigation message is decoded in this process attending to the polarity change of the direct channel waveforms. The navigation message contains the GPS transmission time, satellite ephemerides, and other information such as ionospheric and tropospheric error corrections for positioning. The transmission time is broadcasted in every sub-frame of the navigation message, which allows to determine the emission time of each specific waveform with a precision of 20 ms. This corresponds to the maximum transit time between the GPS satellite and the receiver. For this particular application this precision in the determination of the waveform time is acceptable, as for a (conservative) maximum speed of the aircraft of 100 m/s it would be able to locate the position of the specular points on the ground with a precision of 2 meters.

The complex cross-correlation waveforms are incoherently averaged in batches of 0.1 s in order to geo-reference their position on-ground. This is done by the calculation of the specular point position, which is achieved by two independent modules; the first one performs the propagation of the GPS constellation to the moment of the GPS signal transmission, and the second one calculates the specular point position based on the position of the GPS transmitting satellite and GNSS-R receiver. The basic architecture of these modules is shown in Fig. 8.2. The inputs for the GPS satellite position calculation module are the Yuma File, containing the satellites' almanac, the receiver position, and the time of the simulation, expressed in second of the week and

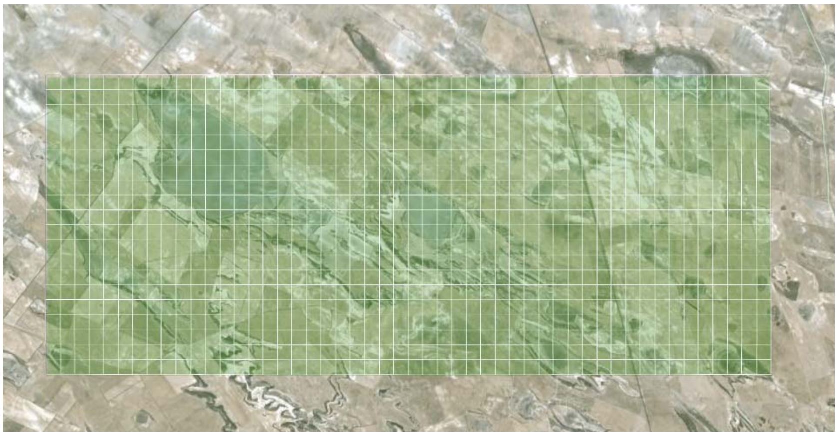

Figure 8.3: Sub-zone 1 grid separation for soil moisture estimation.

GPS week number. For optimal calculation of the GPS satellites position, the provided file should be the one corresponding to the GPS week number of the acquisition. The second module computes the specular point positions based on the receiver position and the previously calculated satellite positions. The module outputs are the specular points in latitude and longitude projected over the WGS-84 reference ellipsoid.

The ratio of the direct and reflected waveforms measured at different polarizations yield the co- and cross- polarization apparent power reflectivities, Γ'_{rl} and Γ'_{rr}. By switching the direct and reflected channels, internal power dissimilarities can be calibrated. The calibration constant K is applied to the measured reflectivity values, which are then geo-referenced according to the calculated specular point positions. The final processing stage entails the calculation of the averaged Γ'_{rl} and Γ'_{rr} according to the terrain classification. These data are finally used to analyze the response of GNSS-R signals to land bio-geophysical parameters.

8.1.2 Soil Permittivity Estimation

For the validation of the SAM sensor, the data recorded during the SAM flight campaign were used to produce a soil moisture map of the area. The estimated soil moisture values were later compared to the ground-truth in-situ measurements. For that, the sub-zones were divided with a grid of 200 x 200 meters resolution cells. The specular point positions for all visible satellites were calculated with respect to the aircraft position and referenced to one of the resolution cells in time intervals of 1 second. The soil's apparent reflectivity measurements associated to each specular point position were obtained by averaging the absolute squared ICF during a certain acquisition time:

$$\Gamma'_{av} = \frac{1}{N}\sum_{i=1}^{N} |\mathrm{ICF}(i)|^2 \tag{8.1}$$

Note that in this case, the average of the ICF squared amplitude was calculated, which accounts for the full field power, and not just the coherent scattering component as considered in section 5.2. This was done because due to the aircraft's movement, the ICF had a fast varying phase, and therefore long coherent averaging resulted in a null

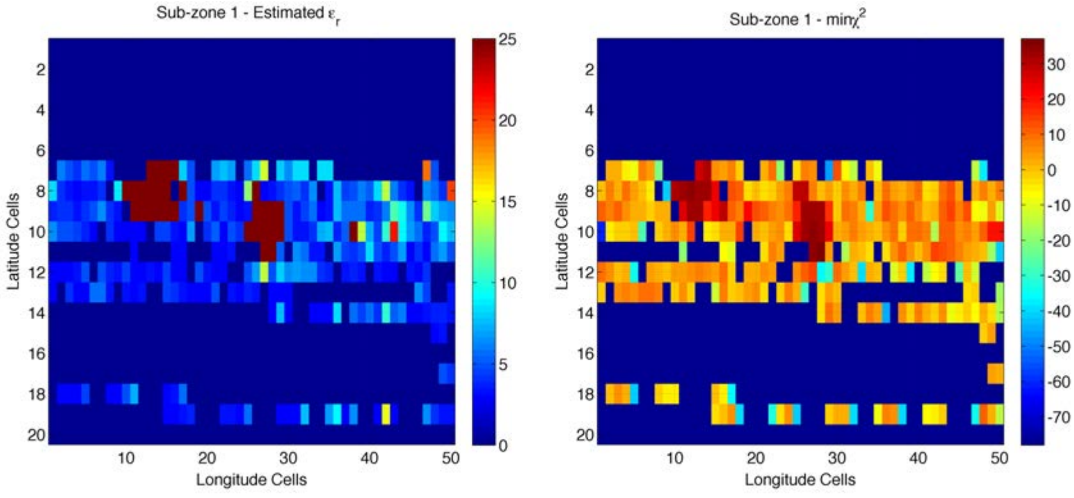

(a) (b)

Figure 8.4: Permittivity estimation for Sub-zone 1: (a) Estimated relative permittivity ε_r; (b) Minimum χ^2 Value [dB]

estimated reflectivity. The error associated to these measurements was calculated as the observation's variance:

$$\sigma^2_{\hat{\Gamma}'_{av}} = \frac{1}{N}\sum_{i=1}^{N}\left(|\mathrm{ICF}(i)| - \hat{\Gamma}'_{av}\right)^2 \tag{8.2}$$

A correction factor accounting for the reflectivity reduction due to the effect of soil roughness, as shown in Eqn. (5.42), was applied to Γ'_{av} measurements considering a standard σ_z of 2 cm for the whole observation area.

For the final estimation of the dielectric permittivity of each resolution cell, a Chi-squared function Maximum Likely-hood estimator was used. The retrieved ε_r value is the one that minimizes the mean quadratic error of the reflectivity measurements Γ'_{av} with respect to the reflectivity model, Γ'_{rl}, presented in section 5.5.3,

$$\chi^2(\varepsilon_r) = \min\left\{\sum_i \frac{\left(\Gamma'_{rl}(\theta_i;\varepsilon_r) - \Gamma'_{av,i}\right)^2}{\sigma^2_{\Gamma'_{av,i}}}\right\} \tag{8.3}$$

where θ is local incidence angle, and the index i accounts for the different averaged reflectivity measurements within the considered resolution cell. For this study it was considered that ε_r is real, since since as pointed out in [Ulaby et al., 1986b] the imaginary part of the permittivity in L band is typically below 0.05, and can therefore be neglected for practical purposes.

Figure 8.4 provides an example of the permittivity maps obtained for sub-zone 1. In Fig. 8.4(a) the estimated ε_r values are shown. The cells with higher permittivity correspond to the seasonal lakes in the area. In the rest of the image, the estimated permittivity are low and homogeneous values, as one would expect from such a semi-arid area. The cells in the image with null permittivity are those that did not have valid specular points within the cell.

Figure 8.4(b) shows the minimum χ^2 value obtained for each resolution cell. The color scale is represented in logarithmic scale for better visualization. In a least mean square minimization, when the χ function value tends to one, it can be said that the model fits appropriately the data at the same time that the σ values associated to the measurements correspond to a realistic measurements noise. In our case, most of the cells present a χ^2 minimum value close to 0 dB (1 in linear scale), except in the area corresponding to the lakes, where the scattering model selected for the soil does not fit the behavior of the reflecting waves over the ponds.

8.1.3 Soil Moisture Estimation and Comparison with Ground-Truth Data

To be able to relate the soil relative permittivity to soil moisture estimates semi-empirical models such as the ones presented in [Hallikainen et al., 1985] and [Wang and Schmugge, 1980] can be used. In the former paper the authors suggested that the relationship between soil moisture and dielectric constant for a frequency around 1.4 GHz can be described by a quadratic relationship of the form:

$$\begin{aligned}\varepsilon_{soil} = 2.862 - 0.012S + 0.001C \; + \; (3.803 + 0.462C - 0.341S) \cdot m_v \, + \\ + (119.003 - 0.500S + 0.633C) \cdot m_v^2\end{aligned} \tag{8.4}$$

where S and C are the weight percentages of sand and clay textural compositions of the soil, and m_v is the volumetric soil moisture content.

This model was used as a semi-empirical model before in [Torres, 2004] with acceptable results. In this case, the lack of knowledge of the observation area soil's composition prevented the direct application of this model for the estimation of soil moisture. However, a quadratic model was fitted directly to the data in order to derive the coefficients of the quadratic relationship. The measured relative permittivity of the cells was compared to the in-situ soil moisture samples acquired during the campaign for those cells with an available soil moisture in situ sample. Because of the lack of a more representative ground-truth dataset, just five data points could be used to perform the comparison. Despite the few data points, a clear quadratic relationship is observed between the measured permittivity and the volumetric soil moisture content, as can be observed in Fig. 8.5(a). The following quadratic relationship was obtained:

$$\varepsilon_r = 0.151 \cdot m_v^2 - 2.435 \cdot m_v + 12.106 \tag{8.5}$$

Equation (8.5) was finally used to calculate the soil moisture estimations. Figure 8.5(b) shows the soil moisture volumetric content retrieved from the SAM measurements represented against the volumetric soil moisture content of the in-situ samples. Despite the fact these were not conclusive results due to the small number of data points available

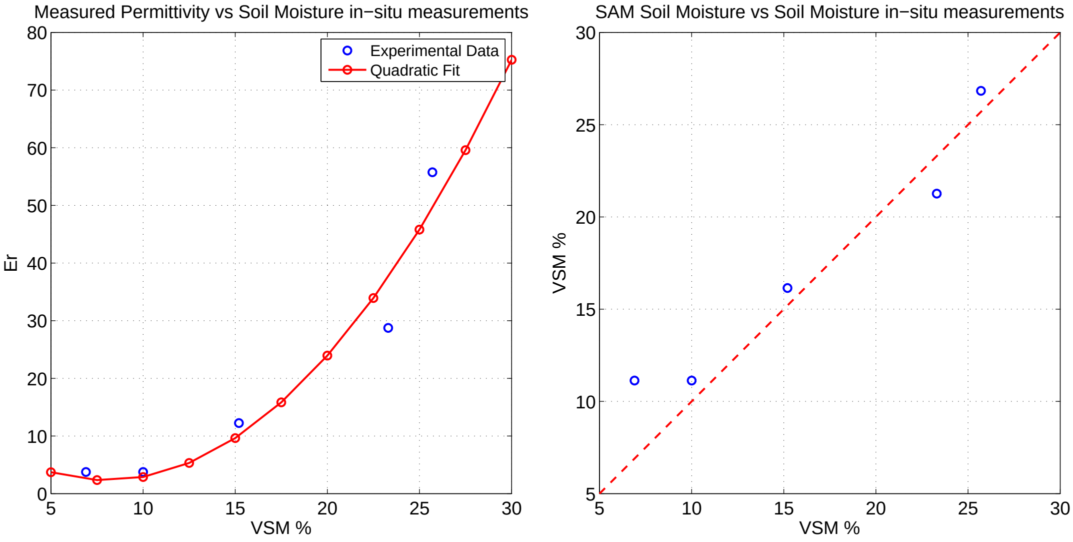

(a) (b)

Figure 8.5: (a) Estimated permittivity and (b) estimated volumetric soil moisture with respect to in-situ soil moisture ground truth measurements.

for the comparison, a good correlation of the soil moisture estimations with the ground-truth data is observed, with a correlation coefficient of 0.95, which allowed to validate the SAM sensor design and data processing approach.

The soil moisture volumetric content was calculated for all the cells in the area under analysis with suitable permittivity values. The result constituted a soil moisture geo-referenced map that was over-imposed on Google Earth. The result is provided in Fig. 8.6. The soil moisture measurements were divided in 12 different soil moisture classes (red to green), and an additional one to represent water areas (blue), for better visualization. As can be seen from the image, the water areas are clearly identified, corresponding to the seasonal lakes in the area. In addition, a soil moisture variation is observed from the sub-zone 1, the driest of all three, with respect to sub-zone 2 and 3. In sub-zone 2, the bottom left corner of the grid is also observed drier than other parts of the grid, which is also expected since this area is not cultivated. The two cells showing high soil moisture content in sub-zone 3 correspond to a populated area, so it is likely that the power of the reflected signal increases due to reflections over buildings, roofs, etc.

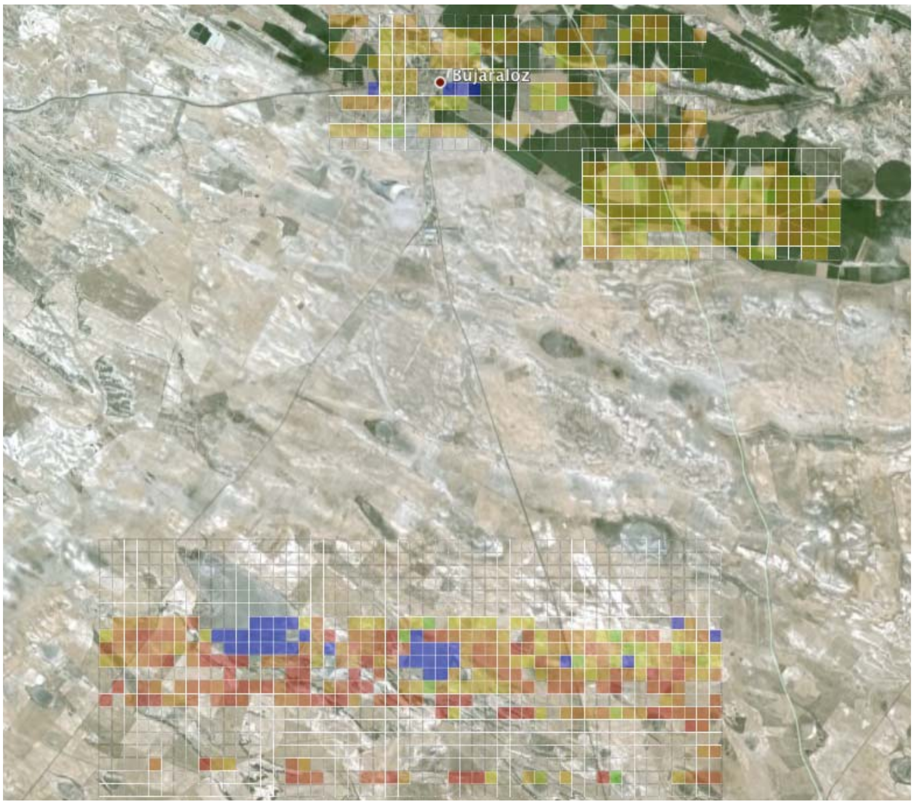

Figure 8.6: Soil moisture map retrieved with GNSS-R data of the area observed in Los Monegros, Zaragoza, Spain. The soil moisture map was over-imposed on a Google Earth image of the area.

8.2 LEiMON Experimental Campaign Data Analysis

The main objective of the LEiMON data analysis was to investigate the scattering properties of GNSS-R signals from land surfaces. For that, as described in section 7.2.3, a six months campaign was performed. A vast amount of GNSS-R and ground truth data in a wide variety of soil conditions were recorded during the campaign.

The first part of the LEiMON data analysis dealt with the investigation of the reflected signal coherent and incoherent scattering components. An optimum observable was derived to concentrate the measurements around the coherent component. The second part of the analysis was aimed at relating the effects of land bio-geophysical parameters on GNSS reflected signals. Firstly, the temporal evolution of the GNSS-R signals was compared to the ground-truth data. Secondly, the spatial distribution of GNSS-R signals and their dependency with incidence angle was investigated. In a final stage, the sensitivity of GNSS-R signals to soil moisture and vegetation was quantitatively determined together with the correlation coefficients of the apparent reflectivity measurements with the ground-truth data.

8.2.1 GNSS-R Signals Scattering Characteristics

As discussed in previous chapters, GNSS signals reflected off land surfaces are composed of a coherent and an incoherent scattering components. The former is originated in the vicinity of the specular point, and its scattering properties are governed by the Fresnel reflection coefficients. The latter is originated as a consequence of the random combination of waves arriving at the receiving antenna from multiple scatterers on the surface. This generates the so called speckle noise, which results in fluctuations and fadings in the received signal amplitude.

In order to study the scattering properties of GNSS-R signals, long data takes were performed during the last part of the LEiMON experimental campaign. Continuous data acquisitions of 10 minutes were recorded to observe the variability of the reflected fields along time. Two sample PRN satellites were selected for this analysis: PRN-09 (incidence angle, 24.3°, azimuth angle 116.9° (East field)) and PRN-30 (incidence angle, 43.8°, azimuth angle 270.2° (West field)), acquired on DoY 245. At that time of the campaign, the sunflowers had already been harvested, therefore both East and West fields were bare and smooth, with some residual vegetation (stalks) on the West field.

The starting point for the analysis are the direct and reflected complex fields, i.e., the time series of the direct and reflected complex waveform peaks. The amplitude of these signals for the two selected PRNs are shown in Fig. 8.7. As can be seen, strong fluctuations occur on the reflected field amplitude for both satellites. This behavior is linked to the presence of an incoherent scattering component on the reflected signal. Nevertheless, the reflected signal SNR, (calculated as the ratio between the mean amplitude of the signal and its standard deviation), yields 8.9 dB and 11.5 dB for PRN-09 and PRN-30, respectively. If the scattering was completely incoherent, the reflected signal SNR would have yield 5.6 dB, as shown in [Ulaby and Dobson, 1989]. The fact that the obtained SNR are higher than this value is an indication of a strong coherent scattering component in the reflected signal. An evidence of this is also the distribution of the reflected fields. Fig. 8.8 shows fthe histogram of the reflected field amplitudes for both PRNs, which resemble a Rice PDF, as explained in section 4.2.

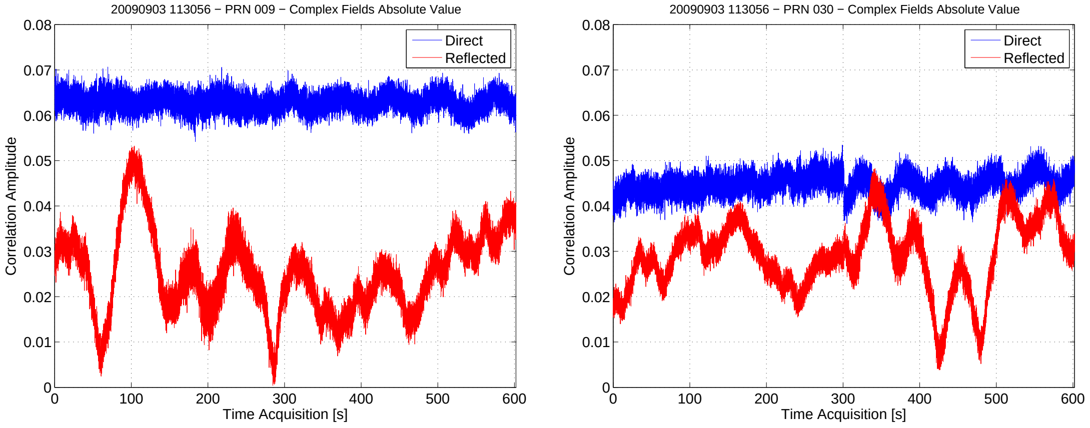

(a) (b)

Figure 8.7: Direct and reflected complex field amplitude for (a) PRN-009, and (b) PRN-030.

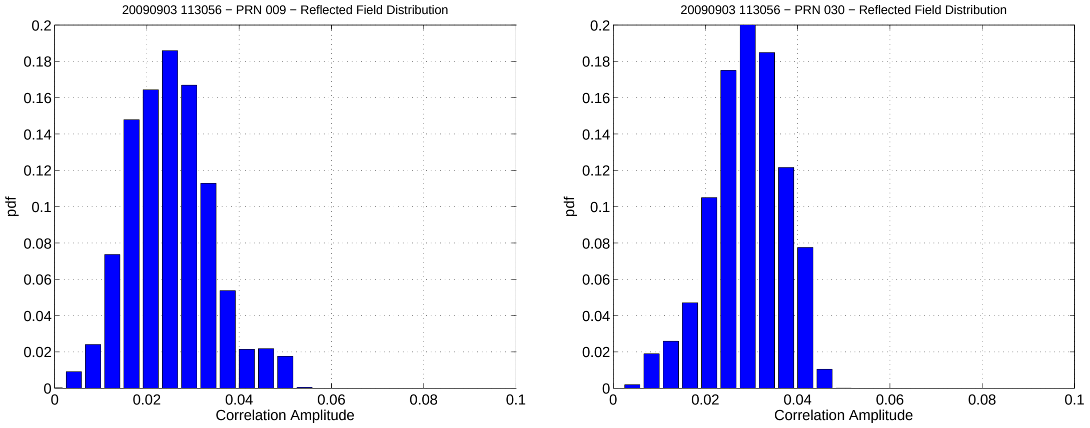

(a) (b)

Figure 8.8: Reflected field amplitude distributions for (a) PRN-009, and (b) PRN-030.

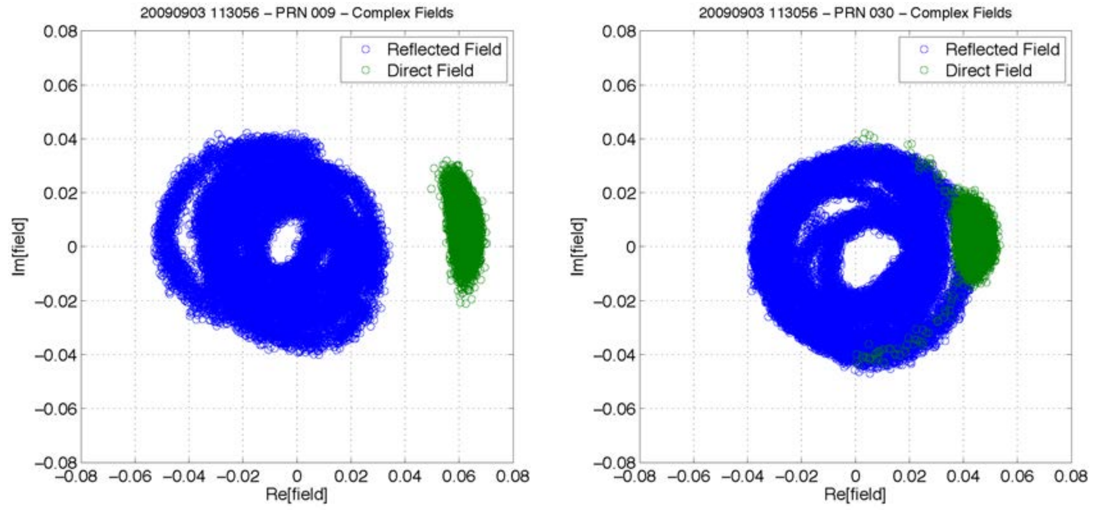

(a) (b)

Figure 8.9: I and Q representation of the direct (in green) and reflected (in blue) complex fields for (a) PRN-009, and (b) PRN-030. The direct fields are concentrated within a single point over the real axis, whereas the reflected fields rotate about the complex plane due to the geometrical phase variation of the reflected signal.

Interesting to see is direct and reflected complex fields distribution on the I/Q plane. This is shown for both PRNs in Fig. 8.9. While the direct fields (in green) are concentrated about a mean value, the reflected fields (in blue) rotate along time around the complex plane. This effect is originated by the relative change in geometry of the direct and reflected paths. In most GNSS-R instruments, the tracking of the incoming GNSS signals is performed on the direct channel, applying the same delay and Doppler information also for despreading the reflected signal in a master-slave tracking scheme. Due to different lengths of the direct and reflected signals' path, applying the same delay in both channels incurs in a displacement of the reflected waveforms with respect to the direct ones, which, in the end is the main observable for GNSS-R altimetry applications. In the same way, this path difference produces a phase shift on the reflected waveforms that varies along time due to a change in the scattering geometry originated from the relative motion of the GNSS satellites with respect to the receivers, as depicted in Fig. 8.10. This effect can also be understood as a residual Doppler frequency in the reflected signal due to the different geometry of the direct and reflected channels, producing the rotation of the reflected field about the complex plane.

As shown in section 5.2, in order to retrieve the coherent scattering component of the GNSS-R signals, the averaging of the ICF needs to be performed. For that phase coherency needs to be kept in order to obtain significant reflectivity estimates. Otherwise, in the case of a fast varying phase $\phi_\rho(t)$, the integral implicit in Eqn. (5.16) tends rapidly to zero, destroying the final reflectivity measurement. Therefore, the geometrical phase drift of the ICF needs to be previously compensated. For a static receiver, the ICF phase can be described using the basic phase altimetry formula:

$$\phi(t) = 2\,k\,h\,\sin(\varepsilon(t)) = \frac{4\pi}{\lambda}\,h\,\sin(\varepsilon(t))\,, \tag{8.6}$$

where h stands for the height of the antennas over the surface, k is the wave-number, and ε is the satellite's elevation, which is a function of time and varies with the satellite's

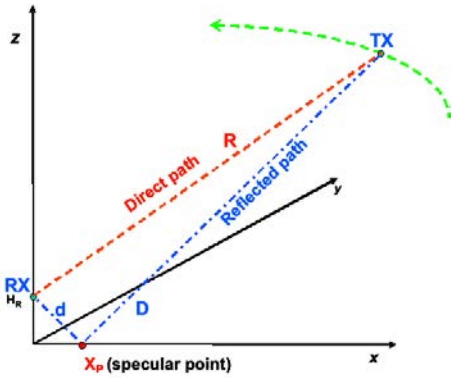

Figure 8.10: Direct and reflected signal's paths. Small geometry variations turn into phase drifts along time of the reflected vs the direct signal, which turns into a rotation of the reflected complex field.

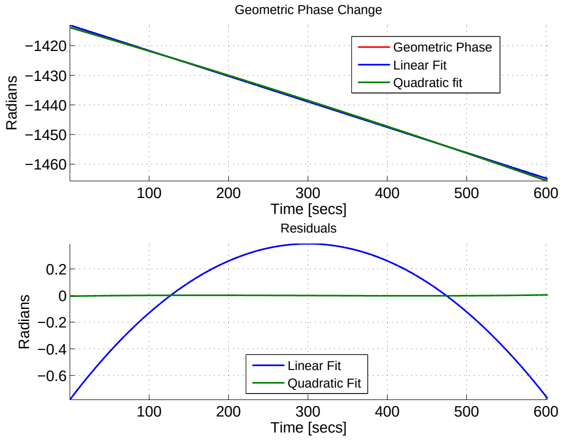

Figure 8.11: Geometrical phase variation: top panel, geometrical phase variation for a fixed receiver at a height of 24 meters over the ground and a conventional GPS satellite geometry over a time span of 10 minutes; in the bottom panel the residuals for a linear and quadratic fit are provided, demonstrating that with a quadratic fit the phase residuals are below 1 degree for the whole simulation time.

position. Using the previous equation to calculate the phase drift of the ICF is subjected to the knowledge of h (the satellite position and the time of acquisition are considered to be known parameters). As the specular point migrates over the surface during the transit of its corresponding GNSS satellite, h can vary along time due to terrain irregularities. Small variations of h with respect to the nominal height of the antennas over the surface can lead to substantial changes in the ICF phase; recall that a variation of 1 wavelength, i.e. 19 cm, corresponds to 2π radians, a full rotation of the reflected field about the I/Q plane. For this reason, the phase variation was approximated by a quadratic polynomial. In the top panel of Fig. 8.11, the theoretical phase drift is plotted together with a linear and a quadratic approximation. In the bottom panel, the residuals for each approximation are depicted, showing an error below 1 degree for a total simulation time of 10 minutes in the case of the quadratic fit.

Subtracting the geometric phase drift from the ICF phase the counter-rotated field is obtained. Figure 8.12 shows the ICF for PRN-09 and PRN-30, blue circles in the plot. Alike the reflected field, before counter-rotation the ICF revolves around the complex I/Q plane. When the geometric phase drift is corrected, the counter-rotated ICF (in red) concentrates around one point over the real axis with a certain dispersion produced by thermal noise. The yellow circles in the plots represent the center of the distributions, calculated as the averaged value of the counter-rotated ICF. Those correspond to the coherent component of the signal and represent the measured reflectivity, value, as shown in section 5.2.

To analyze the distribution characteristics of the counter-rotated ICF, the 2 Dimensional histograms were calculated for both PRNs, see Fig. 8.13. In these plots, it is more clearly apparent how the fields are concentrated about a central point, i.e. the coherent scattering component. The calculated Γ'_{rl} apparent reflectivity for PRN-09 and PRN-30 were -7.44 dB and -4.2 dB, respectively. Given the similar conditions of the East and West fields at that time of the campaign, the variation in the measured reflectivity was linked to the difference of incidence angle between the two considered GPS satellites.

The histograms of the real and imaginary components of the field at the center of the distributions were also calculated, Fig. 8.14. As predicted by scattering theory, those follow a Gaussian distribution; although this is not so evident for PRN-09, Fig. 8.14(a), for PRN-30, Fig. 8.14(b), the real and imaginary ICF distributions can be described by Gaussian functions with different standard deviations. These results confirm the hypothesis of the scattered field Hoyt distribution, presented in section 4.2.1.

The coherent and incoherent scattering components were finally separated by subtracting the mean value of the counter-rotated ICF from the original complex field. In Fig. 8.15 it can be observed that the distribution of the ICF changes from an original Rice-like distribution to a Rayleigh distribution after removing the mean of the distribution, which demonstrates that the remaining field is completely incoherent. The power of the incoherent component was calculated for both PRNs as the average of the absolute squared values of the remaining fields, yielding -13.3 dB and -13.7 dB for PRN-09 and PRN-30, respectively. The small difference between the incoherent components of both PRNs is due to the fact that the incoherent scattering has an isotropic behavior, therefore even for satellites with different incidence angles the incoherent scattering remains almost constant provided that the soil conditions do not change. The ratio between coherent and incoherent scattering components goes from 6 dB in the case of PRN-09, and 10 dB for PRN-30, corresponding to typical values for ground based configurations, as shown in section 4.3.

8.2.2 GNSS-R Observables Obtention

The data processing approach presented above can be used to derive the coherent and incoherent scattering component out of the received direct and reflected GNSS signals. This method relies on the harmonic evolution of the phase of the reflected field according to the geometric variation due to the GPS satellite's movement. However, due to the proper scattering mechanism, the phase of the reflected signal has very often a completely random behavior and cannot be approximated by a quadratic model. For instance, when strong fading events occur, the phase of the signal is completely wrapped around the origin, and cannot be reconstructed. This prevents the correct counter-rotation of the

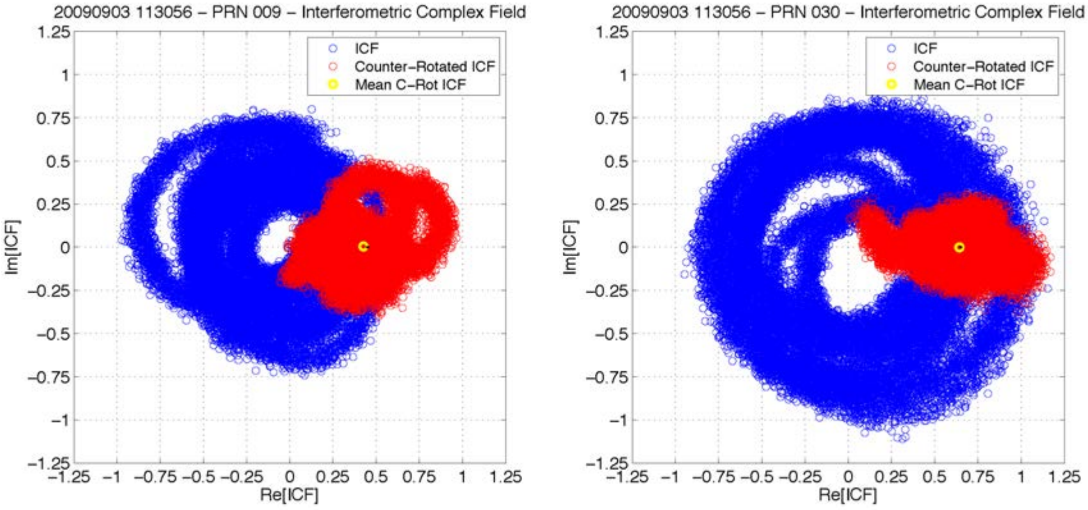

(a) (b)

Figure 8.12: I and Q representation of the ICF (in blue), and the counter-rotated ICF (in red) for (a) PRN-009 and (b) PRN-030. The yellow circles in the plots show the average of the counter-rotated fields, i.e. the coherent scattering component.

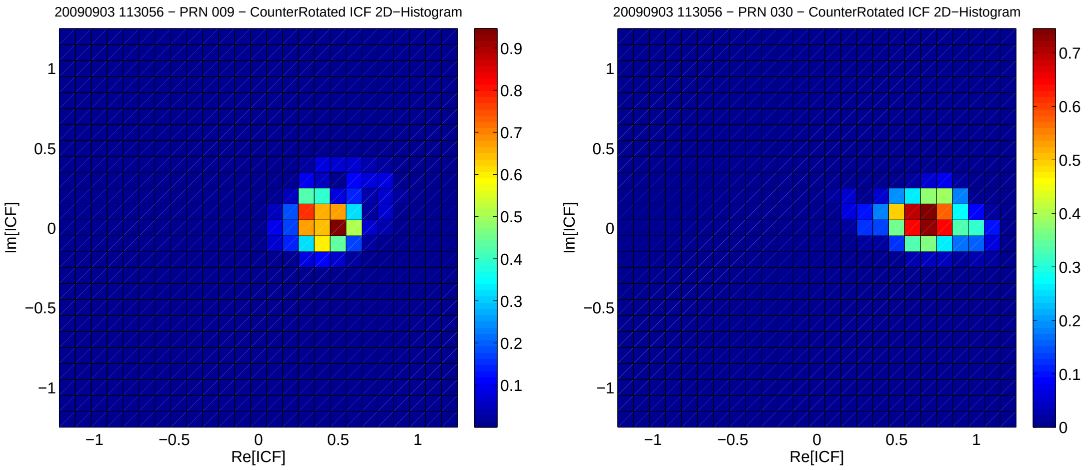

(a) (b)

Figure 8.13: Two dimensional distribution of the counter-rotated ICF for (a) PRN-009 and (b) PRN-030. As can be seen, the field is concentrated around a single point of the complex field.

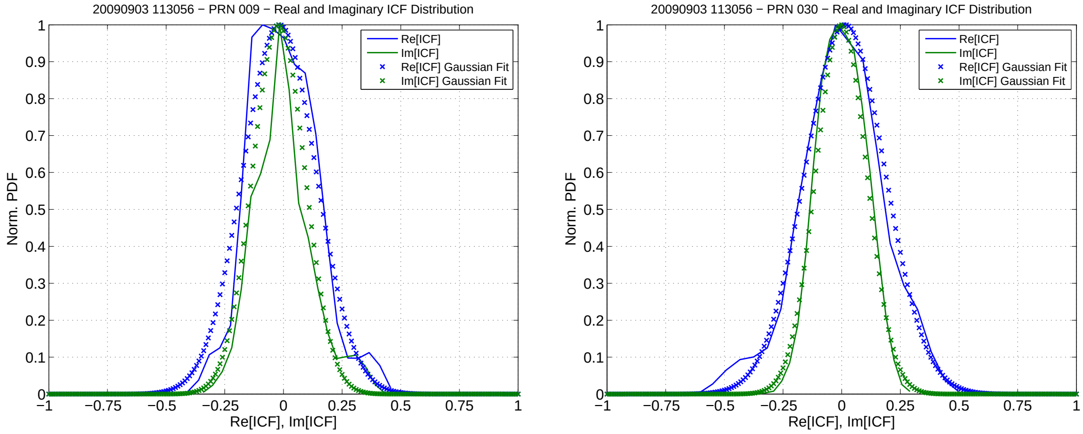

(a) (b)

Figure 8.14: Real and Imaginary cuts of the counter-rotated ICF two dimensional histograms with respect to the center of the distributions; (a) PRN-009, and (b) PRN-30. The Gaussian fits to both real and imaginary cuts are depicted is solid-crossed lines.

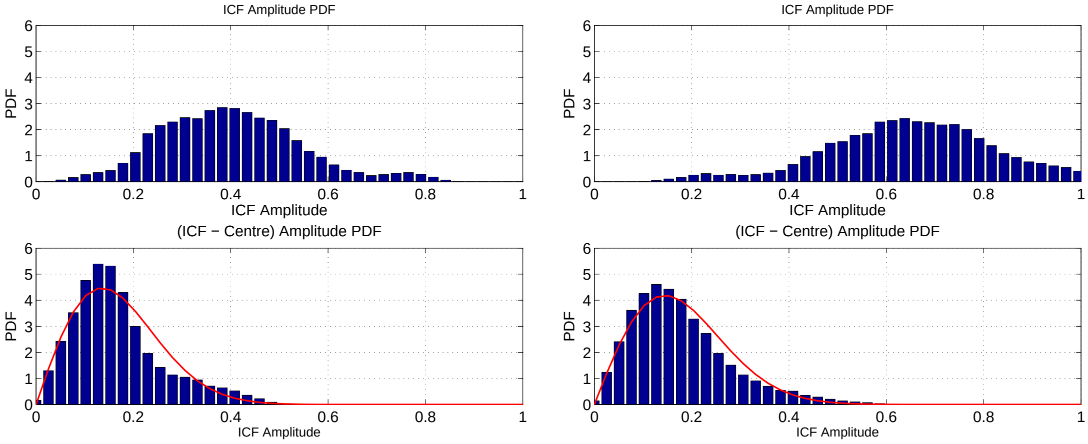

(a) (b)

Figure 8.15: ICF amplitude probability density functions (PDF) before (top) and after subtracting the coherent component (bottom); (a) PRN-009, and (b) PRN-30. In red, a best fit Rayleigh distribution is also depicted.

interferometric complex field and by extension the estimation of the coherent scattering component.

Following the theoretical discussion presented in section 4.2, a new averaging procedure was proposed in order to reduce the contribution of the incoherent scattering component on the finally estimated reflectivity value, and therefore concentrate on the coherent component throughout the data analysis. Identifying the elements in Eqn. (4.11), with the ICF it can be written that:

$$\left\langle |\mathrm{ICF}(t)|^2 \right\rangle = |\langle \mathrm{ICF}(t) \rangle|^2 + \sigma^2_{|\mathrm{ICF}|} \,, \tag{8.7}$$

where it can be seen that the averaged ICF power, equals its mean averaged absolute squared value plus an additional term that corresponds to the ICF's amplitude variance. $|\langle \mathrm{ICF}(t) \rangle|^2$ is precisely the mean apparent reflectivity value obtained in Eqn. (5.17). By straightforwardly manipulating Eqn. (8.7) it is finally obtained that:

$$\Gamma'_{pq} = |\langle \mathrm{ICF}(t) \rangle|^2 = \left\langle |\mathrm{ICF}(t)|^2 \right\rangle - \sigma^2_{|\mathrm{ICF}|} \,, \tag{8.8}$$

which allows to calculate the coherent scattering component out of the ICF amplitude, without having to deal with the ICF phase; a problematic matter due to its random behavior in the event of fadings. These observables were used to estimate the relationship between the bio-geophysical parameters and the GNSS-R signals observed during the LEiMON experiment.

It is worth noting here that in calculating the observable out of the mean power of the ICF, the signal statistics change. Provided that the considered streak of data is sufficiently long, the mean power ICF can be written as:

$$\left\langle |\mathrm{ICF}(t)|^2 \right\rangle = \left\langle \left| \frac{Y_{r,q}(\Delta\tau)}{Y_{d,p}((0)} \right|^2 \right\rangle \approx \frac{\left\langle |Y_{r,q}(\Delta\tau)|^2 \right\rangle}{\left\langle |Y_{d,p}((0)|^2 \right\rangle} \,. \tag{8.9}$$

Considering Eqn. (5.14), the mean power waveform can be rewritten as:

$$\left\langle |Y(\tau)|^2 \right\rangle = \frac{1}{T_i^2 \sigma^2} \left(T_i^2 \, \Lambda^2(\tau) + k\,T\,T_i \right) = s^2 \Lambda^2(\tau) + \frac{1}{T_i B} \,, \tag{8.10}$$

where s stands for the voltage SNR at the input of the correlator, and B accounts for the receiver's intermediate frequency filter bandwidth. This second term introduces an offset in the reflectivity measurements, however, for a coherent integration time of 20 ms, as in the case of LEiMON, its contribution is not significant. With shorter integration times this additional term has a stronger weight, specially for low level signals, and should therefore be accounted for and corrected.

8.2.3 GNSS-R Signal Temporal Data Analysis

For the temporal analysis, the GPS observations recorded during each data take were averaged in order to obtain the time series of the Γ'_{rl} and Γ'_{rr} apparent reflectivities. Despite the fact that the reflectivity changes with incidence angle, this analysis was carried out in order to identify temporal trends on the data, and to establish qualitative relationship among the geo-physical parameters and the GNSS-R signals. A one-day moving average was applied to the time series in order to reduce the intrinsic measurement noise.

Figure 8.16 shows the temporal evolution of the ground truth and GNSS-R data for the whole LEiMON experimental campaign. For simplicity, the temporal axis is represented according to the Day of the Year (DoY). Panel (a) on the figure shows the soil moisture probes data together with the daily accumulated rain recorded by the meteorological station. In panel (b) the most relevant vegetation parameters are depicted, while panel (c) shows the measured surface roughness for the East and West fields. Panels (d) to (f) display the time series for the measured Γ'_{rl}, Γ'_{rr}, and the ratio of both polarizations. Superimposed on these graphs, the daily precipitation and the most significant field works are also presented.

As can be seen from the plots, Γ'_{rl} and Γ'_{rr} experience remarkable increases that are directly related to rain events, producing power variations up to 7 dB in the Γ'_{rl} apparent reflectivity; see for instance DoY 118–119, 153–155, and 182–185. In addition, it can also be observed that the obtained reflectivity coefficients follow the general trend of the SMC measured with the FDR probes, see Fig. 8.16(a). Nonetheless, there are some discrepancies between the soil moisture probe data and the estimated reflectivity coefficients. A remarkable increase in the GNSS-R signals can be observed between DoY 170 and 175. This is related to light rain events that took place on those days. However, the average SMC measured by the probes does not experience a significant variation. The same situation is evidenced for a light rain event that occurred on DoY 217. These results were linked to the fact that GNSS-R signals are sensitive to the soil moisture in the first centimeters of soil, whereas the FDR probes obtain the soil moisture measurements at 10 cm from the surface, which might not suffer appreciable variations in case of light precipitations.

The effect of roughness is also visible in the two reflection coefficients. In the beginning of the campaign, both reflectivity coefficients followed the same behavior, since the soil conditions were the same in both sides of the field. However, after the field works on 28th March, DoY 87, the East and West sides of the field had different soil roughness conditions: 3 cm in the case of the East field and 1.8 cm for the West field. As a result, a 3 dB difference between the West (smooth) and East (rough) fields could be observed in the Γ'_{rl} and Γ'_{rr} apparent reflectivities. After the second plowing event, when both fields were prepared for seeding (3rd to 5th May), DoY 123–125, the roughness of both fields was again homogenized, and therefore the difference in the power of the signals coming from both sides of the field disappeared.

In the beginning of June, DoY 150, the difference between the East and West sides started to increase for Γ'_{rl}, reaching its maximum by late July, DoY 210. This observation was linked to the attenuation introduced by the developing sunflowers on the West field, see Fig. 8.16(b), while the East field remained bare or scarcely vegetated. After the harvest, around 20th August, DoY 232, this difference is reduced. In the case of the RHCP signal, no significant difference between the bare and vegetated sides of the field

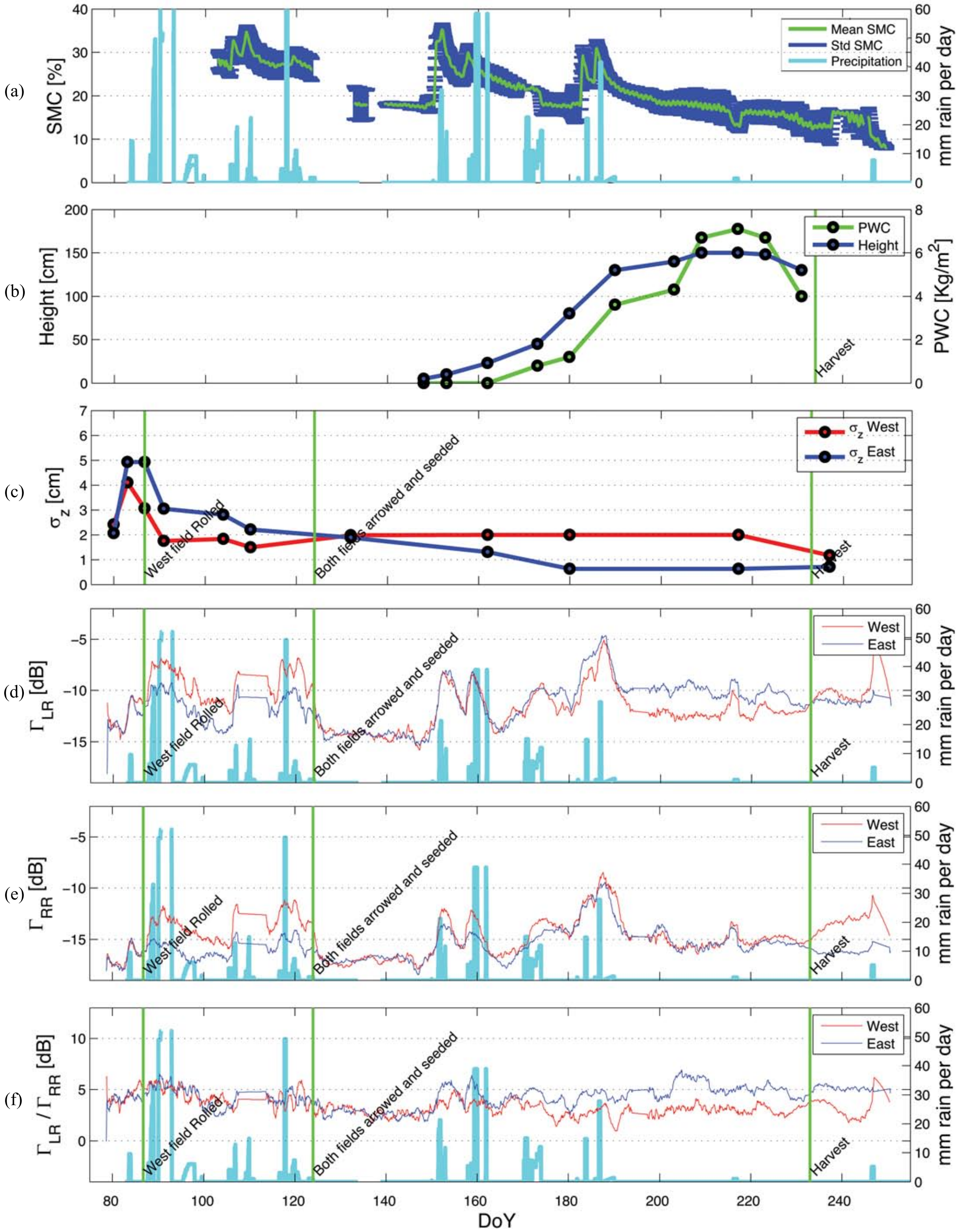

Figure 8.16: Data time series for the LEiMON Experimental campaign: (a) mean and standard deviation of the SMC recorded by the FDR probes, and daily precipitation; (b) sunflower height and plant water content (PWC); (c) measured surface roughness for the East and West fields; (d) Γ'_{rl} time series for the East and West fields; (e) Γ'_{rr} time series; (f) Γ'_{rl} over Γ'_{rr} time series. In panels (d), (e), and (f), the daily precipitation is represented in light blue to show the correlation of the signal with soil moisture changes. The most relevant field works are depicted as green vertical lines.

Period	Dates	DoY	SMC	Roughness	Vegetation
1	8–10 April	98–100	30%	East $\sigma_z = 3.0$ cm, West $\sigma_z = 2.0$ cm	East – bare, West – bare
2	20–23 May	140–143	17%	East $\sigma_z = 2.0$ cm, West $\sigma_z = 2.0$ cm	East – bare, West – bare
3	28–30 June	179–181	17%	East $\sigma_z = 0.7$ cm, West $\sigma_z = 2.0$ cm	East – bare , West – SF 45 cm
4	18–20 July	199–201	20%	East $\sigma_z = 0.7$ cm, West $\sigma_z = 2.0$ cm	East – bare , West – SF 135cm

Table 8.1: Selected time periods for the estimation of the sensitivity of GNSS-R signals to land bio-geophysical parameters.

could be observed. A possible explanation for this is that volume scattering was produced by the sunflower canopy as the GNSS signals traversed the vegetation layer. This incoherent scattering component would compensate for the signal attenuation produced by vegetation.

After the harvest, an important increase on the Γ'_{rr} component on the west side was observed. This effect could be linked to the removal of biomass from the field, thus eliminating the attenuation produced by vegetation. However, vertical sunflower stalks were left on the West field, which could still depolarize the impinging signal by a volume scattering effect. The combination of these two effects could have led to the increase in the Γ'_{rr} component.

Regarding the ratio of the two reflectivity components, it can be observed that it is moderately sensitive to rain events, with about 3 dB difference between wet and dry soil moisture conditions. A remarkable aspect is that, unlike Γ'_{rl} and Γ'_{rr}, variations in surface roughness are not detected by this observable, as can be seen in Figure 8.16(f); despite the soil roughness difference between the East and West field between late March and early May, DoY 87–123, the Γ'_{rl} over Γ'_{rr} ratio does not present any appreciable difference, which could make this observable suitable for roughness-independent soil moisture remote sensing. This result confirms the hypothesis initially proposed in [Zavorotny and Voronovich, 2000a], where it is shown that for moderately rough surfaces the ratio of two orthogonal polarizations does not depend on the surface roughness.

8.2.4 GNSS-R Signals Response to Soil Bio-Geophysical Parameters

In order to study the variability of GNSS-R signals with soil parameters, four different periods were selected considering their stable and diverse soil conditions. Table 8.1 summarizes the soil moisture, roughness and vegetation conditions for these periods. The measured Γ'_{rl} and Γ'_{rr} apparent refletivities were separated among the East and West fields. The dependency with the incidence angle was also considered in order to compare the data with the scattering models.

Figure 8.17 provides the mean value of the estimated reflectivity for both fields and their associated measurement uncertainty. In a first term, contrarily to the expected behavior of the Fresnel reflection coefficients, an increasing trend of both Γ'_{rl} and Γ'_{rr} with the incidence angle can be observed. As exposed in section 5.4.1, this effect is due to the polarization mismatch of the receiving antenna and incoming wave. In conventional Fresnel theory, the reflection coefficients are given in a plane orthogonal to the propagation direction of the reflected wave, however, in a general case, specially for GPS, the antenna plane is not normal to the propagation direction. The reflectivity observed by the GNSS-R receiver is modified due to the projection of the polarization vector of the incident wave on to the antenna plane, which ultimately causes the increasing trend with incidence angle of the measured reflection coefficients.

From the graphs, the effect on GNSS-R signals of soil surface roughness, SMC, and vegetation PWC can be inferred. For soil roughness, in Period 1, Fig. 8.17(a), signals coming from the East field are lower than those of the West field by an average of 2.3 dB due to the difference in surface height standard deviation. On Period 2, Fig. 8.17(b), both fields were arrowed, which reduced the difference in soil roughness between both of them. As can be observed, Γ'_{rl} and Γ'_{rr} show very similar values for both fields. The decrease in reflectivity with respect to Period 1 is linked to a decrease in SMC, i.e. from a high soil moisture condition in Period 1, SMC = 30%, to an dry situation in Period 2, SMC = 17%. For the West field (similar soil roughness conditions), Γ'_{rl} presents a difference of 3.5 dB between wet and dry soil moisture conditions.

The effect of vegetation can be noticed in the bottom panels of Fig. 8.17, corresponding to Periods 3 and 4. An increasing difference in Γ'_{rl} between the East (bare) and the West field (vegetated) can be observed due to the presence of a developing vegetation. Due to the attenuation effect of the vegetation layer, this difference reaches 3 dB when vegetation approaches its maximum development stage in Period 4, specially at high incidence angles when the GNSS signals travel a longer path through the vegetation layer. As mentioned before, in the case of Γ'_{rr} the difference between the bare and vegetated fields is not noticeable, due to the combination of an increasing attenuation due to the vegetation layer, and an additional depolarization due to the vertical structures of the sunflowers' stalks.

Changes of the vegetation PWC can also be seen on the spatial distribution of the measured reflection coefficients. On Fig. 8.18, Γ'_{rl} is depicted on polar plots for Periods 3 and 4, Fig. 8.18(a) and (b) respectively. Pictures of the West field for those periods are also provided in order to show the sunflowers' development stage. The separation between the East and West fields can be readily observed as a consequence of the presence of sunflowers. As expected, this difference is more evident during Period 4, when the sunflowers are fully developed. The bluish colors on the plots over the West field vs. the yellowish colors over the East demonstrate a difference of nearly 5 dB between some areas of the fields. However, remarkable variabilities on Γ'_{rl} can be observed on the West field, due to inhomogeneities of the crop. Eventually this leads to a reduction of the obtained sensitivity of GNSS-R signals to PWC.

A noticeable aspect of this analysis is the difference between the Γ'_{rr} and the Γ'_{rl} apparent power reflectivities. While theoretical models predict a difference between 10 and 20 dB, in some particular situations, the maximum difference measured for the reflection coefficients was around 7 dB. The cause of that was linked to three possible aspects. Firstly, the limited sensitivity of the receiver, which is estimated to be around a reflectivity value of -20 dB, could have prevented the acquisition of the entire dynamic range of the RHCP reflected signal, thus introducing a bias on the measured RR coefficient. Secondly, note the limited cross-polarization isolation of the receiving antennas. The GPS antennas used in the campaign were characterized in an anechoic chamber,

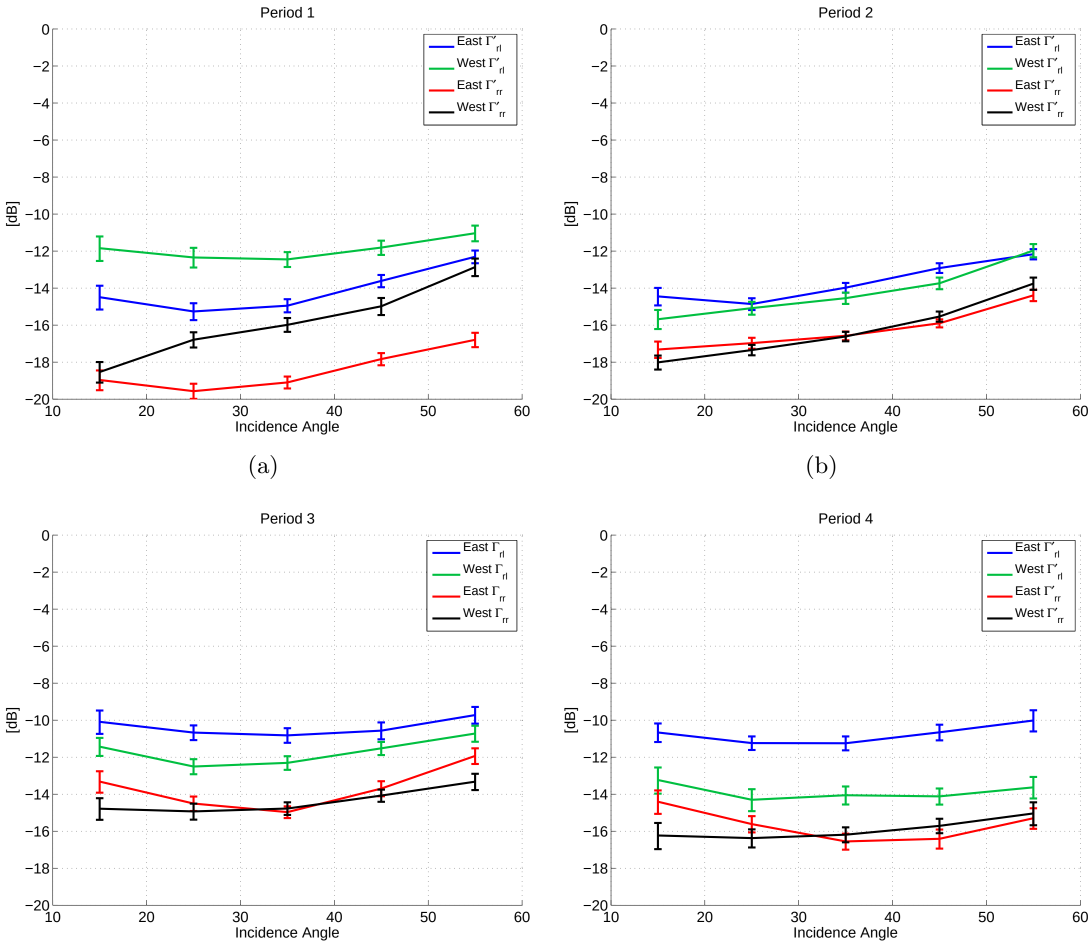

(a) (b) (c) (d)

Figure 8.17: Measured Γ'_{rl} and Γ'_{rr} for the East and West fields in four selected periods over the experimental campaign: (a) Period 1: High SMC, East harrowed and bare, West rolled and bare; (b) Period 2: Low SMC, East rolled and bare, West rolled and bare; (c) Period 3: Low SMC, East rolled and bare, West rolled and sunflowers (height = 45cm); (d) Period 4: Low SMC, East rolled and bare, West rolled and sunflowers (height = 135cm).

and the cross-polarization isolation at boresight was determined to be −17 dB for both LHCP and RHCP down-looking antennas. Thirdly, the ellipticity of the impinging GNSS signals; as stated in the GPS Interface Specifications Document [GPSW, 2010], the ellipticity of GPS incident waves should not exceed 1.2 dB in the whole field of view of the GPS satellites, which is a non-negligible figure that should be considered. These three aspects have an influence in the determination of the absolute value of Γ'_{rr} and should be accounted for and corrected in order to perform polarimetric measurements, however, they are within reasonable limits and should not jeopardize the outcomes of the current analysis.

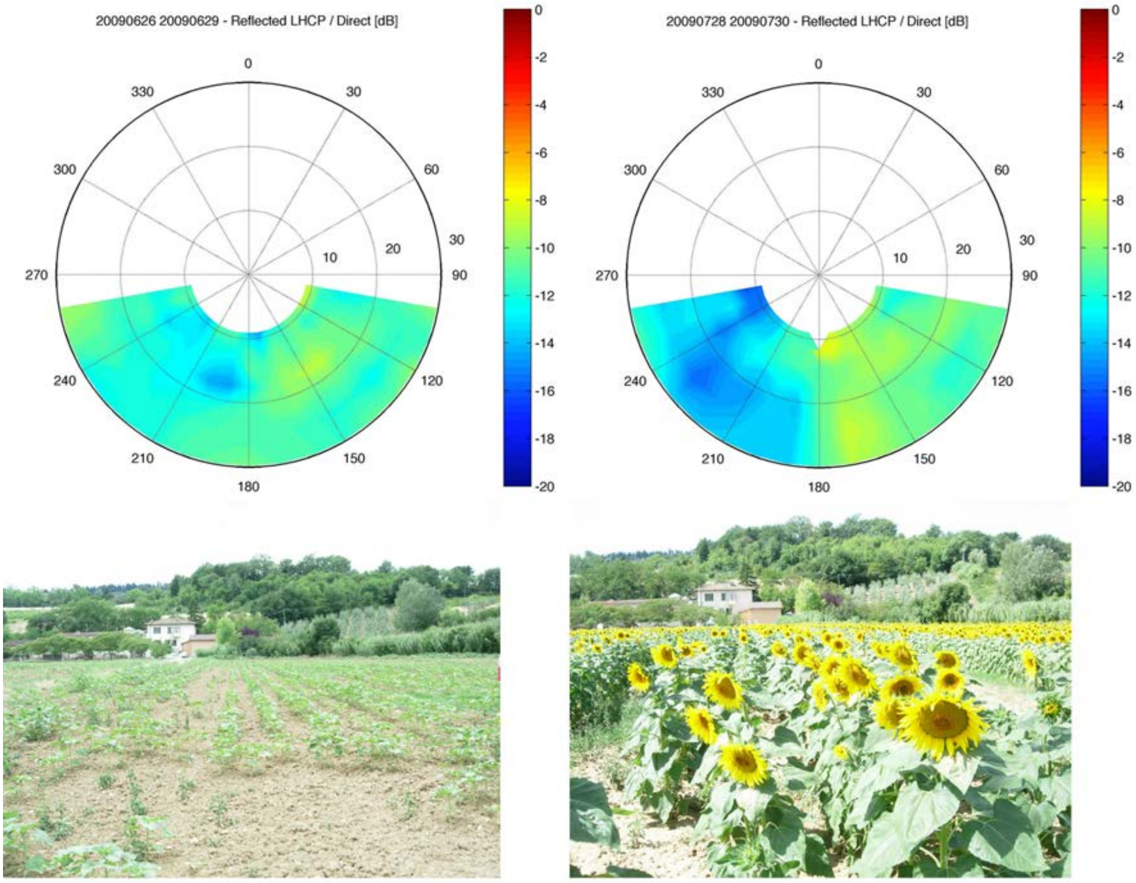

(a)

(b)

Figure 8.18: Measured Γ'_{rl} reflection coefficient spatial distribution for two moments during the sunflower development period: (a) sprouting sunflowers, DoY 140; (b) fully developed sunflowers, DoY 199. The polar plots show the azimuth angle in the angular dimension, and the distance with respect to the boom position in the radial coordinate. The Γ'_{rl} intensity is shown according to the color scale presented at the right of the plots.

8.2.5 GNSS-R Sensitivity to Soil Bio-Geophysical Parameters

In order to determine quantitative indicators of the relationship between GNSS-R signals and land bio-geophysical parameters, the apparent reflectivity values were compared to the soil moisture FDR probes mean values and to the *in situ* plant-related measurements. This sensitivity analysis was done over a dataset of 25 periods of 3 days, distributed over the whole duration of the campaign. The date ranges were selected such that the land conditions could be considered constant during each observation period.

For the analysis of soil moisture sensitivity, the selected period comprised from early April until early June (DoY 90–150). During this period both East and West fields remained bare and a complete soil moisture cycle was covered as a consequence of the seasonal rains in the area. The soil roughness conditions were relatively stable during the whole period in the West field, whereas on the East field, different labour conditions lead to changes on this parameter. This allowed to observe the coupled effect on GNSS-R signals of SMC and roughness. For the analysis of the vegetation development, the period corresponding to the whole sunflower's growing cycle was selected, i.e. between mid-June and early August (DoY 165–210). The PWC was considered, as it is the main parameter representing the above ground biomass. Similarly to the temporal signal analysis, the GNSS-R data were separated among the East and West fields and averaged over a varying range of incidence angles to reduce the uncertainty in the final measurements.

For the SMC analysis, low incidence angles were considered, i.e., between 5° and 25°, as those are the ones that provide a higher sensitivity to this parameter. In the same way, for the analysis of vegetation biomass, higher incidence angles are inspected, i.e., between 35° and 45°, to allow GNSS reflected signals to traverse a longer path through a vegetation layer.

Figure 8.19 gathers the scatter plots of the measured reflection coefficients vs SMC. The sensitivity to soil bio-geophysical parameters was obtained by fitting a linear model to the data. The linear models for the East and West fields are shown as dashed lines in the graphs. For the SMC, low incidence angles were considered, i.e. between 5° and 25°, as those are the ones that provide a higher sensitivity to this parameter. For Γ'_{rl}, Fig. 8.19(a), the sensitivity was determined to be 0.44 dB/SMC(%) for the West field, with a correlation coefficient of $r = 0.82$. For the East field the sensitivity and correlation coefficient decrease due to changes in surface roughness conditions, 0.23 dB/SMC(%) and $r = 0.53$. In the case of Γ'_{rr} both sensitivity and correlation with respect to soil moisture are very low, as can also be observed from Fig. 8.19(b). On the contrary, it was found that the ratio Γ'_{rl} over Γ'_{rr} presents a high correlation coefficient with soil moisture content; the joint correlation coefficient for both the East and West fields yields 0.91, even for varying surface roughness, and the sensitivity is 0.2 dB/SMC(%). This demonstrates that GNSS-R polarimetric measurements can mitigate the effect of surface roughness on soil moisture observables with high sensitivity to this parameter, which makes them a promising parameter for SMC remote sensing applications.

The results for the sensitivity analysis to above ground biomass are shown in Fig. 8.20. In this case, the range of incidence angles averaged to obtain the sensitivity comprises between 35° and 45°, in order to allow a longer transition path of the GNSS impinging waves through the vegetation layer. The correlation coefficient for Γ'_{rl} with respect to PWC is 0.9 and the sensitivity 0.40 dB/(kg/m^2), whereas for Γ'_{rr} the correlation coefficient equals 0.78 and the sensitivity 0.38 dB/(kg/m^2), which clearly indicates an attenuation effect of vegetation, as discussed in sec. 4.3.2.2. This common behavior in both polarizations implies that, unlike for SMC, the ratio of the reflection coefficients does not present a clear correlation with PWC.

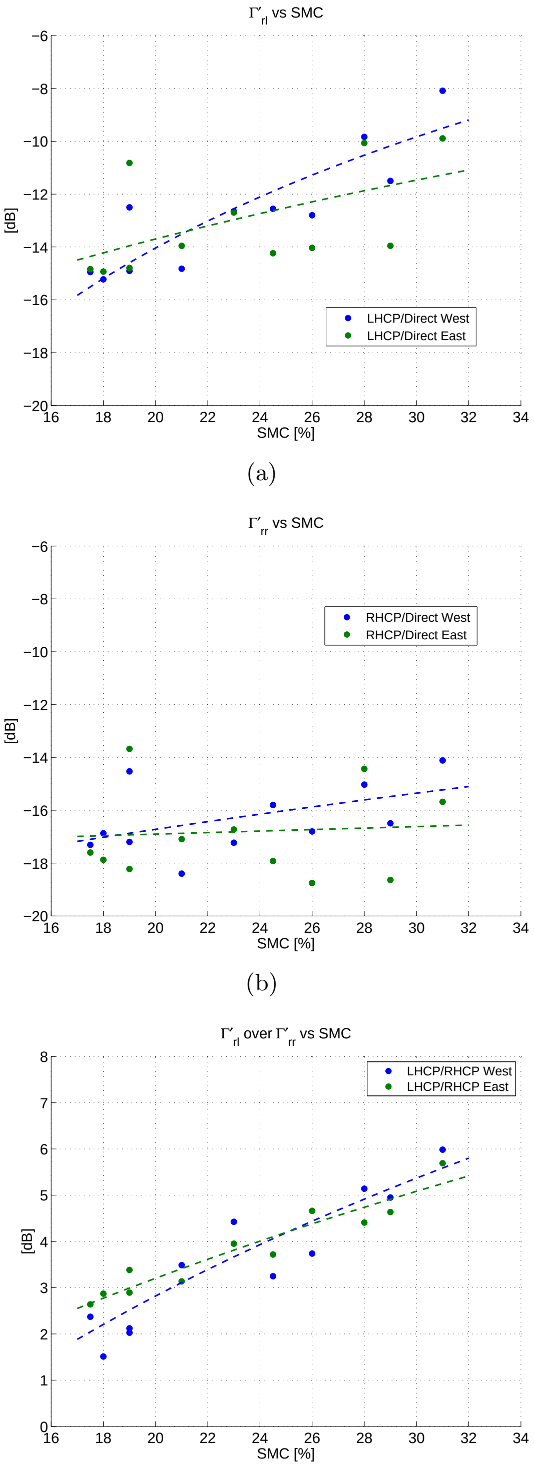

(a)

(b)

(c)

Figure 8.19: Scatter plots of the measured reflectivity coefficients vs SMC: (a) Measured Γ'_{rl} vs SMC; (b) Measured Γ'_{rr} vs SMC; (c) Measured Γ'_{rr} over Γ'_{rl} vs SMC. In green and blue the measured reflectivity coefficients for the East and West fields, respectively.

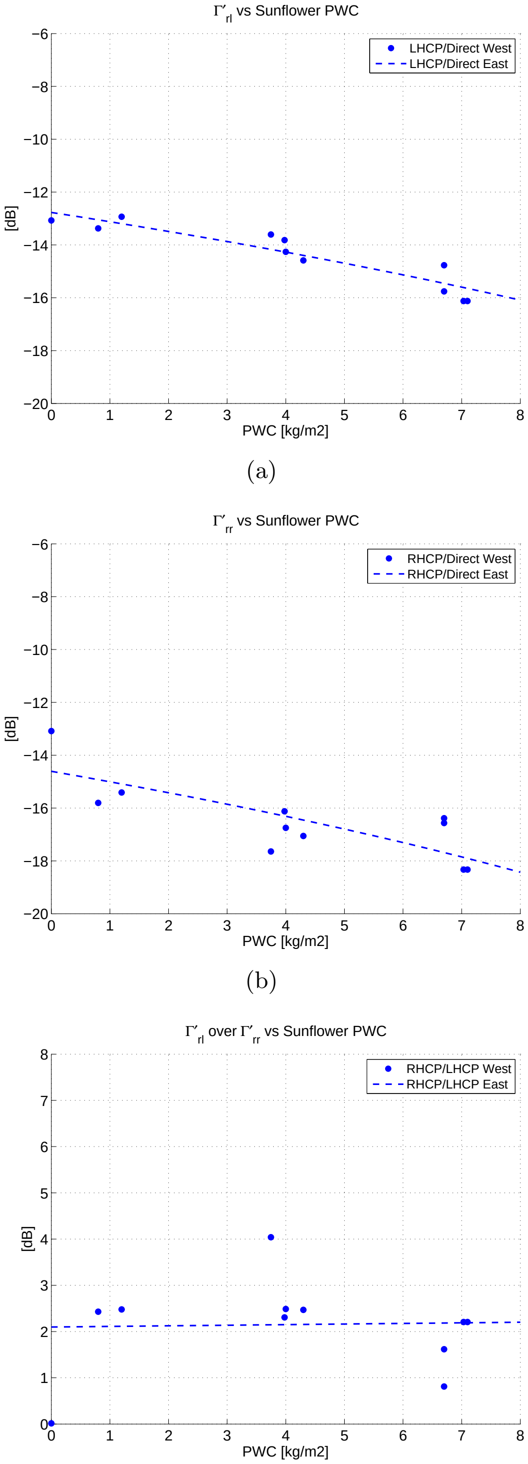

(a)

(b)

(c)

Figure 8.20: Scatter plots of the measured reflectivity coefficients vs PWC: (a) Measured Γ'_{rl} vs PWC; (b) Measured Γ'_{rr} vs PWC; (c) Measured Γ'_{rr} over Γ'_{rl} vs PWC. In green and blue the measured reflectivity coefficients for the East and West fields, respectively.

8.2.6 Bio-Geophysical Parameters Estimation

Soil moisture and plant water content were estimated based on the soil scattering model presented in section 5.5.3. Eqn. (5.49) was implemented within a least-mean squares minimization function to invert the reflectivity measurements and obtain the geophysical parameters. Soil moisture values were calculated for the date periods presented above comprising between DoY 90 and 150, whereas PWC was obtained for date periods between DoY 165 and 210.

Parameters such as the direct and reflected antenna temperatures were set according to the instrument's characteristics. For the calculation of the additional noise term in Eqn. (8.10), T_i was set to the selected coherent integration time, i.e., 20 ms, and B was defined as the front-end's IF bandwidth, i.e., 4 MHz. The direct and reflected antenna noise temperatures were selected according to the values presented in Tables 5.1 and 5.2. The antenna cross-polarization isolation was defined according to the manufacturers specifications. After a characterization in an anechoic chamber, the cross-polarization isolation at boresight was determined to be -17 dB for both LHCP and RHCP down-looking antennas. The incoming signal cross-polarization was set to -23 dB, according to the 1.2 dB axial ratio specified in the GPS Interface Specification Document [GPSW, 2010].

Based on this model, the soil dielectric constant was estimated as the one providing an optimum fit to the data for the considered date period. For SMC the ratio between the *rl* and *rr* apparent reflectivity was used as it is more stable with respect to roughness variations. As in the previous section, high incidence angles, i.e., between 5° and 25°, were used as for the estimation of SMC. Regarding PWC the apparent *rl* reflectivity was selected given its higher stability and correlation coefficient with vegetation biomass. In this case, incidence angles between 25° and 45° were selected as they provide a longer transient path through vegetation, and therefore higher sensitivity.

Figure 8.21 gathers the results for the estimation of the soil dielectric constant as a function of the ground-truth SMC. As in the case of the SAM experiment, and as predicted by semi-empirical models available in the literature, [Hallikainen et al., 1985; Wang and Schmugge, 1980], the estimated permittivity follows a quadratic relationship with respect to soil moisture, see Fig. 8.21(a). A quadratic fit was applied to the data in order to be able to link both SMC and permittivity. The quadratic fit was used to finally obtain the estimated soil moisture values, shown in Fig. 8.21(b). As the soil moisture values were calculated based on the optimum quadratic fit, the bias of the estimated parameters with respect to the measured SMC is null. In any case, the high correlation coefficient achieved, $r = 0.93$, clearly indicates the capabilities of GNSS-R polarimetric for the estimation of soil moisture.

In a similar approach, the PWC was estimated based on the attenuation caused by the presence of vegetation. As discussed in section 5.5.2, this attenuation can be expressed as a function of the vegetation optical depth, which in turn depends on the PWC through a linear relationship, as shown in Eqn. (5.44). The b parameter governing this equation depends on the vegetation type, and as mentioned in [Kerr et al., 2012] it ranges within 0.12 ± 0.03 for most crops and low vegetation types. In this case, the attenuation introduced by vegetation could not be reproduced by this range of the b parameter due to the combined effect of the coherent and incoherent scattering component, which causes

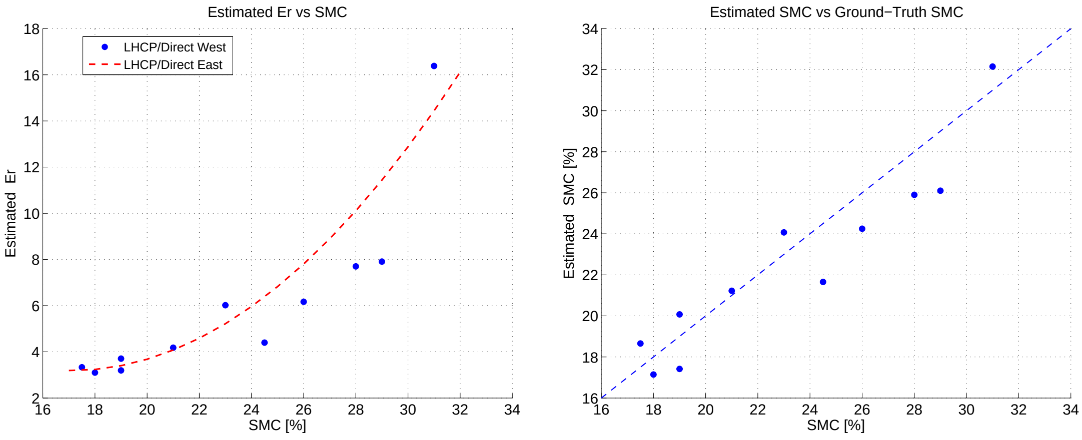

(a) (b)

Figure 8.21: Soil Moisture Content estimation: (a) Estimated ϵ_r vs Ground truth SMC. (b) Estimated SMC vs Ground truth SMC.

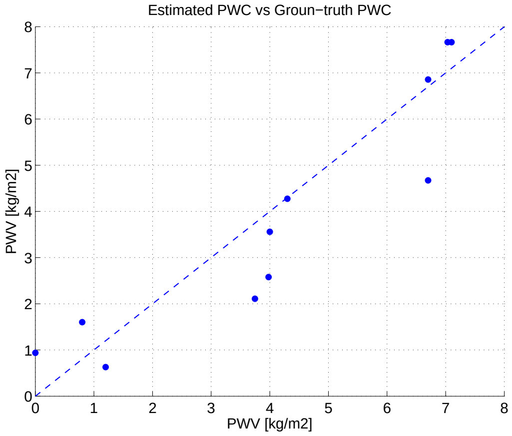

Figure 8.22: Plant Water Content Estimation: Estimated PWC vs measured PWC.

the attenuation to be lower than expected for the observed PWC range. Manipulating Eqn. (5.44) it can be found that:

$$\ln(\gamma) = -\frac{2 \cdot \tau_0}{\cos\theta} = -\frac{2 \cdot b \cdot \mathrm{PWC}}{\cos\theta} \; . \tag{8.11}$$

Adjusting this linear relationship, it was found that the b value that reproduces the observed attenuation equals 0.04. Having defined this parameter, the PWC can be readily inverted. The estimated PWC with respect to the measured vegetation PWC values are shown in Fig. 8.22. As in the case of SMC, the high correlation coefficient, $r = 0.91$, suggests the capabilities of GNSS-R for monitoring vegetation biomass.

Further developments are, however, necessary in order to find a joint inversion algorithm that would allow to simultaneously obtain soil moisture and plant water content estimates. As discussed in previous section, both parameters have similar effects on the apparent reflectivity measurements. Because of this, other type of observables would be necessary in order to be able to separate the contribution of both parameters.

8.3 GRASS Experimental Campaign Data Analysis

As mentioned in the previous section, during the GRASS experimental flights, GNSS-R raw data, i.e. the bitstreams for both the direct and reflected signals, were recorded on the SAM GNSS-R instrument for on-ground post-processing. A total of more than 65 GBytes of data were recorded during the 3 GRASS scientific flights.

The GNSS-R data processing was performed in several steps, from the raw-data down to the geo-located calibrated reflectivity values. As explained for the SAM experiment, the processing is based on the CStarlight software. The direct and reflected complex waveforms are obtained every coherent integration time, set to 20 ms. The selection of the coherent integration is explained further in the next subsection. After the decoding of the GNSS signals, the data is geo-located attending to the specular reflection point position, obtained as the point of minimum distance over the Earth's surface between the GPS transmitter and receiver. This was calculated in batches of 0.1 seconds. In order to prevent fluctuations on the reflectivity measurements due to the aircraft's attitude, the INS information were used to flag the reflectivity estimates; data where the pitch or roll angles were greater than 5 degrees were discarded from the analysis. The final processing stage entails the calculation of the averaged Γ'_{rl} and Γ'_{rr} apparent power reflectivities for the different terrain classes provided in external classification maps. These data are finally used to estimate the sensitivity of GNSS-R signals to land bio-geophysical parameters.

8.3.1 Coherent Integration Time Selection

The coherent integration time to process the cross-correlation waveforms was selected based on the GRASS scenario characteristics. As explained in section 3.4, setting the integration time is equivalent to applying a band-pass filter to the received signal. This has the effect of neglecting contributions from points on the glistening zone whose Doppler frequency differs in more than $1/T_i$ with respect to the one of the specular point. During the correlation time it is assumed that the surface remains frozen, and therefore the contributions of the surface to the received signal should have phase coherence. The surface coherence time can be calculated as:

$$T_c = \frac{R \cdot \lambda}{D \cdot v_R}, \tag{8.12}$$

where R is the range between the surface and the receiver, λ is the wavelength, D is the effective diameter of the active scattering area, and v_R is the receiver's speed. Considering the GRASS scenario, for a nadir or close to nadir observation, T_c yields an approximate value of 4 to 5 ms provided that the limiting factor of the active scattering area is limited by the antenna pattern (antenna beamwidth = $\pm 35°$, $R = 100$ m, $\lambda = 0.19$ m, $D = 2 \cdot 70$ m, and $v_R = 35$ m/s).

The iso-delay and iso-Doppler contours for this scenario are shown in Fig. 8.23. The delay and Doppler values are provided with respect to the specular point. The green arrow shows the flying direction of the receiver, arbitrarily selected towards the East, whereas the blue arrow shows the direction of the azimuth direction of the selected PRN satellite. As can be seen, the iso-Doppler lines are nearly perpendicular to the

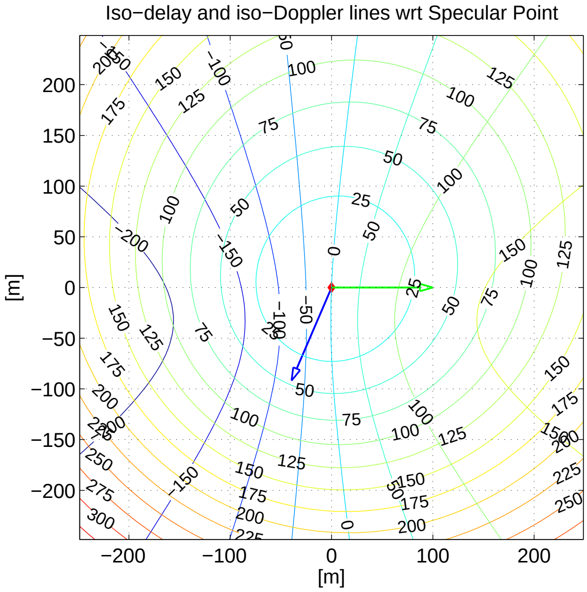

Figure 8.23: Simulated Iso-delay and iso-Doppler lines for a GRASS airborne scenario. The green vectors depicts the platform movement direction, and the blue vectors show the azimuth direction of the corresponding satellite.

receiver's motion direction, while the iso-delay ellipses are oriented along the scattering plane defined by the GPS satellite, the specular point, and the receiver position.

When the coherent integration time is increased, the size of the surface observed by the GNSS-R is reduced accordingly. With a coherent integration time of 1 ms, the available Doppler bandwidth is of (-500,+500) Hz with respect to the specular point's Doppler frequency. The 500 Hz iso-Doppler lines are far away from the specular point in the GRASS configuration, thus the antenna beam is the limiting factor of the active scattering area. Selecting a coherent integration time of 20 ms the Doppler bandwidth is reduced to (-25,+25) Hz, limiting the glistening zone to a narrow stripe on the surface around the specular point. The glistening zone is reduced by a factor of 6 along the receiver's flying direction, which contributes to increase T_c to 10 ms. It should also be considered here that the scattering from land surfaces is highly influenced by the coherent component. As discussed in previous chapters, the coherent scattering components comes essentially from the first Fresnel zone, which will contribute to reduce even further the active scattering area, thus contributing to an additional increase on the surface coherence time.

Attending to the reasoning presented above, a final coherent integration time of 20 ms was selected for the GRASS experiment. Selecting a high integration time has two main implications; firstly, as more points away from the specular one are neglected with higher integration times, the incoherent scattering component is reduced in the finally observed signal. And secondly, the SNR of the processed direct and reflected waveforms is increased given the reduction of the effective noise bandwidth. These two aspects contribute to the improvement of the final observables for geo-physical parameters.

8.3.2 Specular Points Reflectivity Analysis

As mentioned in the previous section, the GNSS-R reflectivity data were incoherently averaged in batches of 0.1 seconds. The specular points' coordinates on the surface were calculated according to the mean aircraft's position during these periods. The Γ'_{rl} and Γ'_{rr} reflectivity measurements were represented over Google Earth images in order to relate features on the surface with the retrieved apparent reflectivity values.

In Fig. 8.24 Google Earth images of the Ponte a Elsa test site are provided. The specular points were represented over the images with a color coding according to their reflectivity. The color scale ranges from reflectivity values between 0.1 (red) and 0.75 (blue); red specular points correlate with very dry or densely vegetated fields, whereas blue specular points coincide with very wet surfaces or water bodies. Figure 8.24(a) depicts the measured Γ'_{rl} reflection coefficient. As can be observed, the specular points in the image colored in blue correspond to the river location. The rapid transition of low to high reflectivity values suggests the existence of a strong coherent scattering component concentrated about a narrow area around the specular point, i.e., the First Fresnel zone. Fig. 8.24(b) shows some of the obtained Γ'_{rr} reflectivity values. In this case, reflectivity variations are not as obvious as for Γ'_{rl}, since the measured reflectivity values are close to the color scale lower range. For example, the increase in reflectivity due to the presence of water is very moderate if compared to the Γ'_{rl} reflection coefficient.

The panels in the bottom row of the figure show data from the November campaign, i.e., Flight 3. In this case Γ'_{rl}, Fig. 8.24(c), shows higher values than in Flight 2, due to a generally higher soil moisture content in the area. In this image it is also noticeable the very low reflectivity values of specular points over forested and densely vegetated areas, that confirms the expected vegetation attenuation effect on the GNSS reflected signals. Fig. 8.24(d) depicts the Γ'_{rr} reflection coefficient, which, as in the previous case, does not show a clear correspondence with features in the area apart from a transition of a specular point track over the river and an artificial irrigation pool.

The last of these set of images are shown in Fig. 8.25. The depicted specular points correspond to data acquired during Flight 4 over the Forcoli area. In Fig. 8.25(a) Γ'_{rl} is shown. A clear sensitivity to the presence of vegetation can be observed as the measured reflectivity experiences a strong increase when the specular points transit from a densely vegetated poplar plot to a bare or scarcely vegetated field (top right in the image). For Γ'_{rr}, Fig. 8.25(b), the transition takes place at a different moment during the flight. Despite this effect being dimmer than in the previous case, a decrease in the reflectivity can also be detected.

The variation on reflectivity due to the transit of the specular points to or from a densely vegetated area is better observed in Fig. 8.26 where the Γ'_{rl} and Γ'_{rr} reflection coefficients are depicted against acquisition time. In Fig. 8.26(a), the measured reflectivity for three PRN satellites is represented for a take in which the specular point moves from Field 9 of the Forcoli Test site (350 t ha^{-1}) to a bare field. This corresponds to the take of the tracks on the top right corner of Fig. 8.25(a). The Γ'_{rl} reflection coefficient experiences an increases of almost 10 dB for the three PRNs, clearly showing a strong sensitivity of GNSS-R signals to the presence of vegetation. In Fig. 8.26(b) Γ'_{rr} is depicted for a take with a transient from a bare field to Field 9. In this case a moderate decrease of about 2 to 3 dBs is observed, depending on the PRN.

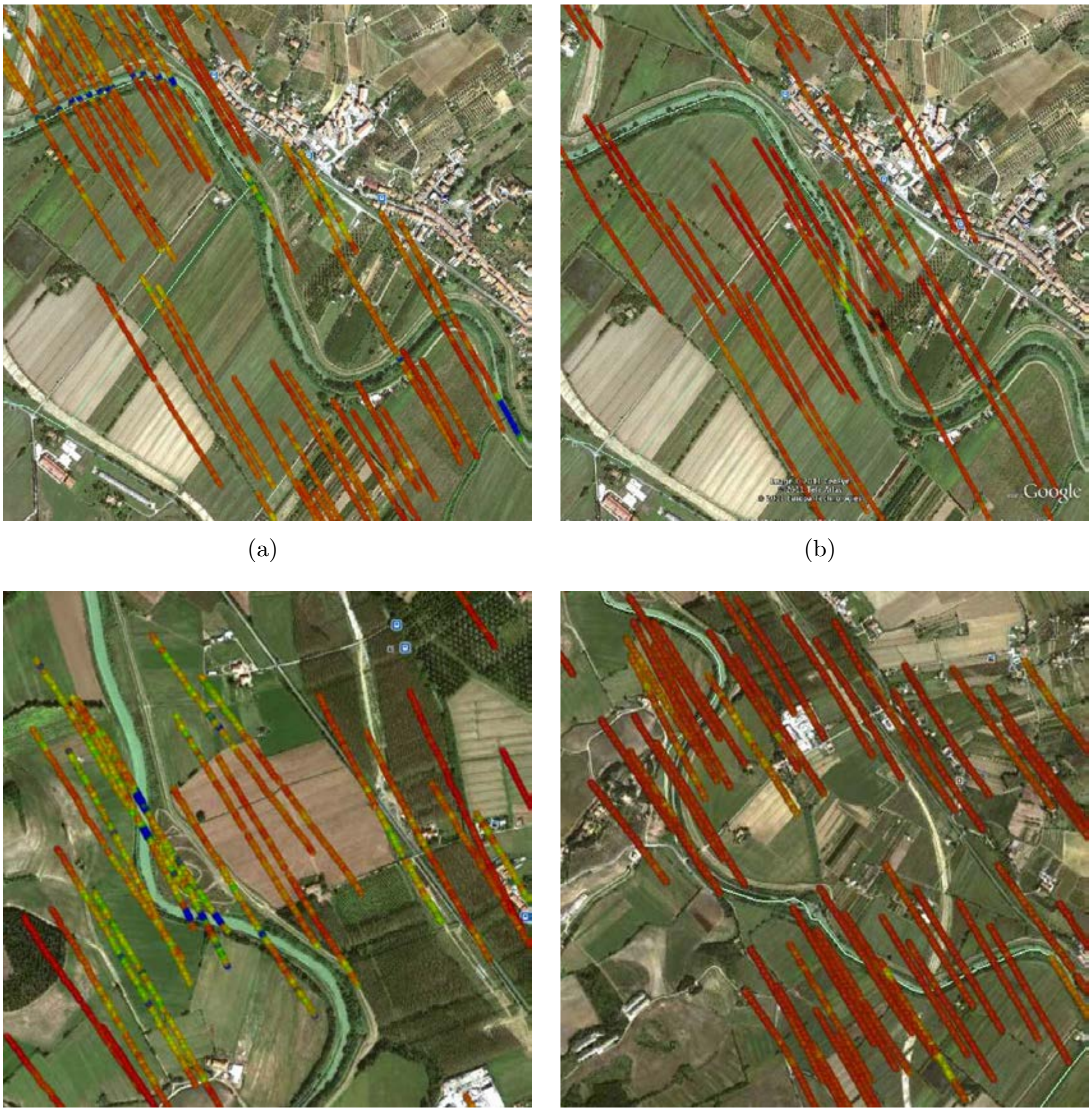

(a) (b)

(c) (d)

Figure 8.24: Geo-referenced specular points over Google Earth images of the Ponte a Elsa Test site. (a) and (b) panels correspond to the measured Γ'_{rl} and Γ'_{rr} apparent reflectivities during the July campaign, whereas panels (c) and (d) show Γ'_{rl} and Γ'_{rr} for the November campaign. The color scale corresponds to the intensity of the reflection coefficients within the range 0.1 (red) up to 0.75 (blue).

(a) (b)

Figure 8.25: Geo-referenced specular points over Google Earth images of the Forcoli Test site. (a) Γ'_{rl} and (b) Γ'_{rr} apparent reflectivities during Flight 4. The color scale corresponds to the intensity of the reflection coefficients within the range 0.1 (red) up to 0.75 (blue).

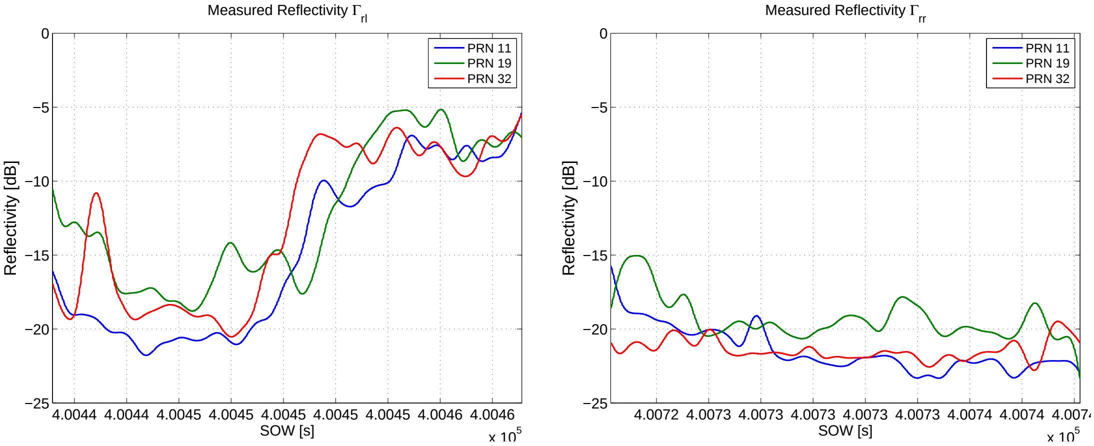

(a) (b)

Figure 8.26: Temporal variation of the (a) Γ'_{rl} and (b) Γ'_{rr} apparent reflectivities, for a transient of specular points from a bare surface to a densely vegetated poplar plot.

The analysis presented above was useful to link specular points reflectivity variations with features on the surface, in agreement with what is expected from theory. The correct functioning of the instrument and data processing chain could also be verified. The strong decrease in the measured reflectivity when the specular points move over a densely vegetated area suggests the sensitivity of GNSS-R signals to forest above ground biomass. However, a more detailed analysis of the reflection coefficients and their comparison with the ground-truth data was done in order to asses the capabilities of the technique for potential retrieval of biomass with this remote sensing technique.

8.3.3 GNSS-R and Ground Truth Data Comparison

The comparison between the GNSS-R and the ground-truth data was performed for each experimental test-site according to the terrain classification maps. The Ponte a Elsa classification maps for the July and November campaigns are provided in Fig. 7.7(a) and Fig. 7.7(b), respectively. The classification map of the Forcoli test-site is shown in Fig. 7.8. The GNSS-R data were grouped according to the terrain classes of each specific specular point position. GPS satellites with an incidence angle up to 45° were allowed in order to observe the angular dependence of the Γ'_{rl} and Γ'_{rr} reflection coefficients. For the determination of the GNSS-R sensitivity to soil bio-geophysical parameters, five representative classes were selected for each test-site. The analysis of the retrieved reflectivities for each of these fields is provided in the next paragraphs.

8.3.3.1 Ponte a Elsa – 1st Flight Campaign – July 2011

The most relevant information for the five selected terrain classes in the Ponte a Elsa test-site during the July experimental campaign are gathered in Table 8.2. The measured Γ'_{rl} and Γ'_{rr} reflection coefficients for each one of the fields are shown together with a picture at the moment of the campaign in Fig. 8.27.

The mean Γ'_{rl} and Γ'_{rr} apparent reflectivities, represented as solid blue and green lines in the plots, respectively, were calculated as the incoherent average of all specular points within the terrain class under analysis. Each data point on the graphs corresponds to an average reflectivity value for each PRN satellite in view. The incidence angle associated to this measurement was calculated as the mean incidence angle of that given satellite. The dashed lines are the associated standard deviation for each averaged reflectivity measurement. In order to prevent misinterpretations of the data caused by data points with few observations, a linear regression model was fit to the measured reflection coefficients, weighted by the number of observations of each data point. The linear regression models are represented by solid-crossed lines on the graphs.

The first terrain class analyzed for the July campaign on the Ponte a Elsa test-site corresponds to a ploughed and uncultivated field, Field 9, see Fig. 8.27(a) and 8.27(b). The high surface roughness, 2.7 cm, and the very low soil moisture content of the field, SMC = 8.5%, make the Γ'_{rl} reflection coefficient to have very low values, and close to the Γ'_{rr} reflectivity, with just a difference of 3 dB.

Fields 10-16-17-C5 correspond to a terrain class of developing sunflower, Fig. 8.27(c) and 8.27(d). Despite of the presence of developing vegetation, Γ'_{rl} is higher than in the previous case due to a higher SMC, i.e. 18%. The difference of Γ'_{rl} with respect to Γ'_{rr}

increases to 5 dB for low incidence angles due to the aforementioned increase in soil moisture.

The third selected class corresponds to a barley field; Field 11 in the test-site classification map. See Fig. 8.27(e) and 8.27(f) for a picture of the field and the incidence plots of the measured reflection coefficients. At the time of the campaign this crop was already dry, and therefore the plant water content was very low. This makes the attenuation of GNSS reflected signals due to the presence of vegetation to be very weak. Γ'_{rl} increases over -15 dB at the same time that Γ'_{rr} decreases, resulting in a total difference between polarization of 7 to 8 dB for low incidence angles.

The last two selected fields for the first experimental campaign were a sugar-beet field and the four poplar plots present in the area, see figures 8.27(g) to 8.27(j). Despite the fact that the terrain classes are very different among each other, the reflectivity values for both fields yield similar results. This could be due to the combination of several factors. On one hand, the attenuation of the vegetation layer on the poplar plots should be higher than the one of the sugar beet, however, the soil moisture content could also be higher. In addition, the small dimensions of the poplar plots in the Ponte a Elsa test-site could lead to a mixed pixel effect on the measured reflectivity for that terrain class. The currently available information did not allow to extract conclusions about the nature of these results.

8.3.3.2 Ponte a Elsa – 2nd Flight Campaign – November 2011

Given the occurrence of seasonal rains in the area during the months of September and October, the second campaign was characterized by a generalized high soil moisture content over the whole experimental test-site. Table 8.3 summarizes the most important geo-physical parameters for each selected terrain class. As can be observed, in this case the soil moisture in all fields was relatively homogeneous, with SMC values in some cases close to the field capacity. The results for the measured reflection coefficients are gathered in Fig. 8.28.

The first analyzed terrain class corresponds to a grazed alfalfa field, Fig. 8.28(a) and 8.28(b). As can be observed from the image, in this case the soil is very smooth in this case with some scarce residual vegetation. The high soil moisture content and low surface roughness makes the Γ'_{rl} reflection coefficient to have very high values with an almost flat trend with incidence angle. At the same time, the cross-polarized reflectivity, Γ'_{rr}, is about 10 dB lower than Γ'_{rl} due to the high soil moisture content. This difference is remarkably higher than the one observed for the LEiMON experiment due to the improvement in the instrument's sensitivity.

The second class corresponds to bare arrowed fields, labeled as Fields 6, 8, and C5 on the Ponte a Elsa classification map. Fig. 8.28(c) provides an image of one of these fields and Fig. 8.28(d) shows the measured reflection coefficients. The soil moisture content is very similar as in the previous case, SMC= 30%, however the surface roughness is significantly higher, $\sigma_z = 1.9$ cm. Because of this, Γ'_{rl} experiences a remarkable decrease. The difference between the reflection coefficients at both polarizations decreases, however, it is maintained around 10 dB. As observed in the LEiMON project, this result confirms the hypothesis that the co- and cross- polarization reflection coefficient ratio could be an optimum observable for soil moisture estimation, as it is significantly more robust to surface roughness variations than the individual reflection coefficients.

The third analyzed class corresponds to Field 11. This field was ploughed during the campaign, as can be observed in Fig. 8.28(e). The surface roughness is very high, around 3.3 cm, which makes the Γ'_{rl} reflectivity coefficient to have even lower values than in the previous case, see Fig. 8.28(f). The steep increase towards higher incidence angles is due to the fact that the effective surface roughness decreases with the cosine of the incidence angle. This can also the observed in Γ'_{rr}. The difference between both reflection coefficients decreases with respect to the previous case, partially due to a decrease in soil moisture, and partially due to the effect of such as high surface roughness. This can be linked to the fact that the instrument's limited sensitivity prevents the measurement of reflectivity values below a certain threshold. This affects in particularly the Γ'_{rr} component and can therefore avoid the ratio of reflection coefficients to be completely independent of the surface roughness. In addition, the presence of an incoherent scattering component due to the high surface roughness could also affect the polarization ratio. This will be explained deeper in the next section.

The fourth field had similar soil conditions to the first one, with high soil moisture content and a relatively smooth surface roughness, see Fig. 8.28(g). The obtained Γ'_{rl} and Γ'_{rr} reflection coefficients for this field, Fig. 8.28(h), have similar values to the ones obtained for the first class, Fig. 8.28(b). As in the previous case, the difference between the reflection coefficients at both polarizations is around 10 dB, due to high SMC.

The fifth class corresponds to the poplar plots in the Ponte a Elsa area. In this case, due to the acquisition scheme of the GNSS-R instrument, those fields could not be sampled with the reflected LHCP polarization, thus only the Γ'_{rr} reflection coefficient could be obtained for this class. In comparison to the Summer campaign, a moderate increase of 2.5 dB is observed in this case due to higher soil moisture conditions.

8.3.3.3 Forcoli Area – 2nd Flight Campaign – November 2011

The selection of fields over the Forcoli area was based on the identification of a sufficiently representative range of above ground biomass to assess the sensitivity of GNSS-R signals to this parameter. The fields were also selected according to their specular point sampling; a statistically representative number of specular points in both reflected polarizations on a particular field was required for the selection in order to reduce as much as possible the uncertainty of the observations. The main characteristics of the finally chosen fields are gathered in Fig. 8.4. Similar soil moisture and roughness conditions were assumed for all the fields: a high SMC, around 30% or higher, and a moderate surface roughness, $\sigma_z \simeq 1.5$ cm.

The first selected field corresponds to a mid biomass poplar plot with an AGB of 100 t ha^{-1}, see Fig. 8.29(a). The measured GNSS-R reflection coefficients, depicted in Fig. 8.29(b), show a strong decrease on the Γ'_{rl} reflection coefficient with respect to a bare field with similar surface characteristics, see for instance the measured reflectivity for Fields 6, 8, and C5 during the second flight campaign, in Fig. 8.28(d). This decrease is caused by the attenuation of the vegetation layer, and ranges from 3 dB, for low incidence angles, up to 5 dB for higher incidences. For Γ'_{rr} there is not a remarkable variation with respect to the bare soil case. The hypothesis here is that the vegetation attenuation is compensated by the generation of an additional incoherent volume scattering originated due to the presence of the vegetation.

The second field is a poplar plot with slightly higher biomass, i.e. 135 t ha^{-1}, figures Figs. 8.29(c) and 8.29(d). A moderate decrease is observed with respect to the previous case for incidence angles above 30°. However, for an incidence angle of 35°, the LR reflectivity decreases abruptly. This result could not be explained by theoretical models. It corresponds to a given track of PRN-19, which appears much lower than the rest, and could represent an outlayer in the dataset.

The third field under analysis is a poplar plot with high above ground biomass: AGB = 250 t ha^{-1}, see Fig. 8.29(e) and Fig. 8.29(f). A remarkable decrease about 2 dB in Γ'_{rl} is observed with respect to the previous cases. As in the other cases, Γ'_{rr} does not experience an appreciable variation.

Finally, the last field considered for this analysis was a densely populated forest. Physical measurements could not be done in the forest as it belongs to a private hunting reserve, however, by comparison with the poplar plot fields, its AGB was determined to be above 300 t ha^{-1}. The Γ'_{rl} and Γ'_{rr} reflection coefficients are shown in Fig. 8.29(h). As can be seen, Γ'_{rl} decreases even further with respect to the previous cases, with a total attenuation of more than 3 dB with respect to the 100 t ha^{-1} field. In addition, a decreasing trend with incidence angle is observed, related to the increasing attenuation that the GNSS reflected signals suffer with incidence angle, as the signal traverses a longer path through the vegetation. These results suggest that GNSS-R could potentially be used to observe a wide range of AGB.

Field ID	SMC	σ_z	Crop	PWV / AGB	Description
9	8.10%	2.7 cm	–	-	Ploughed, very rough
10-16-17-C5	18.00%	–	Sunflower	5 kg/m^2	Growing sunflower
11	–	–	Barley	0.1 kg/m^2	Dry barley
13	–	–	Sugar Beet	2.5 kg/m^2	Green plants
P1-P4	12.50%	–	Poplars	200 t ha^{-1}	Well developed poplar

Table 8.2: Ponte a Elsa test-site selected fields information, first airborne campaign

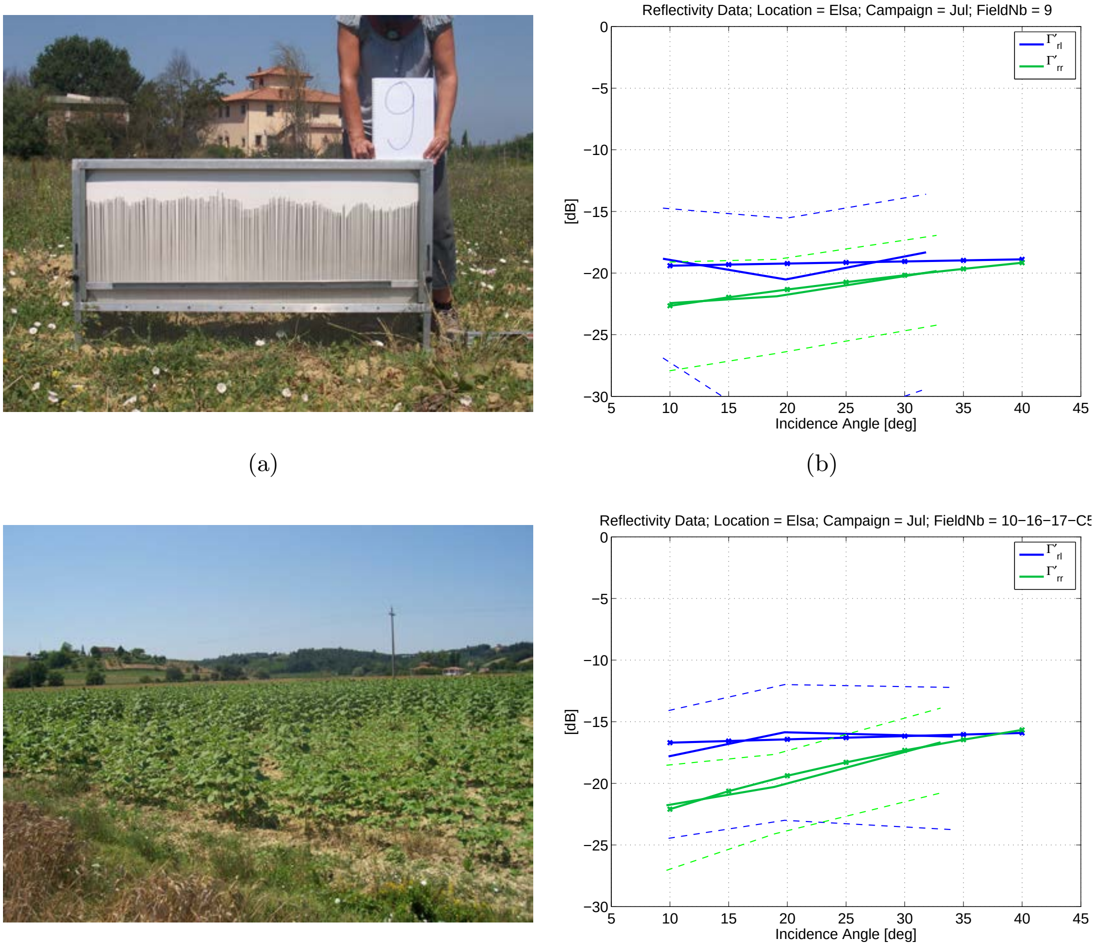

(a)

(b)

(c)

(d)

Figure 8.27: Ponte a Elsa test site - 1st Flight Campaign. Selected fields images and measured Γ'_{rl} (in blue) and Γ'_{rr} (in green). Solid lines represent the averaged reflection coefficients; dashed lines show the standard deviation with respect to the mean; solid-cross lines depict the linear regression of the measured coefficients. (a-b) Ploughed, Field 9; (c-d) sunflower, Fields 10-16-17-C5; ...

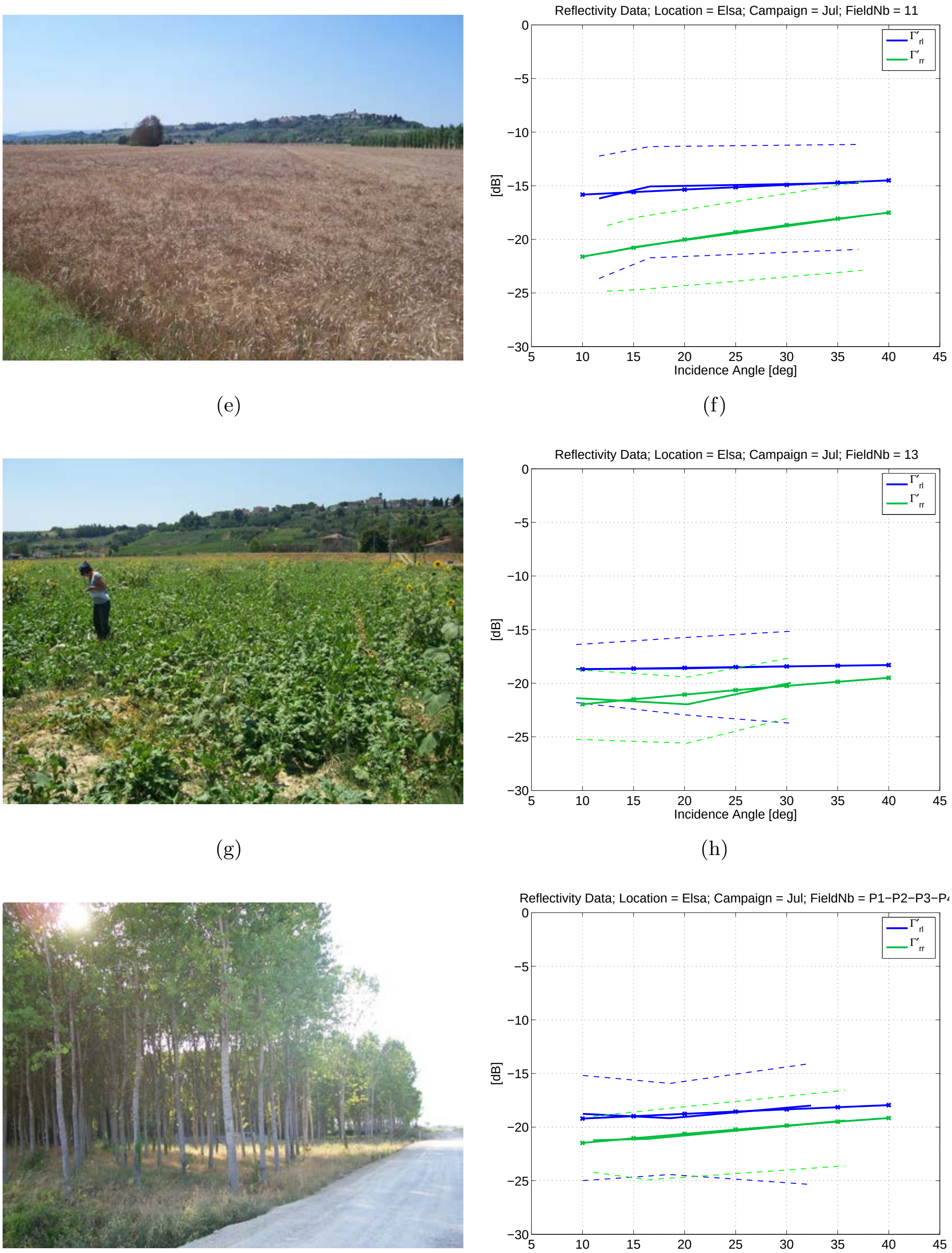

(e) (f)

(g) (h)

(i) (j)

Figure 8.27: (Cont.) (e-f) Dry Barley, Field 11; (g-h) Sugar Beet, Field 13; (i-j) Poplar plots, Fields P1-P2-P3-P4.

Field ID	SMC	$\sigma_\mathbf{z}$	Crop	PWC / AGB	Description
2, 3	28.60%	<1.0 cm	Grazed Alfalfa	–	Smooth
6 - 8 - C5	27.00%	1.9 cm	–	–	Arrowed
11	23.00%	3.35 cm	–	–	Very Rough
13	29.50%	<1.0 cm	–	–	Smooth
P1-P4	26.00%	–	Poplars	200 t ha^{-1}	–

Table 8.3: Ponte a Elsa test-site selected fields information, second airborne campaign

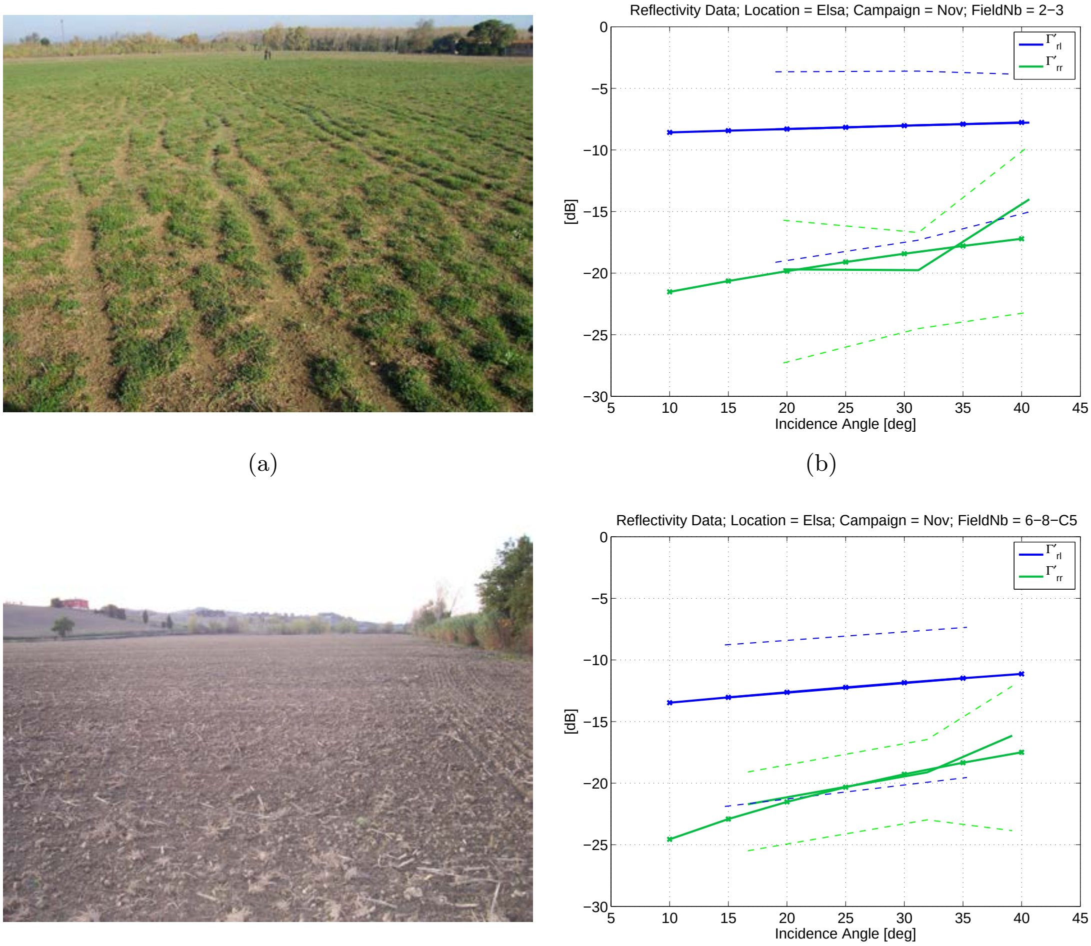

(a) (b)

(c) (d)

Figure 8.28: Ponte a Elsa test site - 2nd Flight Campaign. Selected fields images and measured Γ'_{rl} (in blue) and Γ'_{rr} (in green). Solid lines represent the averaged reflection coefficients; dashed lines show the standard deviation with respect to the mean; solid-cross lines depict the linear regression of the measured coefficients. (a-b) Grazed Alfalfa, Fields 2-3; (c-d) Bare - Arrowed, Fields 6-8-C5; ...

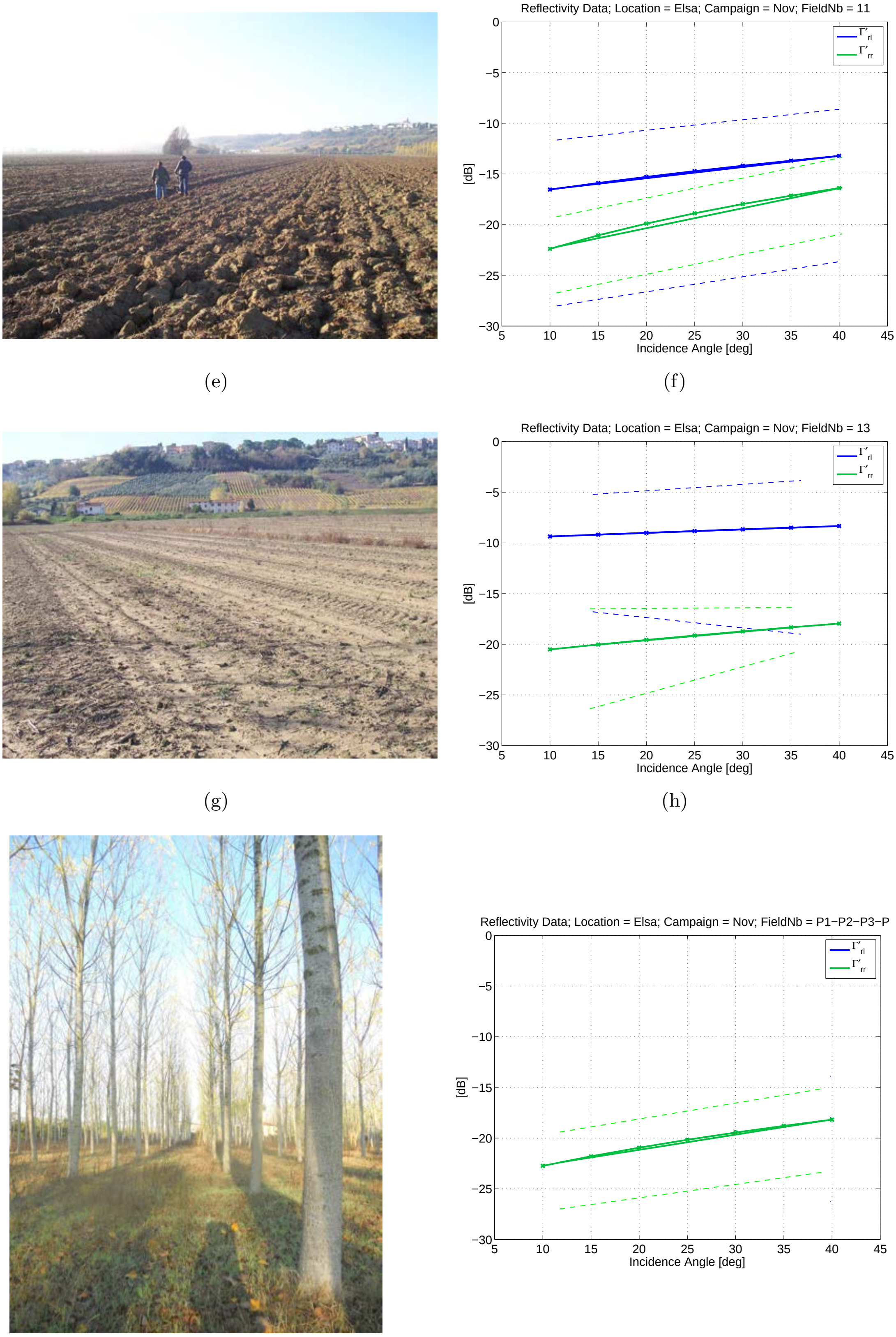

(e) (f)

(g) (h)

(i) (j)

Figure 8.28: (Cont.) (e-f) bare - very rough, Field 11; (g-h) Bare - Smooth, Field 13; (i-j) Poplar plots, Fields P1-P2-P3-P4.

Field ID	SMC	$\sigma_\mathbf{z}$	AGB	Description
11	–	–	101 t ha^{-1}	Mid biomass
4 - 7	35.60%	1.15 cm	135 t ha^{-1}	Mid/high biomass
3	–	–	250 t ha^{-1}	High biomass
Dense Forest	–	–	$>$ 300 t ha^{-1}	Very high biomass

Table 8.4: Summary of the most important field works performed during the experimental campaign

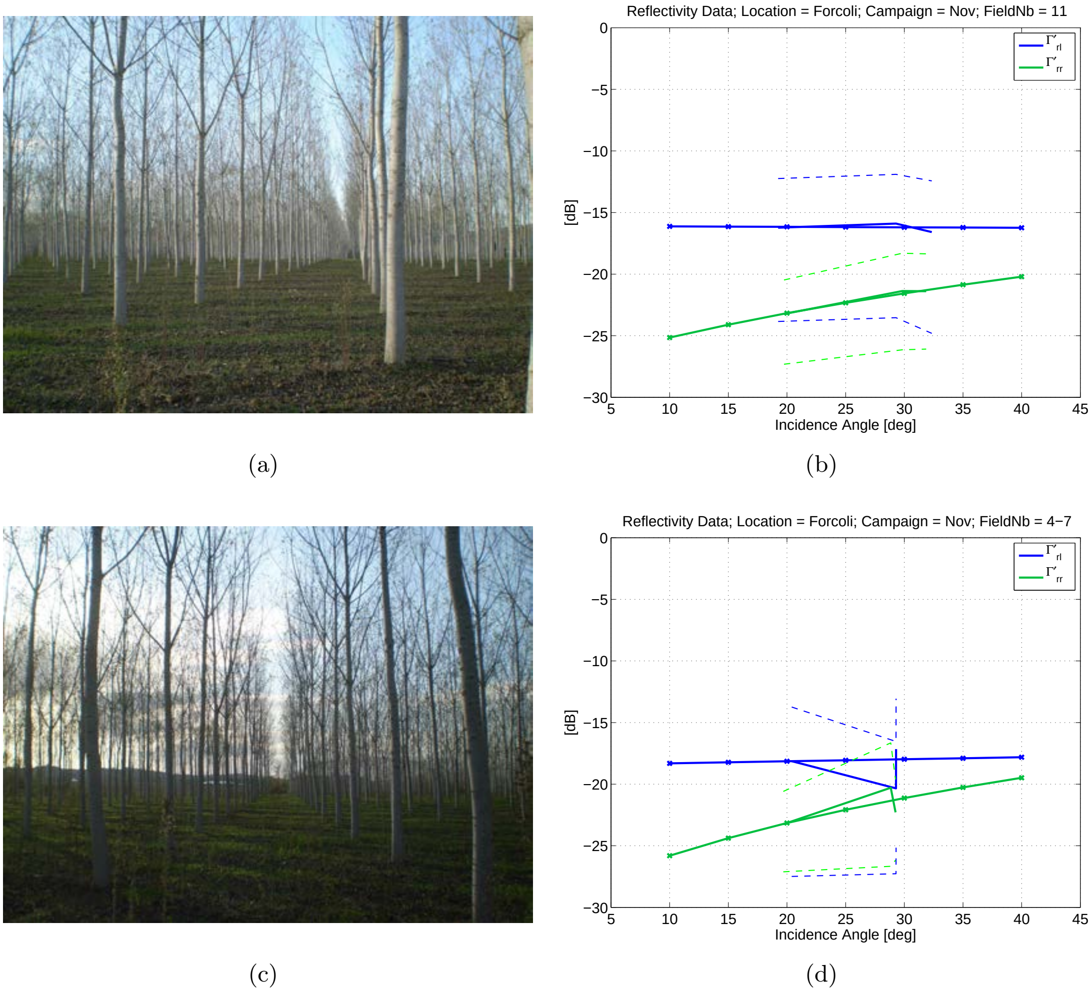

(a) (b)

(c) (d)

Figure 8.29: Forcoli test site - 2nd Flight Campaign. Selected fields images and measured Γ'_{rl} (in blue) and Γ'_{rr} (in green). Solid lines represent the averaged reflection coefficients; dashed lines show the standard deviation with respect to the mean; solid-cross lines depict the linear regression of the measured coefficients. (a-b) Mid biomass, Field 11; (c-d) Mid-High biomass, Fields 4-7; ...

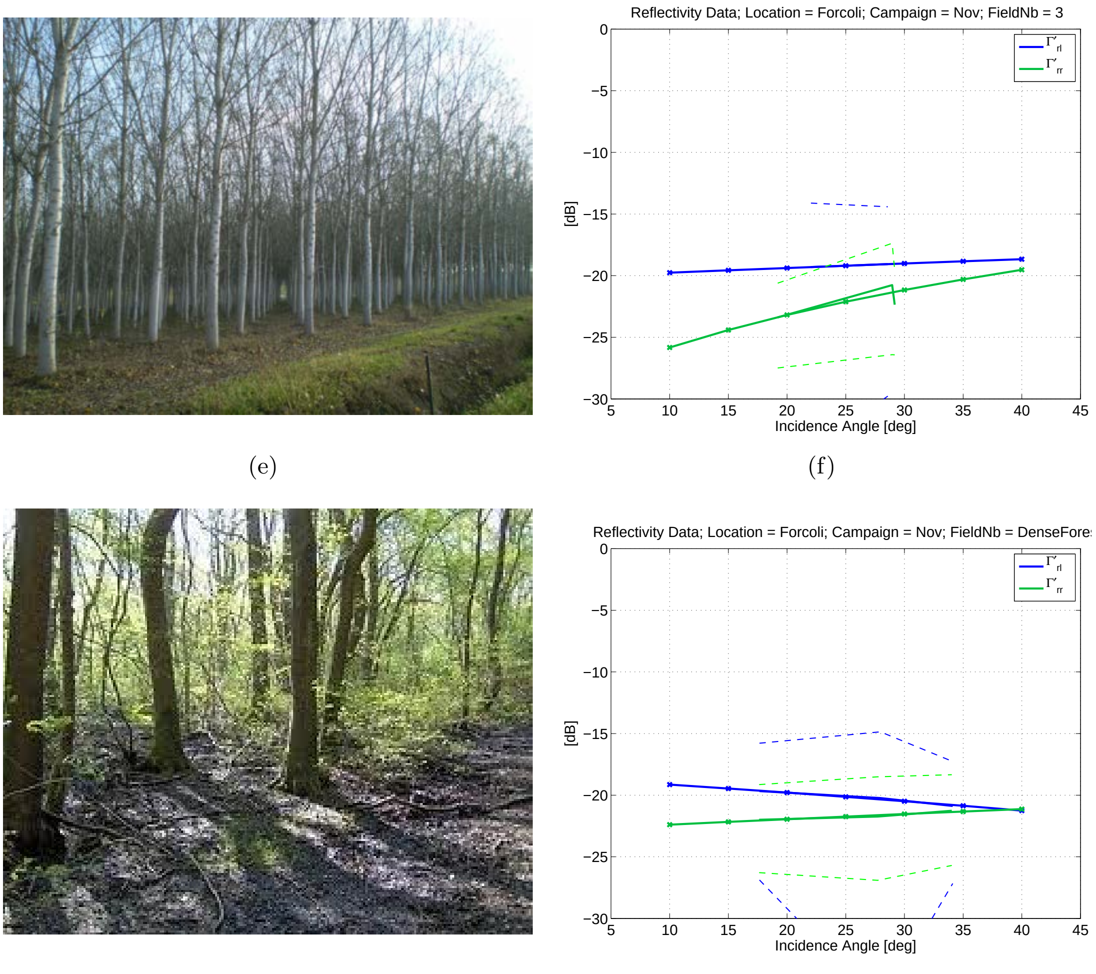

(e) (f)

(g) (h)

Figure 8.29: (Cont.) (e-f) High Biomass, Field 3; (f-g) Very High Biomass, Dense Forest.

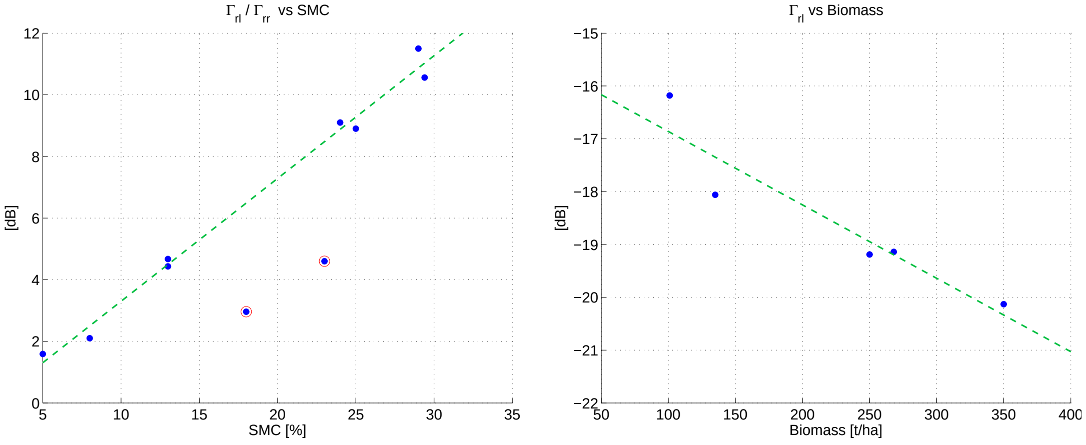

(a) (b)

Figure 8.30: Scatter plots of the measured reflection coefficients ration with respect to (a) soil moisture; and (b) above ground biomass. The dashed green line on the plot shows a linear regression to the data. The points indicated with red circles on the left plot correspond with extreme soil roughness conditions.

8.3.4 GNSS-R Signals Sensitivity to Land Bio-Geophysical Parameters

The retrieved apparent reflectivities during the GRASS experimental campaign were compared to the in-situ soil moisture and forest above ground biomass data for the determination of the GNSS-R sensitivity to this two parameters. In the case of SMC the apparent reflectivity polarization ratio was examined, as this was observed to be stable with respect to surface roughness variations. For forest above ground biomass the measured Γ'_{rl} was used, due to its higher dynamic range with respect to features on the surface. The reflectivity values considered for this analysis were obtained from the linear regression models at an incidence angle of 20°.

In Fig. 8.30(a) the reflectivity polarization ratio is depicted against the TDR soil moisture measurements for several fields on the Ponte a Elsa test-site. It is worth noting here that the dynamic range of the polarization ratio increases remarkably with respect to the LEiMON experiment due to the improvement in the instrument's sensitivity, which allowed measuring lower values of the Γ'_{rr} components. The measured correlation coefficient of the whole distribution yields a sensitivity of 0.2 dB/SMC(%) and a correlation coefficient equal to $r = 0.84$. Inspecting closely the data it can be readily observed that two of the data points, marked with a red circle in the figure, lay remarkably out of the rest of the distribution (the linear regression to these data is represented in a dashed green line on the plot). Those two data points correspond to a sunflower covered field during the July campaign, and a ploughed field during the November campaign with very high soil surface roughness ($\sigma_z = 3.3$ cm).

The previous results suggest the existence of a strong incoherent scattering component in the measured Γ'_{rl} and Γ'_{rr} reflectivity ratio caused by the presence of well developed standing vegetation and high surface roughness conditions. As discussed in section 4.3.1, when σ_z exceeds a certain value, i.e. around 3 cm, the scattering is dominated by the incoherent scattering component, see Fig. 4.9. In this extreme situation the method presented for the estimation of the GNSS-R observables fails to separate the coherent and incoherent scattering components. The measured Γ'_{rl} and Γ'_{rr} apparent reflectivity ratio is therefore no longer independent of soil roughness variations, as the effect is not common in common in both polarizations. Likewise, in the presence of vegetation, the incoherent Γ'_{rr} component increases remarkably and surpasses the coherent one even for low PWC, see Fig. 4.11. This distorts the polarization ratio and therefore decorrelates the observables from SMC. Neglecting these extreme cases from the analysis, the correlation coefficient of the Γ'_{rl} and Γ'_{rr} polarization ratio with soil moisture increases to 0.93, in agreement with the previously obtained r values for the LEiMON experimental data.

For the sensitivity analysis to forest AGB, the observed Γ'_{rl} apparent reflectivity was compared with the measured wet biomass on the field. Poplar lots at different development stages were considered in order to have a considerable variability of biomass. The Camugliano reserve was also considered for this analysis assuming an AGB for this area of 350 t ha^{-1}. The results are shown in Fig. 8.30(b). As expected, the observed Γ'_{rl} reflectivity monotonically decreases with AGB due to the increasing attenuation effect of vegetation. The observed sensitivity is around 1.5 dB/(100 t ha^{-1}) with a correlation coefficient of 0.91. Interesting to see is the fact that a saturation effect is not observed within the AGB range considered in this analysis. This could represent a major improvement with respect to conventional monostatic radars, as the backscattering coefficient at L-band is reported to saturate within the 100 to 150 t ha^{-1} range, depending on the type of forest. This difference in the saturation level to AGB of GNSS-R with respect to monostatic radars is linked to the type of scattering mechanisms observed by each system. Whereas for conventional radars the backscattering response is observed, i.e., the energy scattered in the same direction of the incident wave, GNSS-R observes the attenuation caused by the vegetation in the direction of specular reflection.

8.4 Summary and Conclusions

In the previous sections the results obtained from the analysis of the GNSS-R data were presented. The extensive dataset, gathered during the various experimental campaign allowed to compare the recorded GNSS-R signals with bio-geophysical processes, and to determine the effect of surface roughness, Soil Moisture Content (SMC), and Plant Water Content (PWC) on the GNSS-R reflected signals.

The reflectivity measurements obtained during the SAM airborne experimental campaign were used to validate the instrument design and data processing tools. The ICF mean power measurements were fitted to a reflectivity model in order to retrieve the soil dielectric properties of the area in resolution cells of 200 meters. It was verified that, in agreement with some semi-empirical models, the estimated relative permittivity had a quadratic relationship with the soil moisture samples gathered during the in-situ campaign. Soil moisture measurements were obtained by applying this quadratic model to the data, which allowed to produce a soil moisture map of the area under observation.

During the LEiMON experimental campaign, a long term dataset was acquired from a ground-based GNSS-R receiver. The scattered signals were first analyzed in terms of the coherent and incoherent scattering components. As expected by theoretical models, it was found out that GNSS signals reflected off land surfaces are mainly Rice distributed, as a result of the combination of a coherent and an incoherent scattering components. In order to separate both contributions, the ICF had to be counter-rotated in order to compensate the geometrical phase variation originated by the GNSS satellites' movement. Once this was done, the counter-rotated ICF was averaged in order to extract the estimated soil reflectivity. It was observed that this technique could be applied only in certain conditions, in which the phase evolved harmonically. However, in most situations, due to the signal fadings the phase had a random behavior and therefore the ICF could not be counter-rotated. An alternative technique was proposed in order to estimate the coherent scattering contribution to the reflectivity out of the ICF power.

This observable was used to determine the sensitivity of GNSS-R signals to soil bio-geophysical parameters. Significant variations in the measured reflection coefficients could be detected for different soil moisture and vegetation development stages. For stable soil roughness conditions, the estimated Γ'_{rl} apparent reflectivity, presents a sensitivity to soil moisture of 0.45 dB/SMC(%) with a correlation coefficient of 0.8, whereas Γ'_{rr}, has very low sensitivity and correlation values. Changes in the soil roughness severely affect the reflected GNSS signal power, severely affecting the correlation of Γ'_{rl} with respect to soil moisture observations. In spite of this, it was demonstrated that the ratio between both reflection coefficients is scarcely affected by soil roughness variations; with a sensitivity of 0.27 dB/SMC(%) and a correlation coefficient of 0.91 with respect to SMC. This ratio could therefore represent an optimum observable for soil moisture remote sensing. Regarding the sensitivity to vegetation characteristics, it was observed that Γ'_{rl} and Γ'_{rr} present a significant response to PWC with a correlation coefficient of 0.9 and 0.8, respectively, and a sensitivity of 0.38 dB/(kg/m^2) and 0.34 dB/(kg/m^2). The ratio of both reflection coefficients is not sensitive to the presence of vegetation, indicating an attenuation effect of vegetation on both polarizations of GNSS reflected signal.

During the LEiMON experiment it was identified that in order to perform precise GNSS-R polarimetric measurements, some other relevant aspects had to be addressed. Firstly, the receiver's sensitivity had to be improved in order to observe low power signals, such as the cross-polarized *rr* reflected signal. And secondly, the cross-polarization isolation of the receiving antennas should also be increased in order to prevent the contamination between the reflected signal's measured polarizations. These upgrades were implemented in the instrument during the GRASS project.

The GRASS experimental campaigns comprised a total of four flights, consisting of a test flight and three scientific flights, during which GNSS-R polarimetric observations were obtained over areas with very different soil conditions. The flight campaigns were complemented by extensive in-situ campaigns to measure key bio-geophysical parameters. The estimated Γ'_{rl} and Γ'_{rr} reflectivities were geo-referenced according to the specular point positions and represented over Google Earth images with a color scale according to their reflectivity value. This allowed to relate the obtained data with surface features. It was observed that Γ'_{rl} had a rapid response to terrain reflectivity changes, such as transitions between land and rivers, roads, and housing. The response of Γ'_{rr} was not so evident, however it could still be observed over highly reflective surfaces such as water bodies.

A more detailed comparison of the GNSS-R signals with the ground truth data was performed by assigning the reflectivities of each specular point position to specific fields according to terrain classification maps. The Γ'_{rl} and Γ'_{rr} apparent reflectivities were obtained as a function of the incidence angle. It was determined that, as seen in the LEiMON project, the reflectivity coefficients at both polarizations were sensitive to soil moisture changes. It was also observed that changes in the surface roughness originated strong variations on the signals, however, the ratio between Γ'_{rl} and Γ'_{rr} was determined to be rather independent of this parameter, except in the case of high surface roughness. Due to the instrument's limited sensitivity and the presence of a strong incoherent component, the whole dynamic range of the Γ'_{rr} coefficient could not be observed, therefore, hindering the stability of the Γ'_{rl} over Γ'_{rr} ratio with respect to surface roughness.

Regarding the sensitivity to vegetation, Γ'_{rl} showed remarkable variations originated by the presence of vegetation. The difference in reflectivity between a bare and a vegetated field with mid biomass was of more than 3 dB for low incidence angles, for similar soil moisture and surface roughness conditions. The estimated Γ'_{rr}, does also experience a decrease, however, not so strong as its counterpart. With respect to forest AGB, it was observed that Γ'_{rl} experiences a monotonic decrease up to an above ground biomass of more than 300 t ha^{-1}. The calculated sensitivity yields 1.5 dB/(100 t ha^{-1}). The fact that the measured reflection coefficient does not saturate with biomass is a remarkable result, since conventional monostatic L-band radars saturate for biomass values above 150 t ha^{-1}. This points out the great capabilities of GNSS-R as a remote sensing tool for forest biomass.

Part IV

Outlook and Conclusions

Chapter 9

Technology Prospects

The theoretical and experimental aspects for the estimation of soil moisture and above ground biomass from low altitude GNSS-R receivers have been discussed in previews chapters. It has been demonstrated that, under certain conditions, GNSS-R polarimetric observables can be used for the estimation of land bio-geophysical parameters. The extension of this concept to spaceborne platforms could therefore represent an important break-through given the promising characteristics of this technique.

In this chapter, the capabilities of a Low Earth Orbit (LEO) GNSS-R receiver to retrieve meaningful land bio-geophysical parameters are assessed from the point of view of the instrument's radiometric accuracy. For that, several simulations were performed with varying scattering characteristics, in order to consider a representative set of soil conditions. The PARIS In Orbit Demonstrator (PARIS-IOD) mission was selected as a baseline configuration for this analysis. The simulations were performed by means of the StarGym simulator, a GNSS-R End-to-End simulator developed by Starlab Barcelona within the frame of ESA contracts. Initially designed for oceanographic applications, the modularity of the software allowed to introduce for the current analysis the bistatic coherent and incoherent scattering coefficients calculated with the LEiMON simulator, developed by Tor Vergata and La Sapienza Universities (Italy), [Pierdicca et al., 2007].

The current chapter is organized as follows: the first section provides a high-level description of the PARIS-IOD mission and discusses the main characteristics of the GNSS-R receiver. The second section reviews the main concepts of the StarGym simulator and the integration of the soil scattering characteristics within the simulation tool. Conclusions and recommendations are given in a last section.

9.1 The PARIS-IOD Mission

The PARIS-IOD is a mission promoted by ESA, whose main objective is to demonstrate the capabilities of GNSS-R for mesoscale ocean altimetry applications. The concept is perfectly extensible to land and could therefore be used for soil moisture and forest biomass applications, which, together with other applications such as sea scatterometry and cryosphere, are also secondary objectives of this mission. A pictorial representation of PARIS-IOD is shown in Fig. 9.1.

The high level architecture of the GNSS-R payload can be seen in Fig. 9.2. The instrument is composed of a double phased array antenna that allows to point the up-looking and down-looking beams by means of analogue beam-former networks. As a baseline approach, the beams will be steered to the GNSS satellite and specular point positions. The down-looking beams could also be pointed to other positions different from the specular one in order to observe different scattering directions, up to a maximum incidence angle of 35°. For the PARIS IOD mission a total of 4 GNSS satellites will be received simultaneously. With the existing GPS and GLONASS constellations and the upcoming Galileo and COMPASS, a full operational mission could potentially receive up to 20 GNSS satellites at a time, which will drastically improve the instrument's coverage.

After the initial pre-amplification and signal conditioning stages, the GNSS signals are down-converted to IF, and the Doppler shift difference between the direct and reflected signals is corrected. This can be calculated by the transmitter and receiver relative positions and velocities. The signals are then IQ sampled and time shifted to compensate the additional delay between the direct and reflected signal paths. The resulting bitstreams are complex correlated with each other to obtain the final cross-correlation waveforms. Those are later modulo squared and incoherently averaged in order to reduce the signal speckle noise.

The cross-correlation of the direct and reflected bitstreams allows to despread the GNSS signals without previous knowledge of the PRN codes. This technique, known as PARIS Interferometry, enables the reception of the full signal bandwidth thanks to its ability to receive the full composite GNSS signals, including the military encrypted signals. This characteristic is particularly interesting for altimetry applications, as the precision in the delay estimation is inversely proportional to the power waveform slope [Martin-Neira et al., 2011], which is closely related to the signal bandwidth. As will be shown later, higher bandwidth signals are also beneficial for scatterometric applications as the on-ground resolution is inversely proportional to the signal bandwidth.

The PARIS interferometric technique has a downside; the reduction in SNR due to the correlation of the reflected signal with the direct signal, affected by thermal noise, rather than a clean replica. According to [Martin-Neira et al., 2011], the SNR of the interferometric technique can be expressed as a function of the clean replica correlation signal to noise ratio, SNR_{cr}, with the following relationship:

$$\mathrm{SNR}_I = \frac{\mathrm{SNR}_{cr}}{1 + \dfrac{1 + \mathrm{SNR}_R}{\mathrm{SNR}_D}} \tag{9.1}$$

where SNR_D and SNR_R are the direct and reflected SNR at the input of the correlator. As can be inferred from this equation, the decrease in the interferometric SNR can be mitigated by an increase in the direct signal SNR, which can be achieved by the appropriate selection of the direct antenna.

As a baseline for the PARIS-IOD mission, the GNSS-R instrument will be able to receive signals in both GPS L1 – Galileo E1 and GPS L5 – Galileo E5 bands. The multifrequency observations are necessary in the case of ocean altimetry applications to correct for the ionospheric delay. In scatterometric applications observations at two different frequency bands will allow to double the number of independent observations of the scene, resulting in an improved radiometric accuracy.

The baseline PARIS-IOD mission characteristics were selected as inputs for the StarGym simulator in order to perform this analysis. More details on the selection of the different instrument and mission parameters are given in upcoming sections. The description of the simulation tool is provided next.

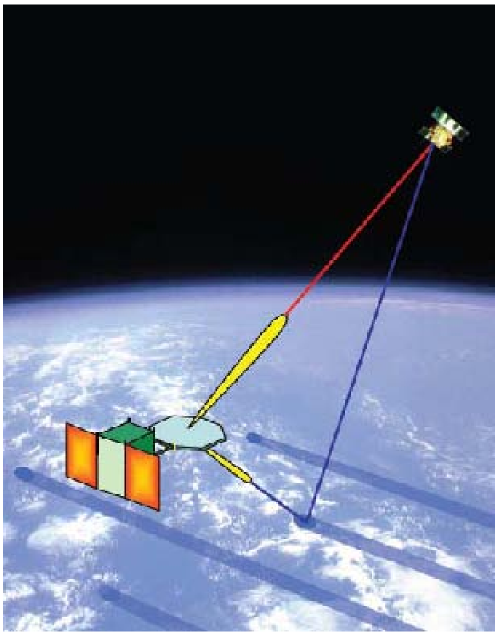

Figure 9.1: Pictorial representation of the PARIS-IOD mission, from [Martin-Neira et al., 2011].

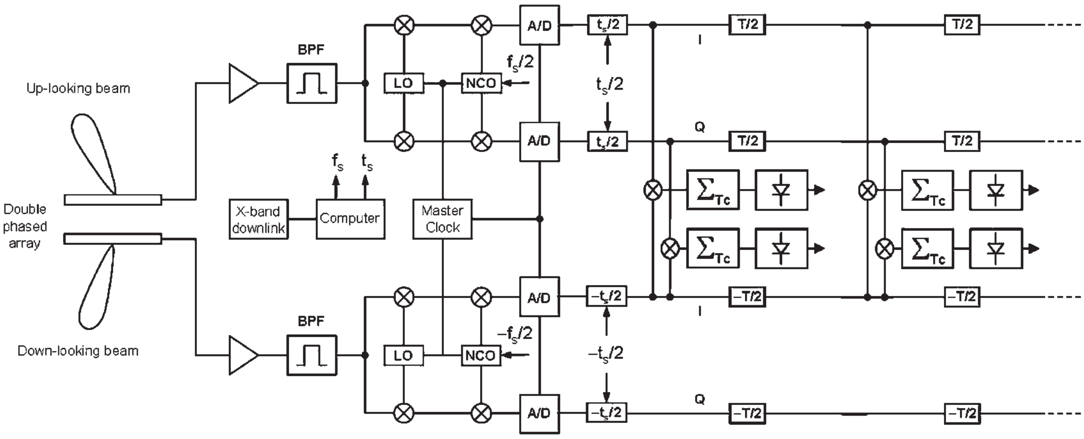

Figure 9.2: Block diagram of the PARIS GNSS-R receiver, retrieved from [Martin-Neira et al., 2011].

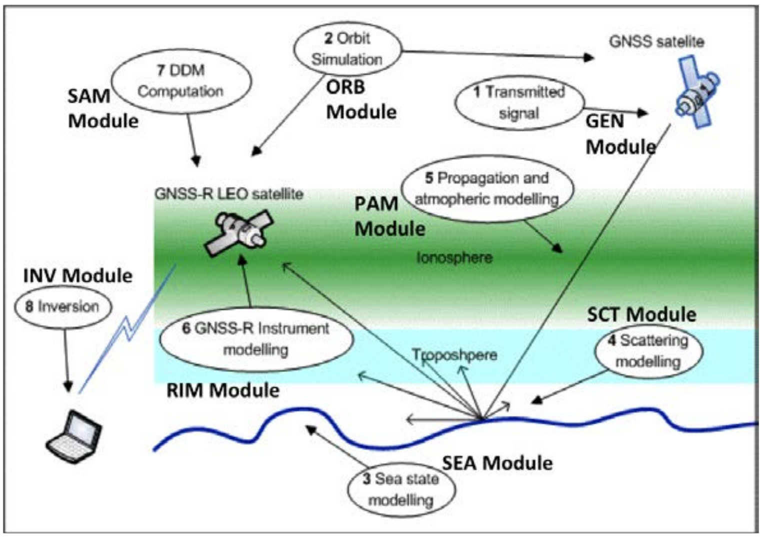

Figure 9.3: StarGym simulator architecture.

9.2 The StarGym GNSS-R End-to-End Simulator

As mentioned above, StarGym is a GNSS-R end-to-end simulator that was developed at Starlab Barcelona during two successive ESA contracts; 21893/08/NL/ST/al and TEC-ETP/2010.85/SD. The software was implemented in IDL, and articulated in 9 basic modules, each one dealing with the basic operations involved in a GNSS-R scenario. A diagram depicting the organization the simulator architecture is sketched in Fig. 9.3. A brief description of the building blocks is provided next, [Garcia-Fernandez et al., 2011].

1. GEN (Signal Generator Module), responsible to generate the spread spectrum code that is going to be used in the simulation. As such, this module: generates the spreading codes, synthesize the BOC subcarriers, builds the composite signal and computes the code autocorrelation. The codes supported by GEN (and thus by StarGym) are the GPS and Galileo code and the following modulations GPS BPSK, Galileo BOC, BOCcos and AltBOC signals.

2. ORB (Geometry and Orbit Module), responsible of setting up the geometry involved in the scenario (satellite position computation, specular point computation, ...). Besides computing the location of the satellites and the specular point, ORB constructs a matrix of patches around the specular point (i.e. Geometry matrix) based on the range selected by the user. This patch matrix will be used by the rest of the modules. This module takes as inputs the description of the orbits of the satellites, in YUMA format. The module propagates the orbits and computes the different geometrical parameters needed by the simulator (satellite positions and velocities, specular point location, position of the glistening zone matrix patches, delays between satellites and patches, patch area, iso-lines, ...).

3. SEA and SCT (Sea and Scattering Modules), responsible of computing the parameters and variables related to the sea surface and the scattering coefficients. Due to the modularity of the simulator, these two building blocks were by-passed in order to introduce the scattering components calculated by the LEiMON simulator, developed by La Sapienza and Tor Vergata University [Pierdicca et al., 2007]. The

coherent scattering component was calculated by means of the Fresnel reflection equations, whereas the incoherent scattering component was obtained by interpolating the bistatic scattering coefficients obtained by the LEiMON simulator to the incidence angles of the points on the surface.

4. PAM (Propagation and Atmospheric Module), responsible of computing the delays due to the neutral atmosphere and the ionosphere. As it is known, in a LEO scenario, both neutral atmosphere and ionospheric delays affects twice the signal reflected by a sea surface. On the one hand, the tropospheric delay is computed using the model used in GNSS (see for instance [Hofmann-Wellenhof B., 2001]). On the other hand, PAM computes also the ionospheric delay based on the VTEC values provided in Global Ionospheric Maps under IONEX format. These maps are publicly availability in the International GNSS Service data centre.

5. RIM (Receiver Instrument Module) is in charge of simulating the GNSS-R receiver/instrument, from the antenna to the input of the correlator (i.e. after the RF front end). RIM generates the necessary data so that the SAM module can compute the waveform/DDM. The operation of this module has a dependency on the operating mode: for the bitstream mode, the actual field resulting from the direct and reflected signals are computed, quantized and delivered as a complex bitstream. The resulting complex sequences will be quantized and delivered to SAM for the waveform/DDM computation. The direct and reflected fields pass through the up and down looking antennas, each with their own gain, LNA and notch band pass filter that limits the incoming noise. The losses from the filter to the down-conversion stage (important for the overall noise budget computations) will be modeled by a cable with losses. For the waveform mode, the key parameters of the reception chain are computed and passed to SAM, such as noise power, and SNR degradation due to quantization. In addition, the RIM module includes an antenna pattern processor in order to project it to the glistening zone matrix, thermal noise module that accounts for the noise generated in the reception chain.

6. SAM (Signal Analyzer Module) computes the waveforms/DDMs. This module is in charge of actually using the Woodward Ambiguity Function (WAF), in waveform mode, or to directly correlate the bitstreams, in bitstream and interferometric modes, in order to obtain the DDM and waveforms that will be later used in INV to retrieve the geophysical parameters.

7. INV (Inversion Module) takes as inputs the waveforms/DDM generated by the SAM module and generates the geophysical parameters (namely height and DMSS). The height is obtained by applying a retracker to the incoming waveform. This retracker can obtain the position of the specular point by both retrieving the peak of the incoherently averaged waveform or by retrieving the peak of the first derivative of the incoherently averaged waveform. Regarding the DMSS, this is found using the DDM and performing a search in a three dimensional space (MSS, direction and isotropy).

8. SCH (Scheduler), coordinates all tasks and ensures the correct distribution of the data at each stage of the processing.

The methodology of StarGym is based on two operational modes (bitstream and waveform operating modes). In terms of organization, mode 1 (bitstream) is characterized by the fact that its processing flow is focused on the Receiver Instrument Module

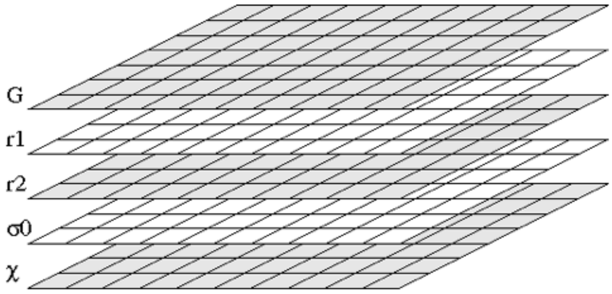

Figure 9.4: StarGym matrix approach diagram representation.

(RIM). In this operation mode, the direct and reflected signal electromagnetic fields are simulated and sampled according to the number of quantization bits specified by the user. The bitstreams resulting from this operation are use to produce the cross-correlation waveforms. This operation mode is computationally intensive as the electromagnetic fields need to be generated at each point of the surface. In mode 2 (waveform), the processing weight lays in the Signal Analyzer Module (SAM) (in charge of generating the waveforms/DDMs). The calculation of the cross-correlation waveforms is based on the evaluation of the radar equation shown in Eqn. (3.15), by weighting the signal power arriving at the receiver from each point on the surface by the WAF.

The working principle for both modes is essentially the same. The glistening zone are represented by different glistening zone matrices, where each matrix element represents a regular patch of the glistening zone. These matrices are generated by the different StarGym modules (i.e. ORB will generate the Doppler and delay for each patch, PAM will generate the atmospheric delay for each patch, SCT will generate the scattering coefficient of each patch, etc.). Fig. 9.4 illustrates this principle. The matrices are then processed by RIM or SAM (depending on the operation mode) in order to generate the outputs. The processing of the reflected signal involves surface integration of several parameters, each of them mapped into the glistening zone (computed by the corresponding building block). Provided the faster execution time and the assumable approximations of the radar equation, the waveform mode was used for this analysis.

9.3 GNSS-R Spaceborne Scenarios Simulation

The current section provides a description of the simulations performed to determine the radiometric accuracy of a PARIS-IOD like instrument for the measurement of land observables. Four different scenarios with varying scattering conditions were simulated for this purpose. Due to the random nature of the scattering process 10 iterations for each scenario for a total simulation time of 1 second were done in order to have an statistically representative sample of the outcome of each test. The scenario characteristics, system parameters, and simulation results are described next.

9.3.1 Spaceborne Scenario Description

A similar scenario to the baseline configuration proposed for the PARIS-IOD mission was selected for this analysis. The main scenario characteristics can be seen in Table 9.1. GPS L1 and L5 bands were considered in this analysis. The results can also be extrapolated to the Galileo bands. The weighted composite codes for these signals are shown in Fig. 9.5.

	Parameter	Value
GNSS Signals	GPS L1	BPSK(1)(CA) + BPSK(10)(P) + BOC(10,5)(M) + CBOC(6,1,1/11)(L1C)
	GPS L5	BPSK(10)(L5I) + BPSK(10)(L5Q)
Orbits	GNSS Satellite	GPS SV-22
	LEO Orbital Height	630 km
	Incidence angle	35 deg
GNSS-R Receiver	Antenna Main Beam	15 deg
	Antenna Directivity	21.25 dB
	Low Noise Amplifier Gain	40 dB
	RF Bandwidth	40 MHz
	Noise Figure	3 dB
	Direct Antenna Temperature	40 K
	Reflected Antenna Temperature	290 K
	System Temperature	290 K
Scattering	Surface Roughness	3 cm
	Coherent Scattering Component	(Test 1) $\Gamma = 0.30$ / -10.45 dB (Test 2) $\Gamma = 0.15$ / -16.48 dB (Test 3) $\Gamma = 0.10$ / -20.00 dB (Test 4) $\Gamma = 0.05$ / -26.02 dB
Signal Processing	Coherent Integration Time	1 ms (GPS L1) 2 ms (GPS L5)
	Incoherent Integration Time	0.1 s (GPS L1) 0.2 s (GPS L5)

Table 9.1: Main configuration parameters for the GNSS-R spaceborne scenarios simulation.

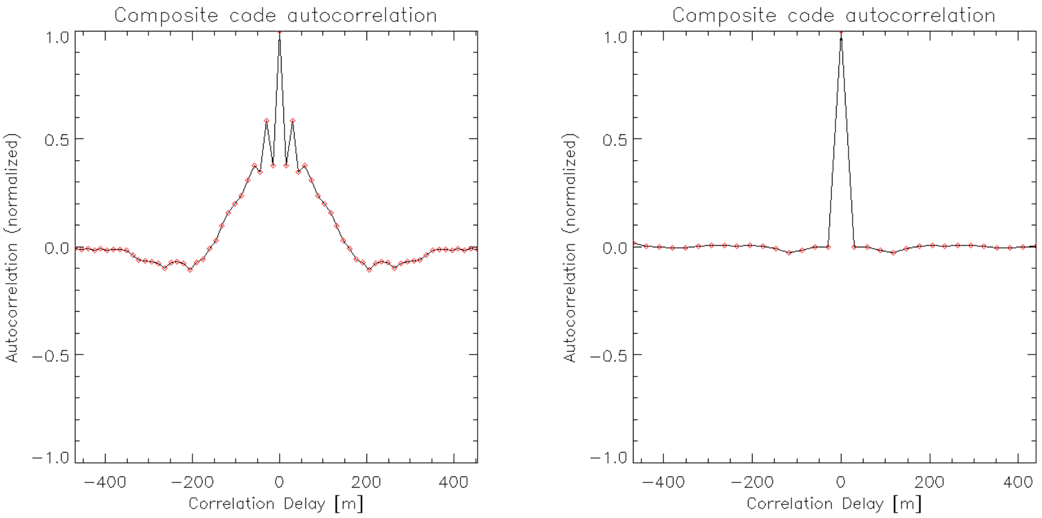

(a)

(b)

Figure 9.5: GPS Composite codes for (a) L1 and (b) L5 signals.

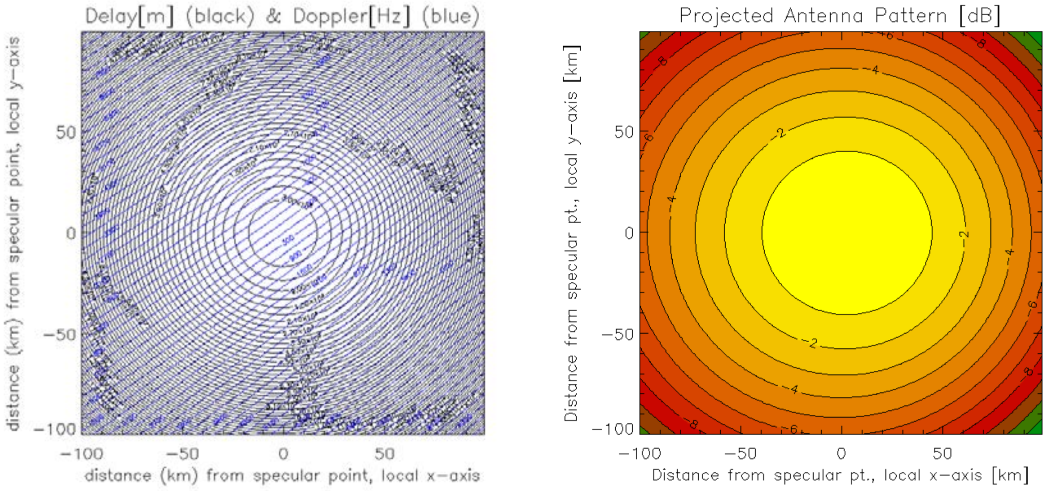

(a) (b)

Figure 9.6: (a) Iso-delay (in black) and iso-Doppler (in blue) lines projected on the surface. The iso-delay lines are depicted every 300 meters, and iso-Doppler lines every 300 Hz. (b) Antenna pattern projected on the surface. The pattern was normalized to the maximum directivity.

In order to ensure cross-test consistency the same orbital parameters for both the GNSS and LEO satellites were considered for all simulations. The scenario geometry was selected so that the position of the GNSS satellite and the PARIS-IOD defined an incidence angle at the specular point of 35°, corresponding to the maximum antenna beam steering angle of the PARIS-IOD receiver, i.e., a worst case scenario for signal SNR. The iso-delay and iso-Doppler lines for the selected configuration are shown in Fig. 9.6(a). The iso-delay curves describe ellipses centered about the specular point and aligned along the incidence plane, i.e. the X axis in the figure. The iso-Doppler lines trace hyperbolas which in the case of a spaceborne scenario are primarily perpendicular to the along track direction of the LEO satellite. The reason for this is that the main Doppler contribution comes from the relative velocity of the GNSS-R receiver with respect to the points on the surface.

The antenna radiation pattern was considered as a Gaussian pattern oriented in the direction of the specular point. The antenna directivity was defined by the width of the main beam, set to 15°, providing a directivity for both up-looking and down-looking antennas of 21.25 dB.

The bistatic scattering coefficient was simulated as the combination of a coherent and an incoherent component. The former comes primarily from the first Fresnel zone, an ellipse around the specular point whose axes can be calculated by applying Eqns. (3.5) and (3.6). For the selected geometry this corresponds to 500 and 400 m for the major and minor axes, respectively. Given the reduced size of this area, the coherent scattering component was considered as a point scatterer located at the specular point position. Four arbitrary reflectivity values were selected within the range of the Fresnel reflection coefficients for different soil conditions; those are indicated in Table 9.1. The incoherent scattering component was obtained by means of the accounted for by using the LEiMON simulator scattering modules. A high soil roughness scenario was selected, $\sigma_z = 3$ cm, resulting in a high incoherent scattering component. As mentioned above, the LEiMON simulator outputs were interpolated to the incidence angles of the points

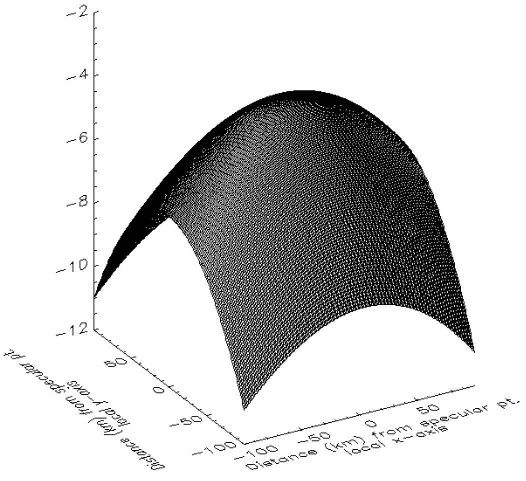

Figure 9.7: Incoherent scattering component (represented in dB) projected on the glistening surface

on the glistening surface. The bistatic σ^0 is shown in Fig. 9.7. The same incoherent scattering component was applied for all the performed tests, resulting in varying weights of the scattering components for the different simulation scenarios.

9.3.2 Coherent Integration Time Selection

The selection of the coherent integration time has a direct impact on the performance of the GNSS-R scatterometric measurements. The optimal coherent integration time, T_i, would be the one that maximizes the overall SNR after the incoherent averaging time. In general, increasing the coherent integration time improves the thermal SNR, SNR_{th}. However, this parameter has an upper boundary; if T_i is selected to be higher than the surface coherence time, the final cross-correlation waveform would decrease and eventually destroy completely the correlation. For that reason, despite the fact that for land surfaces the coherent scattering component could predominate in most cases over the incoherent one, the selection of T_i was done assuming a completely incoherent scattering. In this situation, the final SNR can be calculated as

$$\mathrm{SNR}_{Final} = \frac{1}{\frac{1}{N}\left(\left(1 + \frac{1}{\mathrm{SNR}_{th}}\right) + \left(\frac{1}{\mathrm{SNR}_{th}}\right)\right)} \tag{9.2}$$

where N is the number of independent looks within each incoherent averaging period, which is usually limited by the desired along-track resolution. In order to calculate N the waveform correlation time for consecutive epochs needs to be calculated. This can be obtained based on the waveform autocorrelation model presented in [You et al., 2004], according to which, the autocorrelation of waveforms Y for a delay τ, compensation frequency f_c, and an epoch difference between waveforms $\tilde{t}$, can be written as

$$R_Y(\tilde{t}, \tau, f_c) = T_i^2 \iint \frac{D^2(\rho)}{4R_0^2(\vec{\rho})R^2(\vec{\rho})} |\chi(\Delta\tau, \Delta f)|^2 \sigma^0(\vec{\rho}) \exp\{-2\pi i \Delta f \tilde{t}\} d^2(\vec{\rho}) \tag{9.3}$$

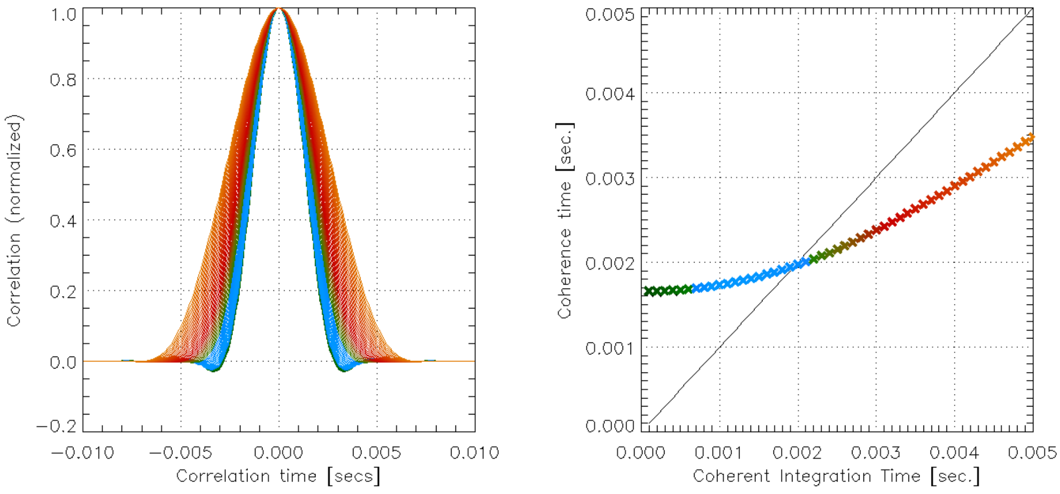

(a)

(b)

Figure 9.8: (a) Waveforms epoch autocorrelation calculated for different coherent integration times. (b) Waveform epoch correlation time vs coherent integration time. The color scale represents the same coherent integration time in both figures.

where D is the projected antenna gain on the surface; R_0 and R the ranges from the transmitter to the surface patches and from the surface to the receiver; χ is the WAF as a function of the difference in delay and Doppler with respect to the considered point, $\Delta\tau$ and Δf, respectively; and σ^0 is the bistatic scattering coefficient.

The waveforms epoch autocorrelation was calculated for different coherent integration times for a delay $\tau = 0$, corresponding to the specular point delay. The correlation time was obtained as the epoch difference, $\tilde{t}$, for which the normalized autocorrelation decays to $1/e$. The obtained epoch autocorrelations for the composite code of the GPS L5 band are depicted in Fig. 9.8(a). The different coherent integration times are represented in color scale: from 0.1 ms in dark green, to 5 ms in orange. As can be seen, the normalized epoch autocorrelation widens towards higher coherent integration times, thus increasing the correlation time. This is readily seen in Fig. 9.8(b).

The monotonic increase of the correlation time with respect to coherent integration time is linked to a decrease of the active glistening area with coherent integration time. As seen in Fig. 9.9, the WAF is the limiting factor of the active glistening zone for a GNSS-R spaceborne receiver, acting as a spatial filter of the scattering area. As explained in section 3.4, the WAF on its side is the combination the annulus zone defined by the code autocorrelation, $\Lambda(\Delta\tau)$, and the Doppler zone defined, $S^2(\Delta f)$ function, which describes a sinc function with respect to Δf. The null-to-null width of this function is equal to the inverse of T_i. The reduction of the WAF reduces the active glistening area, which in turn makes the surface correlation time to increase, as predicted by the Van Cittert–Zernike theorem. This makes consecutive waveforms to be more correlated with each other, thus reducing the number of independent looks within a given incoherent averaging time. As mentioned above, this needs to be considered to calculate the optimum coherent integration time that provides the highest overall SNR.

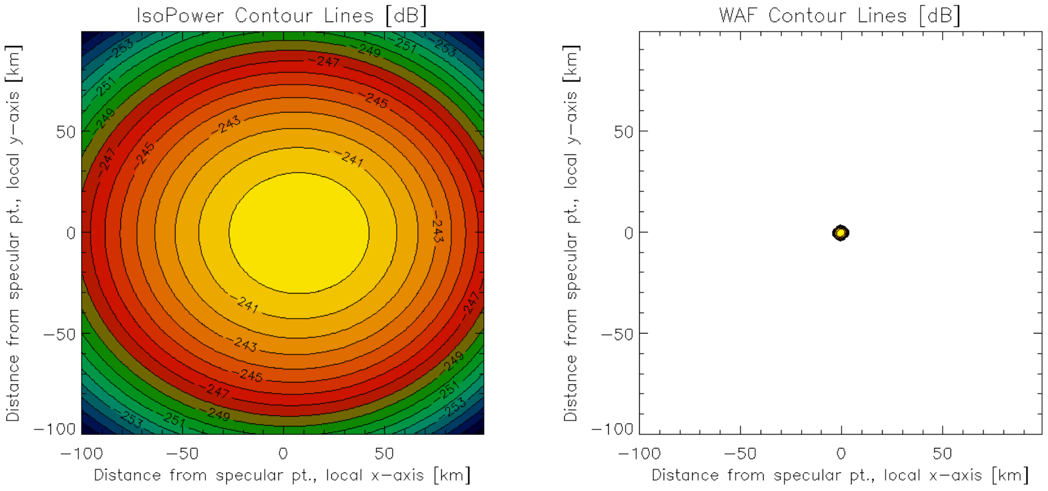

(a) (b)

Figure 9.9: (a) Iso-power countour lines projected on the glistening surface. (b) WAF for the composite GPS L5 signal projected on the glistening surface.

The number of independent looks can be finally calculated as follows:

$$\begin{aligned} N &= \frac{T_{inc}}{\tau_c} \quad , \quad T_i < \tau_c \\ N &= \frac{T_{inc}}{T_i} \quad , \quad T_i > \tau_c \end{aligned} \tag{9.4}$$

where T_{inc}, is the incoherent integration time, and τ_c the correlation time as presented in Fig. 9.8(b). For an arbitrary T_{inc} of 1 second, the final SNR of the composite GPS L1 and L5 signals is provided in Fig. 9.10(a) and 9.10(b), respectively. In blue, the final SNR considering N as the number of averaged waveforms is represented. In red, the final SNR considering N as shown in Eqn. (9.4). As can be seen, if this is not considered, an error in the estimation of the optimal coherent integration time can be made. The final coherent integration time was set to the closest integer ms that provides the highest overall SNR, corresponding to 1 ms in the case of L1 and 2 ms in for L5.

9.3.3 Incoherent Integration Time Selection

As discussed in the previous section, in a spaceborne GNSS-R scenario the WAF is the limiting factor for the active glistening area, i.e. ultimately, the WAF determines the system achievable on-ground resolution. However, the single shot waveforms need to be incoherently averaged in order to reduce the effect of speckle noise. The usually long incoherent integration times determine the along-track resolution. For the PARIS-IOD the along-track resolution requirement for ocean observations is set to 100 km, which, at a reference speed of 7 km/s for a LEO satellite, means that the incoherent integration time can be extended for as much as 15 seconds.

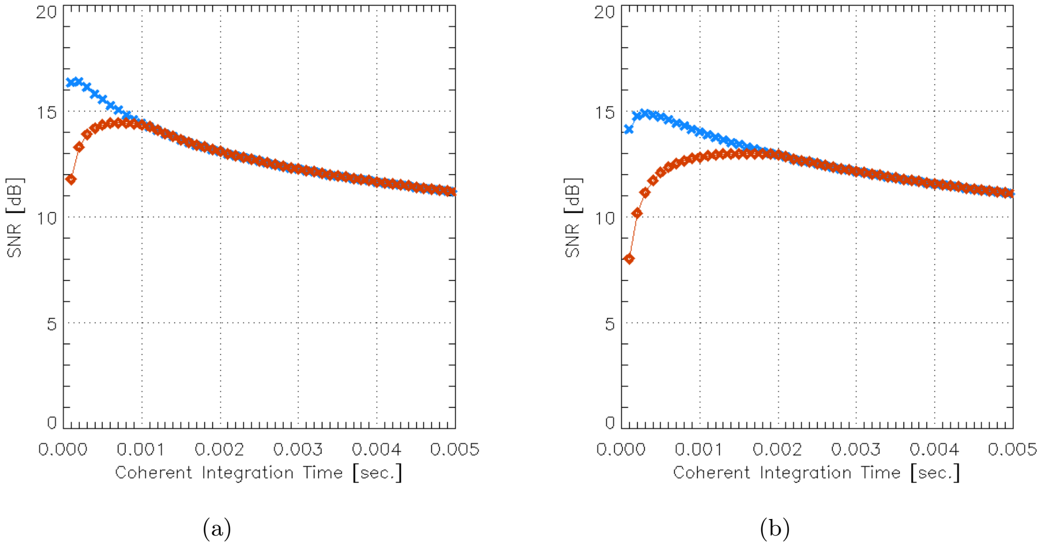

(a) (b)

Figure 9.10: Final overall SNR for (a) L1 and (b) L5 GPS signals. In blue, the final SNR calculated considering the number of independent looks as the number of averaged single shot waveforms. In red, the final SNR calculating the number of independent looks as shown in Eqn. (9.4).

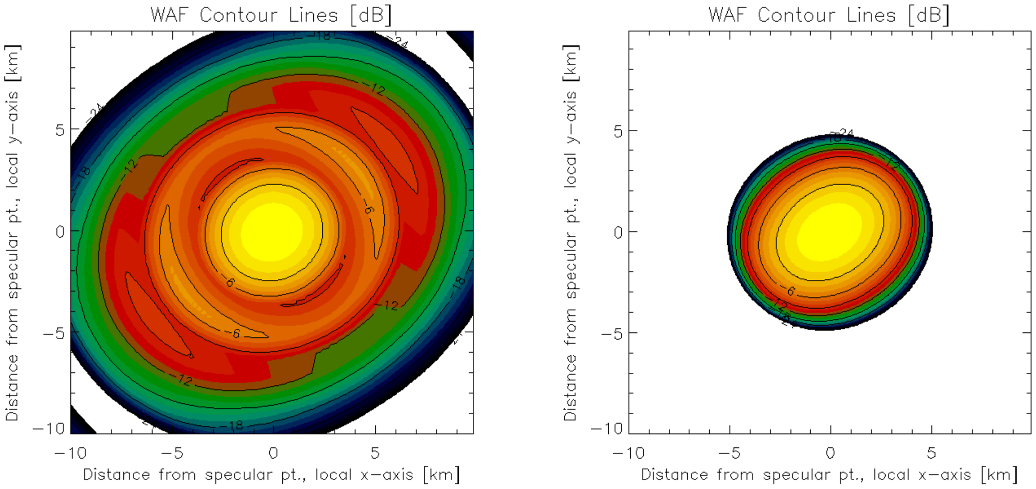

(a) (b)

Figure 9.11: Woodward ambiguity function (WAF) projected on the surface for the GPS L1 (a) and L5 (b) signals. The solid black curves depict the iso-power lines of the WAFs in steps of 3 dB.

For land observations the along-track resolution requirements are more stringent. In this analysis, the incoherent integration time was selected so that the along-track resolution matches the across-track resolution, determined by the WAF. A detailed view of the GPS L1 and L5 signals WAFs projected on the surface are provided in Fig. 9.10(a) and Fig. 9.10(b), respectively. The coherent integration times were set to 1 ms for L1 and 2 ms for L5. The solid black lines depict the iso-power contours in steps of 3 dB. The -3 dB contour line defines the on-ground resolution, which in the case of the GPS L1 signal corresponds to an ellipse of 4.5 km along-track and 5 km across track, and in the case of the L5 signal the -3 dB contour line describes an ellipse of 4 km along-track and 5.5 km across-track. Based on this, the incoherent integration time was selected to be of 0.1 and 0.2 seconds for the GPS L1 and L5 signals, respectively. This should allow to have quasi-circular resolution cells that would overlap between each other along the successive acquisitions along the satellite orbit.

9.3.4 Simulation Results

The incoherently averaged waveforms resulting from the four simulated scenarios are shown in Figures 9.12 and 9.13 for the L1 and L5 signals, respectively. As can be observed from the figures, the obtained waveforms resemble to a large extend the weighted composite codes, shown in Fig. 9.5. This is particularly clear in the case of L5, where only the BPSK code is present. The simulated waveforms can be compared to the ones observed during the UK-DMC experiment, see Fig. 3.9. The simulated waveforms, however, show a much lower noise than the one observed in Fig. 3.9. This could be due to the fact that the antenna gain chosen for the simulation is much higher than the one used in the UK-DMC experiment, which was of 11.8 dBi, resulting in almost 10 dB more SNR.

The fact that the waveforms do not show an appreciable extension towards higher correlation delays suggest that, even for high surface roughness conditions, the coherent component of the scattered signal would be the predominant one from spaceborne platforms. In this situation, by manipulating the equation describing the power carried by the coherent scattering component, Eqn. (4.14), the estimated surface reflectivity, $\hat{\Gamma}$, can be calculated as:

$$\hat{\Gamma} = \frac{\left\langle |Y(\Delta\tau_{sp}, f_{sp})|^2 \right\rangle - P_N}{\dfrac{\lambda^2}{(4\pi)^2} \dfrac{P_t\, G_t\, G_r}{(R_{sp} + R_{0,sp})^2}} \,. \tag{9.5}$$

The noise power, P_N, was subtracted from the averaged power of the cross-correlation waveforms at the delay and Doppler position, $\left\langle |Y(\Delta\tau_{sp}, f_{sp})|^2 \right\rangle$, in order to be consistent with the waveform power statistics, see Eqn. 8.10. P_N can be obtained as the mean average power of the waveform lags previous to the first correlation chip.

The reflectivity estimation results for the GPS L1 and L5 signals are provided, respectively, in Tables 9.2 and 9.3 for the four simulated scenarios. The mean and standard deviations for each test were calculated out of the several simulation runs performed for each test. As can be observed, the estimated reflectivity values, $\hat{\Gamma}$, correspond to the selected reflectivity for each one of the tests, as specified in Table 9.1. The standard deviation for the measurements corresponds to the receiver's radiometric accuracy. The

	Wf. Peak 01	**Wf. Peak 02**	**Wf. Peak 03**	**Wf. Peak 04**
Mean Power [dBW]	−139.58	−145.57	−149.09	−155.03
Mean $\hat{\mathbf{\Gamma}}$ [dB]	−10.41	−16.41	−19.96	−26.04
Std $\hat{\mathbf{\Gamma}}$ [dB]	±0.03	±0.05	±0.08	±0.16

Table 9.2: Reflecticity simulation results for the GPS L1 signal.

	Wf. Peak 01	**Wf. Peak 02**	**Wf. Peak 03**	**Wf. Peak 04**
Mean Power [dBW]	−143.60	−149.62	−153.09	−158.87
Mean $\hat{\mathbf{\Gamma}}$ [dB]	−10.42	−16.47	−19.99	−26.06
Std $\hat{\mathbf{\Gamma}}$ [dB]	±0.06	±0.11	±0.14	±0.25

Table 9.3: Reflecticity simulation results for the GPS 5 signal.

worst case scenario is, as expected, for the lowest selected reflectivity values and for the GPS L5 signal, as it has a much lower transmitted signal power than the GPS L1. In any case, the accuracy for the reflectivity estimation is around ±0.25 dB, which patently suggests the capability of GNSS-R of retrieving accurate reflectivity values in both rl and rr polarizations.

9.4 Conclusions

In the current chapter, the analysis of the capabilities of a GNSS-R receiver of retrieving precise soil surface reflectivity measurements has been presented. The StarGym GNSS-R End-to-End simulator was used for this analysis. The baseline PARIS-IOD mission parameters were selected to perform the simulations. The surface scattering characteristics were considered as the combination of a coherent and incoherent scattering component, the former modeled by conventional Fresnel scattering theory, and the latter simulated by means of the LEiMON simulator, developed at Tor Vergata and Sapienza Universities. High surface roughness conditions were chosen in order to examine an scenario with high incoherent scattering component. Four different scenarios with varying Fresnel reflection coefficients were simulated, corresponding to typical Γ_{rl} and Γ_{rr} reflectivity values.

The selection of optimum coherent and incoherent integration times was also discussed. The selection of an optimal coherent integration time was based on the optimization of the final SNR, whereas the selection of the incoherent integration time was based on the on-ground resolution. For both GPS L1 and GPS L5 signals the final resolution cell corresponds to a quasi-circular pixel of 5 km diameter.

Each test was performed for several simulation runs in order to have a statistically representative sample for the reflectivity estimation. The results showed that the incoherently averaged waveforms were limited to the first correlation chip, which suggests that the effect of the incoherent scattering component on the finally received signal is barely appreciable. In these conditions, the received power of the reflected signal comes primarily from to the first Fresnel zone, which restricts the active scattering area to an ellipse of few hundreds of meters around the specular reflection point.

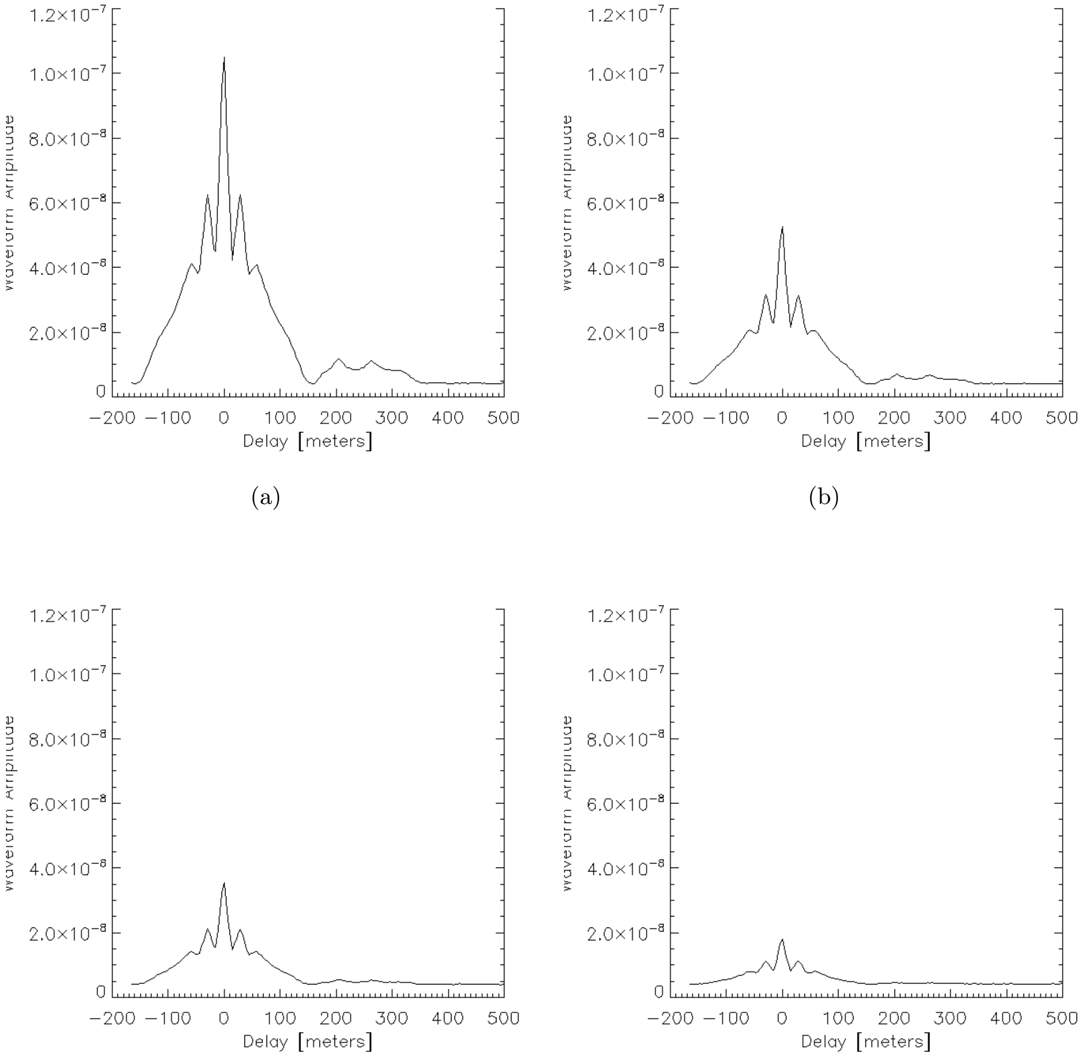

(a) (b)

(c) (d)

Figure 9.12: Composite GPS L1 signal simulated waveforms for different reflectivity conditions: (a) $\Gamma = 0.3$; (b) $\Gamma = 0.15$; (c) $\Gamma = 0.1$; (d) $\Gamma = 0.05$.

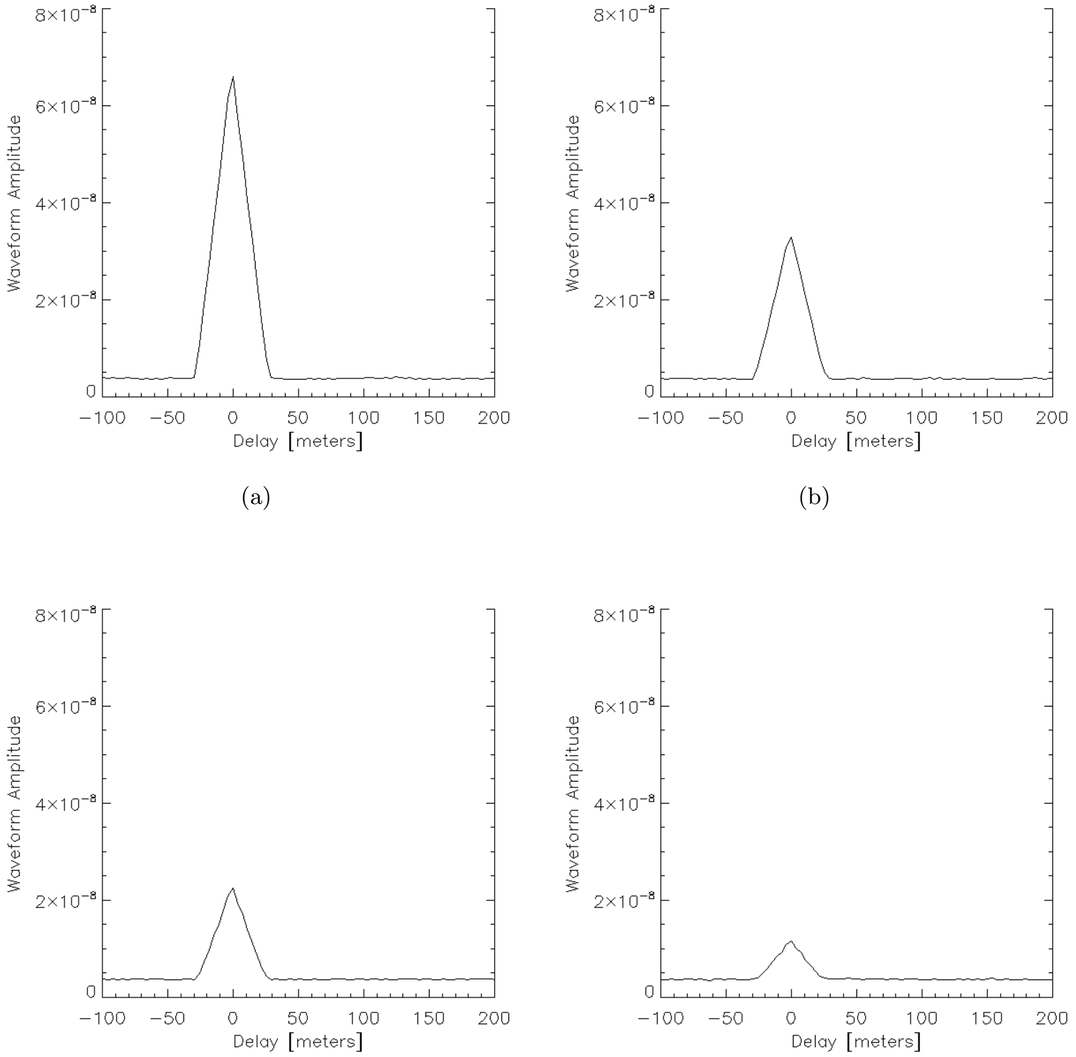

(a) (b)

(c) (d)

Figure 9.13: Composite GPS L5 signal simulated waveforms for different reflectivity conditions: (a) $\Gamma = 0.3$; (b) $\Gamma = 0.15$; (c) $\Gamma = 0.1$; (d) $\Gamma = 0.05$.

The estimated reflectivity matched to a large extent the selected simulation values. The worst case standard deviation of the measurements was determined to be for the lowest reflectivity and signal transmitted power, i.e., ±0.25 dB. The low observed measurement variability suggests the promising capabilities in terms of radiometric accuracy that GNSS-R instruments could have to perform accurate reflectivity measurements from a spaceborne platform.

The current simulations considered the scattering scenario as a flat homogeneous surface. However, surface in-homogeneity and topography could contribute to create multiple reflection points on the surface, which could increase the incoherent scattering component, and therefore jeopardize the reflectivity estimation. Further theoretical work would be necessary in order to account for this effects on the scattering models, at the same time that extensive experimental campaigns would be necessary to validate the obtained results. In any case, for situations in which the terrain topography is not abrupt, spaceborne GNSS reflectometry is expected to extensively contribute to the estimation of soil moisture and above ground biomass on a global scale.

Chapter 10

Summary, Conclusions and Future Work

Soil moisture and vegetation biomass are two essential variables for the understanding of some of the most important natural processes in our planet, such as the hydrological and carbon cycles. The former is responsible of the much of the natural weather variability, whereas the latter has a major influence in climate and climate change. In addition, soil moisture is a factor of main economical relevance, as it is one of the main parameters influencing crop yields, and therefore, essential for improved agricultural and water management techniques. In the same way, above ground biomass provides the basis for an optimized land resource management, crucial for some regional development programs. This PhD Thesis assesses from a theoretical and experimental point of view the capability of measuring soil moisture and vegetation biomass by means of Global Navigation Satellite System (GNSS) reflected signals.

As presented in Chapter 1, several remote sensing systems have been used to measure these two parameters from ground base, airborne and spaceborne platforms. However, despite the recognized relevance of soil moisture and vegetation biomass, their monitorization the required accuracy, spatial and temporal resolutions still remains a major challenge. The use of GNSS signals as sources of opportunity could greatly contribute to this purpose.

As discussed in Chapter 2, given their high quality, stability, and continuous availability, GNSS signals are outstanding candidates for remote sensing applications. In addition, the increasing number of GNSS satellites linked to the several multinational GNSS programs ensure the continuity of the technique, as well as the capability to increase the number of observations in order to improve coverage or the measurements' accuracy.

This remote sensing technique, commonly know as GNSS-Reflectometry (GNSS-R), has gained increasing interest since it was first proposed about two decades ago. The technique was first proposed for ocean altimetry and scatterometry applications, [Martin-Neira, 1993], however, the interest soon moved to land and ice applications. Chapter 3 reviews the fundamentals of the technique, and provides a detailed review of the GNSS-R state of the art for soil moisture and vegetation monitorization. Previous experimental works had already shown the capability of GNSS-R to sense small reflectivity changes on the surface from ground-based and airborne receivers with the co- polarized reflected signal. In other works, the use of the co- and cross- polarization ratio was proposed in an attempt to mitigate the effect of soil roughness in the estimation of soil moisture. Nevertheless, experimental work could not provide an evidence of the suitability of this technique. Other approaches, like the measurement of the interferometric pattern of the direct and reflected GNSS signals, had also been considered and were demonstrated to provide satisfactory soil moisture and vegetation development estimations. The approach proposed in this PhD Thesis focuses on the use of polarimetric information on GNSS reflected signals in order to decouple soil moisture from surface roughness. In addition, the use of GNSS-R for the monitorization of forest was also pursued, in the first known attempt to link GNSS bistatically scattered signals with forest above ground biomass.

In order to gain deep understanding of the interaction of the impinging GNSS signals with land surfaces, the current state of the art scattering models were reviewed in Chapter 4. For smooth surfaces, the circular co- and cross-polar reflection coefficients, Γ_{rl} and Γ_{rr}, respectively, are a linear combination of the hh and vv components, and are therefore governed by the Fresnel reflection theory. In this situation all the energy is reflected in the specular direction. However, as the surface becomes rougher the energy starts scattering in directions different from the specular one, becoming completely isotropic in the case of very rough surfaces.

An exercise was carried out in order to analyze the formation of the final scattered field from a random rough surface. The scattered field was considered as the summation of random phasors with Gaussianly distributed amplitudes and phases. It was observed, that the standard deviation of the phases (assimilated to the surface roughness) had a major impact on the scattered field characteristics: For low phase standard deviations, the scattered complex field followed a two-dimensional Gaussian distribution, i.e., Hoyt Distribution, with a non-zero mean value, identified as the coherent scattering component, and a real and imaginary dispersions whose absolute squared value was linked to the incoherent scattering component. It was observed that as the single scatterers' phase standard deviation increased, the coherent scattering component decreased, at the same time that the incoherent scattering component intensified. With a phase standard deviation of half a wavelength, the scattered field amplitude followed a Rayleigh distribution, proper of completely incoherent scattering mechanisms. A GNSS-R signal scattering simulator developed by the Tor Vergata and La Sapienza Universities was also used to determine the coherent and incoherent scattering components from a ground-based receiver over bare and vegetated soils. It was observed that an increase on the soil moisture content, does not have a major impact on the relative weight of the coherent and incoherent scattering components. However, as mentioned before, an increase on the surface roughness contributes to change the relative weight of the coherent and incoherent scattering components, being the latter the predominant one for surface roughness above 3 cm.

On Chapter 5 an approach to obtain polarimetric measurements out of GNSS scattered signals was examined. It was determined that the ratio of the reflected over the direct waveform peaks, the so called Interferometric Complex Field (ICF), could be used for the estimation of the surface apparent reflectivity, defined as the ratio of the scattered over the incident GNSS signal powers. This measurement does not directly correspond to the Fresnel reflection coefficients: Firstly, the peak of the cross-correlation waveforms is directly proportional to the carrier to noise ratio of the incoming signals; and secondly, since the receiving antennas are not orthogonal to the incident wave propagation direction there is a polarization loss that modifies the observed power ratio. The obtained observable is then the so called apparent reflectivity, noted as Γ'_{rl} and Γ'_{rr}, for both circular polarizations. In this chapter the effects of thermal noise and antenna orientation were analyzed in order to elaborate a simplified scattering model to relate in a straightforward way the obtained GNSS-R polarimetric measurements with soil bio-geo-physical parameters.

For the development of the experimental campaigns a GNSS-R polarimetric instrument was developed within this research work, i.e., the SAM instrument, described in Chapter 6. The instrument development was based on the Oceanpal instrument [Caparrini et al., 2007], initially designed for sea applications. The major upgrades performed on the instrument were the introduction of a second polarization on the down-looking channel and the adoption of a calibration chain for the correction of the relative power mismatches between the direct and reflected channels. In the successive versions of the instrument, developed during this research work, special care was put on the cross-polarization isolation of the receiving antennas, and on the reduction of the receiver noise factor in order to improve the instrument's sensitivity.

A total of three experimental campaigns were performed during this investigation, which are reviewed in Chapter 7. The first one is the so called Monegros Experiment, aimed at demonstrating the capabilities of the SAM sensor of observing small changes on the soil reflectivity. During this campaign, performed on July 2008, the GNSS-R instrument was flown on-board a helicopter in order to cover an extended semi-arid area near Zaragoza, Spain. The second experimental campaign was a long term ground-based experiment aimed at gaining deeper understanding of the combined effects of soil moisture, surface roughness, and vegetation biomass on the scattered signals. The experiment was performed on an agricultural field near Florence, Italy, and lasted for 6 months, between March and September 2009. During this period two complete soil moisture cycles, and a full sunflower development cycle could be observed. The last of the experimental campaigns was devoted to determine the effects of vegetation on GNSS-R signals. For that, the SAM sensor was installed on an ultra-light aircraft and flown over two different areas on the Italian Tuscany: the first one is a crop field area along the Elsa river; the second one is an agricultural area scattered with poplar plots at different developments stages, which allowed to retrieve GNSS reflected signals over a wide range of above ground biomass conditions. Two flight campaigns were performed, in July and November 2011, in order to observe the two test-sites with different soil moisture conditions.

The analysis of the data acquired during those experimental campaigns is provided in Chapter 8. In a first instance, the Monegros Experiment data was used to validate the instrument design and data processing tools. The retrieved direct and reflected GNSS signals were used to estimate the surface reflectivity. The measurements were geo-located according to the specular point positions. The dielectric constant of the observed area was calculated in resolution cells of 200 meters. A quadratic relationship was observed between the obtained data and the ground-truth soil moisture samples, in agreement with soil semi-empirical models. The quadratic relationship was inverted in order to obtain a soil moisture map of the area, which was derived using only the co-polarized reflected signal.

The data retrieved during the LEiMON experimental campaign was used to investigate the reflected signal scattering characteristics. As predicted by theoretical models, it was found that GNSS signals scattered off land surfaces follow a Rice distribution, i.e., the combination of a coherent and an incoherent scattering component. To separate both contributions, the ICF signal had to be averaged for long periods of time, and the geometrical contribution due to the relative movement of the GPS satellite and receiver had to be previously removed. This technique was demonstrated to be suitable for the determination of the coherent scattering component, however, it could only be applied when the ICF phase had a harmonic evolution. Due to the fading characteristics of the signal caused by speckle noise, i.e., the incoherent scattering component, this condition could not be satisfied in most of the cases, and therefore an alternative technique had to be proposed in order to measure the coherent component of the apparent reflectivity by means of the ICF power measurements. These observables were then used to determine the sensitivity of GNSS-R signals to soil bio-geophysical parameters. Significant variations linked to soil moisture could be observed in both measured Γ'_{rl} and Γ'_{rr} apparent reflectivities. However, those were also affected by surface roughness variations. The ratio of both observables was determined to be scarcely sensitive to roughness variations. With a sensitivity of 0.27 dB/SMC(%) and a correlation coefficient over r = 0.9, this measurement was demonstrated to be an optimum observable for soil moisture remote sensing. Regarding the response to vegetation biomass, both Γ'_{rl} and Γ'_{rr} showed an attenuation effect with increasing plant water content (PWC), with a sensitivity of 0.38 dB/(kg/m^2) and a correlation coefficient of r = 0.9 for Γ'_{rl}, and 0.34 dB/(kg/m^2) and r = 0.8 for Γ'_{rr}.

The simplified scattering models presented in Chapter 5 were adjusted with the instrument's parameters in order to fit the apparent reflectivity measurements. The observed Γ'_{rl} and Γ'_{rr} apparent reflectivity ratio was used in order to estimate the soil dielectric properties. As for the Monegros Experiment, the estimated permittivity values showed a quadratic relationship with respect to the measured soil moisture. This relationship was then inverted in order to finally obtain the estimated soil moisture content, showing high correlation with respect to the in-situ measurements. Likewise, the Γ'_{rl} measurements were used to estimate the PWC. For fixed soil moisture and surface roughness conditions, the PWC could be inverted.

Future work entails the development of a joint inversion algorithm for the simultaneous estimation of soil moisture, surface roughness and vegetation biomass. Other observables such as the phase difference, and phase dispersion of the different polarization components, could also be investigated in order to provide further information to the inversion algorithm.

For the GRASS experiment, the specular points position were also geo-located and mapped on Google Earth. This allowed to relate reflectivity changes to characteristics on the surface. The rapid response of the measured Γ'_{rl} and Γ'_{rr} apparent reflectivities suggest the presence of a strong coherent component coming from the First Fresnel zone. The measured reflection coefficients were also related to the retrieved ground-truth data during the experimental campaigns. It was determined that the apparent reflectivity polarization ratio was determined to be relatively independent of surface roughness, except for the cases in which the surface roughness exceeded a surface roughness ranging between 2.5 and 3 cm. In these extreme situations, the ratio was determined to be much lower than expected. Two hypothesis were considered as the cause for this: The first of those is related to the fact that the receiver's sensitivity is limited by the signal to noise ratio. As the *rr* signal has such low values, the whole dynamic range of the Γ'_{rr} coefficient cannot be observed, and therefore the polarization ratio would not be effective in order to mitigate the effect of surface roughness. The second hypothesis is related to the fact that in high surface roughness conditions, the incoherent scattering component is the predominant one, therefore preventing the extraction of the coherent component of the signal.

Regarding the sensitivity of the GNSS-R observables to above ground biomass, Γ'_{rl} showed remarkable variations in the presence of vegetation. The specular point apparent reflectivity had a variation of more than 3 dB when transitioning from a bare surface to a mid-biomass poplar plot with similar soil moisture and roughness conditions. Γ'_{rr} did also experience a decrease, however this was not so obvious as for its counterpart. It was actually observed that Γ'_{rl} experiences a steadily decrease with forest above ground biomass up to a biomass content of 300 t ha^{-1}. The calculated sensitivity yield 1.5 dB/(100 t ha^{-1}), with a correlation coefficient $r = 0.91$. This represents a remarkable improvement with respect to other remote sensing systems, as for example, in the case of conventional monostatic radars, the radar backscattering response saturates for biomass values above 150 t ha^{-1}.

Despite the fact that these results suggest the capabilities of GNSS-R as a remote sensing tool for above ground biomass, further experimental campaigns over different type of forest and understory conditions would be necessary in order to fully validate these findings. The SAM instrument would also need to be developed further in order to allow simultaneous measurements of both direct and reflected RHCP and LHCP polarizations, which would allow to apply polarimetric techniques to the GNSS-R observations.

The capabilities of GNSS-R for retrieving significant reflectivity values from a spaceborne platforms were assessed in Chapter 9. The StarGym GNSS-R End-to-End simulator was used to perform this analysis. The simulations were performed taking the PARIS-IOD mission as the baseline configuration. The full composite GPS–L1 and GPS–L5 signals were considered for this analysis. The incoherent scattering component was determined by means of the LEiMON simulator, whereas for the coherent scattering component typical values of the Γ_{rl} and Γ_{rr} reflection coefficients were selected. The optimum coherent integration time was selected in order to maximize the final signal SNR. The incoherent integration time was chosen in order to obtain consistent across– and along– track resolutions. For the selected averaging period, both the GPS–L1 and GPS–L5 signals provide an on-ground resolution around 5 km. The simulations showed that the coherent scattering component was the predominant one from spaceborne platforms. The selected reflectivity values could therefore be measured with satisfactory accuracy. The lowest simulated reflectivity value, i.e., -26 dB could be estimated with an accuracy of ±0.25 dB, which represents an acceptable value for GNSS-R polarimetric observations.

The results obtained with the StarGym simulator did not take into consideration multiple scattering characteristics within the reflected surface, nor the possible effect of topography on the finally scattered signals. Further scattering models taking into account these two effects would need to be developed and integrated within the simulator in order to have a better estimation of the capabilities of GNSS-R receivers on-board spaceborne platforms. If those initial results were finally confirmed, GNSS-R measurements could represent an excellent complementary observation for a wide range of Earth Observation missions such as SMOS, SMAP, and the recently approved Biomass.

Appendix A

Contributions to Relevant Projects

During the development of the current PhD Thesis, the author has contributed significantly to a set of relevant projects in the field of GNSS-R. Those are listed in Table A.1.

Project Name	Date	Framework	Description	Study Role
Oceanpal	2002-2011	Starlab Internal	Design, development, manufacturing of a GNSS-R based instrument for Earth Observation Applications.	Development of algorithms oriented to SWH monitoring, and code and phase altimetry applications.
SAM	2007-2008	ESA (GSTP)	Design, manufacture and validate an multi polarimetric GNSS-R receiver for soil moisture monitoring.	Coordination of the design, development and validation of the SAM sensor. Coordination of the Experimental campaigns. Main researcher for the GNSS-R data analysis and soil moisture retrieval.
StarGym	2008-2010	ESA (RFQ)	Design and implementation of an End-to-End GNSS-R simulator.	Design and Implementation of key simulator modules, such as the SAM and INV modules. Simulator integration and validation tests.

Table A.1: Relevant contributions to GNSS-R related projects.

LEiMON	2008-2010	ESA (GSP)	Theoretical and Experimental Analysis of GNSS signals scattered from soils with different bio-geophysical parameters.	GNSS-R instrument upgrade, experimental campaign coordination and execution, GNSS-R data analysis and interpretation.
PARIS-ABD	2010-2012	ESA (Astrium)	PARIS Airborne Demonstrator experimental campaigns.	Data analysis for GNSS-R altimetry estimation from an airborne platform.
StarGym2	2011-2012	ESA (RFQ)	Design and implementation of an End-to-End GNSS-R simulator.	Development of key upgrades in the simulator. Simulator final integration tests.
COS-MEMOS	2011-2013	EU	Assessment of benefits of GNSS on board sensors for the meteo-marine environment.	Development of Galileo E1 and E5 tracking algorithms.
GRASS	2011-2012	ESA (EGEP)	Design and implementation of an End-to-End GNSS-R simulator.	SAM instrument upgrades, experimental campaigns coordination, GNSS-R data processing, analysis, and interpretation.
PARIS-IOD Phase-A Study	2011-2013	ESA (EGEP/GSP)	Phase-A Study for the PARIS In Orbit Demonstrator Mission.	Performance analysis of PARIS-IOD mission for sea surface height retrieval by means of the StarGym End-to-End simulator.

Table A.1: (Cont.) Relevant contributions to GNSS-R related projects.

Appendix B

List of Publications

A. Egido, M. Caparrini, G. Ruffini, S. Paloscia, E. Santi, L. Guerriero, N. Pierdicca, N. Floury, "Global Navigation Satellite Systems Reflectometry as a Remote Sensing Tool for Agriculture", *Remote Sensing*, vol. 4, 2012

N. Pierdicca, L. Guerriero, M. Brogioni, and A. Egido, "On the coherent and non coherent components of bare and vegetated terrain bistatic scattering: Modelling the GNSS-R signal over land", in *Proc. Geoscience and Remote Sensing Symposium (IGARSS)*, pp. 3407-3410, 2012

N. Pierdicca, L. Guerriero, R. Giusto, M. Brogioni, A. Egido, and N. Floury, "GNSS reflections from bare and vegetated soils: Experimental validation of an end-to-end simulator," in *Proc. Geoscience and Remote Sensing Symposium (IGARSS)*, pp. 4371-4374, 2011

M. Garcia-Fernandez, A. Egido, and M. Caparrini, "StarGym: a GNSS-R End to End Simulator", in *Proc. Advanced RF Sensors and Remote Sensing Instrument (ARSI)*, ESA/ESTEC, 2011.

A. Egido, M. Caparrini, P. Paloscia, E. Santi, L. Guerriero, and N. Pierdicca, "GNSS-R Polarimetric Long Term Observations of Land Bio-Geophysical Parameters", in *Proc. 3rd Scientific and Fundamental Aspects of the Galileo Programme*, Copenhaguen, 2011

Egido, A., Caparrini, M.; "Monitoring Water Level with GNSS", *GPS World Innovation Column*, September 2010

A. Egido, M. Caparrini, L. Guerriero, N. Pierdicca, S. Paloscia, M. Brogioni, and N. Floury, "GNSS-R for land bio-geophysical parameters monitoring; the LEIMON project", GNSS-R'10 Workshop, Barcelona, 2010

R. Giusto, L. Guerriero, S. Paloscia, N. Pierdicca, A. Egido, N. Floury, "Theoretical simulations of GNSS reflections from bare and vegetated soils", GNSS-R'10 Workshop, Barcelona, 2010.

M. Brogioni M, A. Egido, N. Floury, R. Giusto, L. Guerriero, N. Pierdicca, "A simulator prototype of delay-doppler maps for GNSS reflections from bare and vegetated soils", in *Proc. Geoscience and Remote Sensing Symposium (IGARSS)*, pp. 3809-3812, 2010

A. Egido, M. Delas, M. Garcia-Fernandez, and M. Caparrini, ”Non-space applications of GNSS-R: From research to operational services. Examples of water and land monitoring systems”, in *Proc. Geoscience and Remote Sensing Symposium (IGARSS)*, Vol 2, pp. 170-173, 2009

A. Egido, G. Ruffini, M. Caparrini, C. Martin-Puig, E. Farres, X. Banque, ”Soil Moisture Monitorization Using GNSS Reflected Signals”, *ArXiv e-prints*, 2008

M. Caparrini, A. Egido, F. Soulat, O. Germain, E. Farres, S. Dunne, and G. Ruffini, ”Oceanpal: Monitoring sea state with a GNSS-R coastal instrument”, in *Proc. Geoscience and Remote Sensing Symposium (IGARSS)*, pp. 5080-5083, 2007

Bibliography

Abshire, J. B., Sun, X., Riris, H., Sirota, J. M., McGarry, J. F., Palm, S., Yi, D., and Liiva, P. (2005). Geoscience Laser Altimeter System (GLAS) on the ICESat Mission: On-orbit measurement performance. *Geophysical Research Letters*, 32.

Álvarez-Pérez, J. L. (2001). An extension of the IEM/IEMM surface scattering model. *Waves in Random Media*, 11:307–329.

Attema, E. and Ulaby, F. (1978). Vegetation modeled as a water cloud. *Radio Science*, 13:357–364.

Balanis, C. A. (1989). *Advance Engineering Electromagnetics.* John Wiley and Sons, Inc., 1st edition.

Balanis, C. A. (2005). *Antenna Theory. Analysis and Design.* John Wiley and Sons, Inc., 3rd edition.

Barre, H., Duesmann, B., and Kerr, Y. (2008). SMOS: The Mission and the System. *Geoscience and Remote Sensing, IEEE Transactions on*, 46(3):587 –593.

Barrett, B. W., Dwyer, E., and Whelan, P. (2009). Soil Moisture Retrieval from Active Spaceborne Microwave Observations: An Evaluation of Current Techniques. *Remote Sensing*, 1(3):210–242.

Beckmann, P. and Spizzichino, A. (1963). *The Scattering of Electromagnetic Waves from Rough Surfaces.* Artech House Inc.

Beidou (2013). BeiDou Navigation Satellite System (Development plan). `http://en.beidou.gov.cn/index.html`.

Belmonte-Rivas, M. (2007). Bistatic scattering of global positioning system signals from arctic sea ice. *PhD Thesis, University of Colorado.*

Bevington, P. and Robinson, K. (1969). *Data Reduction and Error Analysis for the Physical Sciences.* McGraw-Hill.

Bracaglia, M., Ferrazzoli, P., and Guerriero, L. (1995). A fully polarimetric multiple scattering model for crops. *Remote Sensing of Environment*, 54:170–179.

Brogioni, M., Egido, A., Floury, N., Giusto, R., Guerriero, L., and Pierdicca, N. (2010). A simulator prototype of Delay-Doppler Maps for GNSS reflections from bare and vegetated soils. In *Proc. International Geoscience and Remote Sensing Symposium*, pages 3809–3812. IGARSS 2010, Honolulu, Hawaii, USA.

Brown, M., Pinzon, J., Didan, K., Morisette, J., and Tucker, C. (2006). Evaluation of the consistency of long-term NDVI time series derived from AVHRR,SPOT-vegetation, SeaWiFS, MODIS, and Landsat ETM+ sensors. *IEEE Transactions on Geoscience and Remote Sensing*, 44(7):1787 –1793.

Camps, A., Vall-llossera, M., Duffo, N., Torres, F., and Corbella, I. (2005). Performance of sea surface salinity and soil moisture retrieval algorithms with different auxiliary datasets in 2-D L-band aperture synthesis interferometric radiometers. *IEEE Transactions on Geoscience and Remote Sensing*, 43(5):1189 – 1200.

Caparrini, M., Egido, A., Soulat, F., Germain, O., Farres, E., Dunne, S., and Ruffini, G. (2007). Oceanpal: Monitoring sea state with a GNSS-R coastal instrument. In *Proc. International Geoscience and Remote Sensing Symposium (IGARSS)*, pages 5080 – 5083.

Cihlar, J., Dobson, M. C., Schmugge, T., Hoogeboom, P., Janse, A. R. P., Baret, F., Guyot, G., Le Toan, T., and Pampaloni, P. (1987). Review Article Procedures for the description of agricultural crops and soils in optical and microwave remote sensing studies. *International Journal of Remote Sensing*, 8(3):427–439.

Cloude, S. (2007). Dual-Baseline Coherence Tomography. *Geoscience and Remote Sensing Letters, IEEE*, 4(1):127 –131.

Cloude, S. and Papathanassiou, K. (1998). Polarimetric SAR interferometry. *IEEE Transactions on Geoscience and Remote Sensing*, 36(5):1551 –1565.

Curlander, J. C. and McDonough, R. N. (1991). *Synthetic Aperture Radar: Systems and Signal Processing*. Wiley Series in Remote Sensing and Image Processing. John Wiley & Sons Inc.

Das, N., Entekhabi, D., and Njoku, E. (2011). An Algorithm for Merging SMAP Radiometer and Radar Data for High-Resolution Soil-Moisture Retrieval. *IEEE Transactions on Geoscience and Remote Sensing*, 49(5):1504 –1512.

de Roo, R. D. and Ulaby, F. T. (1994). Bistatic Specular Scattering from Rough Dielectric Surfaces. *IEEE Transactions on Antennas and Propagation*, 42(2):220–231.

Dobson, M. C., Ulaby, F. T., Hallikainen, M., and El-Rayes, M. (1985). Microwave Dielectric Behavior of Wet Soil - Part II: Dielectric Mixing Models. *IEEE Transactions on Geoscience and Remote Sensing*, GE-23(1):35–46.

Duong, H. V., Lefsky, M. A., Ramond, T., and Weimer, C. (2012). The Electronically Steerable Flash Lidar: A Full Waveform Scanning System for Topographic and Ecosystem Structure Applications. *IEEE Transactions on Geoscience and Remote Sensing*, PP(99):1 –12.

Durden, S., J.J., J. V., and Zebker, H. (1989). Modeling and observation of the radar polarization signature of forested areas. *IEEE Transactions on Geoscience and Remote Sensing*, 27:290–301.

Egido, A. and Caparrini, M. (2010). Friendly Reflections – Monitoring Water Level with GNSS. *GPS World, Richard Langley Innovation Column*, pages 50–55.

Egido, A., Caparrini, M., Guerriero, L., Pierdicca, N., Paloscia, S., Santi, E., and Brogioni, M. (2011). Land Monitoring with Navigation Signals, Final Report of ESA/ESTEC Contract No. 22117/08/NL/AF. Technical report, European Space Agency, Noordwijk, The Netherlands.

Egido, A., Delas, M., Garcia, M., and Caparrini, M. (2009). Non-space applications of GNSS-R: From research to operational services. Examples of water and land monitoring systems. In *Proc. Geoscience and Remote Sensing Symposium*, pages 170–173. IGARSS 2009, Cape Town, South Africa.

Elachi, C. and van Zyl, J. (2006). *Introduction to the Physics and Techniques of Remote Sensing*. Wiley Series in Remote Sensing. John Wiley & Sons, Inc., 2nd edition.

Elfouhaily, T., Chapron, B., Katsaros, K., and Vandemark, D. (1997). A Unified Directional Spectrum for Long and Short Wind-Driven Waves. *Journal of Geophysical Research*, 102:15781–15796.

Elfouhaily, T., Thompson, D., and Linstrom, L. (2002). Delay-doppler analysis of bistatically reflected signals from the ocean surface: theory and application. *IEEE Transactions on Geoscience and Remote Sensing*, 40(3):560–573.

Englhart, S., Keuck, V., and Siegert, F. (2012). Modeling Aboveground Biomass in Tropical Forests Using Multi-Frequency SAR Data; A Comparison of Methods. *IEEE Journal of Selected Topics in Applied Earth Observations and Remote Sensing*, 5(1):298 –306.

Entekhabi, D., Njoku, E., O'Neill, P., Kellogg, K., Crow, W., Edelstein, W., Entin, J., Goodman, S., Jackson, T., Johnson, J., Kimball, J., Piepmeier, J., Koster, R., Martin, N., McDonald, K., Moghaddam, M., Moran, S., Reichle, R., Shi, J., Spencer, M., Thurman, S., Tsang, L., and Van Zyl, J. (2010). The Soil Moisture Active Passive (SMAP) Mission. *Proceedings of the IEEE*, 98(5):704 –716.

Eom, H. and Fung, A. (1984). A scatter model for vegetation up to Ku-band. *Remote Sensing of Environment*, 15:185–200.

ESA (2010). SMOS: ESA's Water Mission. Technical report, ESA Communication Production Office, Noordwijk, The Netherlands.

ESA (2012a). Report for Mission Selection: Biomass, ESA SP-1324/1. Technical report, ESA Communication Production Office, Noordwijk, The Netherlands.

ESA (2012b). What is Galileo? http://www.esa.int/esaNA/galileo.html. Retrieved on Apr. 2012.

EU (2010). European GNSS (Galileo) Open Service, Signal in Space Interface Control Document - OD SIS ICD, Issue 1.1. Technical report, European Union.

EU (2012). Satellite Navigation Programme. http://ec.europa.eu/enterprise/policies /satnav/galileo/programme/index_en.htm.

Evans, J. and Hudak, A. (2007). A Multiscale Curvature Algorithm for Classifying Discrete Return LiDAR in Forested Environments. *IEEE Transactions on Geoscience and Remote Sensing*, 45(4):1029 –1038.

Fabra, F., Cardellach, E., Nogues-Correig, O., Oliveras, S., Ribo, S., Rius, A., Belmonte-Rivas, M., Semmling, M., Macelloni, G., Pettinato, S., Zasso, R., and D'Addio, S. (2010). Monitoring sea-ice and dry snow with GNSS reflections. In *Proc. International Geoscience and Remote Sensing Symposium*, pages 3837 –3840. IGARSS 2010, Honolulu, Hawaii, USA.

Fabra, F., Cardellach, E., Rius, A., Ribo, S., Oliveras, S., Nogues-Correig, O., Belmonte Rivas, M., Semmling, M., and D'Addio, S. (2012). Phase Altimetry With Dual Polarization GNSS-R Over Sea Ice. *IEEE Transactions on Geoscience and Remote Sensing*, 50(6):2112 –2121.

Fensholt, R., Sandholt, I., and Stisen, S. (2006). Evaluating MODIS, MERIS, and VEGETATION vegetation indices using in situ measurements in a semiarid environment. *IEEE Transactions on Geoscience and Remote Sensing*, 44(7):1774 –1786.

Ferrazzoli, P. and Guerriero, L. (1995). Radar sensitivity to tree geometry and woody volume: A model analysis. *IEEE Transactions on Geoscience and Remote Sensing*, 33(2):360–371.

Ferrazzoli, P., Guerriero, L., Pierdicca, N., and Rahmoune, R. (2010). Forest biomass monitoring with GNSS-R: Theoretical simulations. *Advances in Space Research*, 47(10):1823 – 1832.

Ferrazzoli, P., Guerriero, L., and Solimini, D. (2000). Simulating bistatic scatter from surfaces covered with vegetation. *J. Electromagnetic Waves and Applications*, 14:233–248.

Ferrazzoli, P., Paloscia, S., Pampaloni, P., Schiavon, G., Sigismondi, S., and Solimini, D. (1997). The potential of multifrequency polarimetric SAR in assessing agricultural and arboreous biomass. *IEEE Transactions on Geoscience and Remote Sensing*, 35(1):5 –17.

Fornaro, G., Lombardini, F., and Serafino, F. (2005). Three-dimensional multipass SAR focusing: experiments with long-term spaceborne data. *IEEE Transactions on Geoscience and Remote Sensing*, 43(4):702 – 714.

Fung, A. and Eom, H. (1983). Coherent scattering of a spherical wave from an irregular surface. *IEEE Transactions on Antennas and Propagation*, 31:68–72.

Fung, A., Li, Z., and Chen, K. (1992). Backscattering from a randomly rough dielectric surface. *IEEE Transactions on Geoscience and Remote Sensing*, 30(2):356 –369.

Fung, A. and Ulaby, F. (1978). A scatter model for leafy vegetation. *IEEE Transactions on Geoscience and Remote Sensing*, 16:281–286.

Fung, A. K. (1994). *Microwave scattering and emission models and their applications*. Artech House.

Garcia-Fernandez, M., Egido, A., and Caparrini, M. (2011). StarGym, a GNSS-R end-to-end simulator. In *Proc. Third Workshop on Advanced RF Sensors and Remote Sensing Instruments*, ESA-ESTEC. European Space Agency.

Garestier, F., Dubois-Fernandez, P., and Champion, I. (2008a). Forest Height Inversion Using High-Resolution P-Band Pol-InSAR Data. *IEEE Transactions on Geoscience and Remote Sensing*, 46(11):3544 –3559.

Garestier, F., Dubois-Fernandez, P., and Papathanassiou, K. (2008b). Pine Forest Height Inversion Using Single-Pass X-Band PolInSAR Data. *IEEE Transactions on Geoscience and Remote Sensing*, 46(1):59 –68.

Garestier, F. and Le Toan, T. (2010). Estimation of the Backscatter Vertical Profile of a Pine Forest Using Single Baseline P-Band (Pol-)InSAR Data. *IEEE Transactions on Geoscience and Remote Sensing*, 48(9):3340 –3348.

Garrison, J. (2007). Techniques of bistatic radar using GNSS-R signals for earth remote sensing. *Universitat Politecnica de Catalunya, TSC distinguished lectures series (slides).*

Garrison, J., Komjathy, A., Zavorotny, V., and Katzberg, S. (2002). Wind speed measurement using forward scattered GPS signals. *IEEE Transactions on Geoscience and Remote Sensing*, 40(1):50–65.

GCOS (2012). Global Climate Observing System Essential Climate Variables. http://www.wmo.int/pages/prog/gcos/index.php?name=EssentialClimateVariables.

Germain, O., Caparrini, M., and Ruffini, G. (2005). First Analysis of SSTL GPS-R experiment. *Starlab Technical Notes, available at starlab.es.*

Germain, O., Ruffini, G., Soulat, F., Caparrini, M., Chapron, B., and Silvestrin, P. (2004). The Eddy Experiment: GNSS-R speculometry for directional sea-roughness retrieval from low altitude aircraft. *Geophys. Res. Letters.*

Gleason, S. (2005). Sensing Ocean, Ice and Land Reflected Signals from Space: Results from the UK-DMC GPS Reflectometry Experiment. In *Proc. International Technical Meeting of the Satellite Division of The Institute of Navigation, ION GNSS*, pages 1679 – 1685.

Gleason, S. (2006a). Detecting Bistatically Reflected GPS Signals from Low Earth Orbit Over Land Surfaces. In *Proc. Geoscience and Remote Sensing Symposium*, pages 3086–3089. IGARSS 2006, Denver, Colorado, USA.

Gleason, S. (2006b). Remote Sensing of Ocean, Ice and Land Surfaces Using Bistatically Scattered GNSS Signals From Low Earth Orbit. *Ph.D Thesis, University of Surrey.*

Gleason, S., Hodgart, S., Sun, Y., Gommenginger, C., Mackin, S., Adjrad, M., and Unwin, M. (2005). Detection and Processing of Bistatically Reflected GPS Signals From Low Earth Orbit for the Purpose of Ocean Remote Sensing. *IEEE Transactions on Geoscience and Remote Sensing*, 43(6):1229–1241.

GPSW (2010). Navstar GPS Space Segment/Navigation User Interfaces (IS-GPS-200 Revision E) . Technical report, Global Positioning System Wing Systems Engineering & Integration.

Grant, M., Acton, S., and Katzberg, S. (2007). Terrain Moisture Classification Using GPS Surface-Reflected Signals. *Geoscience and Remote Sensing Letters, IEEE*, 4(1):41 –45.

Hajj, G. A. and Zuffada, C. (2003). Theoretical description of a bistatic system for ocean altimetry using the GPS signal. *Radio Science*, 38(5):1–10.

Hallikainen, M., Ulaby, F. T., Dobson, M. C., El-Rayes, M., and Wu, L. (1985). Microwave Dielectric Behavior of Wet Soil-Part 1:Empirical Models and Experimental Observations. *IEEE Transactions on Geoscience and Remote Sensing*, GE-23(1):25–34.

Hoekman, D. and Quiriones, M. (2000). Land cover type and biomass classification using AirSAR data for evaluation of monitoring scenarios in the Colombian Amazon. *IEEE Transactions on Geoscience and Remote Sensing*, 38(2):685–696.

Hofmann-Wellenhof B., Lichtenegger H., C. J. (2001). *GPS Theory and Practice*. Artech House.

Huete, A., Didan, K., Miura, T., Rodriguez, E., Gao, X., and Ferreira, L. (2002). Overview of the radiometric and biophysical performance of the MODIS vegetation indices. *Remote Sensing of Environment*, 83(1):195–213.

Huete, A. R., Didan, K., Shimabukuro, Y. E., Ratana, P., Saleska, S. R., Hutyra, L. R., Yang, W., Nemani, R. R., and Myneni, R. (2006). Amazon rainforests green-up with sunlight in dry season. *Geophys. Res. Lett.*, 33(6).

IPCC (2007). IPCC Fourt Assesment Report: Climate Change 2007, The Physical Science Basis. Technical report, Cambridge University Press, Cambridge, UK.

Jackson, T. and Schmugge, T. (1991). Vegetation effects on the microwave emission of soils. *Remote Sensing of Environment*, 36(3):203 – 212.

Jiang, Z., Huete, A. R., Didan, K., and Miura, T. (2008). Development of a two-band enhanced vegetation index without a blue band. *Remote Sensing of Environment*, 112(10):3833 – 3845.

Kasischke, E., Christensen, N., and Haney, E. (1994). Modeling of geometric properties of loblobby pine tree stand characteristics for use in radar backscatter studies. *IEEE Transactions on Geoscience and Remote Sensing*, 32:800–822.

Katzberg, S. and Garrison, J. (1996). Utilizing GPS to determine ionospheric delay over the ocean. *NASA Technical Memorandum 4750, NASA.*

Katzberg, S. and Garrison, J. (1997). Detection of ocean reflected GPS signals: theory and experiment. *Proceedings of the IEEE SOUTHEASTCON.*

Katzberg, S. J., Garrison, J., and Howell, C. (1999). Simple over-water altimeter using GPS reflections. In *Proc. ION GPS Conference*, pages 1819–1827.

Katzberg, S. J., Torres, O., Grant, M. S., and Masters, D. (2006). Utilizing calibrated GPS reflected signals to estimate soil reflectivity and dielectric constant: Results from smex02. *Remote Sensing of Environment*, 100(1):17 – 28.

Kavak, A., Vogel, W., and Xu, G. (1998). Using GPS to measure ground complex permittivity. *Electronics Letters*, 34(3):254–255.

Kerr, Y., Waldteufel, P., Richaume, P., Wigneron, J., Ferrazzoli, P., Mahmoodi, A., Al Bitar, A., Cabot, F., Gruhier, C., Juglea, S., Leroux, D., Mialon, A., and Delwart, S. (2012). The SMOS Soil Moisture Retrieval Algorithm. *IEEE Transactions on Geoscience and Remote Sensing*, 50(5):1384 –1403.

Koetz, B., Morsdorf, F., Sun, G., Ranson, K., Itten, K., and Allgower, B. (2006). Inversion of a lidar waveform model for forest biophysical parameter estimation. *IEEE Transactions on Geoscience and Remote Sensing*, 3(1):49 – 53.

Komjathy, A., Armatys, M., Masters, D., Axelrad, P., Zavorotny, V., and Katzberg, S. (2004). Retrieval of ocean surface wind speed and wind direction using reflected GPS signals. *Journal of Atmospheric and Oceanic Technology*, pages 515–526.

Kurvonen, L., Pulliainen, J., and Hallikainen, M. (1999). Retrieval of biomass in boreal forests from multitemporal ERS-1 and JERS-1 SAR images. *IEEE Transactions on Geoscience and Remote Sensing*, 37(1):198 –205.

Larson, K., Braun, J., Small, E., Zavorotny, V., Gutmann, E., and Bilich, A. (2010). GPS Multipath and Its Relation to Near-Surface Soil Moisture Content. *Selected Topics in Applied Earth Observations and Remote Sensing, IEEE Journal of*, 3(1):91 –99.

Le-Toan, T., Quegan, S., Davidson, M., Balzter, H., Paillou, P., Papathanassiou, K., Plummer, S., Rocca, F., Saatchi, S., Shugart, H., and Ulander, L. (2011). The BIOMASS mission: Mapping global forest biomass to better understand the terrestrial carbon cycle. *Remote Sensing of Environment*, 115(11):2850 – 2860.

Lefsky, M. A. (2010). A global forest canopy height map from the moderate resolution imaging spectroradiometer and the geoscience laser altimeter system. *Geophys. Res. Lett.*, 37(15).

Lefsky, M. A., Cohen, W. B., Parker, G. G., and Harding, D. J. (2002). Lidar Remote Sensing for Ecosystem Studies. *BioScience*, 52(1):19–30.

Lim, K., Treitz, P., Wulder, M., St-Onge, B., and Flood, M. (2003). LiDAR remote sensing of forest structure. *Progress in Physical Geography*, 27(1):88–106.

Lim, K. S. and Treitz, P. M. (2004). Estimation of above ground forest biomass from airborne discrete return laser scanner data using canopy-based quantile estimators. *Scandinavian Journal of Forest Research*, 19:558–570.

Lohan, E. S. (2010). Analytical performance of CBOC-modulated Galileo E1 signal using sine BOC(1,1) receiver for mass-market applications. In *Proc. Position Location and Navigation IEEE Symposium*, pages 245–253.

Lowe, S., LaBrecque, J., Zuffada, C., Romans, L., Young, L., and Hajj, G. (2002a). First spaceborne observation of an earth-reflected GPS signal. *Radio Science*, 37(1):7–1–7–28.

Lowe, S., Zuffada, C., Chao, Y., Kroger, P., Young, L., and LaBrecque, J. (2002b). 5-cm-precision aircraft ocean altimetry using GPS reflections. *Geophys. Res. Letters*, 29(10):13–1–13–4.

Macelloni, G., Nesti, G., Pampaloni, P., Sigismondi, S., Tarchi, D., and Lolli, S. (2000). Experimental validation of surface scattering and emission models. *IEEE Transactions on Geoscience and Remote Sensing*, 38(1):459 –469.

Macelloni, G., Paloscia, S., Pampaloni, P., Marliani, F., and Gai, M. (2001). The relationship between the backscattering coefficient and the biomass of narrow and broad laf crops. *IEEE Transactions on Geoscience and Remote Sensing*, 39(4):873–884.

Marchan, J. (2009). Sea State Determination Using GNSS-R Techniques: Contributions to the PAU Instrument. *PhD Thesis, Universitat Politecnica de Catalunya.* `http://hdl.handle.net/10803/6932`.

Martin-Neira, M. (1993). A Passive Reflectometry and Interferometry System (PARIS): Application to Ocean Altimetry. *ESA Journal*, 17(4):331–355.

Martin-Neira, M., D'Addio, S., Buck, C., Floury, N., and Prieto-Cerdeira, R. (2011). The PARIS Ocean Altimeter In-Orbit Demonstrator. *IEEE Transactions on Geoscience and Remote Sensing*, 49(6):2209 –2237.

Masters, D. (2004). Surface remote sensing applications of GNSS bistatic radar, soil moisture and aircraft altimetry. *PhD Thesis, University of Colorado.*

Masters, D., Axelrad, P., and Katzberg, S. (2004). Initial results of land-reflected GPS bistatic radar measurements in SMEX02. *Remote Sensing of Environment*, 92:507–520.

Masters, D., Zavorotny, V., Katzberg, S., and Emery, W. (2000). GPS signal scattering from land for moisture content determination. In *Proc. Geoscience and Remote Sensing Symposium. IGARSS 2000*, volume 7, pages 3090–3092. Honolulu, Hawaii, USA.

Matzler, C. (1994). Microwave (1-100 ghz) dielectric model of leaves. *IEEE Transactions on Geoscience and Remote Sensing*, 32:947–949.

Means, J. E., Acker, S. A., Harding, D. J., Blair, J., Lefsky, M. A., Cohen, W. B., Harmon, M. E., and McKee, W. (1999). Use of Large-Footprint Scanning Airborne Lidar To Estimate Forest Stand Characteristics in the Western Cascades of Oregon. *Remote Sensing of Environment*, 67(3):298 – 308.

Misra, P. and Enge, P. (2006). *Global Positioning System: Signals, Measurements, and Performance.* Ganga Jamuna Press, 2nd edition.

Mitchard, E. T. A., Saatchi, S. S., White, L. J. T., Abernethy, K. A., Jeffery, K. J., Lewis, S. L., Collins, M., Lefsky, M. A., Leal, M. E., Woodhouse, I. H., and Meir, P. (2011). Mapping tropical forest biomass with radar and spaceborne LiDAR: overcoming problems of high biomass and persistent cloud. *Biogeosciences Discussions*, 8(4):8781–8815.

Mitchard, E. T. A., Saatchi, S. S., Woodhouse, I. H., Nangendo, G., Ribeiro, N. S., Williams, M., Ryan, C. M., Lewis, S. L., Feldpausch, T. R., and Meir, P. (2009). Using satellite radar backscatter to predict above-ground woody biomass: A consistent relationship across four different African landscapes. *Geophys. Res. Lett.*, 36:1–6.

Myneni, R., Ramakrishna, R., Nemani, R., and Running, S. (1997). Estimation of global leaf area index and absorbed par using radiative transfer models. *IEEE Transactions on Geoscience and Remote Sensing*, 35(6):1380 –1393.

NASA (2008). The Water Cycle. NASA Earth's Sciences webpage: http://science.nasa.gov/earth-science/oceanography/ocean-earth-system/ocean-water-cycle/. Retrieved in Feb. 2012.

NASA News & Features Webpage (2010). First-of-its-kind map depicts global forest heights. http://www.nasa.gov/topics/earth/features/forest-height-map.html. Data from M. Lefsky. Retrieved in August 2012.

Neumann, M., Saatchi, S., Ulander, L., and Fransson, J. (2012). Assessing Performance of L- and P-Band Polarimetric Interferometric SAR Data in Estimating Boreal Forest Above-Ground Biomass. *IEEE Transactions on Geoscience and Remote Sensing*, 50(3):714 –726.

Njoku, E., Jackson, T., Lakshmi, V., Chan, T., and Nghiem, S. (2003). Soil moisture retrieval from AMSR-E. *IEEE Transactions on Geoscience and Remote Sensing*, 41(2):215 – 229.

Paloscia, S., Santi, E., Fontanelli, G., Pettinato, S., Egido, A., Caparrini, M., Guerriero, L., and Pierdicca, N. (2013). GRASS: GNSS Reflectometry Analysis for biomaSS monitoring. ESA/ESTEC Contract No. 4000103329/11/NL/CVG. Technical report, European Space Agency, Noordwijk, The Netherlands.

Papathanassiou, K. and Cloude, S. (2001). Single-baseline polarimetric SAR interferometry. *IEEE Transactions on Geoscience and Remote Sensing*, 39(11):2352 –2363.

Parkinson, B. W. and Spilker, J. J. (1996). *Global Positioning System: Theory and Applications*. Progress in Astronautics and Aeronautics. American Institute of Aeronautics and Astronautics, Inc., 1st edition.

Pathe, C., Wagner, W., Sabel, D., Doubkova, M., and Basara, J. (2009). Using Envisat ASAR Global Mode Data for Surface Soil Moisture Retrieval Over Oklahoma, USA. *IEEE Transactions on Geoscience and Remote Sensing*, 47(2):468 –480.

Pierdicca, N., Pulvirenti, L., Ticconi, F., Pampaloni, P., Macelloni, G., Brogioni, M., Pettinato, S., Guerriero, L., Ferrazzoli, P., della Pietra, G., and Capobianco, F. (2007). Use of Bistatic Microwave Measurements for Earth Observation, Final Report of ESA Contract 19173/05/NL/GLC. Technical report, European Space Agency, Noordwijk, The Netherlands.

Piles, M., Camps, A., Vall-Llosera, M., and Talone, M. (2009). Spatial-Resolution Enhancement of SMOS Data: A Deconvolution-Based Approach. *IEEE Transactions on Geoscience and Remote Sensing*, 47(7):2182 – 2192.

Reigber, A. and Moreira, A. (2000). First demonstration of airborne SAR tomography using multibaseline L-band data. *IEEE Transactions on Geoscience and Remote Sensing*, 38(5):2142 –2152.

Rodriguez-Alvarez, N., Camps, A., Vall-llossera, M., Bosch-Lluis, X., Monerris, A., Ramos-Perez, I., Valencia, E., Marchan-Hernandez, J., Martinez-Fernandez, J., Baroncini-Turricchia, G., Perez-Gutierrez, C., and Sanchez, N. (2011). Land Geophysical Parameters Retrieval Using the Interference Pattern GNSS-R Technique. *IEEE Transactions on Geoscience and Remote Sensing*, 49(1):71 –84.

Rodriguez-Alvarez, N., Marchen, J., Camps, A., Bosch-Lluis, E. V. X., Ramos-Perez, I., and Nieto, J. (2008). Soil moisture retrieval using GNSS-R techniques: measurement campaign in a wheat field. In *Proc Geoscience Remote Sensing Symposium*, pages II–245. IGARSS 2008, Boston, USA.

Ruffini, G. and Soulat, F. (2000). Monte-Carlo simulations for L-band electromagnetic reflections, Technical report, OPPSCAT I WP3230 - ESA ESTEC Contract No. 13461/99/NL/GD. Technical report, European Space Agency.

Ruffini, G. and Soulat, F. (2004). On the GNSS-R Interferometric Complex Field Coherence Time. *arXiv:physics/0406084v2*.

Ruffini, G., Soulat, F., Caparrini, M., and Germain, O. (2003). The GNSS-R eddy experiment i: altimetry from low altitude aircraft. *Proc. Workshop on Oceanography with GNSS-R*.

Saatchi, S., Halligan, K., Despain, D., and Crabtree, R. (2007). Estimation of Forest Fuel Load From Radar Remote Sensing. *IEEE Transactions on Geoscience and Remote Sensing*, 45(6):1726 –1740.

Sabia, R., Caparrini, M., Camps, A., and G.Ruffini (2007). Potential Synergetic Use of GNSS-R Signals to Improve the Sea-State Correction in the Sea Surface Salinity Estimation: Application to the SMOS Mission. *IEEE Transactions on Geoscience and Remote Sensing*, 45(7):2088–2097.

Santoro, M., Beer, C., Cartus, O., Schmullius, C., Shvidenko, A., McCallum, I., Wegmuller, U., and Wiesmann, A. (2011). Retrieval of growing stock volume in boreal forest using hyper-temporal series of Envisat ASAR ScanSAR backscatter measurements. *Remote Sensing of Environment*, 115:490–507.

Schiffer, R. and Thielheim, K. O. (1979). Light scattering by dielectric needles and disks. *J. Appl. Phys*, 50:2476–2483.

Simard, M., Pinto, N., Fisher, J. B., and Baccini, A. (2011). Mapping forest canopy height globally with spaceborne lidar. *J. Geophys. Res.*, 116(G4).

Sims, D. A., Rahman, A. F., Cordova, V. D., El-Masri, B. Z., Baldocchi, D. D., Flanagan, L. B., Goldstein, A. H., Hollinger, D. Y., Misson, L., Monson, R. K., Oechel, W. C., Schmid, H. P., Wofsy, S. C., and Xu, L. (2006). On the use of MODIS EVI to assess gross primary productivity of North American ecosystems. *J. Geophys. Res.*, 111(G4).

Skolnik, M. I. (1990). *Radar Handbook*. MvGraw Hill, 2nd edition.

Soulat, F. (2003). Sea Surface Remote Sensing with GNSS and Sunlight Reflections. *PhD Thesis*.

Starlab (2008). *SAM : An Innovative Microwave System for Soil Moisture Monitoring, D5 and D6, Commercial Activities Report*. ESTEC Contract No. 20898/07/NL/ST/na.

Steven, M. D., Malthus, T. J., Baret, F., Xu, H., and Chopping, M. J. (2003). Intercalibration of vegetation indices from different sensor systems. *Remote Sensing of Environment*, 88(4):412–422.

Sun, G. and Ranson, K. (2000). Modeling lidar returns from forest canopies. *IEEE Transactions on Geoscience and Remote Sensing*, 38(6):2617 – 2626.

Tebaldini, S. and Rocca, F. (2012). Multibaseline Polarimetric SAR Tomography of a Boreal Forest at P- and L-Bands. *IEEE Transactions on Geoscience and Remote Sensing*, 50(1):232 –246.

Thompson, A. R., Moran, J. M., and Swenson Jr., G. W. (2001). *Interferometry and Synthesis in Radio Astronomy*. Wiley-Interscience.

Thompson, D. R., Elfouhaily, T. M., and Garrison, J. L. (2005). An Improved Geometrical Optics Model for Bistatic GPS Scattering from the Ocean Surface. *IEEE Transactions on Geoscience and Remote Sensing*, 43(12):2810–2821.

Torres, O. (2004). Analysis of Reflected Global Positioning System Signals as a Method for the Determination of Soil Moisture. *Master Thesis, University of Texas.*

Twomey, S., Jacobowitz, H., and Howell, H. (1966). Matrix methods for multiple scattering problems. *Journal of Atmospheric Sciences*, 23:289–295.

Ulaby, F. and El-Rayes, M. (1987). Microwave dielectric spectrum of vegetation - Part II: Dual dispersion model. *IEEE Transactions on Geoscience and Remote Sensing*, 25:550–556.

Ulaby, F., Sarabandi, K., McDonald, K., Whitt, M., and Dobson, M. (1990). Michigan microwave canopy scattering model. *Int. J. Remote Sensing*, 11:1223–1253.

Ulaby, F. T. and Dobson, M. C. (1989). *Handbook of Radar Scattering Statistics for Terrain.* Artech House.

Ulaby, F. T., Moore, R. K., and Fung, A. K. (1986a). *Microwave Remote Sensing, Active and Passive*, volume 2. Addison Wesley.

Ulaby, F. T., Moore, R. K., and Fung, A. K. (1986b). *Microwave Remote Sensing, Active and Passive*, volume 1. Addison Wesley.

Valencia, E., Camps, A., Marchan-Hernandez, J., Rodriguez-Alvarez, N., Ramos-Perez, I., and Bosch-Lluis, X. (2010). Experimental Determination of the Sea Correlation Time Using GNSS-R Coherent Data. *Geoscience and Remote Sensing Letters, IEEE*, 7(4):675 –679.

Wang, J. R. and Schmugge, T. J. (1980). An Empirical Model for the Complex Dielectric Permittivity of Soils as a Function of Water Content. *IEEE Transactions on Geoscience and Remote Sensing*, GE-18(4):288 –295.

Wang, X., Xie, H., Guan, H., and Zhou, X. (2007). Different responses of MODIS-derived NDVI to root-zone soil moisture in semi-arid and humid regions. *Journal of Hydrology*, 340:12–24.

Wigneron, J.-P., Kerr, Y., Waldteufel, P., Saleh, K., Escorihuela, M.-J., Richaume, P., Ferrazzoli, P., de Rosnay, P., Gurney, R., Calvet, J.-C., Grant, J., Guglielmetti, M., Hornbuckle, B., Maetzler, C., Pellarin, T., and Schwank, M. (2007). L-band Microwave Emission of the Biosphere (L-MEB) Model: Description and calibration against experimental data sets over crop fields. *Remote Sensing of Environment*, 107(4):639 – 655.

Wu, T.-D. and Chen, K.-S. (2004). A reappraisal of the validity of the IEM model for backscattering from rough surfaces. *IEEE Transactions on Geoscience and Remote Sensing*, 42(4):743 – 753.

You, H., Garrison, J., Heckler, G., and Zavorotny, V. (2004). Stochastic voltage model and experimental measurement of ocean-scattered GPS signal statistics. *IEEE Transactions on Geoscience and Remote Sensing*, 42(10):2160–2169.

Zavorotny, V., Larson, K., Braun, J., Small, E., Gutmann, E., and Bilich, A. (2010). A Physical Model for GPS Multipath Caused by Land Reflections: Toward Bare Soil Moisture Retrievals. *Selected Topics in Applied Earth Observations and Remote Sensing, IEEE Journal of*, 3(1):100 –110.

Zavorotny, V., Masters, D., Gasiewski, A., Bartram, B., Katzberg, S., Axelrad, P., and Zamora, R. (2003). Seasonal polarimetric measurements of soil moisture using tower-based GPS bistatic radar. In *Proc. Geoscience and Remote Sensing Symposium*, volume 2, pages 781 – 783 vol.2. IGARSS 2003, Toulouse, France.

Zavorotny, V. and Voronovich, A. (2000a). Bistatic GPS signal reflections at various polarizations from rough land surface with moisture content. In *In Proceedings Geoscience and Remote Sensing Symposium*, volume 7, pages 2852 –2854. IGARSS 2000, Honolulu, HI, USA.

Zavorotny, V. and Voronovich, A. (2000b). Scattering of GPS signals from the ocean with wind remote sensing application. *IEEE Transactions on Geoscience and Remote Sensing*, 38(2):951–964.

Zuffada, C., Fung, A., Parker, J., Okolicanyi, M., and Huang, E. (2004). Polarization Properties of the GPS Signal Scattered off a Wind-Driven Ocean. *IEEE Transactions on Antennas and Propagation*, 52(1):172–188.